Mutations in the Inner Pore of a Cav2.1 Voltage-Gated Calcium Channel Differentially Affect the Efficacy, Potency, and Binding Kinetics of an *(R)*-Roscovitine-Derived Positive Allosteric Gating Modifier

by

Stephanie Beatrice Aldrich

B.A. Neuroscience, Clark University, 2013

Submitted to the Graduate Faculty of the

Dietrich School of Arts and Sciences in partial fulfillment

of the requirements for the degree of

Doctor of Philosophy

University of Pittsburgh

2021

UNIVERSITY OF PITTSBURGH

DIETRICH SCHOOL OF ARTS AND SCIENCES

This dissertation was presented

by

Stephanie Beatrice Aldrich

It was defended on

November 23, 2021

and approved by

Tija C. Jacob, Assistant Professor, Department of Neuroscience, University of Pittsburgh

Jon W. Johnson, Professor, Department of Neuroscience, University of Pittsburgh

Diane Lipscombe, Professor, Department of Neuroscience, Brown University

Oliver Schlüter, Associate Professor, Department of Neuroscience, University of Pittsburgh

Ivet Bahar, Distinguished Professor, Computational & Systems Biology, School of Medicine, University of Pittsburgh

Rozita Laghaei, Research Scientist, Pittsburgh Supercomputing Center, Carnegie Mellon University

Thesis Advisor/Dissertation Director: Stephen D. Meriney, Professor and Chairman, Department of Neuroscience, University of Pittsburgh

Mutations in the Inner Pore of a $Ca_V2.1$ Voltage-Gated Calcium Channel Differentially Affect the Efficacy, Potency, and Binding Kinetics of an *(R)*-Roscovitine-Derived Positive Allosteric Gating Modifier

Stephanie Beatrice Aldrich, PhD

University of Pittsburgh, 2021

Insufficient release of neurotransmitter from motor neurons is a cause of debilitating muscle weakness in multiple types of neuromuscular disease, including Lambert-Eaton Myasthenic Syndrome and Spinal Muscular Atrophy. Neurotransmitter release from motor neurons is controlled by the Ca_V2 family of voltage-gated Ca^{2+} channels (VGCCs), which open in response to an action potential, causing an influx of Ca^{2+} that triggers vesicle fusion. The drug GV-58, an analog of the CDK inhibitor *(R)*-roscovitine, has been found to rescue neuromuscular transmission in animal disease models by selectively prolonging the opening of Ca_V2 VGCCs, thereby enhancing Ca^{2+} influx during action potentials and increasing the probability of vesicle fusion. Other analogs of *(R)*-roscovitine have been shown to have similar effects on VGCCs, with varying degrees of selectivity, potency, efficacy, and speed of action.

Understanding where *(R)*-roscovitine analogs bind to VGCCs and the mechanism by which they prolong channel opening would aid in the design of new analogs with improved therapeutically-relevant characteristics, as well as providing new insight into the structural basis of VGCC gating. To investigate these questions, my colleagues and I used homology models of the structure of the VGCC subtype $Ca_V2.1$ to guide mutagenesis experiments aimed at identifying specific amino acid residues that may interact with *(R)*-roscovitine analogs.

In Chapter 3, we describe our *in silico* predictions of GV-58 binding, which support the interpretation that the *(R)*-roscovitine analog binding site is accessible from the plasma membrane

through a fenestration in the channel protein. In Chapter 4, we present whole-cell patch clamp electrophysiology data from channels in which we had individually mutated amino acid residues that are unique to Ca_V2 channels and were predicted *in silico* to bind *(R)*-roscovitine analogs. We found multiple mutations that affect the drug's ability to bind the channel and/or the extent to which drug binding prolongs channel opening. In chapter 5, we show how mutating key residues implicated in VGCC gating affects *(R)*-roscovitine analog action. Finally, in Chapter 6, we propose a mechanistic hypothesis of *(R)*-roscovitine analog action in VGCCs.

Table of Contents

List of Tables

List of Figures

List of Equations

Preface

I would like to acknowledge and thank Dr. Rozita Laghaei and Dr. Mary Cheng for their work on the computer modeling side of the project. The *in silico* work described in Chapter 3 is theirs, and was the foundation of my mutagenesis experiments and mechanistic hypotheses. I could not have pursued this approach to my research questions without their contributions. I would also like to acknowledge and thank my colleague Chris Yang for his assistance with creating the $Ca_V2.1$ mutant channels, and my undergraduate assistants Sahil Kumar and Ellie Cowen for assisting with the collection of electrophysiological data.

I thank all the friends and family who have supported me through this final stage of my graduation education, whether by giving feedback on this document and my defense presentation, sending me encouragement and takeout food as I approached the deadline, or just lending an ear. I thank my parents for providing me with a start in life that gave me the freedom to pursue my academic aspirations, which is a privilege that I do not take lightly. I thank my best friend Katherine, who has been my rock and my moral beacon for more than a decade. I thank my undergraduate mentor, Néva Meyer, who guided me through the first steps of my research journey. I thank my committee members, whose advice and expertise have been invaluable these past years. Above all I thank my adviser Stephen Meriney, who showed me the value of cross-disciplinary collaboration, and whose unwavering support and encouragement gave me the confidence to challenge myself in my research and greatly benefited my development as a scientist.

1.0 Background: Calcium channel structure, function, and role in LEMS disease mechanism

1.1 Introduction

Voltage-gated calcium channels (VGCCs) are transmembrane proteins that react to membrane depolarization by briefly becoming selectively permeable to calcium ions (Ca^{2+}), permitting passive influx of extracellular Ca^{2+} into the cell. Ca^{2+} is a second messenger in a variety of intracellular pathways responsible for functions such as gene expression, excitation-contraction coupling in muscle cells, secretion in endocrine cells, and neurotransmission at synapses (Catterall, 2000; Catterall, 2011; Clapham, 2007). VGCCs therefore act as critical signal transducers for many cellular processes, converting the electrical signal of membrane depolarization into an intracellular Ca^{2+} signal.

1.2 Structure and Function of Voltage-Gated Calcium Channels (VGCCs)

The VGCC complex is made up of multiple subunits. The primary subunit is the transmembrane α1 protein that contains both the Ca^{2+}-selective permeation pathway (or pore) and the voltage-sensing structures. The Ca_V α1 subunit is a pseudo-tetrameric protein in which a single ~2000-amino-acid-long sequence is organized into four homologous domains (DI through DIV), which are symmetrically arranged in a cylindrical manner around the central pore (Figure 1). Each domain consists of six transmembrane α-helices termed segments S1-S6, with S1-S4 forming the

voltage-sensing domain (VSD) of each domain, and the S5-S6 segments of all four domains together lining the pore, which forms the pathway for ion flow across the plasma membrane (PM) (Catterall, 2000; Catterall, 2011; Guidelli, 2020). The VSD of each domain is adjacent to the pore-forming segments of a neighboring domain, proceeding clockwise around the channel (Gao et al., 2021; Hering et al., 2018; Wu et al., 2016). The Ca_V α1 subunit shares this basic functional organization with voltage-gated sodium (Na^+) and potassium (K^+) channels; Na^+ channels have the same pseudo-tetrameric arrangement of a single, long amino acid sequence, while the domains of K^+ channels are individual protein subunits (Catterall, 1995; Yu and Catterall, 2004).

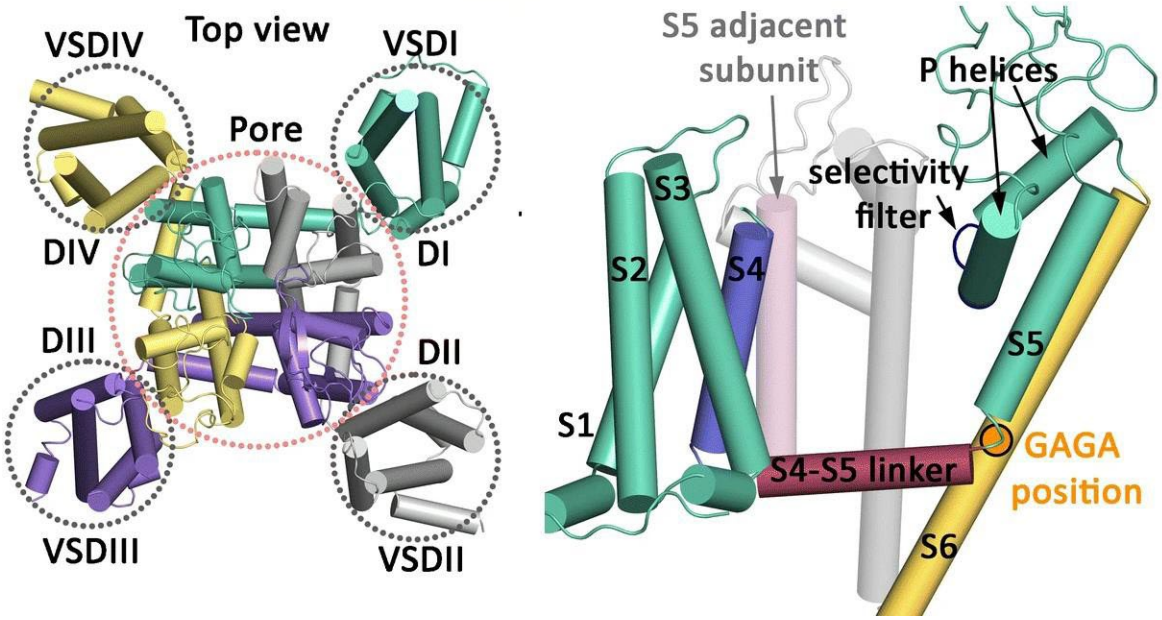

Figure 1: Structure and organization of the voltage-gated calcium channel α1 subunit.

Left: Representation of a top-down (i.e., from outside the cell) view of a voltage-gated calcium channel α1 subunit, showcasing the clockwise arrangement of domains I-IV and the organization of transmembrane segments into the VSD and pore domains. The VSD of each domain is adjacent to the pore-forming segments of the next domain in the sequence. **Right**: Side view of one domain of the VGCC. Segments S1-S4 make up the VSD. The voltage sensor S4 is connected to S5 by the S4-5 linker, and it is also in close proximity to the S5 of an adjacent domain. The loop between the S4-5 linker and S5 is shown interacting with a conserved "GAGA ring" residue on S6 to couple voltage sensor movement to pore opening and closure. Figure adapted from (Hering et al., 2018), open access (http://creativecommons.org/licenses/by/4.0/)

The function of the VSDs of voltage-gated ion channels is to couple membrane depolarization to the opening of the ion-selective pore, such that the probability of channels being in the open state, P_o, is voltage dependent (Bezanilla, 2000). VSDs are able to directly react to depolarization by means of their voltage-sensing S4 segments, which contain highly conserved arginine and lysine amino acid residues, called gating charges, at every third or fourth position (Durell and Guy, 1992; Noda et al., 1984; Yang and Horn, 1996). At resting membrane potential, the attraction of these positively charged residues to the relatively negative intracellular charge holds each S4 segment in a "down" or resting configuration (Yarov-Yarovoy et al., 2012); membrane depolarization then allows S4 to translocate across the membrane into its activated or

“up" conformation, during which the gating charges form transient ion-pair interactions with conserved negative charges on neighboring segments, which stabilizes the gating charges in the hydrophobic transmembrane environment (Fernández-Quintero et al., 2021; Vargas et al., 2012; Tao et al., 2010; Yarov-Yarovoy et al., 2012). Upon membrane repolarization, S4 segments deactivate, or return to the resting state. (See Bezanilla, 2000 and Catterall, 2010 for review of VSD structure and the voltage-sensing process). In VGCCs, the kinetics of S4 deactivation are strongly voltage dependent (the more hyperpolarized the membrane, the faster deactivation occurs), whereas the kinetics of S4 activation have weaker voltage dependence, suggesting that hyperpolarized membrane voltages force S4 segments into the down configuration rather than depolarized voltages forcing them into the up configuration (Beyl et al., 2009; Hering et al., 2018). The movements of S4 gating charges across the membrane can be measured macroscopically (i.e., collectively from a large number of channels) as the gating currents Q_{on} (activation) and Q_{off} (deactivation) (Bezanilla, 2018; Schneider and Chandler, 1973; Yarotskyy and Elmslie, 2009). The movement of S4 segments induces pore opening (activation) or closing (deactivation) by causing a change in the conformation of the pore-forming segments (S5 and S6) (Hering et al., 2018; Long et al., 2005).

The S5 and S6 segments are each linked by an extended pore loop, or P-loop (MacKinnon, 1995). The four P-loops together form the Ca^{2+} selectivity filter at the extracellular end of the pore, with each P-loop contributing one of four highly conserved glutamate residues (or two glutamates and two aspartates in the Ca_V3 family of VGCCs (Senatore et al., 2016); see section 1.2) that together coordinate the binding of Ca^{2+} (or Ba^{2+}) ions (Gao et al., 2021; Wu et al., 2016; Yang et al., 1993). Intracellular to the selectivity filter is the inner pore, lined by the S6 segments. Residues from the lower third of each S6 segment converge to form the activation gate; when the channel

closes, the activation gate residues converge to seal the pore at the intracellular end and prevent ion permeation (Gao et al., 2021; Wu et al., 2016; Xie et al., 2005; Zhen et al., 2005). Upon VSD activation, the upward translocation of the S4 sensor pulls on the helix connecting S4 and S5 (the S4-5 linker), which interacts directly with residues in the lower third of the S6 segment (Long et al., 2005). Another way to put this is to say that VSD *de*activation *pushes* the S4-5 linker; see Gao et al., 2021. Through this interaction, the S4-initiated movement of the S4-5 linkers allows the S6 helices to rotate away from the pore, separating the residues of the activation gate and creating an opening through which ions can enter the cell after passing the selectivity filter (Hering et al., 2018; Long et al., 2005). Upon repolarization of the membrane, the channel deactivates: VSDs return to their resting position, and the pore closes (Beyl et al., 2009). During prolonged depolarization, the pore can close while the VSDs remain in the up position, in a process called voltage-dependent inactivation (Akaike et al., 1988; Branchaw et al., 1997; Stotz et al., 2003).

The S4-5/S6 interaction is likely mediated by the conserved "GAGA ring" residues, which consist of a glycine or alanine residue at the same position in each S6. These residues are energetically coupled with S4 charges via the S4-5 linker, and participate in interactions with bulky hydrophobic pore residues that stabilize the closed activation gate (Beyl et al., 2012; Depil et al., 2011).

Broadly speaking, the "stability" of a protein conformation refers the difference in free energy between the folded and unfolded protein (essentially, the energetic cost of the protein being folded into that conformation (Alvares et al., 2016)), with lower-energy conformations being more stable (Matthews, 1993). The interactions of amino acid residues in a protein with each other and the surrounding environment influence stability. For example, burying of hydrophobic residue side groups, exposure of polar side groups to water, and interactions between residues (such as

hydrogen bonding and electrostatic or hydrophobic interactions) all contribute to stabilizing a given conformation (Kumar and Nussinov, 2002; Matthews, 1993; Pace, 1995). Proteins more readily transition into stable conformations, and "prefer" to do so via energetically favorable transitional motions. The structure of a protein encodes the intrinsic stability of states and motions it must access to carry out its physiological functions, and specific states may become more favorable under certain conditions, e.g., upon ligand binding or membrane depolarization (Bahar et al., 2015; Haliloglu and Bahar, 2015).

Thus, through their energetic coupling with S4 gating charges and direct involvement in mechanisms that stabilize the closed pore, the GAGA residues may participate in transferring or inducing conformational changes in the pore region in response to movement of the voltage sensors. Interestingly, gating charges in the VGCC domain II S4 (IIS4) are energetically coupled with all four GAGA residues, suggesting that cooperative interactions between S6 segments may allow the domain II VSD to modulate them as an ensemble rather than individually (the "cooperative gating model") (Beyl et al., 2012). Coupling between GAGA residues and gating charges in domains I, III and IV has not been evaluated, but would be consistent with the interpretation that the observed VSD II coupling with residues in other domains is mediated by residue interactions within the pore. Another pathway by which VSDs may be able to modulate the pore-forming segments of other domains is through the clockwise organization of the channel (see Figure 1), which positions the S4 segment of each domain immediately adjacent to the S5 segment of a neighboring domain (Gao et al., 2021; Hering et al., 2018; Wu et al., 2016). Additionally, residues in the IIS4-5 linker have been found to be energetically coupled with residues in the adjacent IIIS6 (Demers-Giroux et al., 2013).

In the simplest model of VGCC opening, any deactivated VSD "locks" the pore in its closed configuration even if other VSDs are activated, such that pore opening requires all four VSDs to be in the active conformation simultaneously (the "obligatory model"). In this scheme, the channel occupies multiple different closed states prior to opening, depending on the positions of the VSDs (Pantazis et al., 2014). In reality, the relationship of VSD activation to pore opening is likely to be more complicated. This is in part because the four domains of VGCCs are not identical in sequence or structure. Accordingly, the voltage sensors of each domain have been found to activate with different kinetics and voltage dependence, and to contribute differently to initiating pore opening; e.g., there is evidence that channel opening in one family (see section 1.2, below) of VGCCs is facilitated primarily by IIS4 and IIIS4 activation with little to no contribution from IVS4 (Pantazis et al., 2014), and conversely there is also evidence that that IS4 activation may be rate-limiting for channel opening (Beyl et al., 2016; Fernández-Quintero et al., 2021). As an alternative to the obligatory VSD activation model in which all four VSDs must be activated for the pore to open, it has been proposed that pore opening is an independent process that is energetically unfavorable (and therefore extremely unlikely) when all VSDs are at rest, and that the effect of VSD activation is to stabilize (rather than unlock) the open conformation of the pore, increasing the probability that opening will occur (Pantazis et al., 2014). In this scheme, the channel can exist in multiple distinct open states in which different combinations of VSDs (not necessarily all four) are active, with each active VSD contributing a different proportion of energy to stabilizing the open pore; the rate at which the channel transitions from a closed to an open state thus increases with the activation of more VSDs, or of VSDs that contribute more stabilizing energy (Pantazis et al., 2014). The concept that structural mechanisms intrinsic to VGCCs may energetically stabilize the open or closed pore will be revisited in the following chapters.

The Ca_V α_1 subunit on its own is a functional voltage-gated channel, in that it is capable of conducting Ca^{2+} currents in response to membrane depolarization, but it has been observed to have low membrane expression and abnormal gating properties in the absence of the auxiliary VGCC subunits. A complete high-voltage-activated (see section 1.2) VGCC consists of the α_1 subunit in association with an $\alpha_2\delta$, a β, and sometimes a γ subunit (Arikkath and Campbell, 2003; Meriney and Fanselow, 2019) (Figure 2A). The $\alpha_2\delta$ subunit is a disulfide-linked dimer of α_2 and δ peptides, where α_2 interacts extracellularly with α_1 and is anchored to the membrane by the transmembrane δ (Gurnett et al., 1997). Coexpression of $\alpha_2\delta$ enhances α_1 membrane trafficking, among other effects. The cytosolic Ca_V β subunit associates with a highly conserved motif in the intracellular DI-II linker of α_1 (the α_1 interaction domain, or AID) (Arikkath and Campbell, 2003; Richards et al., 2004; Pragnell et al., 1994). The β subunit's functions include facilitating the trafficking of α_1 to the membrane and mediating its regulation by protein kinases and GTP-binding proteins (Buraei and Yang, 2009; Dolphin, 2009). The more recently identified γ subunit primarily affects α_1's inactivation kinetics (Buraei and Yang, 2009). Different subtypes of each of these auxiliary subunits vary in their effects on α_1 membrane expression and biophysical properties (e.g., voltage dependence and kinetics of activation and inactivation, macroscopic current amplitude) (Dolphin, 2006; Dolphin, 2012).

1.3 Characteristics of VGCC Subtypes

There are ten distinct subtypes of the Ca_V α_1 subunit in mammals. These subtypes share the basic structure described above, but differ in their biophysical properties and physiological roles (Catterall, 2005; Catterall, 2011). VGCCs are categorized according to their $\alpha 1$ subtype and

divided into three families based on the type of Ca^{2+} current they conduct (Ertel et al., 2000) (Figure 2C).

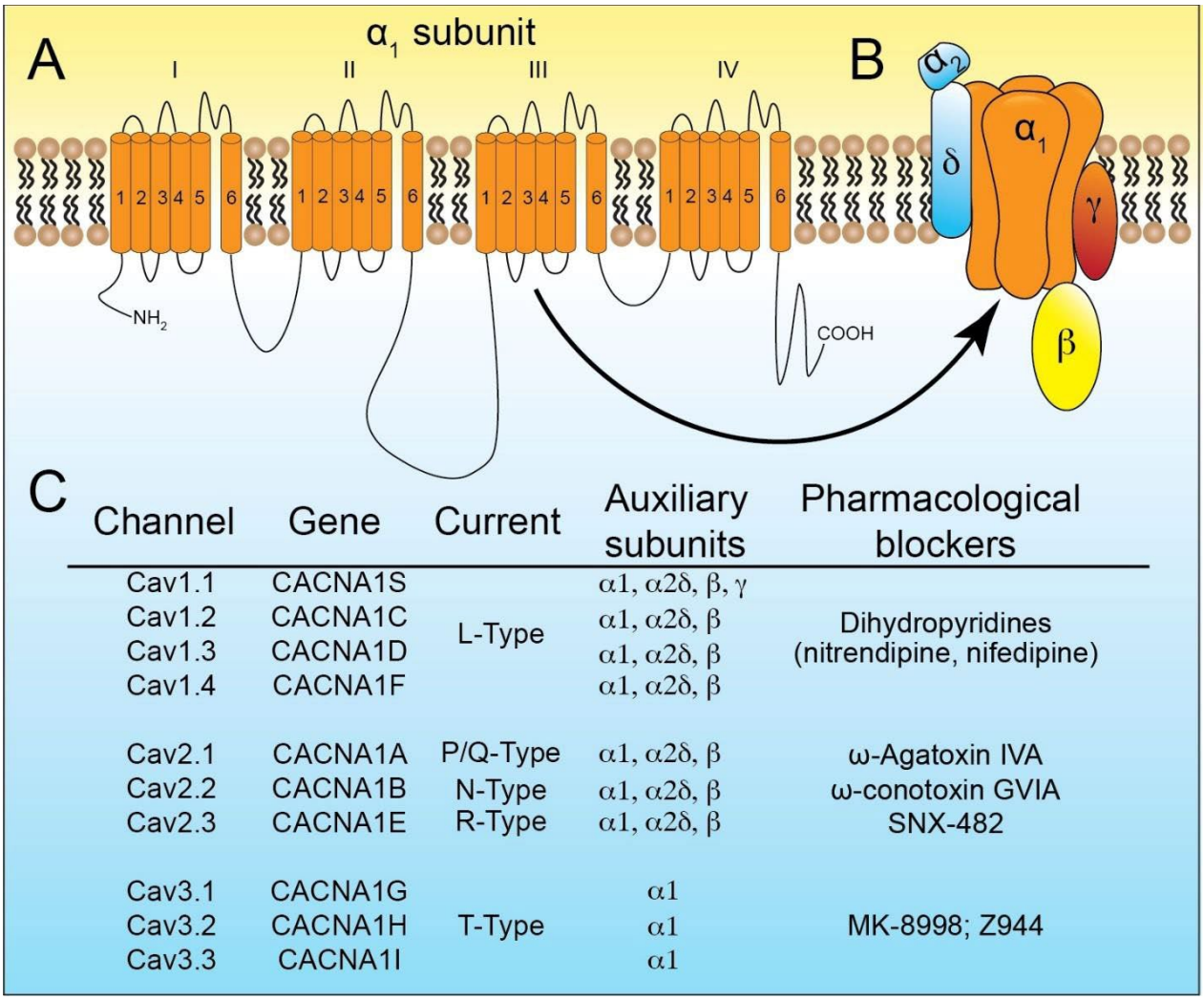

Figure 2: The structural organization and diversity of voltage-gated calcium channels.

A. The predicted topology of all voltage-gated calcium channels. The α_1 subunit is shown with the 6 transmembrane segments of its four domains connected by flexible intra- and extra-cellular loops. **B**. Assembly of the α_1 subunit of a VGCC (orange), in combination with auxiliary subunits: the transmembrane γ subunit (red), the cytosolic β subunit (yellow), and the $\alpha_2\delta$ complex (blue) consisting of the extracellular α_2 and the transmembrane δ subunit. C. Table listing the subtypes of the CaV1, CaV2, and CaV3 VGCC families, including their gene names, the type of current they conduct, the assembled subunits that make up the channel complex, and the selective pharmacological blockers used to study each family or subtype. The high-voltage-activated Ca_V α1 subunit families (Ca_V1 and Ca_V2) are expressed in complexes with auxiliary subunits, while Ca_V3 channels are expressed as the α1 subunit alone. Figure from (Meriney and Fanselow, 2019), used with permission.

The Ca_v1 family ($Ca_v1.1$-1.4) conducts "L-type" currents. These channels activate at high voltages (above -40 mV), have slow voltage-dependent inactivation, and have high single-channel conductance; these properties allow them to mediate long-lasting Ca^{2+} influx (Catterall et al.,

2011). Their functions include mediating excitation-contraction coupling in muscle cells, initiating hormone secretion in neuroendocrine cells, and regulating gene expression (Catterall, 2011). These channels are sensitive to a variety of dihydropyridine (DHP) agonists and antagonists, and are the major target in symptomatic treatment of hypertension (Hockerman et al., 1997a; Zamponi et al., 2015).

The Ca_V3 family ($Ca_V3.1$-3.3) conduct "T-type" Ca^{2+} currents. These channels activate at low voltages (above -70mV), inactivate rapidly during sustained depolarization, and have low single-channel conductance (Catterall, 2011; Fox et al., 1987). Ca_v3 VGCCs mediate transient Ca^{2+} influx in response to small membrane depolarizations and can regulate repetitive or oscillatory activity, e.g. the pacemaker function of the sinoatrial node and the generation of delta and spindle waves in sleep (Catterall, 2011; Lee et al., 2004; Mangoni et al., 2006). They have little sequence similarity to channels in the Ca_v1 and Ca_v2 families.

Finally, the Ca_V2 family ($Ca_V2.1$-2.3) conduct "P/Q-", "N-", and "R-type" currents respectively. These currents have similar characteristics to one another and were initially distinguished by their sensitivities to different classes of peptide toxins (Dolphin, 2018). Like Ca_V1 channels, Ca_V2 channels activate at high voltages, but their speed of inactivation and their single-channel conductance fall between the extremes of the Ca_V1 and Ca_V3 channels (Fox et al., 1987). $Ca_V2.1$ (P/Q) and $Ca_V2.2$ (N) channels are primarily expressed in neurons, and their major function is mediating fast action-potential-evoked release of neurotransmitter at synapses (Catterall, 2011). $Ca_V2.1$ channels are important in signaling at mammalian neuromuscular junctions (NMJs) and in the cerebellum; accordingly, mutation or disruption of this subtype is implicated in familial hemiplegic migraine (Cao and Tsien, 2005; Ophoff et al., 1996), cerebellar ataxia and degeneration (Fletcher et al., 2001; Fukuda et al., 2003; Ophoff et al., 1996; Zhuchenko

et al., 1997), and Lambert-Eaton Myasthenic Syndrome (Eaton and Lambert, 1957; Fukuda et al., 2003; Motomura et al., 1999; Vincent et al., 1989; see section 1.4). Cav2.2 channels, in addition to also playing a minor role in healthy mammalian neuromuscular transmission, are implicated in pain signaling; this has led to the use of $Ca_V2.2$ channel blockers to treat chronic pain. Cav2.3 (R) channels are activated at somewhat lower voltages than Cav2.1 and Cav2.2 (though they are still considered high-voltage-activated channels) and are less efficient at mediating synaptic transmission because they do not associate directly with the vesicle release machinery (Catterall, 2000; Dietrich et al., 2003; Wu et al., 1998; Wu et al., 1999)(see **1.3**). $Ca_V2.3$ VGCCs are widely expressed, including in neuronal, endocrine, cardiac, kidney, and other tissues (Schneider et al., 2013). In neurons, they can be found in the cell body, axon terminal, and dendritic processes (Yokoyama et al., 1995), and have been implicated in regulation of synaptic plasticity (Dietrich et al., 2003).

From here on we will focus on the Ca_v2 family of VGCCs, especially the $Ca_v2.1$ subtype, whose role in neuromuscular transmission makes it a promising therapeutic target in certain neuromuscular diseases. Further discussion of Ca_v1 channels will be in the context of their sequence and structural differences from $Ca_v2.1$. In particular, we are interested in how $Ca_v2.1$'s structural characteristics relate to the modification of its gating kinetics by a novel class of Cav2-selective trisubstituted purines.

1.4 The Cav2 Family of VGCCs in the Organization and Function of the Neuromuscular Synapse

One of the critical functions of Ca_v2 VGCCs is to mediate the transmission of action potentials from nerve to muscle. Since an electrical signal cannot cross the NMJ directly, Cav2 VGCCs convert the motor neuron action potential to a chemical signal, which crosses the synapse and re-initiates the electrical signal in the muscle cell (Figure 3, left). When an action potential reaches the presynaptic motor neuron axon terminal, the resulting membrane depolarization activates VGCCs, allowing calcium to enter the terminal. Calcium ions bind to the synaptic vesicle protein synaptotagmin, triggering vesicles containing neurotransmitter (usually acetylcholine) to fuse to the membrane and release their contents into the synapse (Figure 3, right**)**. This mechanism is termed "quantal release," since neurotransmitter is released only in multiples of the contents of a single vesicle; one fused vesicle equals one quantum of released neurotransmitter. Acetylcholine diffuses across the synapse and binds to receptors on the muscle endplate, resulting in depolarization of the postsynaptic terminal (termed an end-plate potential, or EPP) which at the healthy NMJ is sufficient to generate an action potential in the muscle cell. This in turn leads to muscle cell contraction. (See Slater, 2015 for review.)

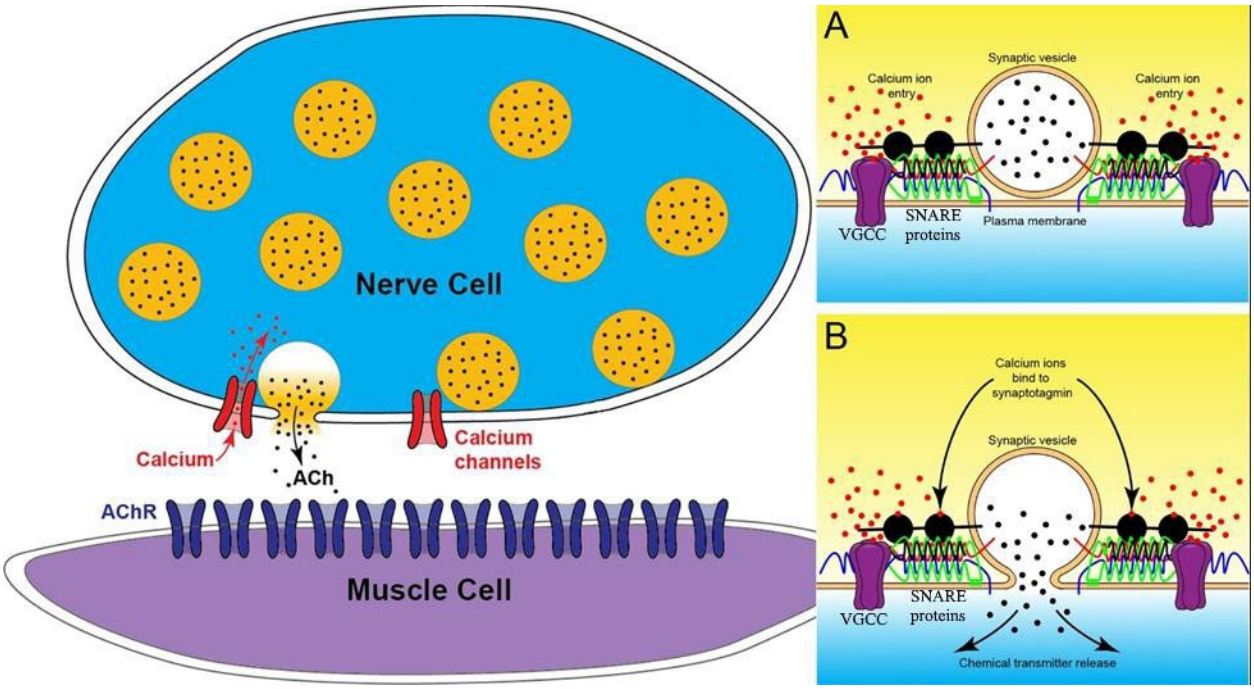

Figure 3: Action-potential-evoked release of neurotransmitter at the neuromuscular junction.

Left: Diagram of neurotransmitter release at the synapse. Calcium enters the nerve cell axon terminal through calcium channels, which causes vesicles to fuse with the plasma membrane and dump their acetylcholine contents into the synapse, where the acetylcholine diffuses across to the receptors on the muscle cell endplate. **Right**: Diagram of a synaptic vesicle docked to the synaptic release machinery in an active zone. Calcium ions enter through VGCCs (purple) that are tightly associated with the release machinery (SNARE proteins depicted as red, green, and blue coils) and are able to bind nearby synaptotagmin (black), triggering synaptic vesicle fusion. Left, adapted from (https://www.mda.org/disease/lambert-eaton-myasthenic-syndrome/causes-inheritance) with permission; right, from (Meriney and Fanselow, 2019), used with permission.

The healthy NMJ is a strong and reliable synapse: strong, meaning that a single action potential triggers the release of neurotransmitter in excess of what is needed to produce an action potential (and thus initiate contraction) in the muscle cell; and reliable, meaning that the neuron's ability to release large quantities of neurotransmitter is sustained over periods of high-frequency activity (Meriney and Dittrich, 2013). These properties depend heavily upon Cav2.1 VGCCs, which play critical roles in both the organization and function of the synaptic release machinery.

The mammalian NMJ's presynaptic axon terminal contains thousands of single vesicle release sites, which are clustered into hundreds of "active zones" containing 2-3 docked vesicles

apiece (Nagwaney et al., 2009; Ruiz et al., 2011; Tarr et al; 2015). At each release site, a small number of $Ca_V2.1$ channel α and β subunits directly interact with SNARE proteins, synaptotagmin, and the active zone proteins Bassoon and CAST/Erc2 in the presynaptic cell, as well as with laminin β2, a "synapse organizer" protein that is located in the synaptic cleft atop the postsynaptic density (the part of the postsynaptic terminal where acetylcholine receptors are concentrated) (Chen et al., 2011; Nishimune et al., 2004) (Figure 4). The interactions of the Ca_V2 channel complex with presynaptic and postsynaptic active zone proteins serve to, 1. tether the release machinery to the membrane; 2., align the release machinery with the postsynaptic density; and 3., position the release machinery in immediate proximity to where calcium ions will flow through the activated channel and trigger vesicle fusion.

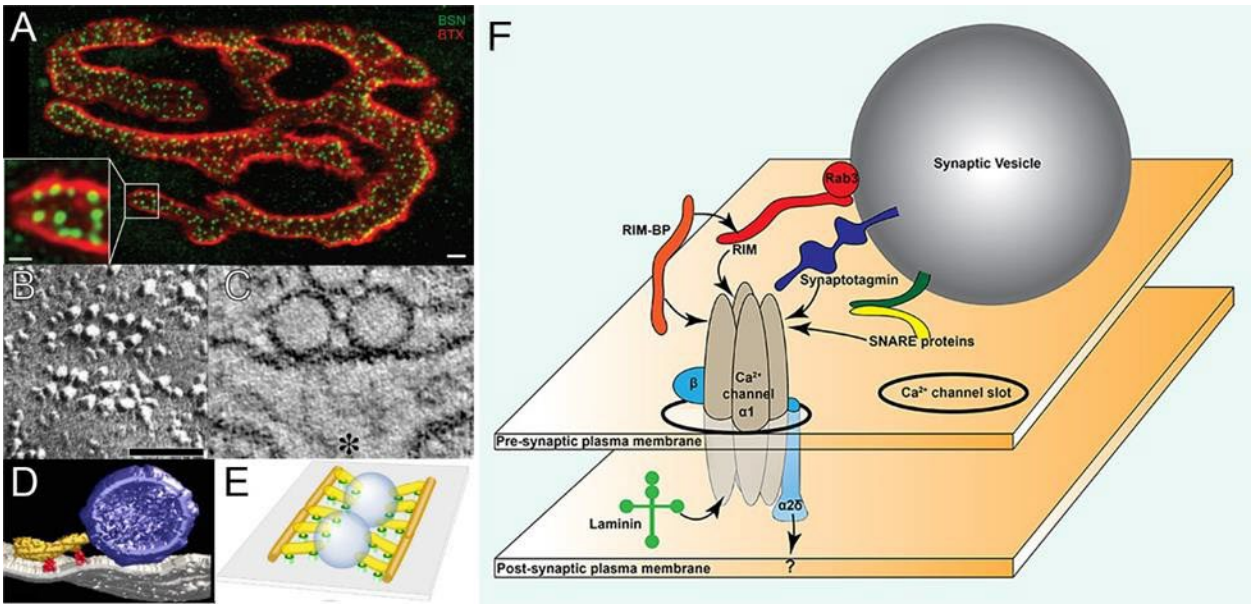

Figure 4: Active zone distribution and structure at the mammalian NMJ.

A. Fluorescent light microscopy view of a mouse neuromuscular junction stained for postsynaptic acetylcholine receptors (red) and the presynaptic active zone protein bassoon (green). Active zones revealed by bassoon staining can be identified as small green "dot-like" structures within the nerve terminal regions of the image (scale bar = 2µm). The inset shows an enlarged view of one part of the never terminal (scale bar = 0.5 µM). **B**. Freeze-fracture electron micrograph of a mouse active zone. The large "bumps" are thought to be transmembrane proteins associated with this site of vesicle fusion, including VGCCs. Scale bar = 100nm. **C.** Transmission electron micrograph of docked vesicles at a single active zone in the mouse NMJ. The two circular structures represent synaptic vesicles that are docked at the active zone (note close apposition to the plasma membrane). The synaptic cleft is labeled with an asterisk. **D.** Electron microscope tomography representation of a single synaptic vesicle (blue-purple sphere) docked at an active zone in the mouse NMJ by unidentified proteins (yellow and red). **E.** Artist's rendering of the mouse active zone that contains two docked synaptic vesicles (blue spheres), based on the electron microscope tomography data shown in D. Undefined components of the active zone structure include elements (orange and yellow) that appear to coordinate the position of the synaptic vesicles and green "pegs" that are interpreted to either be connections to transmembrane proteins, or the transmembrane proteins themselves. **F.** Simplified diagram of the organization of active zone proteins. A VGCC is tethered close to the docked synaptic vesicle through its interactions with synaptotagmin (the calcium sensor), SNARE proteins (mediators of vesicle fusion), and various active zone scaffolding proteins (here, RIM and RIM-binding protein are shown interacting with the VGCC). An interaction with laminin β2 aligns the active zone protein assembly with the postsynaptic density (not shown). A adapted from (Laghaei et al., 2018) with permission; B adapted from (Fukuoka et al., 1987) with permission; C-E adapted from (Nagwaney et al., 2009) with permission; F from (Meriney et al., 2014). The organization of A-E is adapted from (Meriney and Fanselow, 2019) with permission.

When an action potential reaches the terminal, each individual docked vesicle has a very low probability of undergoing fusion. Research in the frog NMJ suggests that this is because each

Cav2 channel has a low probability of opening during an AP, there are very few (~1 per vesicle) Cav2 channels in each active zone, and the probability that a vesicle will fuse is low even in the rare event of a nearby Cav2 channel opening and exposing it to Ca2+ ion flux (Luo et al., 2011; Luo et al., 2015); this may also be true for the mammalian NMJ (Meriney and Dittrich, 2013). As a result, only a small fraction of the pool of docked vesicles is released in response to a single action potential. Because of the large pool of available vesicles, even the small fraction that is released consistently contains enough acetylcholine to trigger an action potential in the muscle cell, and yet a very large pool of vesicles remains available for release even during prolonged high-frequency presynaptic action potential activity (Tarr et al., 2013a). It is therefore the organization of synaptic vesicles in the NMJ into thousands of unreliable single vesicle release sites in active zones that grants the synapse its strength and reliability, and Cav2 VGCCs are critical to both the organization and function of these active zones (Meriney and Dittrich, 2013; Tarr et al., 2013a).

1.5 $Ca_V2.1$ VGCCs in the Pathophysiology and Treatment of Lambert-Eaton Myasthenic Syndrome

The important role of Cav2-family voltage-gated calcium channels in neuromuscular transmission makes them an attractive target for treating muscle weakness caused by inadequate neurotransmission at the NMJ.

For example, patients with Lambert-Eaton Myasthenic Syndrome (LEMS) suffer debilitating muscle weakness most commonly caused by autoantibodies targeting $Ca_V2.1$ VGCCs. The removal of many of these channels from the synapse not only reduces the total amount of presynaptic Ca^{2+} influx resulting from an action potential, but also disrupts the organization of the

active zones that, in a healthy synapse, ensures that Ca^{2+} enters the terminal in proximity to docked vesicles' synaptic release proteins (Fukunaga et al., 1983) (Figure 5). (About 15% of LEMS patients lack anti-$Ca_V2.1$ antibodies; it has been suggested that symptoms in these cases are due to antibodies against other active zone proteins (Nakao et al., 2002; Oh et al., 2007; Tarr et al., 2015).) Although individual release sites normally have a low probability of vesicle fusion during an action potential, antibody-mediated removal of calcium channels and disruption of active zones further lowers this probability. The result is that, although each individual vesicle still contains the same amount of neurotransmitter as in a healthy synapse (the amplitude of the mini-EPPs, or mEPPs, evoked by spontaneous release of single vesicles is unchanged), the overall number of vesicles released (the "quantal content", measured by dividing EPP amplitude by mEPP amplitude) is greatly reduced (Lambert and Elmqvist, 1971). As a result, the strength of the synapse is impaired; a single action potential no longer consistently evokes the release of enough neurotransmitter to bring the muscle cell to threshold (Lambert and Elmqvist, 1971).

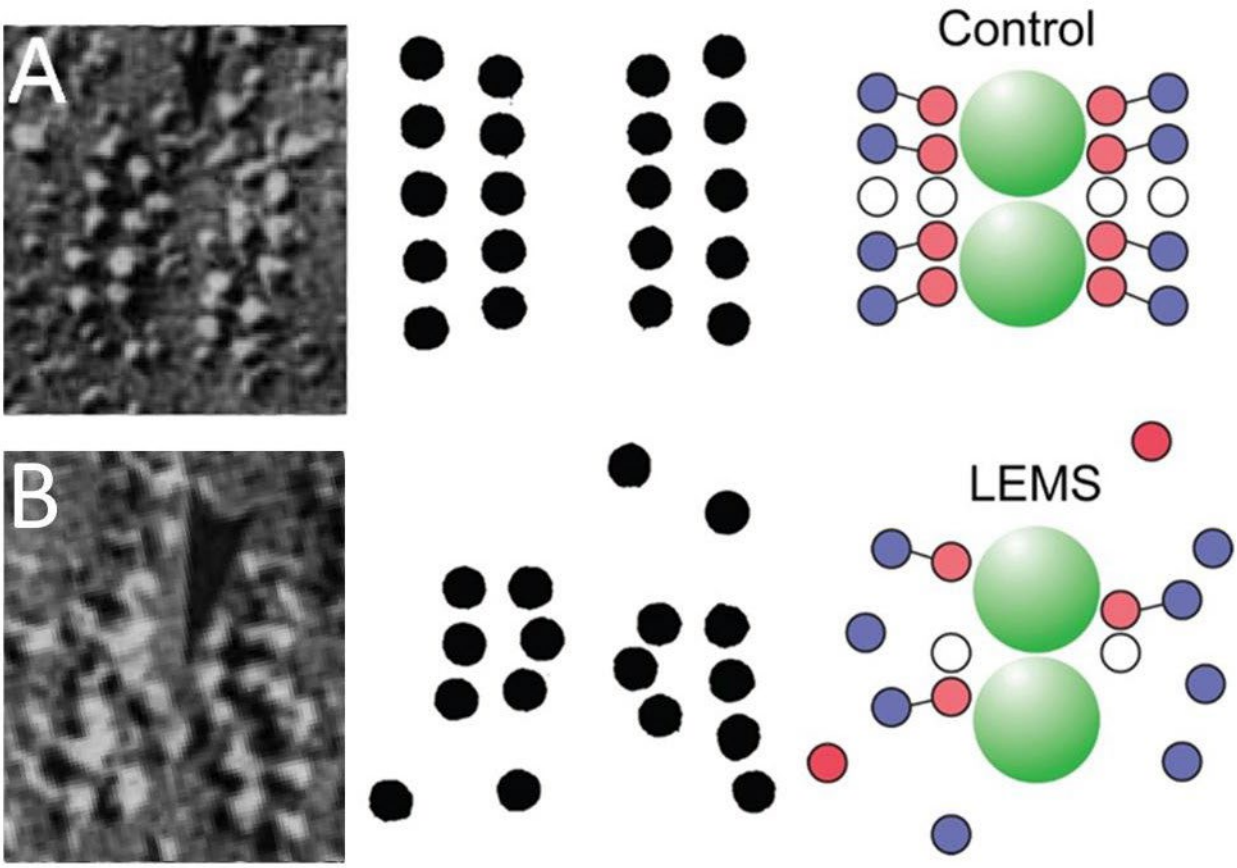

Figure 5: Disruption of the active zones at LEMS neuromuscular synapses.

A. **Left***:* Representative healthy control mouse AZ organization (freeze fracture replica, scale = 50 nm). The "dots" are active zone proteins, likely including VGCCs. **Center***:* Diagram of protein organization based on freeze fracture data. *Right:* Predicted distribution of synaptic vesicles (green spheres) based on EM tomography data (Nagwaney et al., 2009), Ca^{2+} channels (red circles), and BK channels (blue circles) in the active zone. B. **Left***:* Representative LEMS-modified AZ organization from nerve terminal of mouse passively transferred with LEMS serum. Center: diagram of protein organization as in A, in the LEMS-modified synapse. *Right*: predicted distribution of synaptic vesicles and channels, as in A, in the LEMS-modified synapse. Left and center images adapted from (Fukuoka et al., 1987) with permission.

There is evidence that the loss of Cav2.1 channels leads to compensatory upregulation of other Ca^{2+} channel types. For example, in LEMS passive-transfer model mice (mice treated with LEMS patient serum to transfer autoantibodies, causing LEMS-like impaired transmission and muscle weakness; see Meriney et al., 2018 for review), Cav1-type currents have been found to contribute to neuromuscular transmission (Flink and Atchison, 2002), and Cav2.3-type channels

are upregulated at the NMJs of Cav2.1 VGCC knockout mice (Urbano et al., 2003)—but this is not sufficient to restore the strength of the synapse (Smith et al., 1995), likely because these channels do not bind laminin β2 and therefore do not rescue Cav2.1's role in active zone organization (Nishimune, 2012; Nishimune et al., 2004). Antibodies to other active zone proteins have also been found in LEMS patient serum (Takamori et al., 1995; Takamori et al., 2007; reviewed in Takamori, 2008), likely contributing to active zone disruption.

LEMS patients suffer from weakness primarily in the proximal limb muscles (but eventually also spreading to distal limbs; see Titulaer et al., 2011), and autonomic symptoms and impaired tendon reflexes are also common (Kesner et al., 2018; Mareska and Gutmann, 2004; O'Neill et al., 1988; Pascuzzi, 2002). It is a hallmark of LEMS that muscle strength temporarily improves following short exercise or high-frequency nerve stimulation; for example, one of the diagnostic criteria is "Lambert's sign", an increase in the strength of a patient's grip as it is sustained over several seconds (Mareska and Gutmann, 2004; Pascuzzi, 2002). The increase in the strength of the weakened muscle can be quantified via repetitive nerve stimulation and electromyographic recording of the resulting compound muscle action potentials (CMAP) (Oh et al., 2005) (Figure 6). This post-exercise facilitation distinguishes LEMS from myasthenia gravis, another disorder of neuromuscular transmission (Eaton and Lambert, 1957; Mareska and Gutmann, 2004; Oh, 2017). Facilitation of EPPs during high-frequency stimulation is similarly observed *in vitro* at the level of the individual LEMS synapse, indicating a temporary improvement in quantal release (Lambert and Elmqvist, 1971; Lang et al., 1983). This is because calcium accumulates in the diseased active zones as the motor neuron fires repeatedly, increasing the probability for subsequent action potentials to trigger vesicle fusion (a form of short-term synaptic plasticity).

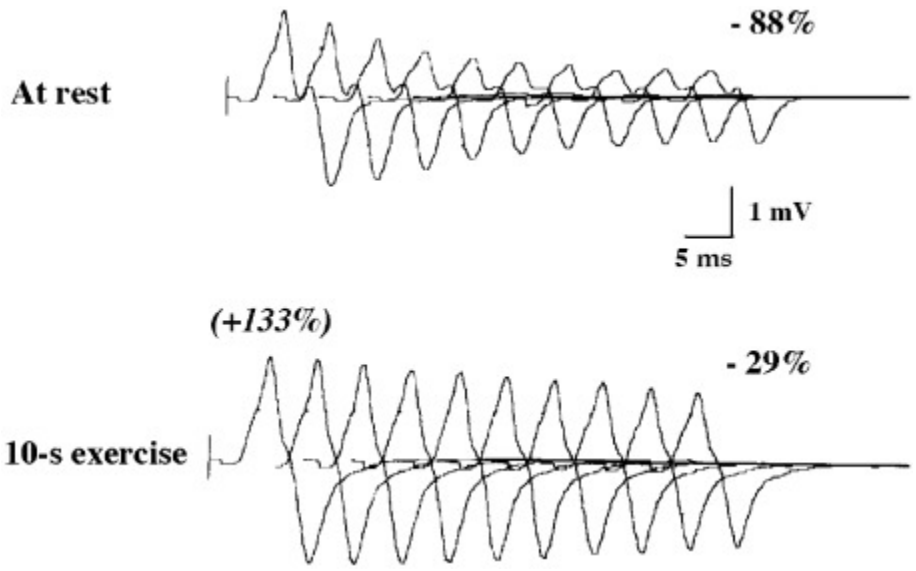

Figure 6: Post-exercise facilitation of the compound muscle action potential in LEMS.

Representative CMAP recordings from a repetitive nerve stimulation test in a LEMS patient. The ulnar nerve is stimulated 10 times at a frequency of 3 Hz and the resulting CMAP for each stimulus recorded from the abductor digiti quinti muscle of the hand. Each of the 10 recorded sweeps are graphically represented as an overlay with an offset to represent decrements in amplitude during the 3 Hz stimulus train. Top: Recordings taken at rest. The CMAP amplitude is small and decrements rapidly (-88% amplitude by the end of the stimulus). Bottom: Recordings taken after 10 seconds of exercise. The CMAP amplitude is larger initially (+133%), and decrements more slowly (-29%), than in the recording taken at rest. Post-exercise facilitation is part of the diagnostic criteria for LEMS. Figure adapted from (Oh et al., 2005) with permission.

The gold standard for symptomatic treatment of LEMS is the potassium channel blocker 3,4-diaminopyridine (3,4-DAP) (Oh et al., 2009), which received FDA approval in 2018 (U.S. Food and Drug Administration, 2018). 3,4-DAP indirectly enhances calcium influx by broadening the motor neuron action potential waveform (Figure 7; Ojala et al., 2021), allowing more openings of remaining Cav2 channels to occur before the membrane repolarizes. This increases the probability of synaptic vesicle fusion at release sites (compensating for the reduced probability caused by loss of Ca^{2+} channels and active zone disruption), and therefore the quantal content of acetylcholine released in response to an action potential (Ojala et al., 2021). Because the probability of vesicle fusion is superlinearly related to the amount of Ca^{2+} at active zones (Dodge

and Rahamimmof, 1969; Schneggenburger and Neher, 2000; reviewed in Schneggenburger and Neher, 2005), even small increases in Ca^{2+} influx can greatly improve quantal release. However, while 3,4-DAP is well tolerated and offers some symptomatic relief at low doses (which only mildly broaden the AP; see Ojala et al., 2021), higher doses can cause serious side effects such as seizures (Lindquist and Stangel, 2011; Oh et al., 2009; Verschuuren et al., 2006). In fact, a meta-analysis concluded that 3,4-DAP is able to provide only modest improvement for most patients (Sedehizadeh et al., 2012). Patients for whom the maximum safe dose does not provide adequate symptomatic relief, as well as those for whom the drug is contraindicated (e.g., patients with epilepsy), would benefit from a new symptomatic treatment to be used in combination with or as an alternative to 3,4-DAP.

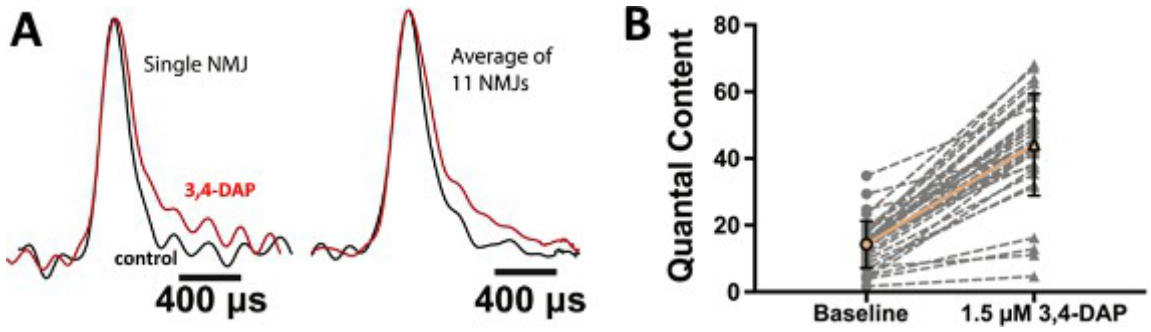

Figure 7: 3,4-DAP broadens the presynaptic AP and increases quantal release at the mammalian NMJ.

A. Individual and averaged AP waveforms recorded at a mouse NMJ before (black) and after (red) application of a therapeutic concentration of 3,4-DAP (1.5 µM). Application of 3,4-DAP broadens the waveform. **B.** Quantal content (calculated from EPP and mEPP size) at mouse NMJs before ("baseline", left) and after application of 1.5 µM 3,4-DAP. The mean and standard error (SE) in each condition are shown in black, and data for each individual NMJ are shown in grey. Application of 3,4-DAP increases quantal release by the presynaptic terminal. Figure adapted from (Ojala et al., 2021), open access (https://creativecommons.org/licenses/by/4.0/).

Given that 3,4-DAP is able to restore muscle strength by indirectly increasing action-potential-evoked calcium influx, a treatment that enhances calcium influx by another mechanism might also be effective. This raises the question: Could a drug that directly targets Cav2 VGCCs, enhancing their ability to conduct calcium current, restore NMJ transmission in LEMS and other neuromuscular diseases of presynaptic origin— for example, spinal muscular atrophy (SMA), muscle-specific tyrosine kinase (MuSK)-associated myasthenia gravis, old-age-related dynapenia (frailty), and the paralytic effects of botulinum toxin A?

There is precedent for the use of direct modifiers of VGCCs in clinical and research contexts. As mentioned in section 1.2, a variety of dihydropyridine (DHP) compounds have been found to have agonist or antagonist effects on Ca_v1 VGCCs, and DHP antagonists are used to treat hypertension (Hockerman et al., 1997a; Zamponi et al., 2015). However, using this approach to treat deficits of neuromuscular transmission would require an agonist that targets Ca_v2 VGCCs selectively, since modulation of Ca_v1 channels could cause cardiac and vascular side effects. In

addition, this drug would need to be incapable of crossing the blood-brain barrier, since Ca_v2 VGCCs are widely expressed in the brain (where adverse effects would be likely); it would need to promote calcium influx only during an action potential, since it could otherwise cause unwanted spontaneous neurotransmitter release; and it would need to be capable of modifying channels within the <1ms action potential timeframe. As we will discuss in Chapter 2, all of these characteristics can be found in analogs of the drug *(R)*-roscovitine.

2.0 Background: Novel compounds based on *(R)*-roscovitine are promising candidates for the treatment of impaired neuromuscular transmission.

2.1 Discovery and characterization of a positive allosteric action of *(R)*-roscovitine on Ca_V2 VGCCs

The drug *(R)*-roscovitine ((2R)-2-{[6-(Benzylamino)-9-isopropyl-9H-purin-2-yl] amino}-1-butanol; Figure 8A) is a trisubstituted purine that inhibits a broad range of cyclin-dependent kinases (CDKs) (Collins and Garrett, 2005; De Azevedo et al., 1997), which regulate cell proliferation at various "checkpoints" in the cell cycle. CDKs (like other kinases) function by transferring phosphate groups from ATP to target proteins, and *(R)*-roscovitine inhibits this activity through direct competition with ATP at CDKs' ATP-binding site (De Azevedo et al., 1997). Because of CDKs' roles in advancing the cell cycle, *(R)*-roscovitine has been investigated as a potential treatment for cancer and other diseases that involve excessive cell proliferation (Cicenas et al., 2015). However, it has also been found to have an unrelated positive modulatory effect on the Cav2 family of VGCCs (Yan et al., 2002).

In Cav2.1 (Buraei et al., 2007, Yan et al., 2002), Cav2.2 (Buraei et al., 2005, Buraei et al., 2007), and Cav2.3 VGCCs (Buraei et al., 2007), *(R)*-roscovitine has been observed to prolong mean open time (the duration channels remain in an open, Ca^{2+}-conducting state after activation). In the absence of the drug, Ca_V2 channels have been found to undergo frequent short openings and infrequent longer openings during a depolarizing voltage step (DeStefino et al., 2010). These fast and slow openings may represent distinct open states of the channel. Long openings are infrequent in the absence of drug, but *(R)*-roscovitine application further prolongs the long openings and

greatly increases their frequency (which can be observed in single-channel recordings; see Figure 8), without affecting the duration of short openings or the single-channel conductance (DeStefino et al., 2010).

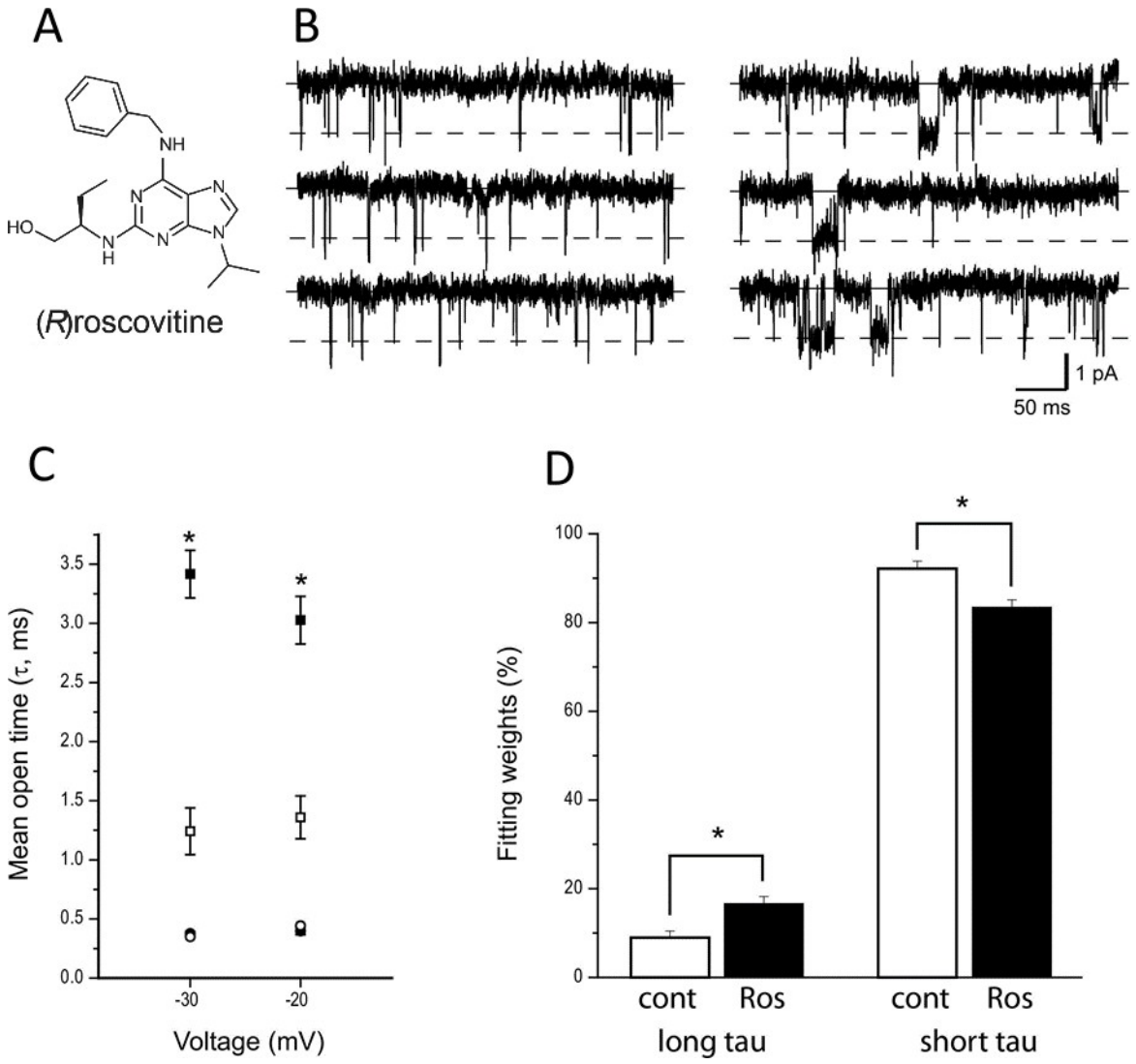

Figure 8: (R)-roscovitine prolongs the mean open time of Cav2 VGCCs.

A. The molecular structure of *(R)*-roscovitine. **B.** Representative recordings of single-channel openings in the absence (left) and presence (right) of *(R)*-roscovitine. **C.** Summary plot of the effect of *(R)*-roscovitine on the duration of short and long openings during steps to -30mV and -20mV. Open symbols represent the control duration and filled symbols represent the duration in the presence of *(R)*-roscovitine. The drug has little effect on the duration of short openings (circles), but significantly increases the average duration of long openings (squares). **D.** Summary graph showing the relative probabilities of short and long single-channel openings during steps to -30mV. *(R)*-roscovitine increases the proportion of long openings. A adapted from (Wu et al., 2018) with permission; B-D adapted from (Destefino et al., 2010) with permission.

In whole-cell physiological recordings of cells expressing Ca_V2 channels, a large "tail current" occurs upon repolarization following a depolarizing voltage step to activate channels,

representing ion influx through the channels that were open at the end of the step. The tail current decays as these channels close due to the membrane repolarization, and this decay is best fit by a double exponential. The majority of the tail current decays with a short time constant or tau (the fast component of decay), representing short openings of individual VGCCs, and the remainder decays more slowly with a long tau (the slow component of decay), representing longer openings (DeStefino et al., 2010). In the presence of *(R)*-roscovitine, current through the drug-modified channels exhibits an enhanced slow component of decay (Figure 9), while current through unmodified channels is represented by the fast component. The extent of slowing can be measured by calculating the slow tau, or by calculating the normalized integral of the tail current during drug application (the integral, or the area under the curve of the tail current, normalized to its peak amplitude to correct for the drug's effects on channel inactivation) and calculating the fold change from the pre-drug normalized integral (Liang et al., 2012; Wu et al., 2018). The amplitudes of the fast and slow components of decay can be used to determine the proportion of activated channels modified by *(R)*-roscovitine (Buraei et al., 2005; DeStefino et al., 2010).

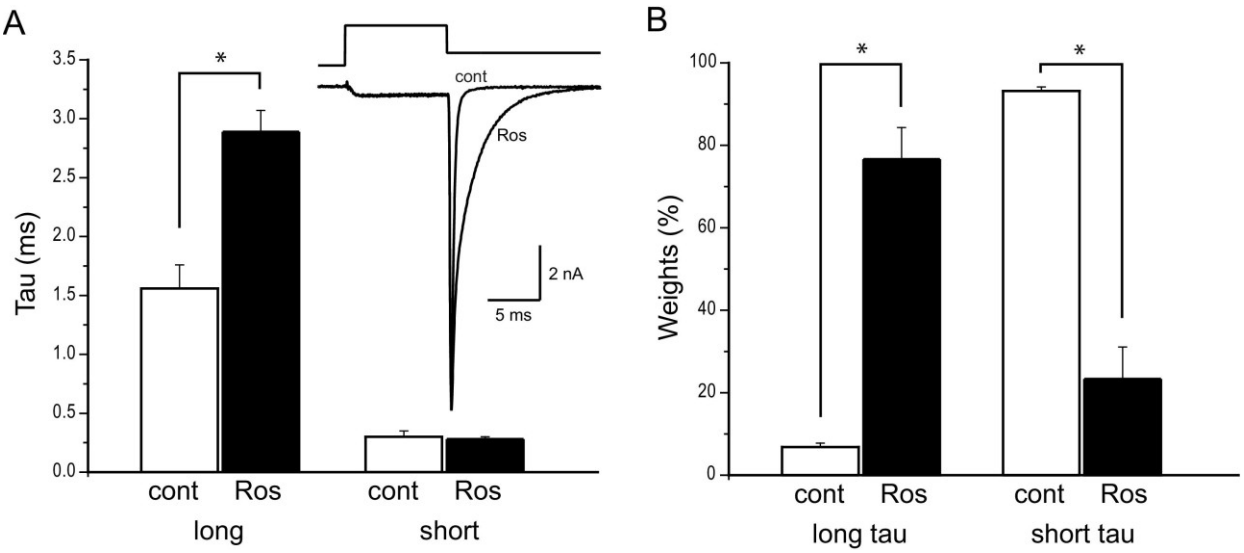

Figure 9: (R)-roscovitine-mediated prolongation of Ca_V2 VGCC mean open time slows the decay of whole-cell $Ca_V2.2$ currents.

A. Decay of the whole-cell $Ca_V2.2$ tail currents occurring upon repolarization after a depolarizing step to activate channels (see inset) was best fit with a double exponential representing a slow and a fast component of decay. The slow decay is the product of single-channel long openings (see Fig. 8C), and the fast decay is the product of single-channel short openings. Application of *(R)*-roscovitine lengthens the time constant (tau) of the slow decay component, but does not affect the tau of the fast component. **B.** Application of *(R)*-roscovitine increases the fitting weight of the slow decay component (the proportion of the tail current amplitude whose decay is fit with the slow exponential) and decreases the fitting weight of the fast decay component, revealing an increased probability of long-single channel openings (see Fig. 8D). Figure adapted from (Destefino et al., 2010) with permission.

(R)-roscovitine modification of tail currents is dependent on the length of the depolarizing step used to activate channels. In all three Ca_V2 subtypes (2.1, 2.2, 2.3), the amplitude of the slow component of deactivation increases with the length of the voltage step, while the amplitude of the fast component declines, indicating that a greater proportion of activated channels are modified by the drug after longer voltage steps (Buraei et al., 2005; Buraei et al., 2007; DeStefino et al., 2010) (Figure 10). This suggests that *(R)*-roscovitine only modifies channels when they are in an open state, or possibly during a transitional state as they are opening; longer depolarizations trigger more openings of VGCCs and therefore provide the drug with more opportunities to bind and modify them. (Interestingly, experiments using structurally related Cav2 modifiers suggest that a prior interaction with closed-state channels is required for the drug to then modify them when they enter the open state; see section 2.3 below.)

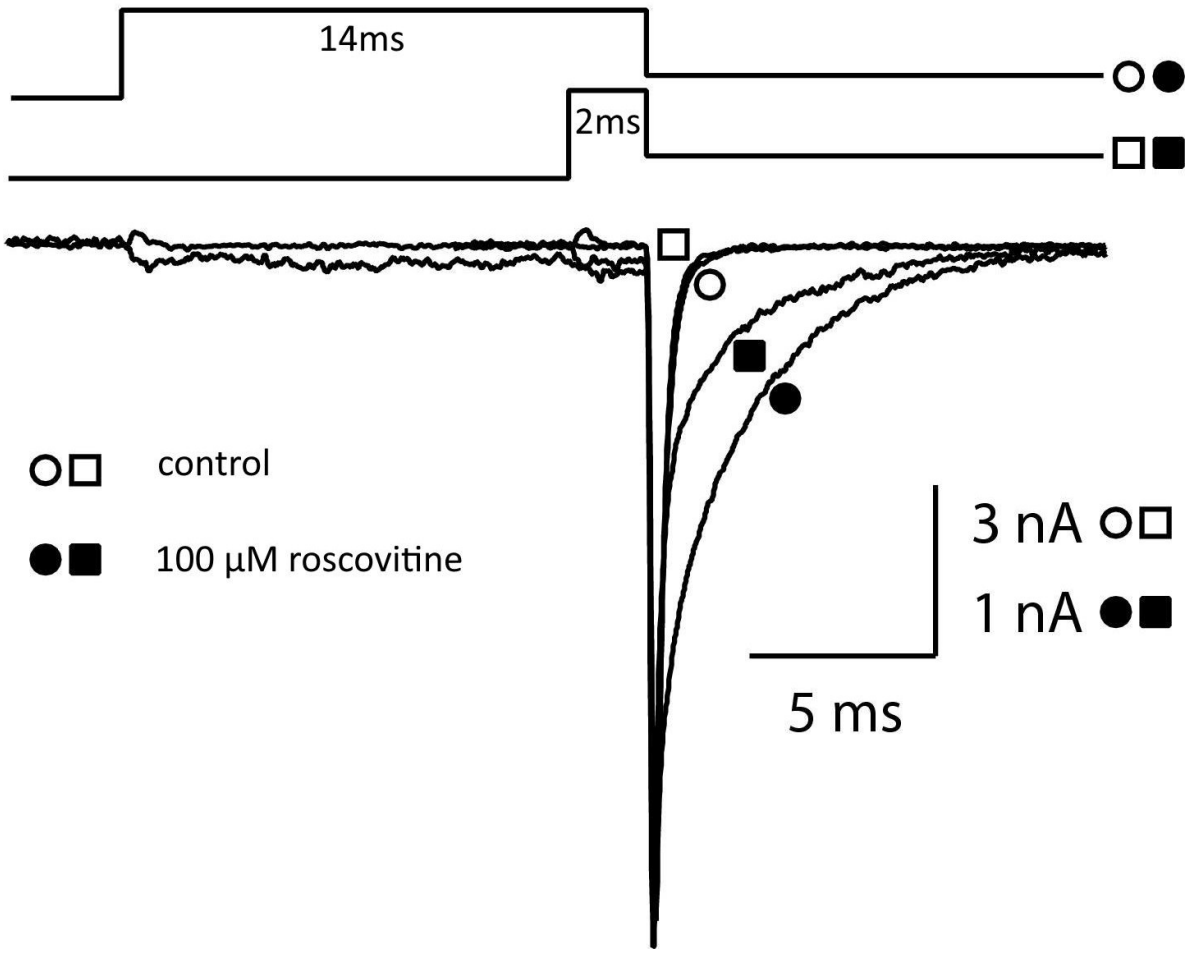

Figure 10: The proportion of the Ca_V2 tail current modified by (R)-roscovitine increases with the length of the depolarizing step. Representative tail currents are shown before (open symbols) or during (filled symbols) application of 100 µM *(R)*-roscovitine. The length of the depolarizing voltage step to +53mV used to activate channels is 2ms (squares) or 14ms (circles). The length of the step does not affect the decay of the control (pre-drug) tail currents, but a larger proportion of the tail current decay is slowed by 100 µM *(R)*-roscovitine after the 14ms step than after the 2ms step. Figure adapted from (Destefino et al., 2010) with permission.

The mechanism by which *(R)*-roscovitine prolongs channel mean open time is not known, but some models can be plausibly ruled out. For example, a "foot-in-door" mechanism, in which the drug physically obstructs channel closure for as long as it remains bound, is unlikely. Given that Ca_V2 tail currents deactivate faster the more negative the repolarization potential, if *(R)*-roscovitine unbinding were necessary for the channel to close, then repolarizing to increasingly negative potentials would reveal a plateau in the speed of decay where unbinding becomes rate-

limiting; however, no such plateau is observed (Buraei et al., 2005). If deactivation resulted directly from unbinding, one would also expect the drug's time constant of unbinding, derived from the dissociation rate constant k_{off}, to be rate-limiting for the time constant of current decay, which we have observed is not the case; see section 4.3.4.

In addition to prolonging pore opening, *(R)*-roscovitine has been found to slow the gating current Q_{off} (which represents the return of the voltage sensors to their resting positions). In the presence of the drug, the time course of Q_{off} is similar to the time course of ionic current decay, indicating that relaxation of the gating charges becomes coupled to pore closure (Yarotskyy and Elmslie, 2009). It can be concluded that channels remain in an open and activated conformation during *(R)*-roscovitine-mediated long opening, as opposed to the pore being held open independent of VSD activation. It has been proposed that the effect of *(R)*-roscovitine in Ca_V2 VGCCs is to stabilize a high P_o open state of the channel that "traps" the voltage sensors in their activated positions (Yarotskyy and Elmslie, 2009). Given the voltage-dependence of deactivation findings discussed above, which suggest that *(R)*-roscovitine unbinding is not required for channel closure (Buraei et al., 2005), the channel's slow exit from this high P_O state is likely to be independent of drug unbinding.

Other VGCC subtypes, notably the Ca_V1 channels, are insensitive to *(R)*-roscovitine-mediated slowing of deactivation (Buraei et al., 2007; Yarotskyy et al., 2010). Sensitivity to this effect appears to be localized to the domain III of Cav2 VGCCs. In experiments using chimeric VGCCs containing different combinations of domains from $Ca_V2.2$ and $Ca_V1.2$ channels, *(R)*-roscovitine slowed deactivation in channels containing the $Ca_V2.2$ domain III and did not slow deactivation in channels containing the $Ca_V1.2$ domain III, regardless of the identities of the other three domains (Yarotskyy et al., 2012). Deactivation in the chimera containing only the $Ca_V2.2$

domain III (with the other three domains being $Ca_V1.2$-type) was not slowed as much by *(R)*-roscovitine as in wildtype $Ca_V2.2$; however, the inclusion of Cav2.2 domain IV alongside the domain III restored the extent of slowing to nearly wild-type levels (Yarotskyy et al., 2012). One interpretation of these findings is that the *(R)*-roscovitine binding site that mediates slowed deactivation is located within domain III and contains critical amino acid residues that are conserved across Ca_V2 (but not Ca_V1) VGCCs, while Ca_V2-specific residues in domain IV contribute to the increased duration of the mean open time.

In addition to slowing deactivation in Ca_V2 VGCCs, *(R)*-roscovitine also inhibits both Ca_V2 and Ca_V1 VGCCs (Buraei et al., 2007), by enhancing closed-state inactivation in Cav2 (Buraei and Elmslie, 2008) and voltage dependent inactivation in Ca_V1 (Yarotskyy and Elmslie, 2007). In whole-cell recordings, this can be observed as a gradual decline in the amplitude of Ca^{2+} current that exceeds normal current run-down. It is unlikely that *(R)*-roscovitine exerts its effects on both inactivation and deactivation by binding to the same site, given that the inactivation effect develops much more slowly than the slowed-deactivation effect and that *(R)*-roscovitine's EC_{50} (half-maximal effective concentration) for inactivation is several times higher than for slowed-deactivation (Buraei et al., 2005). Additionally, (S)-roscovitine inactivates Ca_V2 VGCCs at similar potency to (R)-roscovitine, yet its EC_{50} for slowing of deactivation is 10-20 times higher than *(R)*-roscovitine's (Buraei et al., 2005; Buraei and Elmslie, 2008). Based on these findings, it is likely that Ca_V2 VGCC inhibition and slowed deactivation are mediated by separate binding sites for *(R)*-roscovitine: a stereosensitive site where high-affinity *(R)*-roscovitine binding leads to rapid slowing of deactivation, and a non-stereosensitive site where lower-affinity *(R)*-or-*(S)*-roscovitine binding leads to a slower enhancement of closed-state inactivation.

2.2 : (R)-roscovitine analogs are promising candidates for the treatment of impaired neuromuscular transmission

As this section has covered, *(R)*-roscovitine has characteristics that could make it a candidate for treating impaired neuromuscular transmission by directly targeting VGCCs. It increases total calcium influx specifically through open Ca_V2 VGCCs; it does not cross the blood-brain barrier; and its speed of action is fast enough to permit modification of VGCCs on the timeframe of a physiological action potential (Buraei et al., 2007). Furthermore, application of *(R)*-roscovitine to the *Rana* (frog) NMJ was found to increase the quantal content of action-potential-evoked acetylcholine release, confirming that the drug does in fact enhance NMJ neurotransmission (Cho and Meriney, 2006). (The experiments in frog NMJ did not explicitly confirm that the enhanced transmission is due to slowed deactivation of VGCCs, but this interpretation is supported by a later finding that direct application of *(R)*-roscovitine to rat cerebellar synapses increased quantal release in a Ca^{2+}- and VGCC-dependent manner (Satake and Konishi, 2020).) *(R)*-roscovitine's additional effect of promoting VGCC inactivation apparently does not prevent it from enhancing quantal release, and indeed is not expected to do so in a clinical context. This is partly because the comparatively large EC_{50} of this effect means that little drug-induced inactivation occurs at dosages sufficient to slow VGCC deactivation, and partly because the much slower timescale over which drug-induced inactivation occurs is unlikely to be relevant in the context of an action potential (Buraei et al., 2005). *(R)*-roscovitine's off-target (in this context) effects on CDKs are therefore the main barrier to its potential usefulness as a therapeutic in LEMS and other neuromuscular diseases.

Fortunately, although Ca_V2 channels can be phosphorylated by cdk5 (which is abundantly expressed in neurons and is among the CDK subtypes inhibited by *(R)*-roscovitine), there is

substantial evidence that *(R)*-roscovitine's effect on VGCC deactivation is independent of CDK inhibition. For example, when *(R)*-roscovitine is applied intracellularly (where CDKs are expressed), it does not slow VGCC deactivation (Yan et al., 2002); structurally related CDK inhibitors, including olomoucine and *(S)*-roscovitine, either do not slow VGCC deactivation or do so only at much higher EC_{50} (not correlated to their effectiveness at CDK inhibition) (Buraei and Elmslie, 2008; Yan et al., 2002); *(R)*-roscovitine's effect on VGCC deactivation is maintained in neurons from mice with a mutation that essentially eliminates cdk5 activity (Chae et al., 1997; Yan et al., 2002); and *(R)*-roscovitine increases quantal release at the frog NMJ in a CDK-independent manner (Cho and Meriney, 2006). In other words, inhibition of CDKs does not in and of itself cause slowed VGCC deactivation, and *(R)*-roscovitine having physical access to active CDKs is neither necessary nor sufficient for it to modify VGCCs. Therefore, it is reasonable to conclude that *(R)*-roscovitine's CDK inhibition and slowing of VGCC deactivation are mediated by entirely separate binding sites and mechanistic pathways.

This conclusion raised the possibility that modifications to the structure of *(R)*-roscovitine could reduce or eliminate its ability to inhibit CDKs, while retaining its effect on VGCC deactivation. (The likely existence of separate *(R)*-roscovitine binding sites for inactivation and slowed deactivation effects similarly implies that a structure could be optimized for one effect or the other; although we have discussed that inactivation is unlikely to be relevant in a therapeutic context, this would nevertheless be valuable in developing analogs as experimental tools to investigate VGCC gating.) Therefore, several years after the discovery that *(R)*-roscovitine modifies Cav2 VGCCs, the Meriney group, in collaboration with Peter Wipf's group, set out to synthesize a structural analog with little to no CDK activity and improved characteristics of action on Cav2 VGCC deactivation kinetics (Liang et al., 2012).

For purposes of exploring the structure-activity relationship (SAR) of *(R)*-roscovitine analogs, the structure of the parent molecule was divided into four "zones" representing the core purine and its three side chains (Figure 11A). Many analogs of *(R)*-roscovitine were synthesized with exploratory modifications to different zones, and each was evaluated for its CDK activity and effects on VGCCs (Liang et al., 2012).

Liang et al. (2012)'s early investigation showed that the slowed-deactivation effect is extremely sensitive to modifications in zone 3 (as is the inactivation effect, to a lesser degree), with small changes to the C2 side chain dramatically weakening the efficacy and potency of the effect; this was consistent with prior findings by the Elmslie group (Buraei and Elmslie, 2008). Modifications to other zones were more successful. Of the first set of *(R)*-roscovitine analogs to be evaluated, the most promising therapeutic candidate was one then termed "13x" and later renamed GV-58 (Figure 11B). "GV-58" refers specifically to the *(R)*-enantiomer of the molecule. In this structure, the substitution of the zone 4 iso-propyl side chain with an n-propyl group improved the potency of the slowed-deactivation effect while simultaneously greatly reducing CDK activity, and the substitution of the Zone 2 benzylamine side chain with a methylthiophenyl group further enhanced the potency of the slowed-deactivation effect. Overall, the IC50 of CDK activity was increased 22-fold compared to the parent molecule, while the EC_{50} of slowed deactivation was reduced 4-fold in Cav2.1 and $Ca_V2.2$ VGCCs (8.8 μM and 7.21 μM, respectively) (Liang et al., 2012). Wu et al. (2018) later also showed a larger maximal effect of GV-58 on deactivation compared to *(R)*-roscovitine, by measuring the fold change in normalized tail current integral upon applying each drug at a saturating concentration of 50 μM. Tail currents modified by GV-58 decayed much more slowly than tail currents modified by *(R)*-roscovitine (Figure 11C).) These experiments generated both valuable insight into the SAR of *(R)*-roscovitine analogs, and a

promising compound for further evaluation as a treatment for impaired neuromuscular transmission.

In subsequent experiments, GV-58, like *(R)*-roscovitine, was found to be selective for Ca_V2 VGCCs over Ca_V1, having no detectable slowed-deactivation effect on $Ca_V1.3$ channels even at concentrations up to 100 μM. GV-58 also appears to only modify open channels, like *(R)*-roscovitine (Tarr et al., 2014; Wu et al., 2018). In addition, GV-58's effects on CDK activity were further characterized. The measurements of GV-58-mediated CDK inhibition discussed above, which showed that GV-58 is a less potent CDK inhibitor than *(R)*-roscovitine but can nevertheless inhibit CDKs at micromolar concentrations, were carried out in the presence of low levels of ATP (Liang et al., 2012). However, physiological levels of ATP are higher than those used in the CDK inhibition experiments. Cell survival assays performed in physiological levels of ATP showed that unlike *(R)*-roscovitine, whose CDK activity inhibits cell survival *in vitro*, GV-58 concentrations up to 50 μM did not inhibit cell survival (Figure 11D) (Tarr et al., 2014), which implies that GV-58 does not have significant inhibitory effects on CDKs in the presence of physiological ATP. It is likely that higher levels of ATP mitigate GV-58's effects on CDKs because GV-58 acts by competing with ATP for CDK ATP-binding sites. The results of the cell survival experiments suggest that therapeutically-relevant concentrations of GV-58 are unlikely to cause side effects related to CDK activity.

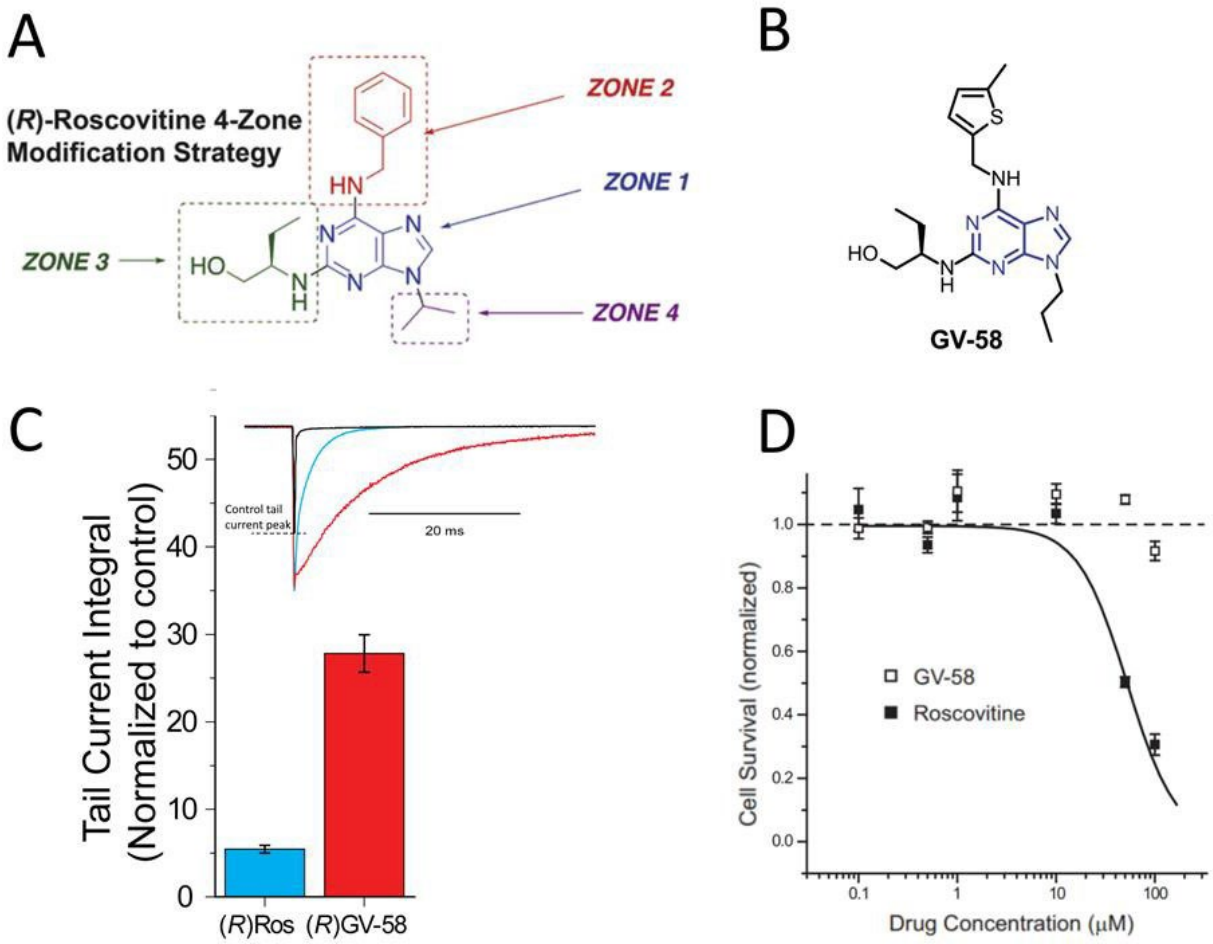

Figure 11: The (R)-roscovitine analog GV-58 is a more efficacious and potent modifier of VGCCs and has greatly reduced CDK activity compared to the parent molecule.

A. Structure of the parent molecule (R)-roscovitine, divided into four "zones" to systematize the synthesis of structural analogs. **B.** Structure of GV-58. Zones 2 and 4 have been modified from the parent molecule. **C.** Comparison of the fold increase in the tail current integral (compared to the pre-drug control integral) upon application of 50 μM *(R)*-roscovitine or GV-58. GV-58 slows tail current decay much more than *(R)*-roscovitine. Inset: Representative control, *(R)*-roscovitine-modified, and GV-58-modified tail currents. **D.** Plot of cell survival in cells treated at six different concentrations of *(R)*-roscovitine and GV-58. The dotted line represents no inhibition of cell survival. GV-58 does not inhibit cell survival at concentrations up to 50 μM. Panels A-C adapted from (Wu et al., 2018) with permission; Panel D adapted from (Tarr et al., 2014) with permission.

The above findings support the specificity of GV-58's proposed therapeutic mechanism. The next critical question to address was whether GV-58's effects on VGCCs can, in fact, enhance quantal release of neurotransmitter at impaired NMJs. Sure enough, GV-58 was found to improve the quantal content of action potential-evoked neurotransmitter release at a LEMS passive-transfer model mouse NMJ *ex vivo* (Tarr et al., 2013b), though this treatment alone did not completely restore quantal release to healthy control levels. It was then hypothesized that co-application of GV-58 and 3,4-DAP at LEMS model synapses might improve action-potential-evoked calcium influx (and therefore quantal release) synergistically, with 3,4-DAP broadening the action potential to permit extra openings of VGCCs, and GV-58 prolonging those openings. Indeed, the two drugs in combination had a supra-additive effect on quantal release, completely restoring it to the levels observed in healthy control synapses (Figure 12A) (Tarr et al., 2014). GV-58 has also been shown to improve grip strength *in vivo* in LEMS model mice (unpublished Meriney lab data).

GV-58 shows similar promise in restoring NMJ quantal release in other disease models. In nerve-muscle preparations intoxicated by botulinum toxin type A (BoNT/A) to the point of completely eliminating action-potential-evoked release (as evidenced by the consistent failure of nerve stimulation to elicit an EPP), GV-58 was shown to supra-additively restore quantal release to near-control levels in combination with 3,4-DAP (Figure 12B) (Beske et al., 2017). The combination of GV-58 and 3,4-DAP also restored quantal release to control levels in a mouse model of SMA (SMNΔ7) (Figure 12C), and improved grip strength *in vivo* in the same model (Figure 12D) (Ojala et al., 2020).

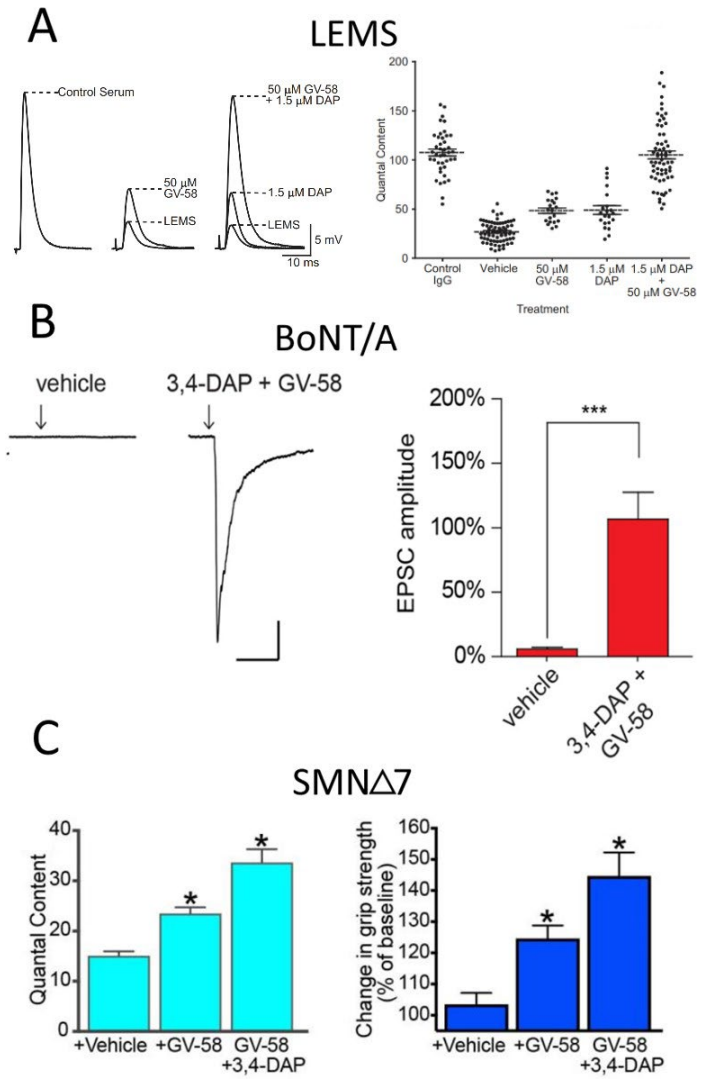

Figure 12: Combination treatment with GV-58 and 3,4-DAP restores neuromuscular transmission in multiple disease models.

A. *Left:* Representative EPPs at the NMJs of healthy or LEMS model mice. Treatment with either 50 µM GV-58 or 1.5 µM 3,4-DAP partially restores EPP amplitude at LEMS synapses, and combination treatment with both drugs restores EPP amplitude nearly to the level of the healthy control synapse. *Right:* Mean and distribution of quantal content measured at control, vehicle-treated LEMS, GV-58-treated LEMS, 3,4-DAP-treated LEMS, or combination-treated LEMS synapses. B. *Left:* Representative excitatory post-synaptic current (EPSC) amplitudes in BoNT/A-intoxicated synapses treated with vehicle or a combination of 3,4-DAP and GV-58. The BoNT/A intoxication prevents nerve stimulation from triggering an EPSC, but the combination drug treatment restores the EPSC. *Right:* Comparison of mean EPSC amplitudes in BoNT/A intoxicated synapses treated with vehicle or a combination of 3,4-DAP and GV-58, where 100% is the baseline EPSC at unintoxicated synapses. The combination drug treatment restores the baseline EPSC. C. *Left:* Quantal content at mouse SMA model (SMNΔ7) NMJs is significantly increased by 50 µM GV-58, alone or in combination with 1.5 µM 3,4-DAP. *Right:* SMNΔ7 mouse grip strength is increased by 50 µM GV-58, alone or in combination with 1.5 µM 3,4-DAP. Panel A adapted from (Tarr et al., 2014) with permission; Panel B adapted from (Beske et al., 2017), open access (http://creativecommons.org/licenses/by/4.0/); Panel C from (Ojala and Meriney) unpublished observations.

Given GV-58's promising effects in these preclinical experiments, it would be beneficial to optimize its structure to derive a further improved therapeutic candidate. For example, improved efficacy (in terms of the maximum slowing of current decay, which is representative of how greatly the drug prolongs Ca_V2 mean open time) could translate into improved symptomatic relief; improved potency would allow treatment at lower doses and minimize side effects; and improved speed of action would increase the fraction of channels modified by a given concentration of drug during an action potential.

To gain further insight into the structure-activity relationship of *(R)*-roscovitine analogs, several new structures were synthesized using GV-58 as the parent molecule (Wu et al., 2018). Wu et al., (2018) found that adjustments to different parts of the structure differentially affected efficacy, potency, and speed of action (Figure 13). For example, in the analog MF-06, replacing the Zone 1 purine with a pyrazolo[1,5-a]-1,3,5-triazine and the Zone 4 n-propyl with an iso-propyl group resulted in higher efficacy: in the presence of MF-06, compared to GV-58, Ca^{2+} currents decayed more slowly and total Ca^{2+} influx was increased, indicating a greater increase in mean open time. Wu et al. (2018) also found that MF-06 was more potent than GV-58, with an EC_{50} of 2.56μM. However, they additionally found that MF-06's speed of action is slower than GV-58's, with the drug having little effect during brief depolarizing steps on the timescale of a physiological action potential. Conversely, Wu et al. (2018) found that substituting an unsaturated n-propyl group in Zone 4 resulted in the analog KK-20, whose speed of action is increased over GV-58's. The evaluated structures also varied in their effects on CDK activity; for example, MF-06 was found to strongly inhibit CDKs, while GV-58 and KK-20 evidenced little to no CDK inhibitory activity (unpublished observations).

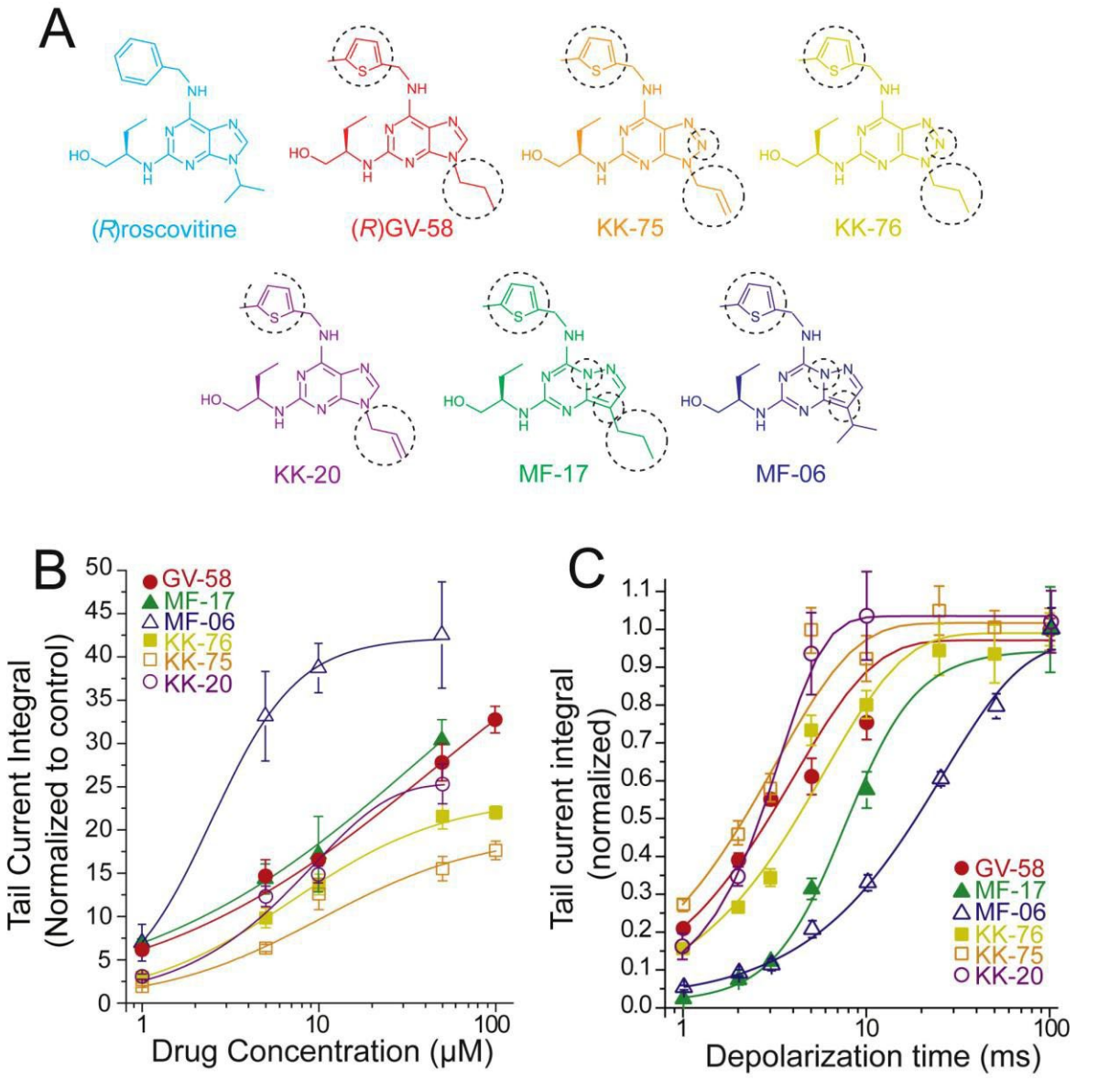

Figure 13: Modifications to the structure of (R)-roscovitine can tune efficacy, potency, and speed of action.

A. Structures of the parent molecule *(R)*-roscovitine, its analog GV-58, and five new analogs descended from GV-58. **B.** Concentration-response relationships in $Ca_V2.1$ channels for the six analogs of *(R)*-roscovitine shown in A, showcasing differences in efficacy and potency. Of note is the analog MF-06 (open triangles), whose efficacy and potency are greatly increased over GV-58's. **C.** Activity-dependence plots for the six analogs, showcasing differences in speed of action. The effects of all analogs on tail currents increase with the length of the depolarizing step used to activate channels, suggesting that they retain *(R)*-roscovitine's property of modifying channels that are in the open state. Of note are KK-20 (open circles),whose speed of action is increased over GV-58's, and MF-06 (open triangles), whose speed of action is much slower than GV-58's despite its higher efficacy and potency. Figure adapted from (Wu et al., 2018) with permission.

This second round of exploratory synthesis of *(R)*-roscovitine analogs demonstrated that it is possible to tune the therapeutically-relevant characteristics of their effects on VGCCs. However, synthesizing new compounds is a time-intensive process, so making unsuccessful modifications is very costly. An understanding of where and how drugs in this class of modifiers interact with Ca_v2 channels could be used to more efficiently guide the synthesis of improved analogs. In addition, insight into the mechanism by which these drugs alter VGCC state transitions would advance our understanding of the structure-function relationships underlying Ca_v2 channel gating.

2.3 Narrowing down how *(R)*-roscovitine analogs access and modify channels

One clue to how *(R)*-roscovitine analogs interact with VGCCs comes from a recent investigation into the effects of very brief applications of the fast-acting analog KK-20. Like the parent molecule, KK-20 apparently only modifies channels in the open state, based on the finding that the proportion of current decay slowed by the drug depends on the length of the depolarizing voltage step used to activate channels. Despite this, when a fast-perfusion system (Glasgow et al., 2017) was used to precisely time application and washout of the analog KK-20, the drug had little effect when applied only *during* the depolarizing step (Figure 14A, 14B) (Wu et al., 2018). However, when the drug was applied for 100ms while the cell was held at -100mV, then washed out of the extracellular saline 200ms prior to the depolarizing step, current decay was slowed nearly as effectively as it had been by continuous application of the drug in previous experiments (Figure 14C) (Wu et al., 2018). The time constant for termination of drug action after washout was calculated at approximately 1 s (Figure 14D) (Wu et al., 2018).

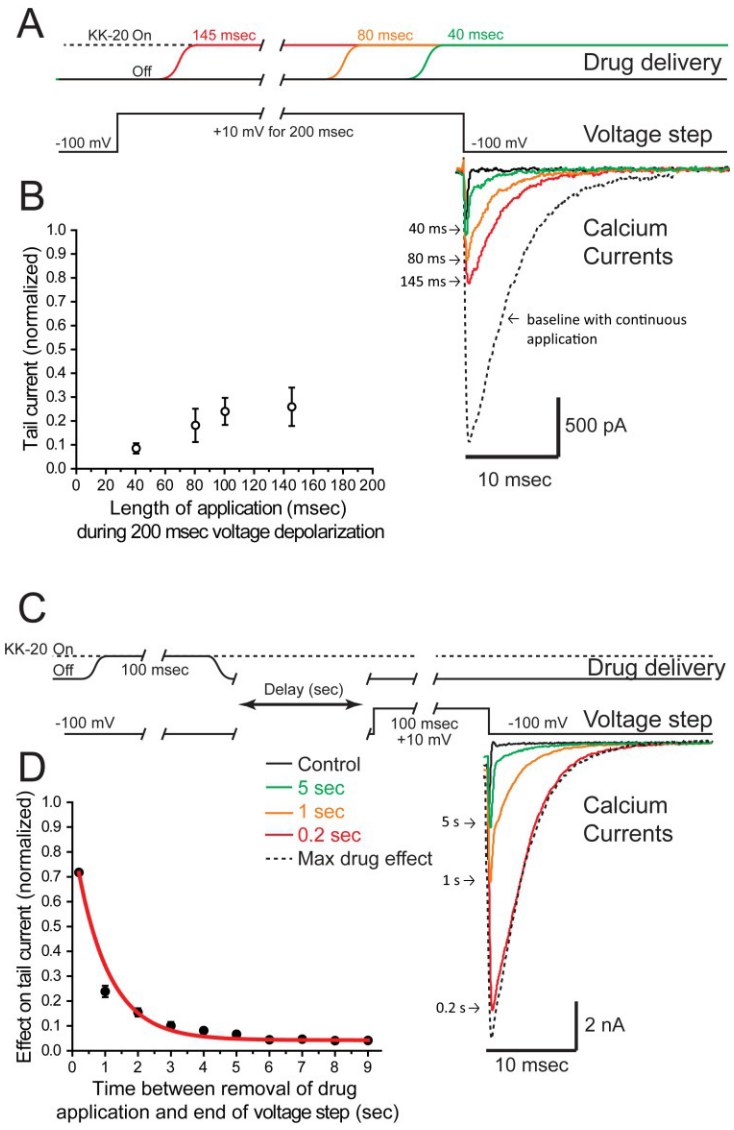

Figure 14: The (R)-roscovitine analog KK-20 is less effective when applied during the depolarizing step than when applied and washed out prior to the depolarizing step.

A. 50 μM KK-20 was rapidly applied and washed off during a 200 ms depolarizing step to +10 mV, followed by repolarization to −100 mV to elicit tail currents. *Top:* the duration of KK-20 application during the step. *Middle:* The depolarizing voltage step. *Bottom right:* representative tail currents for each duration of KK-20 application. The tail current shown as a dotted line represents the maximum tail current elicited by the continuous application of KK-20 throughout the stimulus and tail current, beginning 1 s before the voltage step. **B.** Plot of the effect of KK-20 on tail current integral, normalized to the maximum tail current integral (shown with the dotted line in A). The effect of KK-20 increases with longer applications during the step, but does not exceed 30% of maximum. **C.** KK-20 was rapidly applied and washed out before onset of the depolarizing step. The longer the interval between washout of the drug and the end of the depolarizing step, the less effect of KK-20 on tail currents. *Bottom right:* Representative tail currents for each interval between drug washout and the end of the voltage step. **D.** Effect of KK-20 on normalized tail current integral vs the length of the interval between washout and the end of the depolarizing step. The data are fit with a single exponential (red line) to calculate the time constant of termination of drug action, 0.99 s. Figure from (Wu et al., 2018), used with permission.

These unexpected results could be explained by a model (Figure 15) in which the drug does not bind to an extracellular site on the channel or access an internal site via the pore, but instead enters the channel laterally through a fenestration (an opening or tunnel) which it accesses from the plasma membrane (PM). This mode of entry has been described for other lipid-soluble modifiers of voltage-gated ion channels, including K+ (Lenaeus et al., 2014) and Na+ (Boiteux et al., 2014; Hille et al., 1977a) channel modifiers as well as modifiers of VGCCs. For example, a shared binding site for DHP agonists and antagonists in Cav1 VGCCs is located within a fenestration at the interface of domains III and IV, which it is presumed to access by diffusing through the PM (Gao and Yan, 2021; Hockerman et al., 1997b).

In the case *(R)*-roscovitine analogs, access via the PM would be consistent with the slow termination of action after washout, as residual drug in the PM is not washed away and continues to act on channels until it slowly partitions back out of the membrane. In this interpretation, the fenestration that leads to or contains the binding site is most accessible from within the PM when the channel is closed. Once inside the fenestration, the drug is unable to modify the channel until it opens in response to membrane depolarization, changing the positions of nearby residues to form the binding pocket. This would explain why drug applied during the depolarizing voltage step is ineffectual despite the activity-dependence of its effect: The drug must interact with the channel in its closed state to gain access to the vicinity of the binding site, and the channel must then open in order for the drug to occupy the binding site and slow deactivation. We will refer to this proposed explanation as the "state-dependent fenestration access hypothesis" (Figure 15).

Although this hypothesis proposes that the binding site is inaccessible from outside the channel while it is in the open state, a small amount of current modification does occur when the drug is applied during the depolarizing step. However, channels are not open continuously

throughout the step, but flicker between open and closed states; the maximum P_O for wild-type $Ca_V2.1$ channels is unlikely to exceed ~0.6 (Fellin et al., 2004; Tottene et al., 2005). Therefore, the partial modification of currents Wu et al. (2018) observed (up to ~30%) when the drug was rapidly applied during the depolarizing step may still be due to the drug accessing channels while they are closed.

The state-dependent fenestration access hypothesis can also be reconciled with the fact that *(R)*-roscovitine is only effective when applied to the outside of the cell. When the cell is bathed by this lipophilic drug, it is likely that the PM and intracellular concentration quickly equalizes with the external concentration, as has been shown for the lipophilic form of lidocaine (Hille, 1977b) whereas intracellularly-applied drug likely diffuses across the PM and escapes into an effectively infinite extracellular "sink" (Jo and Bean, 2014). Rapid membrane permeation of lipophilic compounds has previously been discussed as a complicating factor in experiments that rely on "selective" extra- or intra-cellular application of drugs (Hille, 1977b), and has been proposed as the reason that lipophilic drug carbamazepine inhibits Na^+ channels when applied externally or to an inside-out patch, but not when applied intracellularly (Jo and Bean, 2014).

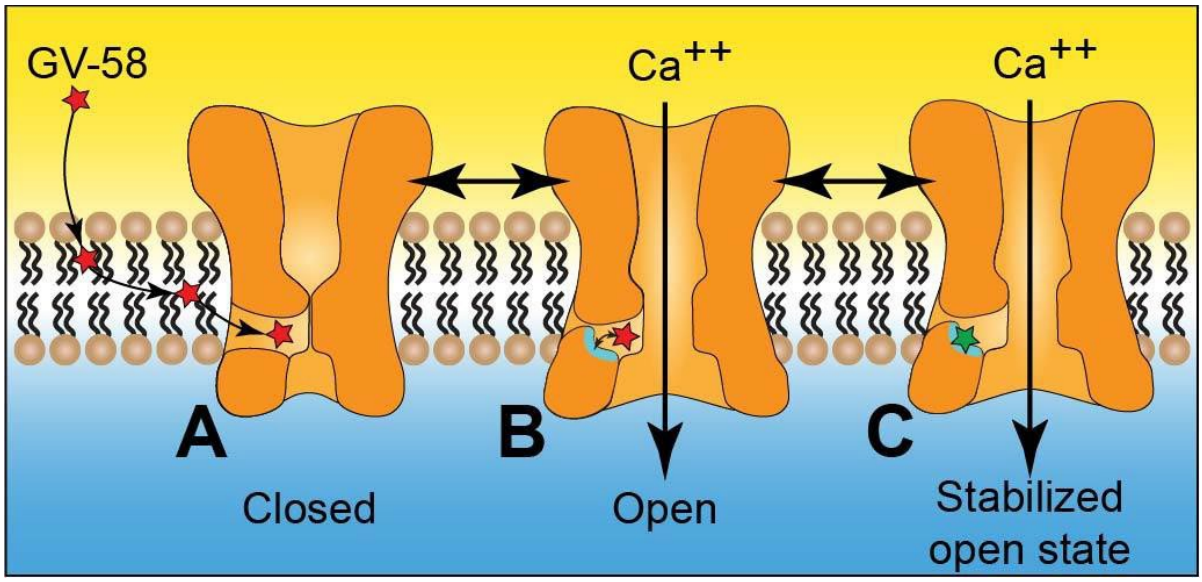

Figure 15: The state-dependent fenestration access hypothesis for (R)-roscovitine and (R)-roscovitine-derived compounds.

A. Step 1: We hypothesize that GV-58 (red star) partitions into the plasma membrane (PM), from which it enters a fenestration that is wide enough to move through when the channel is in the closed state. In this state, the binding site is not in the correct conformation for GV-58 binding. **B.** Step 2: When the channel opens during membrane depolarization, the fenestration narrows and prevents GV-58 entry, and a change in structure allows GV-58 that has already entered the channel to bind at a state-dependent binding site (light blue). The example site shown is within the fenestration, but it is also possible that the drug enters through the fenestration to access a binding site in the central cavity. **C.** GV-58 bound to the state-dependent site (green star) stabilizes the open state, lengthening the mean open time. While GV-58 is used in this example, we hypothesize that this pathway for drug access and binding is shared by *(R)*-roscovitine and all of its derivatives that prolong mean open time in Ca_V2 channels.

The above findings, in combination with previous investigations into *(R)*-roscovitine and related compounds, narrow down the location and likely characteristics of the binding site that mediates slowing of deactivation. The Ca_V2-specificity of these drugs (Buraei et al., 2007) suggests that the binding pocket contains one or more residues that are conserved across Ca_V2 subtypes, but are not found in Ca_V1; the fact that the Ca_V2 domain III is both necessary and sufficient for slowed deactivation (Yarotskyy et al., 2012) suggests that the binding pocket is located in this domain; the activity-dependence of the effect suggests that the residues of the pocket are only in the drug-binding conformation when the channel is open (Buraei et al., 2005; Tarr et al., 2014; Wu et al., 2018); and the evidence supporting the state-dependent fenestration access

hypothesis (Wu et al., 2018) suggests that the binding pocket is accessible from within the membrane via a fenestration in the side of the closed channel. These assumptions became the starting point for our evaluation of specific VGCC residues predicted to play a role in *(R)*-roscovitine analog-mediated slowing of deactivation.

3.0 The use of computational methods to generate testable predictions about how *(R)*-roscovitine analogs interact with $Ca_V2.1$ channels

3.1 Introduction

In the conclusion to Chapter 2, we described characteristics of a binding site for *(R)*-roscovitine analogs that would be consistent with prior experimental findings about how this drug affects Ca_V2 channels. To summarize, the site should include binding residues specific to the CaV2 domain III; it should be accessible from the plasma membrane, via a fenestration that is wide enough to enter only when the channel is closed; and the binding residues should be in the correct conformation to bind the drug only when the channel is open (or possibly in a transitional state).

However, this information alone is not sufficient to locate the binding site. Drug-binding pockets and fenestrations are both properties of the three-dimensional channel structure or example, the binding of *(R)*-roscovitine analogs may be coordinated by residues that are widely separated in the primary sequence, but are structurally in close proximity to one another. Therefore, a binding site meeting the characteristics described above cannot be identified solely from the primary amino acid sequence.

Another important factor is that protein structures are not static. They must be regarded as occupying a broad conformational space, defined by their intrinsic structural dynamics (the conformational rearrangements that are energetically favorable for a given protein given its sequence and structure, including large functional motions like VGCCs' voltage sensor movements and opening and closure of the pore). A binding pocket might not be represented in a static "snapshot" of the structure if it only takes shape in a subset of accessible conformations.

Given our hypothesis that GV-58 enters the channel through a state-dependent fenestration and binds to a state-dependent site, we needed to be able to examine the structure of $Ca_V2.1$ in different states in order to make predictions about GV-58 binding.

At the stage of the project when it was first necessary to examine the three-dimensional structure of $Ca_V2.1$, no experimentally solved Ca_V2 VGCC structures were available. We used homology modeling, an approach in which the primary sequence of the protein of interest is mapped onto the experimentally solved structure of a related protein, to model the $Ca_V2.1$ α1 subunit in an open and an inactivated state. We were then able to use these models in drug-docking and molecular dynamics simulations to generate testable predictions about the location and structure of the GV-58 binding site.

Recently, a cryogenic electron microscopy (cryo-EM) structure was published for an inactivated $Ca_V2.2$ channel (Gao et al., 2021). Although different VGCC subtypes share a high degree of structural similarity, some structural elements in the solved $Ca_v2.2$ channel were not represented in our inactivated homology model, which was based on a Ca_V1 template. The cryo-EM $Ca_V2.2$ structure presents an opportunity for us to consider our experimental findings in light of structural characteristics that may be unique to the Ca_V2 family of VGCCs, and we will refer to this structure where relevant throughout the following chapters.

3.2 Methods

3.2.1 Construction of $Ca_V2.1$ open and inactivated state homology models

Dr. Mary Cheng (Computational & Systems Biology, University of Pittsburgh) made the open homology model with MODELLER (Webb and Sali, 2016), using a crystal structure of the Na_vMs Na+ channel (Sula et al., 2017; PDB:5HVD) as the template. Dr. Rozita Laghaei (Pittsburgh Supercomputing Center, Carnegie Mellon University) made the inactive homology model with Phyre2 (Protein Homology/analogy Recognition Engine v2.0; Kelley et al., 2015), using a cryo-EM structure of a $Ca_V1.1$ channel as the template (Wu et al., 2016; PDB:5GJV).

3.2.2 Automated GV-58 docking simulations

Simulations of GV-58 ligand docking to the open and inactive state $Ca_V2.1$ homology models were performed by Dr. Rozita Laghaei using AutoDock4 and its AutoGrid4 tool (Morris et al., 2009). Docking calculations were run on both the open-state and inactive-state homology models of $Ca_V2.1$. AutoGrid4 default settings were used for grid generation in the channel. The docking region was specified as a cubic box of side-length of 120 grids with a grid spacing in each direction of 0.375 Å (each side 45 Angstrom).

3.2.3 Predicting the size and shape of $Ca_V2.1$ fenestrations and modeling GV-58 movement through the fenestrations

To model GV-58 access through fenestrations in open and inactive state models, we first predicted the location of fenestrations with CAVER 3.0 (Chovancova et al., 2012), using the default parameters for CAVER calculations (probe radius = 0.9 Å; shell radius = 3 Å; shell depth = 4 Å; clustering threshold = 3.5; number of approximating balls = 12). Within modeled fenestrations, we analyzed bottlenecks along the pathway to determine candidate residues for mutations designed to reduce or enlarge the pathway diameter.

We ran several molecular dynamics (MD) simulations to predict GV-58 movement through the fenestrations identified in the open and inactive $Ca_V2.1$ homology models, using several models of docked GV-58 that we obtained from our AutoDock4 simulations described in 3.2.2 above. We ran these simulations in the open and inactive state homology models under the following conditions: 1. all-atom and not fixed; 2. the backbone fixed and Side chains free to move; and 3. the backbone and all side chains fixed. All simulations were run in the presence of explicit water and lipid bilayer, which is considered the most accurate and unbiased approach for observing the sequence of events leading to drug binding in a transmembrane protein.

For the MD simulations, we used the NAMD (NAnoscale Molecular Dynamics) software package (Phillips et al., 2005; Phillips et al., 2020) and ran in-house codes to analyze the output trajectories. (NAMD was developed by the Theoretical and Computational Biophysics Group in the Beckman Institute for Advanced Science and Technology at the University of Illinois at Urbana-Champaign; http://www.ks.uiuc.edu/Research/namd/). We carried out multiple runs starting with different conformers (homology models of wild-type and mutant $Ca_V2.1$ in open and inactive states), and with GV-58's starting position in the entrance of the fenestration tunnel (both

open and inactive states) or in the channel pore (open state) to observe the diffusion and binding events. In parallel, we conducted coarse-grained simulations using the CaverDock software tool (Vavra et al., 2018, in preparation), which is particularly suited for evaluating drug trajectories through fenestrations.

3.2.4 Preparation of figures

Structural images were prepared using the PyMOL Molecular Graphics System (PyMOL, Version 2.0 Schrödinger, LLC), UCSF Chimera (Pettersen et al., 2004; developed by the Resource for Biocomputing, Visualization, and Informatics at the University of California, San Francisco, with support from NIH P41-GM103311), and Visual Molecular Dynamics (VMD) (Humphrey et al., 1996). Data plots were prepared using gnuplot (Williams and Kelley, 2011) or Prism version 9.2.0 for Windows (GraphPad Software, San Diego, California USA, www.graphpad.com).

3.3 Results

3.3.1 Homology modeling of Cav2.1 in open and inactivated conformations

Given the chimeric channel experiments which showed that the $Ca_V2.1$ DIII sequence is likely to contain (R)-roscovitine/GV-58 binding residues (Yarotskyy et al., 2012), we wanted to use single-site mutagenesis in this part of the channel to identify individual residues involved in the binding and/or slowed deactivation effect of the drug. However, the Ca_V2 DIII contains over

300 residues, so more information was needed to refine our search. We also considered it likely that residues outside of domain III participate in GV-58 binding and/or action, given that, although the $Ca_V2.2$ DIV was not sufficient for sensitivity to the parent *(R)*-roscovitine in the chimera experiments, it did enhance the effect of the drug when included alongside the $Ca_V2.2$ DIII (Yarotskyy et al., 2012). To locate candidate GV-58 binding residues for our mutagenesis experiments, we would need to predict favorable binding sites for the drug in the context of CaV2.1's three-dimensional structure.

We began by building homology models of the $Ca_V2.1$ α1 subunit in open and inactivated states (Figure 16). The amino acid sequence of the $Ca_V2.1$ α1 subunit was mapped onto the solved structures of related voltage-gated ion channels in open and inactivated conformations. To determine the most energetically favorable positions of $Ca_V2.1$ side chains given its primary sequence, we refined our models with energy minimization and molecular dynamics (MD) simulations in the presence of an explicit solvated lipid bilayer (Figure 17**)**. The inclusion of the lipid bilayer was important because $Ca_V2.1$ is a membrane-embedded channel, and the plasma membrane imposes constraints on protein folding.

The open state homology model was made by our collaborator Dr. Mary Cheng (Computational & Systems Biology, University of Pittsburgh) using MODELLER (Webb and Sali, 2016), which generates 3D structural models along with their confidence scores using structurally resolved homologs as templates. The template used for the open state $Ca_V2.1$ homology model was the crystal structure of an evolutionarily related prokaryotic Na^+ channel, Na_vMs (Sula et al., 2017; PDB:5HVD). In this model, the pore can be observed to be open. In the $Ca_V1.1$ subtype of VGCCs, the activation gate—the hydrophobic residues that converge in the central cavity to block ion permeation in the closed conformation of the pore—has been reported

to consist of an S6 residue in each domain at positions analogous to V357, F711, F1457, and F1757 in $Ca_V2.1$. As expected, these residues are separated in the open state model and do not occlude the pore (Figure 16C).

The inactivated state homology model was made by our collaborator Dr. Rozita Laghaei (Pittsburgh Supercomputing Center, Carnegie Mellon University) using Phyre2 (Protein Homology/analogy Recognition Engine v2.0; Kelley et al., 2015), which produces a set of 3D models based on alignment to known structures, detects distant sequence homologs with PSI-BLAST (Altschul et al., 1997), and applies a hidden Markov model to construct models based on sequence alignments. The template used for the inactivated state $Ca_V2.1$ homology model was a cryo-EM structure of a $Ca_V1.1$ channel (Wu et al., 2016; PDB:5GJV), which at the time was the closest evolutionary relative to $Ca_V2.1$ whose structure had been solved experimentally. In the inactivated state, the VSDs are in the activated conformation as in the open state model, but the channel pore is closed; as in the template structure, rotations of the S6 helices have caused the predicted activation gate residues V357, F711, F1457, and F1757 to converge into the pore and physically obstruct it (although the recent cryo-EM structure of $Ca_V2.2$ disagrees with this activation gate structure; see section 3.2.2 and Figure 21 below).

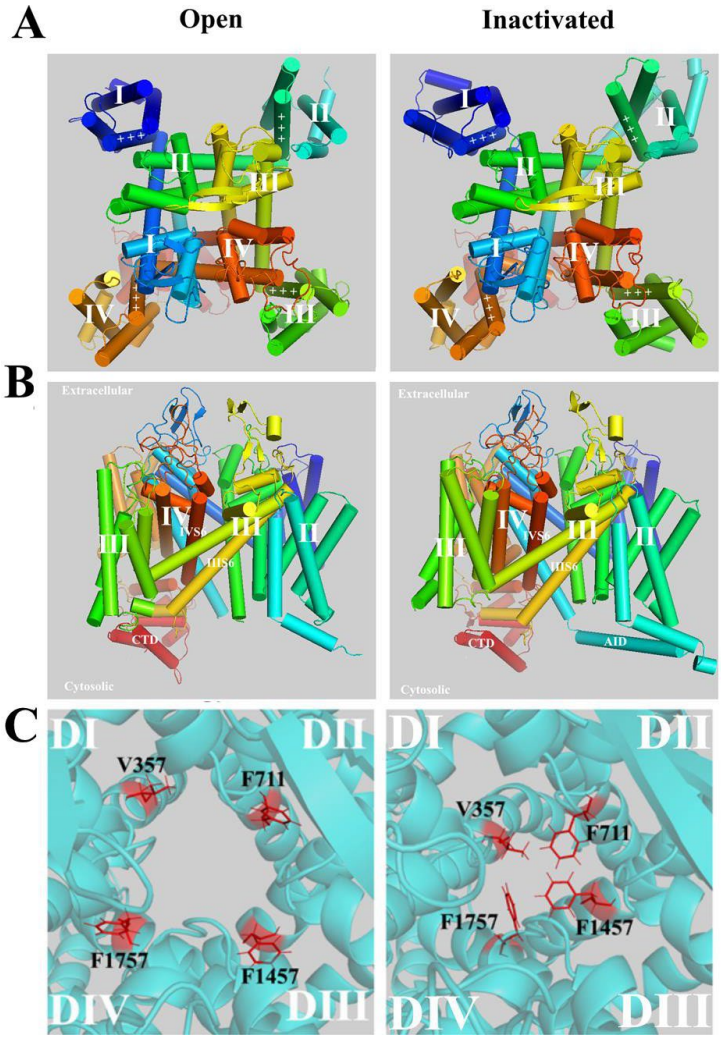

Figure 16: Open and inactivated homology models of $Ca_V2.1$ α1.

A. Top views (i.e., from an extracellular perspective) of our open and inactivated state homology models, shown in cartoon representation with helices rendered as cylinders. The VSDs and pore-forming segments are labeled with the domain they belong to (I-IV), showcasing the clockwise arrangement of the domains. The S4 segments are labeled with plus signs, and all four are in activated positions in both the open and inactivated state models (although their positions differ slightly, likely due to differences between the Na_VMs and $Ca_V1.1$ templates). The S6 segments (not labeled) can be seen converging into the pore in the inactivated state. B. Side views of our open and inactivated state homology models, at the interface of domains III and IV. The domain III and IV S6 segments are labeled. The domain III and II VSDs are visible in the foreground, flanking the pore-forming segments, and the cytosolic C-terminal domain (CTD) can be seen in the background. The alpha-interaction domain (AID), which mediates the interaction of the Ca_V α1 subunit with the β subunit (Arikkath and Campbell, 2003), is represented only in the inactivated model, since this helix is not present in the Na_VMs template used to construct the open state model. C. Top-down view of the activation gate of our open state $Ca_V2.1$ homology model (left) and our inactivated state $Ca_V2.1$ homology model (right). The channel backbone (cyan) is shown in a semi-transparent ribbon cartoon representation. The residues that form the activation gate in our homology models are shown in stick representation and colored red. In the open state homology model, all four residues are oriented away from the dilated pore. In the inactivated homology model, the S6 segments have converged to narrow the pore, and the activation gate residues have rotated into the pore to form a hydrophobic seal against ion permeation.

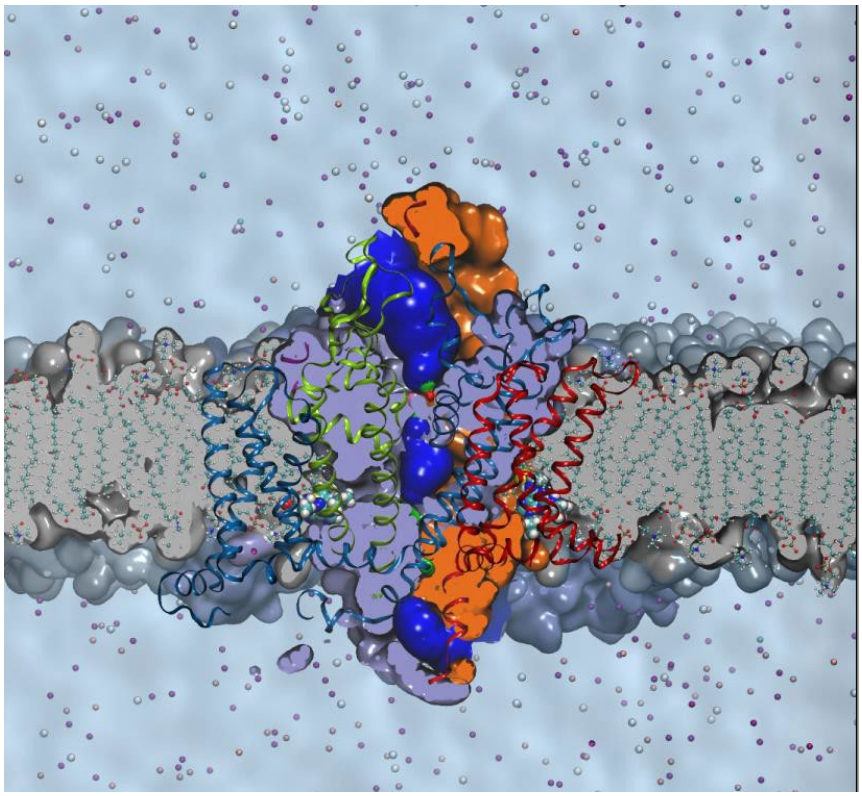

Figure 17: A representation of a typical MD system used in this study.

The VGCC (shown by surface and cartoon representations, with domain III colored orange) was embedded in a lipid bilayer and solvated with water and ions. The dark blue spaces were calculated using the software program HOLE (Smart et al., 1996; http://www.holeprogram.org/) and show the sealed-off calcium ion pathway in the inactivated state.

We used CAVER 3.0 (Chovancova et al., 2012), a software tool for analysis and visualization of protein fenestrations that is also available as a PyMol plugin (PyMOL Molecular Graphics System, Version 2.0 Schrödinger, LLC), to estimate the size and shape of the $Ca_V2.1$ fenestrations in both the open and inactive states. This software can be used to analyze either single static structures, or sets of structures such as MD simulation outputs. The identification of cavities is based on Voronoi calculation for all atoms of the protein, and Voronoi diagrams describe the skeleton of tunnels within the structure. Both the open and inactivated state models were found to have fenestrations extending from the central cavity to each of the four domain interfaces, with the entrance to each fenestration accessible to the PM (Figure 18).

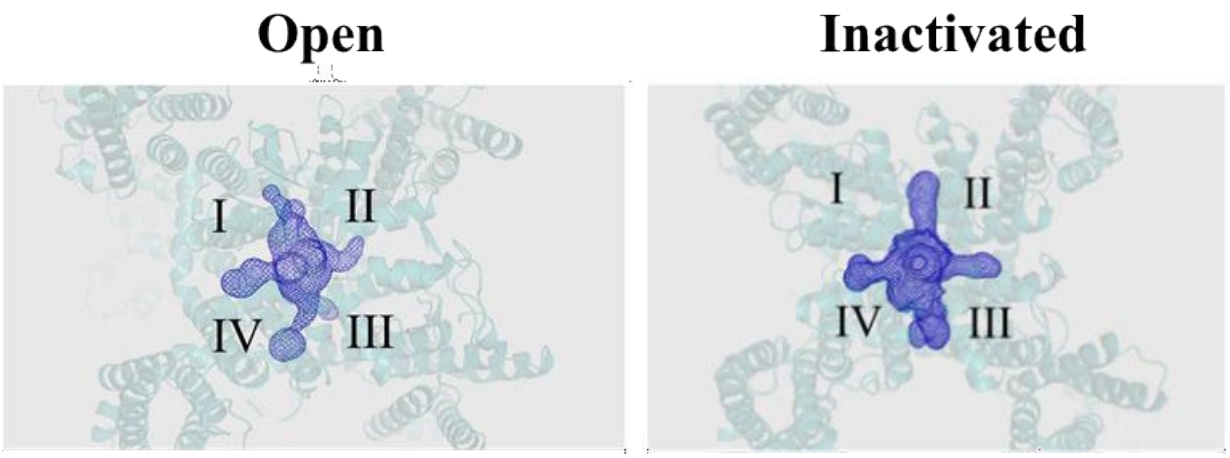

Figure 18: Fenestrations in the pore domains of our open and inactivated state $Ca_V2.1$ homology models.

Top-down views of in our open and inactivated state $Ca_V2.1$ homology models of the cavities detected with CAVER 3.0 (shown in mesh representation, blue), including the central cavity and fenestrations. Pore domains are labeled. Of note are the four fenestrations extending from the central cavity (the ion permeation pathway) to the PM at the interfaces of each domain, and the differences in shape and diameter of these fenestrations between the open and inactivated states, particularly the "bottleneck" in the domain III/IV fenestration in the open state.

Using CAVER 3.0, we found that the fenestration that connects the PM to the central cavity at the interface of domains III and IV, which we will refer to as the "domain III/IV fenestration", is state-dependent in shape and diameter **(**Figure 19**)**. In the closed pore, the diameter of the domain III/IV fenestration remains relatively constant at ~5 Å, while in the open pore, this fenestration is "pinched" to a minimum diameter of ~2 Å between its PM entrance and where it opens into the central cavity (Figure 19C). In our models, the "pinching" of the fenestration is coordinated by three phenylalanine residues, F1453 and F1457 in domain III and F1747 in domain IV (Figure 19A,B). As the channel opens, these "pinching residues" orient into the fenestration, narrowing it.

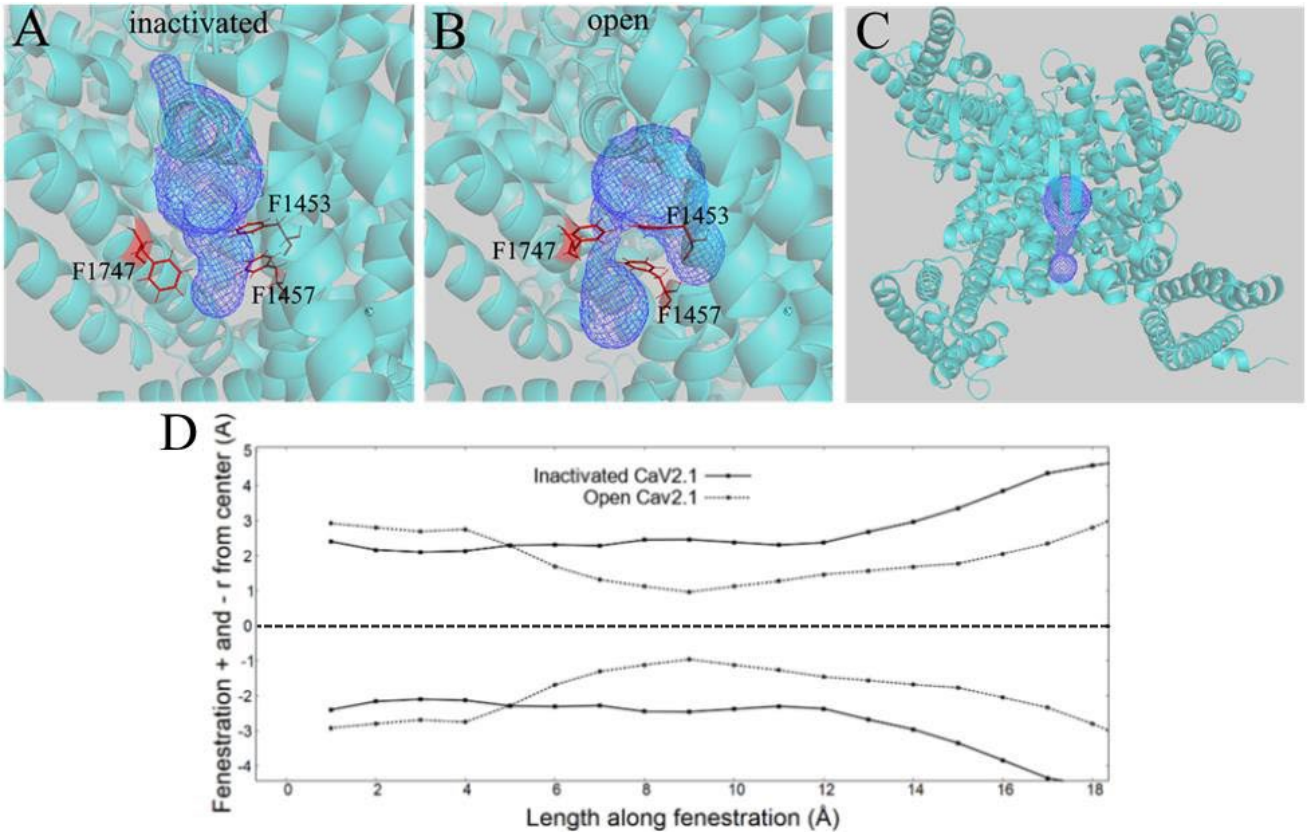

Figure 19: The state-dependent fenestration at the interface of domains III and IV in our $Ca_V2.1$ homology models.

A. View of the state-dependent domain III/IV fenestration in the $Ca_V2.1$ inactivated state homology model, with the fenestration and central cavity shown in mesh representation (blue). Three residues lining the fenestration (F1453, F1457, F1747) are shown in red. The view of the channel is tilted for better visibility of the shape of the domain III/IV fenestration. **B.** View of the $Ca_V2.1$ open state homology model from the same angle as A., with the fenestration and central cavity shown in mesh representation (blue). F1453, F1457, and F1747 (red) can be seen to have shifted position from the inactivated-state model, and now "pinch" the fenestration into a bottleneck, narrowing its diameter between the PM and central cavity. **C.** The III/IV fenestration and central cavity shown in a top-down view of the entire open-state channel, to provide context for the close-up images in A and B. **D:** Plot representing the diameter along the length of the domain III/IV interface fenestration in our homology models of open vs inactivated $Ca_V2.1$. The length of the fenestration is defined in 1 Å increments, beginning at its interface with the PM. At each length increment, the radius (r) of the fenestration is plotted above and below 0, as +r and -r, with 0 representing the center of the fenestration (dashed line). The distance along the y-axis between points at each length increment thus represents the diameter of the fenestration (the shortest distance separating the Van der Waals surfaces of the fenestration-lining residues). In the open state (dotted lines), the bottleneck visualized in B can be seen as a shrinking of the diameter to a minimum of ~2 Å at 9 Å into the fenestration, while the diameter in the inactivated state (solid lines) remains at roughly 5 Å. Past 12 Å, the fenestration widens in both states as it opens into the central cavity.

As we have discussed, the homology model representing the closed pore is an inactivated state model, with the voltage sensors in their "up" positions as they are in the open state (see Figure 15). While a true closed state would have been preferable to compare with the open state, it is typical for VSDs to be activated in the solved structures of voltage-gated ion channels that can be used as homology model templates, since the proteins are crystallized or frozen in the absence of a hyperpolarized membrane potential. Furthermore, our hypothesis (based on the fast perfusion experiments discussed in **2.3** above) is that GV-58 accesses its binding site through a fenestration that narrows in the open state. Since all of the fenestrations we observed in the open and inactivated structures are located within the pore domain, comparing our model of the closed pore in the inactivated state to our model of the open pore was sufficient for evaluating the state-dependence of fenestration diameter.

3.3.2 A comparison of the structural predictions of our open and inactivated Ca_V2 homology models with available substituted-cysteine accessibility data and an experimentally solved structure of $Ca_V2.1$

As we have discussed, $Ca_V1.1$ (like all Ca_V1 channels) is insensitive to the slowed-deactivation effect of GV-58. It is possible that structural features unique to Ca_V1 channels contribute to their GV-58 insensitivity. Therefore, for our models to be useful in predicting GV-58 binding, we needed to be confident that they accurately reflected the $Ca_V2.1$ structure despite being based on a $Ca_V1.1$ template. Given our hypothesis that GV-58 accesses the channel through a state-dependent fenestration and binds to a state-dependent binding pocket, it was especially important to validate our predictions of the open vs closed pore domain architecture in our open and inactivated models.

To assess the validity of the inner pore structural predictions of our $Ca_V2.1$ homology models, we compared them with the results of Zhen et al. (2005)'s substituted cysteine accessibility method (SCAM) experiments. In this SCAM study, each residue in the four S6 segments that line the inner pore of the Cav2.1 tetramer was individually mutated to a cysteine, and a cysteine-modifying reagent (MTSET) was applied internally to cells expressing each mutant. The ability of MTSET to modify a given residue strongly supports that it is accessible from the cytoplasm (due to being located below the membrane/cytoplasm interface, or via the open pore or aqueous crevices between segments). These SCAM data have previously been used to validate the pore domain architecture of open and closed $Ca_V2.1$ homology models based on solved voltage-gated potassium channel structures (Bruhova and Zhorov, 2010). We considered only residue positions that were modified by MTSET to validate our model; we could not assume that unmodified positions are *not* accessible to the cytoplasm, since lack of modification could mean either that a residue position is inaccessible or that the MTSET modification is functionally silent.

Zhen et al. (2005) systematically mutated the residues of all four S6 segments of $Ca_V2.1$ and identified 54 MTSET-modified positions, 50 of which our homology model of the $Ca_V2.1$ open state agrees are accessible from the cytoplasm. Our model was also consistent with Zhen et al.'s interpretation that some regions of segments S5 and S6 are loosely packed, with an aqueous crevice between them. Of these 54 residues, 5 were found *not* to be modified by MTSET if it was applied only while the pore was closed, suggesting state-dependent exposure to the cytoplasm (Xie et al., 2005). Our models replicated the state-dependent exposure of all five of these residues, which lent us further confidence in their predictions of the differences between the conformations of the open and closed pore.

Four MTSET-modified residues—I714, F1441, F1451, and F1745—are hydrophobically embedded in our open and inactive state models, in apparent contradiction of the SCAM data. However, the recently solved cryo-EM structure of the closely related $Ca_V2.2$ subtype agrees with our predicted orientations for I714, F1441, and F1745 (Figure 20, A-C) (Gao et al., 2021; PDB accession code 7MIY), and a hydrophobically embedded I714 is also consistent with evidence that this highly conserved isoleucine participates in stabilizing the closed pore through hydrophobic interactions with residues on neighboring segments (Hering et al., 2008; Hohaus et al., 2005; Stary et al., 2008). One possible explanations for these positions being modified by MTSET are that they become accessible to the cytoplasm (via the pore or an aqueous crevice between S5 and S6) when mutated to cysteine due to accompanying conformational rearrangements. Another is that they become temporarily accessible in an intermediate conformation sampled during gating; this hypothesis could be confirmed or ruled out by knowledge of the state-dependence of MTSET modification of the I714, F1441, and F1745 residues, which has not been reported. The F1451 residue, on the other hand, is oriented toward the central cavity in the $Ca_V2.2$ cryo-EM structure (Figure 19D), so our homology models may not accurately predict the orientation of this specific residue.

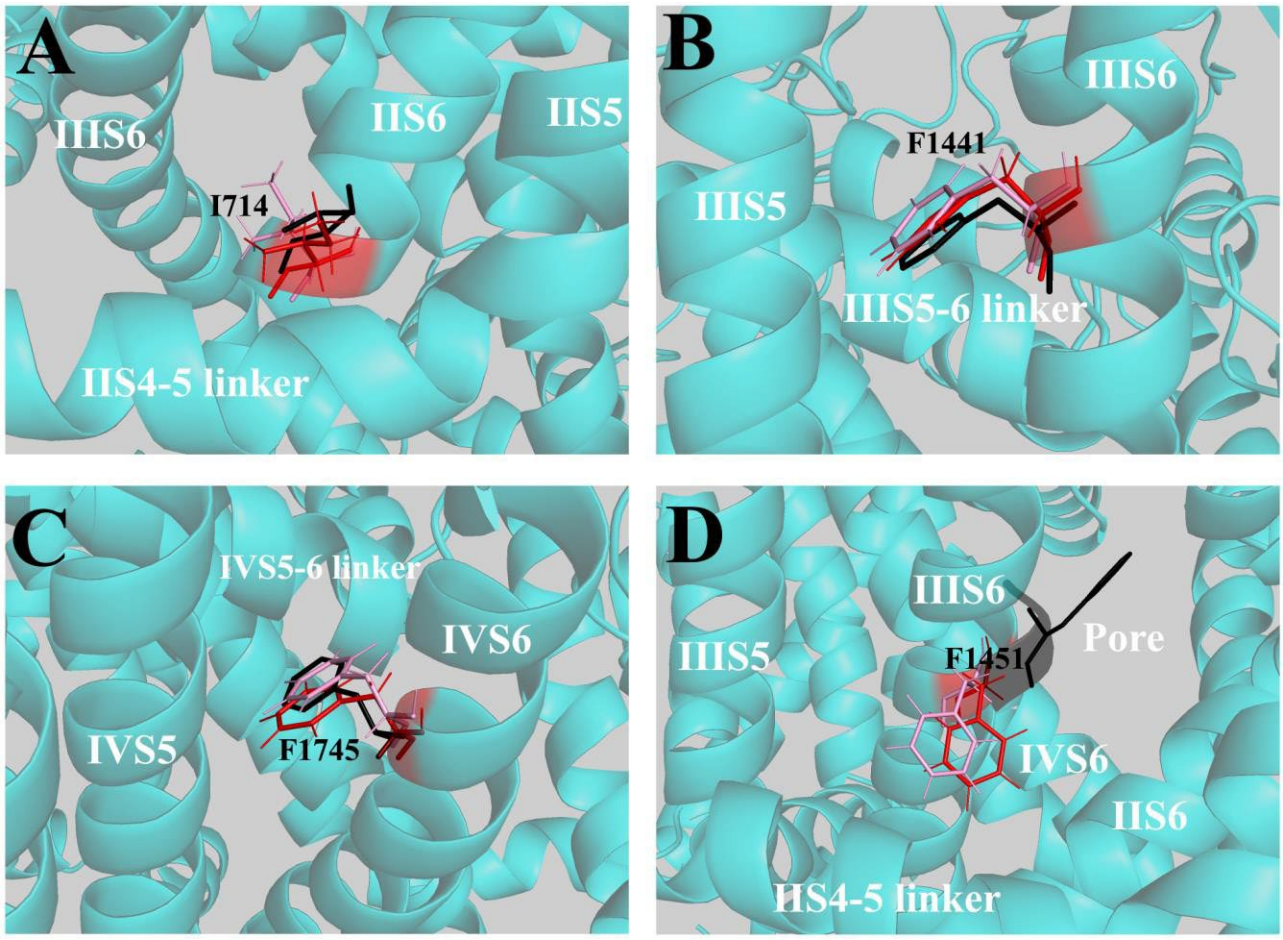

Figure 20: Residues that are hydrophobically buried in our $Ca_V2.1$ homology models in contradiction of existing SCAM data, compared with the analogous residues of a solved cryo-EM structure of $Ca_V2.2$.

A. Closeup of the I714 residue in our open (red) and inactivated (pink) $Ca_V2.1$ homology models, and the analogous residue in Gao et al. (2021)'s $Ca_V2.1$ cryo-EM structure (black), shown against the semi-transparent ribbon backbone of the open-state homology model. Nearby segments and linkers are labeled. Despite existing SCAM data supporting that this residue is accessible to the cytoplasm (Zhen et al., 2005) the cryo-EM structure of $Ca_V2.2$ validates the hydrophobically embedded position of I714 in our models. **B.** As in A, comparing the positions of the residue F1441 between models. **C.** As in A, comparing the positions of the residue F1745 between models. **D.** As in A, comparing the positions of the residue F1451 between models. Unlike the residues shown in A, B, and C, F1451 is hydrophobically embedded in our homology models while the analogous cryo-EM $Ca_V2.2$ residue faces the pore, due to a rotation of the IIIS6 helix compared to its position in our homology models (a portion of the cryo-EM backbone is shown in semi-transparent black to illustrate this). The cryo-EM $Ca_V2.2$ prediction of this residue's position is consistent with the Zhen et al. (2005)'s SCAM findings, while the predictions of our homology models are not.

An important discrepancy between our models and the cryo-EM structure of $Ca_V2.2$ is the location and structure of the activation gate. Although homology modeling can be a powerful tool

for predicting how a protein's unique primary sequence influences its structure, an important limitation is that it cannot effectively model major structural elements that are not represented in the template. Our models of $Ca_V2.1$ exclude a long stretch of sequence in domain II for which there is no analogous sequence, and therefore no template structure, in $Ca_V1.1$ or Na_VMs. The cryo-EM structure of $Ca_V2.2$ reveals that this sequence encodes an extremely long cytosolic extension of IIS6 (seven helical turns) and two additional cytosolic helices ($CH1_{II}$ and $CH2_{II}$), features that are apparently unique to Ca_V2 channels (Gao et al., 2021). Although we do not expect the cytosolic structures to contain the *(R)*-roscovitine analog binding site (since the drug does not slow deactivation when applied intracellularly), they do contribute to the activation gate structure and possibly to a Ca_V2-specific mechanism of pore closure, factors which may be relevant to *(R)*-roscovitine analogs' mechanism of action.

As we discussed in section 3.3.1**,** our inactivated $Ca_V2.1$ model predicts an activation gate formed by the residues V357, F711, F1457, and F1757, which converge into and occlude the pore. In the inactivated $Ca_V2.2$ cryo-EM structure, these residues remain in a separated configuration (as they do in our open-state homology model) and do not occlude the pore (Gao et al., 2021) (Figure 21A). The $Ca_V2.2$ structure instead features an activation gate made up of multiple layers of hydrophobic residues, located intracellularly to the gate in our model (Figure 21B). At the base of this gate are residues analogous to $Ca_V2.1$'s A366, A720, I1463, and F1765, which converge into the pore surrounding a $CH2_{II}$ tryptophan that is not represented in our models. Gao et al. (2021) propose that $CH2_{II}$ facilitates pore closure by pulling the S6 segments together and "securing" the pore with the central tryptophan, which we infer participates in stabilizing interactions with other residues at the base of the activation gate. $CH2_{II}$ is also accommodated by the unwinding of the last three helical turns of IIIS6, which results in a shorter IIIS6 compared to

the $Ca_V1.1$ cryo-EM structure and our $Ca_V2.1$ homology models, where IIIS6 extends to residue M1473. The $Ca_V2.2$ IIIS6 ends with the residue analogous to I1463, whose position at the base of the activation gate agrees with Xie et al. (2005)'s SCAM experiments, which place I1463 at the membrane-cytoplasm interface.

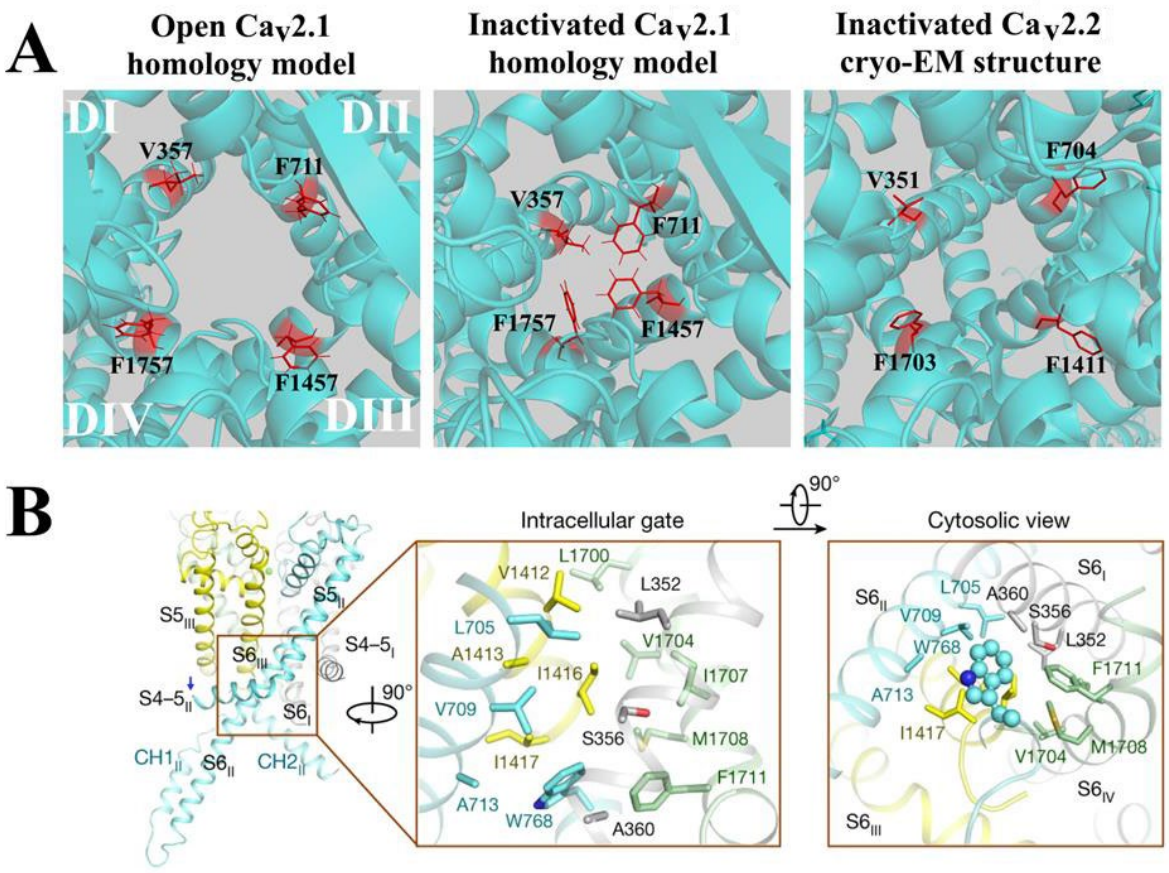

Figure 21: Cytoplasmic helices unique to Ca_V2 channels contribute to an activation gate structure that is not representented in our $Ca_V2.1$ inactive state homology model.

A. Top-down view of the inner pore of our open state $Ca_V2.1$ homology model (left), our inactivated state $Ca_V2.1$ homology model (center), and Gao et al. (2021)'s solved cryo-EM structure of inactivated $Ca_V2.1$ (PDB: 7MIY). The open and inactivated homology model images were previously shown in Figure 16C. The channel backbone (cyan) is shown in a semi-transparent ribbon cartoon representation. The organization of the S6 segments by domain, labeled in the open state image, is consistent across all three images. The residues that form the activation gate in our homology models, and the analogous residues in $Ca_V2.2$, are shown in stick representation and colored red. In the open state homology model, all four residues are oriented away from the dilated pore. In the inactivated homology model, the S6 segments have converged to narrow the pore, and the activation gate residues have rotated into the pore to form a hydrophobic seal against ion permeation. In the inactivated cryo-EM $Ca_V2.2$ model, these residues do not seal the pore, but face away from it as in the open state homology model, although the S6 segments still converge to narrow the pore. The apparently Ca_V2-specific $CH2_{II}$ helix is visible at the intracellular mouth of the pore. The analogous residues of $Ca_V2.2$ vs $Ca_V2.1$ are as follows: V351 = V357; F704 = F711; F1411 = F1457; F1703 = F1757. B. The activation gate in the $Ca_V2.2$ cryo-EM structure, which is located intracellular to the $Ca_V2.1$ homology models' activation gate shown in A. *Left:* Side view of base of the $Ca_V2.2$ cryo-EM structure, showing the extremely long IIS6 segment and the $CH1_{II}$ and $CH2_{II}$ helices that may be unique to Ca_V2 channels. *Right:* Close-up views of the $Ca_V2.2$ activation gate from side and bottom-up perspectives, showing the multiple layers of residues that seal the closed pore. The residue W768 (shown in stick form in the side view and as spheres in the bottom-up view), corresponding to W777 in the $Ca_V2.1$ sequence, is contributed by the $CH2_{II}$ helix. Panel B adapted from (Gao et al., 2021) with permission.

Another discrepancy lies in the structure of the fenestrations in the pore domain. Our homology models have PM-accessible fenestrations at each domain interface. Conversely, Gao et al. (2021) report only the fenestration at the domain III/IV interface in their cryo-EM structure of $Ca_V2.2$.

Given the >92% agreement of our models with the available SCAM data, we were satisfied at the time that that they represent $Ca_V2.1$'s pore structure accurately enough for the purpose of simulating drug-binding interactions with the channel (see **3.3.3**, below) to identify candidate GV-58 binding residues for experimental evaluation. Nevertheless, the discrepancies between our model of the activation gate and the unique activation gate structure observed in the $Ca_V2.2$ cryo-EM model may be relevant to GV-58 action, especially if the drug slows deactivation by disrupting the mechanisms that stabilize the closed conformation of the gate. Knowledge of the unique features of the Ca_V2 activation gate will help us to interpret our experimental findings in the following chapters.

3.3.3 Automated docking simulations predict a candidate binding region for GV-58 in a fenestration at the interface of $Ca_V2.1$ domains III and IV

Using our homology models of $Ca_V2.1$ open and inactivated states, we were able to use the program Autodock4 (Morris et al., 2008) to predict candidate GV-58 binding residues *in silico*. These docking simulations were the work of Dr. Rozita Laghaei.

AutoDock4 uses a Lamarckian genetic algorithm to identify favorable ligand-binding conformations (Morris et al., 1998; Morris et al., 2008). Briefly, it generates a population of simulated ligand molecules—in this case, a population of GV-58 molecules—with randomized variables describing their position, orientation, and conformation. The "fitness" of each individual

(each ligand molecule in the population) is defined by the absolute binding free energy of its interaction with the simulated protein structure, with lower binding energy being favored. Individuals randomly search the local conformational space for energy minima (through random permutations of the individuals' position/orientation/conformation variables), and in an emulation of natural selection, random pairs of individuals from the resulting population are "mated" to pass on combinations of the "parent" individuals' position/orientation/conformation values, with the highest-fit individuals producing proportionately more offspring. To preserve computational resources, the protein target is static. This process is iterated to globally select for the most energetically favorable binding conformations. Autodock4 performs a cluster analysis based on all-atom root mean square deviation (RMSD) between binding conformations to sort similar conformations into groups, and ranks the results of docking according to the binding free energies of the candidate binding poses, with lower-energy poses being the most favorable.

The advantage of this docking simulation approach is that it is less computationally intensive than more rigorous methods, such as molecular dynamics (MD) simulations, in which the motions of the drug and protein target are simulated in full atomic detail (Goodsell and Olson, 1990). This makes it feasible to explore a large conformational space for an unknown binding site while still generating useful predictions; for example, validation experiments have shown that, in a little over half of cases, AutoDock4 adequately reproduces the binding poses observed in the solved structures of protein-ligand complexes (Morris et al., 2008).

To be able to run molecular docking simulations with Autodock4, we needed select our docking region. The docking region we specified is a cubic box of side-length of 120 grids with a grid spacing in each direction of 0.375 Å (each side 45 Å), centered in a position that encompasses

most of the pore domain, including the domain III/IV fenestration and the central cavity (Figure 22).

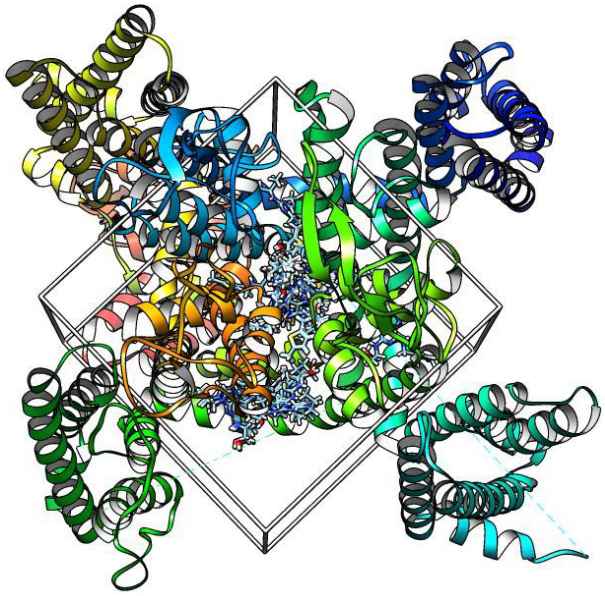

Figure 22: The docking region selected for our AutoDock4 simulations.

The position of the grid box within which the AutoDock4 docking simulations were run, shown in a ribbon cartoon representation of the open-state $Ca_V2.1$ homology model. The grid box encompasses the pore domain, including the III/IV fenestration and central cavity, and excludes the VSDs. Predicted GV-58 binding poses are shown in stick representation (examined in detail in Figure 23).

We chose this docking region because we consider the domain III/IV fenestration, and the part of the central cavity near this fenestration's inner mouth, to be the regions of the channel most likely to contain the GV-58 binding site. We refer here to the binding site that mediates GV-58's effect of slowing channel deactivation; it is possible that GV-58 binds elsewhere to enhance inactivation, or that slowed-deactivation and inactivation are each mediated by different binding poses within the domain III/IV fenestration, but exploration of the inactivation site is beyond the scope of this project. We formed the hypothesis that the binding site is located in the domain III/IV

fenestration or central cavity based on prior experimental findings discussed in Chapter 2**,** as well as on the structural predictions of our homology models discussed in section 3.3.1 above. Our reasoning was as follows:

First, the chimeric channel experiments conducted by Yarotskyy et al. (2012) suggest that binding residues for *(R)*-roscovitine are located in the Ca_V2 domain III. A binding site in the domain III/IV fenestration would be consistent with these findings.

Second, if the state-dependent fenestration access hypothesis (derived from the fast-perfusion experiments discussed in Chapter 2) is correct, then GV-58 should bind within a fenestration that is only wide enough for it to enter when the channel is closed. As we discussed in section 3.3.1, the domain III/IV fenestration is narrower in the open pore than in the closed pore (Figure 19). To assess whether this narrowing could plausibly impede GV-58 entry in the open state, we used CaverDock, a software tool for rapid analysis of transport processes in proteins. CaverDock uses the optimized docking program Autodock Vina (Filipovic et al., 2019; Vavra et al, 2019) for molecular docking of ligands and implements a parallel heuristic algorithm for searching the space of possible trajectories of drug movement through fenestrations. The software simulates the step-wise movement of the ligand along a fenestration pre-calculated using CAVER 3.0. In each step, the drug is docked close to its position in the previous step and its orientation and conformation are changed. CaverDock evaluates the minimum binding free energy of the drug passing through the tunnel by using the scoring function from AutoDock Vina. The high energy barrier to the drug moving through narrow parts of the fenestration can be seen as sharp peaks in the binding free energy profile.

We found that the binding free energy of GV-58 in the domain III/IV fenestration becomes very high over the “pinched” section in the open pore, but that the drug molecule is able to freely

move through the wider fenestration in the closed pore (Figure 23). This high energy barrier means that while the channel is in the open site, it is extremely unlikely for GV-58 to move deeper into the domain III/IV fenestration than the vestibule at its entrance from the PM. Therefore, a binding site for GV-58 located within or beyond the part of the fenestration that "pinches" in the open state would be consistent with the fast perfusion experiments' finding that little modification of channels by KK-20 (which is nearly identical to GV-58 in structure and action) occurs when the drug is applied only during a depolarizing voltage step; see section 2.3 above. (In retrospect, it is also encouraging that the domain III/IV fenestration is the only PM-accessible fenestration reported in the inactivated cryo-EM structure of $Ca_V2.2$. If GV-58 does access its binding site within or through a fenestration, this cryo-EM structure tells us that it is likely to be the domain III/IV fenestration.)

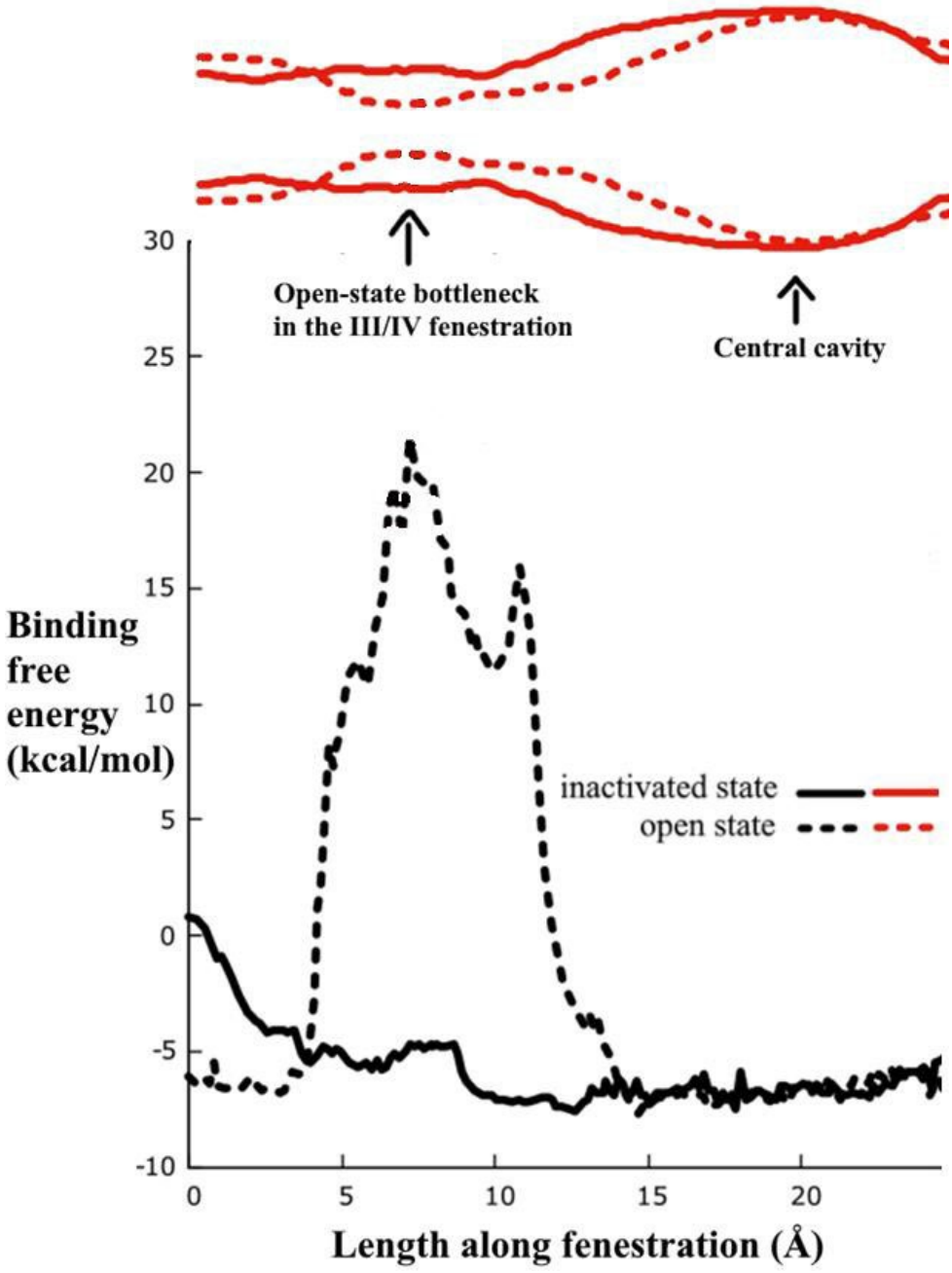

Figure 23: Increased binding free energy for GV-58 in the open-state III/IV fenestration bottleneck.

Shown in black is the binding free energy of GV-58 poses at points along the fenestration that connects the domain III/IV PM entrance to the domain I/II PM entrance via the central cavity, calculated with CaverDock in 1 Å increments beginning at the domain III/IV entrance. The fenestration diameter (+r and -r) plot shown in part in Figure 19 is shown above the plot in red as a visual reference for where each point lies along the fenestration. The domain III/IV fenestration can be seen to the left of the "bulge" on the right that represents the large central cavity. In the open state (dashed lines), the binding free energy is low at the entrance to the domain III/IV fenestration, increases dramatically as the fenestration narrows, and falls again in the central cavity and along much of the domain I/II fenestration. In the inactivated state (solid lines), the binding free energy remains low throughout, though it is slightly higher at the domain III/IV entrance.

Finally, there is evidence that interactions between inner pore residues affect the relative stability of the open vs the closed conformation of the pore. Mutating the inner pore residues in certain conserved motifs has been shown to prolong channel opening, like GV-58 does. If GV-58 binds within the domain III/IV fenestration at or close to where it meets the central cavity, then the bound GV-58 would be in close proximity to residues implicated in pore-stabilizing interactions, which suggests a possible mechanistic explanation for the drug's effect.

Our automated docking simulations using AutoDock4 generated populations of 40 energetically favorable binding poses for GV-58 within the designated docking region (the grid box) in our open and inactivated state $Ca_V2.1$ homology models. The binding poses in the starting population were placed at arbitrary positions throughout the grid box, including within the central cavity, which allowed AutoDock to locate favorable binding sites for which there might not be a viable access pathway from the PM; for example, GV-58 molecules did not need to navigate the "pinch" in the open-state domain III/IV fenestration in order to bind in the central cavity. It was important that binding poses inside the channel be accessible without molecules needing to navigate the fenestration, given our hypothesis that the GV-58 binding site is only available to bind in the open state, yet only accessible to the PM in the closed/inactivated state.

Predicted binding poses in the inactivated channel (Figure 24) were widely distributed throughout the network of fenestrations extending from the central cavity (as shown in Figure 18): 6 in the domain II/III fenestration, 17 in the domain III/IV fenestration, 11 in the domain I/IV fenestration, and 5 in the central cavity, as well as one isolated pose near the domain IV P-loop. Of the poses in the domain III/IV fenestration, most were clustered close to where this fenestration's bottleneck lies in the open pore. The predicted binding poses in the open state (Figure 24) were more concentrated in specific areas: 9 at the entrance of the DIII/DIV fenestration

(before the bottleneck), one each at the entrances to the DI/DII and DII/DIII fenestrations; and the rest in the central cavity.

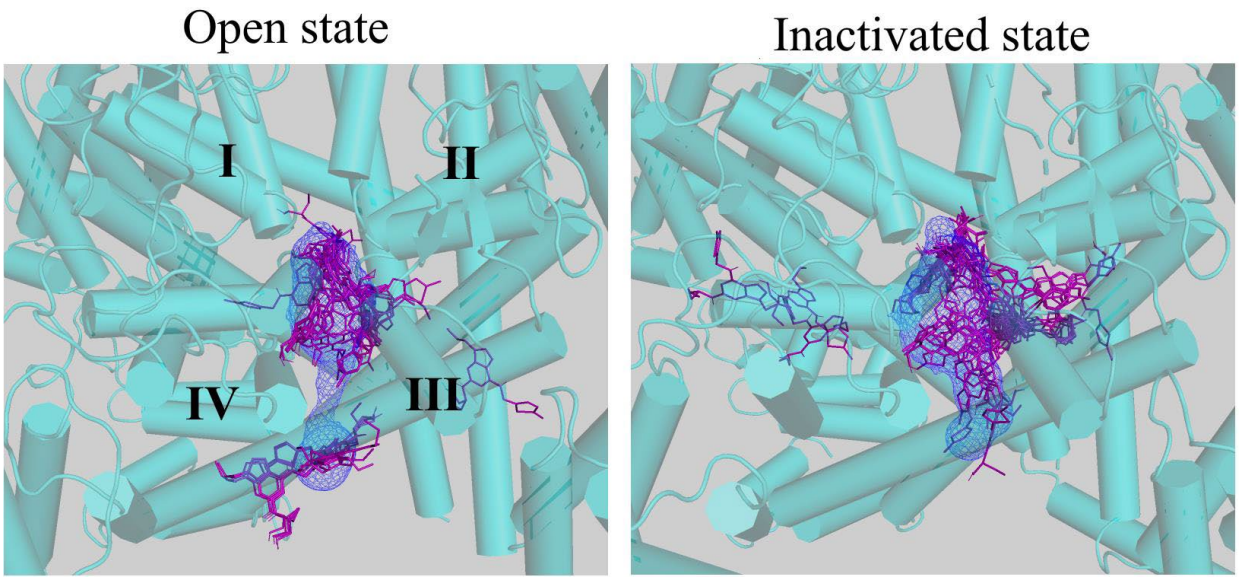

Figure 24: Automated docking simulations in the $Ca_V2.1$ homology models predicted different candidate binding poses in the open vs the inactive state.

AutoDock4 results are shown for the open state (left) and inactive state (right) of $Ca_V2.1$. Candidate GV-58 binding poses are shown in stick representation (purple). The view of the channel is tilted to better show the domain III/IV fenestration and central cavity in each model, as calculated using CAVER 3.0; these are shown in mesh representation (blue). Other fenestrations are not shown. It can be seen that no GV-58 binding poses were predicted within the fenestration bottleneck in our open-state model.

As we discussed in section 2.3, *(R)*-roscovitine, GV-58 and other analogs are believed to bind and modify the channel in the open state, since the proportion of current modified depends on the length of the depolarizing step used to activate channels. Our expectation was that if the binding site is in a favorable conformation to bind GV-58 only in the open state, there would be a region of the channel where our docking simulations would favor GV-58 poses more in the open than in the inactivated model. In the open state model, a much larger proportion of AutoDock4's final population of binding poses binding poses were located in the central cavity and at the

entrance of the domain III/IV fenestration than in the inactivated state model. We considered the vestibule at the fenestration entrance from the PM as a possible site of GV-58 binding, but our CaverDock analysis showed that the drug's access to this vestibule is not impeded by the fenestration narrowing in the open state, because the fenestration bottleneck lies beyond the vestibule. Therefore, a binding site near the PM entrance to the fenestration would be inconsistent with the results of the fast-perfusion experiments discussed in section 2.3, which suggest that the binding site is located in a part of the channel that is only accessible from the PM while the channel is closed.

Instead, we hypothesized that GV-58 enters the central cavity through the state-dependent domain III/IV fenestration while the channel is closed, then binds to domain III (and possibly also IV) inner pore residues within the cavity while the channel is open. As we mentioned previously, the new inactivated $Ca_V2.2$ cryo-EM structure is supportive of this hypothesis in that the domain III/IV fenestration was the only one reported in the solved structure. If the domain III/IV fenestration is truly the only access point connecting the central cavity to the PM, this would explain why, when this fenestration is pinched in the open state, GV-58 does not simply enter the central cavity through other fenestration entrances. In the following chapter, we will describe how we tested this hypothesis by individually mutating domain III and IV residues that line the fenestration pathway and central cavity.

3.3.4 In silico mutagenesis of $Ca_V1.1$ domain III/IV fenestration bottleneck residues is predicted to widen the fenestration to a $Ca_V2.1$-like diameter

Using CAVER 3.0 as described in section 3.3.1, we calculated the diameter of the domain III/IV fenestration in the cryo-EM structure of inactivated $Ca_V1.1$ (Wu et al., 2016). We found that

this subtype has a fenestration bottleneck of 3-4 Å, only slightly wider than the open-state $Ca_V2.1$ bottleneck (~2 Å) . If GV-58 binds in the central cavity, this $Ca_V1.1$ bottleneck is one possible explanation for Ca_V1 VGCCs' insensitivity to the drug (as the bottleneck might prevent drug access via the fenestration to a central cavity binding site, even if such a binding site exists in Ca_V1), although we have not yet experimentally investigated this possibility.

Mutating the I843 and I1134 $Ca_V1.1$ residues to alanines *in silico* widened the bottleneck so that the minimum diameter was ~5 Å, approximately equal to the minimum diameter of the $Ca_V2.1$ inactivated-state fenestration (Figure 25). Based on our CaverDock calculations in the inactivated state $Ca_V2.1$ homology model, this should be wide enough to allow GV-58 to access the central cavity via the mutated fenestration. It would be interesting to experimentally mutate these residues in a Ca_V1 channel and evaluate whether this renders the channel sensitive to *(R)*-roscovitine analogs. The approach of predicting fenestration-widening or fenestration-narrowing residues *in silico* will also facilitate future experimental investigation of the role of fenestration access in *(R)*-roscovitine analog modification of Ca_V2 channels.

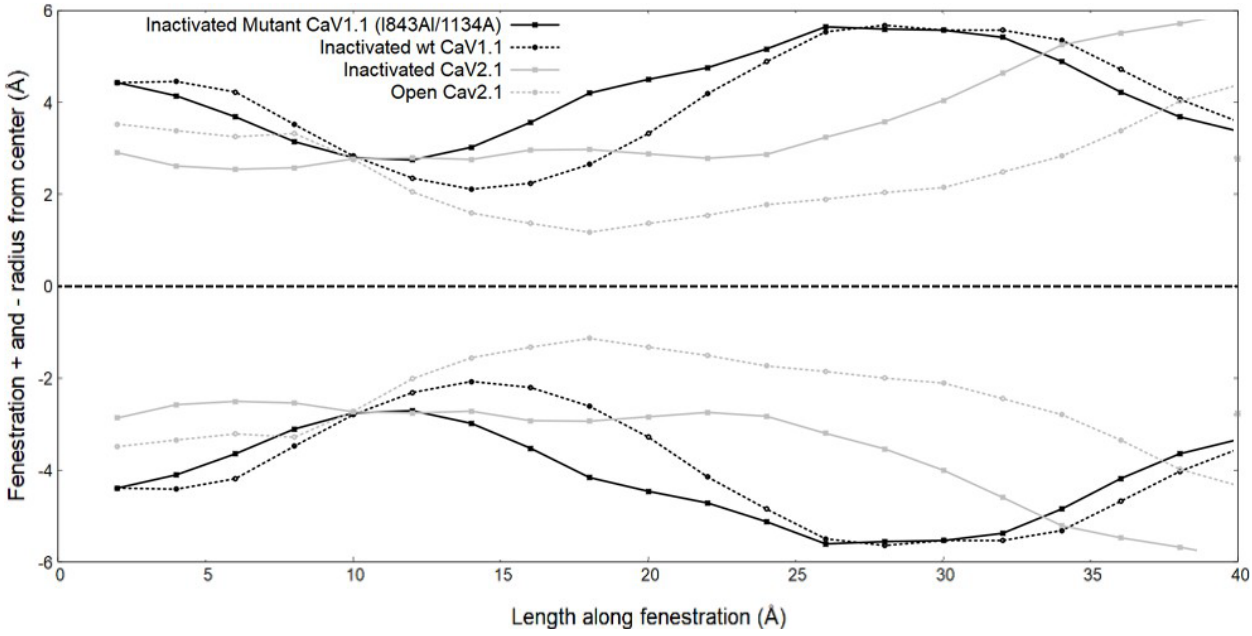

Figure 25: *In silico* mutation of fenestration bottleneck residues in $Ca_V1.1$ widens the fenestration.

Plot of the diameter (as in Figure 19, represented as +r and -r on either side of the center of the fenestration width (dashed black line), designated as 0 Å on the y-axis) along the length of the domain III/IV interface fenestration in a cryo-EM structure of $Ca_V1.1$ in the inactivated state (Wu et al., 2016), calculated with CAVER 3.0. The length of the fenestration is defined in 1 Å increments, beginning at its interface with the PM. At each length increment, the distance between points represents the shortest distance separating the Van der Waals surfaces of the fenestration-lining residues. The diameters are shown for the wild-type $Ca_V1.1$ channel (solid black line) and for $Ca_V1.1$ with the fenestration-lining residues I843 and I1134 mutated to alanine *in silico* (dotted black line). The domain III/IV fenestration diameters of our $Ca_V2.2$ inactive (solid grey line) and open (dotted grey line) states are shown for comparison.

3.4 Discussion

Using homology models of the open and inactivated $Ca_V2.1$ channel, we were able to simulate GV-58 docking with the channel and predict energetically favorable binding poses it might adopt. We used the results of prior experimental characterization of the action of *(R)*-roscovitine and GV-58 to narrow down the likely binding region to a fenestration connecting the

PM at the interface of domains III and IV to the central cavity, and we generated populations of candidate GV-58 binding poses to compare between the open and inactivated states.

The recently solved structure of an inactivated $Ca_V2.2$ channel (a subtype that shares $Ca_V2.1$'s sensitivity to *(R)*-roscovitine analogs) validates the existence of the domain III/IV fenestration, but also reveals structural features of the activation gate that are apparently unique to Ca_V2 VGCCs and are not represented in our inactivated $Ca_V2.1$ homology model. It is unclear to what extent this discrepancy affects our models' predictions about GV-58 binding. If GV-58 does indeed bind to residues in the inner pore, or if its mechanism of action involves disrupting residue interactions that stabilize the closed activation gate, then the Ca_V2-specific activation gate structure could potentially be responsible for these channels' sensitivity to the drug. As a counterpoint, the differences between the $Ca_V2.2$ and $Ca_V1.1$ activation gates are due primarily to the extended IIS6 sequence in $Ca_V2.2$—indeed, with that sequence excluded from our inactive $Ca_V2.1$ homology model, the activation gate adopts a Ca_V1-like conformation—yet the Ca_V2 DII is not necessary for GV-58 sensitivity in chimeric channels.

Despite the discrepancies between the solved $Ca_V2.2$ structure and our $Ca_V2.1$ homology models, our experimental findings (discussed in Chapter 4, below) ultimately validated our prediction, based on these models, that *(R)*-roscovitine analogs bind to $Ca_V2.1$ domain III and IV inner pore residues. Nevertheless, we will take the $Ca_V2.2$ cryo-EM structure into account in interpreting our results and forming hypotheses about *(R)*-roscovitine analogs' mechanism of action.

The methods described for predicting the effects of residue mutations on fenestration diameter, and for predicting the binding free energy of drug molecules moving through a fenestration, will be useful for guiding future experiments to investigate the proposed fenestration

access pathway for *(R)*-roscovitine analogs. It would be especially interesting to experimentally narrow the fenestration in the closed pore of $Ca_V2.1$ and determine whether this inhibits *(R)*-roscovitine's ability to modify channel gating.

4.0 Single-residue substitutions in the $Ca_V2.1$ inner pore alter the binding and action of the *(R)*-roscovitine analog KK-20

4.1 Introduction

In Chapter 3, we discussed how we used drug-docking and molecular dynamics simulations to predict interactions of the *(R)*-roscovitine analog GV-58 with a homology model of the $Ca_V2.1$ α1 subunit. These simulations identified a region of interest in the inner pore, encompassing a fenestration at the interface of domains III and IV and central-cavity-lining residues accessible from this fenestration, that is likely to contain the *(R)*-roscovitine analog binding site that mediates slowing of channel deactivation. Of course, our *in silico* methods alone could not confirm the precise location and structure of the binding site. For one thing, they generated many possible drug binding poses and residue contacts within the region of interest, rather than a single definitive pose. For another, without experimental validation, we could not conclude that our predictions were accurate—especially since the solved structure of an Na^+ channel (not known to be sensitive to *(R)*-roscovitine) was used as a template for our open-state homology model, meaning we could not guarantee that this model accurately represented the structure of the binding site.

The value of these *in silico* models of GV-58 binding lay, instead, in the fact that they made an experimental investigation of *(R)*-roscovitine analog binding possible at the single-residue level. Previously, the pool of possible binding residues was too large to interrogate them individually; the $Ca_V2.1$ α1 subunit is made up of over 2300 amino acid residues (Richards et al., 2007), and even the $Ca_V2.1$ DIII sequence that has been found to be sufficient for *(R)*-roscovitine action is over 300 residues long (Yarotskyy et al., 2012). Narrowing the search area to where the

III-IV fenestration extends into the inner pore made it feasible to evaluate individual residues for involvement in drug binding and action. We used the analog KK-20 for our experimental analyses, since it is very similar to GV-58 in structure but causes less inactivation of channels over long recordings.

A straightforward approach to determining whether a specific residue is important to drug action is to mutate that residue, then observe how this affects drug action; for example, if a residue is part of the binding site, mutating it would be expected to lower the channel's affinity for the drug. The risk of introducing mutations to a voltage-gated channel is that this might alter its control (i.e., non-drug-modified) gating behavior, or even prevent it from conducting current entirely. Here, we benefit from the specific action of *(R)*-roscovitine analogs on the Ca_V2 family of VGCCs. As we discussed in Chapter 1**,** Ca_V2 channels, but not Ca_V1 channels, are sensitive to (*R)*-roscovitine analog-mediated slowing of deactivation. Ca_V2 channels have less than 40% sequence identity with Ca_V1 (Catterall, 2000), but all VGCCs share the overall structure and intrinsic dynamics that give rise to their voltage-sensing and calcium-permeation functions (Yu and Catterall, 2004). This suggests that a residue in one subtype can be substituted with its counterpart (i.e., the residue at the analogous position in the primary sequence) in another subtype without significantly perturbing channel structure or (by extension) function, compared to substituting an arbitrary residue. Indeed, as shown in Yarotskyy et al. (2012)'s Ca_V1/Ca_V2 chimeric channel experiments, even large regions of sequence can be exchanged between Ca_V1 and Ca_V2 VGCCs without loss of functional expression. Individual residue substitutions of this nature can be expected to have little impact on $Ca_V2.1$'s control gating behavior, especially since the very fact that the residues in question are different between subtypes suggests that VGCCs tolerate mutations at these positions; residues whose identity is critical to channel function tend to be

conserved across families (Fernández-Quintero et al., 2021; Hohaus et al., 2005; Raybaud et al., 2007; Tyson and Snutch, 2013; Yang et al., 1993).

The individual substitution approach has previously been used to characterize a high-affinity binding site for dihydropyridine (DHP) modifiers of Ca_V1 VGCCs. This class of drug includes both agonists and antagonists for Ca_V1 channels, but Ca_V2 channels are insensitive to DHPs. Substituting any of nine residues conserved in Ca_V1 channels with the analogous Ca_V2 residue or alanine reduced Ca_V1 channels' affinity for DHPs, suggesting that these residues might be responsible for the selective action of DHPs on Ca_V1 VGCCs (Mitterdorfer et al., 1996; Peterson et al., 1996; Peterson et al., 1997; Schuster et al., 1996). Interestingly, substituting all nine Ca_V1 residues into a Ca_V2 VGCC rendered the channel sensitive to DHPs, which supports the interpretation that these residues form a DHP binding site (Hockerman et al., 1997b). Structures of a $Ca_V1.1$ channel in complex with DHP modifiers, resolved by single-particle cryogenic electron microscopy (cryo-EM), have since corroborated the results of the mutagenesis experiments: The nine candidate DHP-binding residues closely surround the bound drug, and several of them directly participate in hydrophobic or hydrogen bond interactions with the drug (Gao and Yan, 2021).

The DHP binding experiments are of particular interest because the DHP site binds an agonist, (S)-Bay K 8644 (SBK), whose action in Ca_V1 VGCCs bears striking similarities to the action of *(R)*-roscovitine and its analogs in Ca_V2. Like *(R)*-roscovitine and KK-20, it slows current deactivation by prolonging the open time of channels (Figure 26A), and it apparently does so by enhancing an existing mode of gating behavior in which P_o is high and channel opening is prolonged (Nowycky et al., 1985) (Figure 26B), which was also shown for *(R)*-roscovitine (Destefino et al., 2010; Yarotskyy and Elmslie, 2009). Its agonist effect, like *(R)*-roscovitine's and

KK-20's, is stereospecific; (R)-Bay K 8644 functions instead as an antagonist (Franckowiak et al., 1985). Additionally, (S)-Bay K 8644's binding site is located in the pore domain within a fenestration at the interface of the Ca_V1 α1 domains III and IV, which the drug accesses from within the PM (Gao and Yan, 2021; Zhao et al., 2019) (Figure 26C). As we discussed in Chapter 3, we have reason to believe that *(R)*-roscovitine analogs also access their binding site by entering a fenestration from within the PM, and our *in silico* predictions of *(R)*-roscovitine analog binding in a homology model of $Ca_V2.1$ led us to that same III/IV fenestration in the Ca_V2 α1.

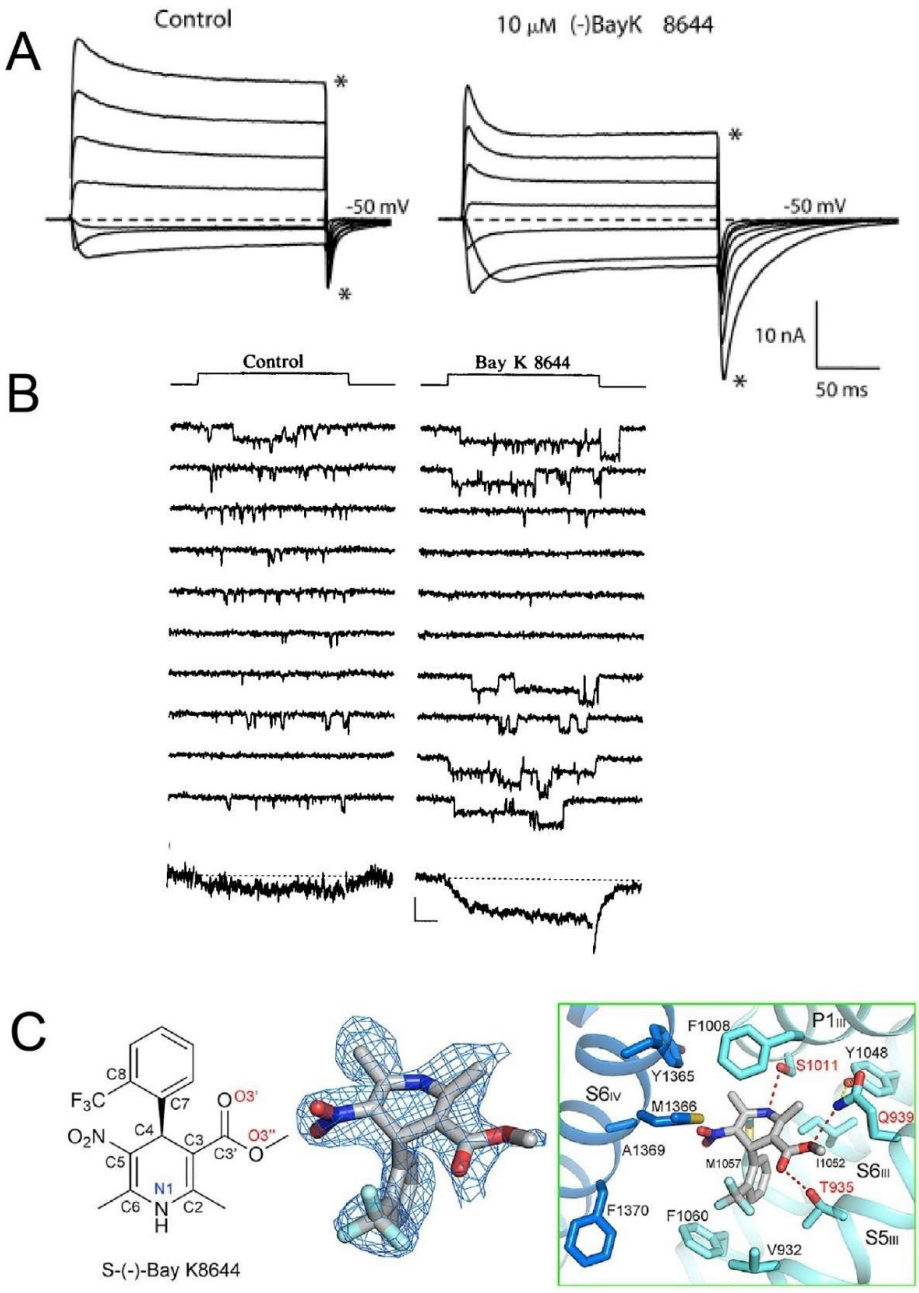

Figure 26: (S)-Bay K 8644 prolongs mean open time in Ca_V1 channels and binds at the interface of domains III and IV in a pore fenestration.

A. Representative Ca^{2+} current traces before (left) and after (right) application of the DHP agonist *(S)*-Bay K 8644. Application of the drug slows the decay of tail currents. **B.** Representative recordings of Ca_V1 single-channel openings in the absence (left) and presence (right) of Bay K 8644. **C.** *Left:* chemical structure of *(S)*-Bay K 8644 and EM map of its bound configuration. *Right:* Close-up of IIIS5/S6 and IVS6 residues coordinating *(S)*-Bay K 8644 binding in a cryo-EM structure of $Ca_V1.1$. The binding site is located within a fenestration at the interface of domains III and IV. A. adapted from (Leuranguer et al., 2003) with permission; B. adapted from (Nowycky et al., 1985) with permission; C. adapted from (Zhao et al., 2019) with permission.

As in the DHP binding experiments, we selected several residues within our predicted binding region in $Ca_V2.1$ for exploratory mutagenesis. Although key residues conserved across all VGCC subtypes may also participate in KK-20 binding or action, we focus here on residues that are specific to Ca_V2 channels and could therefore be evaluated by substituting with the analogous Ca_V1 residues. To investigate the effects of single-site mutations on the action of KK-20, we recorded currents in cells transfected with wild-type and mutant $Ca_V2.1$ VGCCs in the absence and presence of the drug. We identified five single-site mutations in the III/IV fenestration that impair KK-20's ability to slow deactivation, two of which may alter the channel's binding affinity for the drug, and we further characterized the effects of a subset of mutations on KK-20's potency and binding kinetics. We also found that mutating two or more of these residues together can have a cumulative effect on KK-20 action.

4.2 Methods

4.2.1 Provenance of plasmids used for transfection and mutagenesis

All plasmids encoding calcium channel subunits were gifts from Diane Lipscombe: $Ca_V1.2$ (Addgene plasmid #26572; Genbank accession number AY728090; Helton et al., 2005), $Ca_V2.1$ (Addgene plasmid # 26578, Genbank accession number AY714490; Richards et al., 2007), $Ca_V\beta3$ (Addgene plasmid #26574), $Ca_V\alpha2\delta1$ (Addgene plasmid #26575, Genbank accession #AF286488; Lin et al., 2004). The green fluorescent protein (GFP) plasmid, pGFP (Addgene plasmid #64904; Ferreira-Camargo et al., 2015) was a gift from Stephen Mayfield.

4.2.2 Site-directed mutagenesis

In most cases, single-site mutations were introduced to the $Ca_V2.1$ α1 plasmid via whole-plasmid PCR. Primers containing the desired mutation were designed by generating initial candidate primers using New England Biolab (NEB)'s NEBaseChanger tool (https://nebasechanger.neb.com/), evaluating these candidate primers using the Integrated DNA Technologies (IDT) OligoAnalyzer (https://www.idtdna.com/calc/analyzer) and NEB Tm Calculator (https://tmcalculator.neb.com/#!/main) tools, and adjusting the lengths of the primers to reduce differences in melting temperature between primer pairs and minimize the risk of secondary structure generation. All primers were custom ordered from IDT. PCR reactions contained 0.5 µL Q5 High-Fidelity DNA Polymerase (NEB); 1.25µL each of 10 µM forward and reverse primers; 0.5µL of the wild-type $Ca_V2.1$ α1 template DNA at 13 ng/µL; 5 µL Q5 Reaction Buffer; 5µL Q5 High GC Enhancer; 0.5 µL of 10 µM dNTPs; and MQ water to a final volume of 50 µL. The thermal cycling conditions used were as follows: a 30s initial denaturation at 98°C; 22-30x cycles of a 10 s, 98°C denaturation step, 20-40 s 50-72°C annealing step, and 7 minute 72°C extension step; and a 2 minute 72°C final extension step. Annealing temperatures were calculated using the NEB Tm Calculator and, when necessary, optimized via gradient PCR.

Whole-plasmid PCR products were run on an electrophoresis gel to confirm amplification of the entire ~12kb plasmid, digested with KLD Enzyme Mix (NEB) to remove the template (using the unmodified protocol supplied by NEB), and transformed into 5-alpha Competent E. Coli (NEB). Colonies were picked and grown up overnight in liquid culture and plasmid DNA was isolated from cultures using the QIAprep Spin Miniprep Kit (QIAGEN), following the protocol supplied with the kit with the sole modification that all reagents other than the lysis buffer were stored and used at 4°C.

Because the $Ca_V2.1$ α1 plasmid is large and contains regions of high GC content, whole-plasmid PCR was not always successful. In such cases, mutations were instead introduced using a Gibson assembly® approach (Gibson et al., 2009). Briefly, the $Ca_V2.1$ α1 plasmid sequence was divided into three 3-5kb fragments. These fragments were amplified by PCR using primers designed such that each fragment would have 15-20bp overlapping ends with the sequentially adjacent fragments, and the overlapping ends of two of the fragments would contain the mutation site. Forward primers were designed by first mutating the sequence *in silico*, selecting 30-40bp centered on the junction between two fragments and containing the desired mutation, then manually adjusting the primer design to reduce differences in melting temperature between primer pairs and to minimize the risk of secondary structure generation, based on assessments performed with Integrated DNA Technologies' (IDT) OligoAnalyzer tool and New England Biolabs' (NEB) Tm Calculator. The reverse primer for each fragment was designed by reverse complementing the forward primer of the downstream fragment. All primers were custom ordered from IDT. PCR amplification of the fragments was as described for whole-plasmid mutagenesis, except that the reaction volume was doubled, two reactions per fragment were run in parallel to increase the total yield of amplified DNA, and the extension time was 1 minute/kb of the fragment.

The three fragments were gel-purified using the QIAex II Gel Extraction Kit (Qiagen) and its supplied protocol, modified only by the inclusion of an extra 250µL Buffer PE wash step. Using NEBuilder HiFi DNA Assembly Master Mix (NEB) and its supplied protocol, the purified fragments were seamlessly assembled into a complete mutant plasmid. 5µL of the assembly reaction was transformed into NEB 5-alpha Competent E. Coli (using the protocol supplied by NEB) and plated on ampicillin-resistant LB agar plates. Amplification of plasmid in bacteria and isolation of the plasmid DNA was then carried out as described for whole-plasmid mutagenesis

above. The seamless assembly of the fragments yielded a complete plasmid containing the desired mutation, but otherwise identical to the wild-type plasmid.

Multi-site mutagenesis was accomplished by applying one of the above methods to introduce additional mutations to a previously generated mutant $Ca_V2.1$ α1 plasmid, or, when possible, by including two or more mutations in the primers used for a single round of whole-plasmid mutagenesis or Gibson assembly®.

Regardless of the method used to introduce a given mutation, samples of isolated DNA from each miniprepped colony were linearized by HindIII-HF™ (NEB) digestion and run on an electrophoresis gel to confirm the presence of a single band matching the size of the wild-type $Ca_V2.1$ α1 plasmid. A sample of each plasmid that passed this test was submitted to GENEWIZ (Genewiz, Inc; South Plainfield, NJ, USA) for sequencing of the region containing the desired mutation site, in order to confirm the presence of the mutation and the absence of off-target mutations. Plasmids that had been assembled from multiple fragments were sequenced across each junction site. Mutant plasmids were used in electrophysiology experiments only after passing these quality control tests.

4.2.3 Whole-cell perforated patch clamp electrophysiology

Recordings were performed as previously described (Tarr et al., 2013b), using tsA-201 cells transiently transfected using FuGENE 6 (Promega Corp., Madison, WI, USA) with wild-type or mutant $Ca_V2.1$ α1 subunits, along with the β3 and α2δ auxiliary subunits and GFP as an indicator of transfection (250ng of each plasmid per 35mm culture plate).

All recordings were performed at room temperature (20-22 °C). Cells were bathed in a saline containing 130 mM choline chloride, 10 mM HEPES, 10 mM TEA-Cl, 5 mM $BaCl_2$, and 1

mM $MgCl_2$ at pH 7.2. The pipette solution contained 70 mM CH_3CSO_3S, 60 mM CsCl, 10 mM HEPES, and 1 mM $MgCl_2$ at pH 7.2. Patch pipettes were fabricated from borosilicate glass and pulled to a resistance of ~1-4 MΩ. Before each experiment, 3 mg amphotericin-B was dissolved in 50 µL DMSO. Approximately every 30 minutes, 2-3 µL of this stock amphotericin solution was freshly mixed with 130 µL pipette solution. Pipettes were filled in a two-step process. The tip was dipped into a droplet of pipette solution for 1-3 s, and then the remainder of the pipette was back-filled with the amphotericin-B/pipette solution mixture using a syringe and a 34 G quartz needle (MicroFil MF34G, World Precision Instruments, Sarasota, FL). This pipette was then used to make a GΩ seal with a fluorescent cell and given time for the amphotericin-B to perforate the patch of membrane isolated under the pipet in order to gain electrical access to the whole cell (5-10 min). Access resistances ranged from 4 to 10 MΩ and were compensated by 80-85%. All chemicals were obtained from Sigma-Aldrich Corp. (St. Louis, MO, USA) unless otherwise noted.

Voltage clamp of cells was controlled by an Axopatch 200B amplifier driven by Clampex 9 or 10 software (Molecular Devices, Sunnyvale, CA). Data were filtered at 5 kHz and digitized at 10 or 50 kHz. Data were analyzed using Clampfit 10 software (Molecular Devices). Capacitive transients and passive membrane responses to the voltage steps were subtracted, and a liquid junction potential of 11.7 mV was corrected before each recording.

Current through calcium channels was activated by depolarizing steps from a holding potential of -100 mV to +60 mV for 2, 3, 5, 50, or 100 ms before repolarizing to -60mV for evaluation of KK-20 on tail current. For the initial exploratory mutagenesis experiments, a single 100 ms depolarizing step was applied (Figure 27A). For the experiments used to calculate the dissociation constant (K_D), one of two protocols was used in each cell: a 2 ms depolarization followed by a 150 ms repolarization and 100 ms hold, then a 3ms depolarization followed by a

150 ms repolarization and 200 ms hold, then a 50 ms depolarization followed by a 200ms repolarization and a 10 ms hold (the 2-3-50 ms protocol); or a 5 ms depolarization followed by a 150 ms repolarization and 150 ms hold, then a 10ms depolarization followed by a 150 ms repolarization and 500ms hold, then a 100ms depolarization followed by a 300 ms repolarization and 10ms hold (the 5-10-100 ms protocol) (Figure 27B). For the experiments used to calculate the half-maximal effective concentration (EC_{50}) of KK-20 in wild-type and mutant channels, only the 5-10-100 ms protocol was used. A delay of 10 s was included after each set of depolarizing steps to allow VGCCs to recover between stimuli.

To calculate the voltages of half-maximal activation (VD_{50}) and current-voltage relationships of wild-type and mutant channels, currents were activated with a 20 ms depolarizing step ranging from -40 mV to +150 mV, incrementing by +10 mV per sweep ("sweep" meaning iteration of the stimulus protocol) (Figure 27C). Tail current peak amplitudes were normalized to the largest amplitude recorded in the same cell to calculate fractional activation at each potential. Fractional activation vs voltage curves were fit to a Boltzmann sigmoidal function in Prism to calculate the VD_{50}.

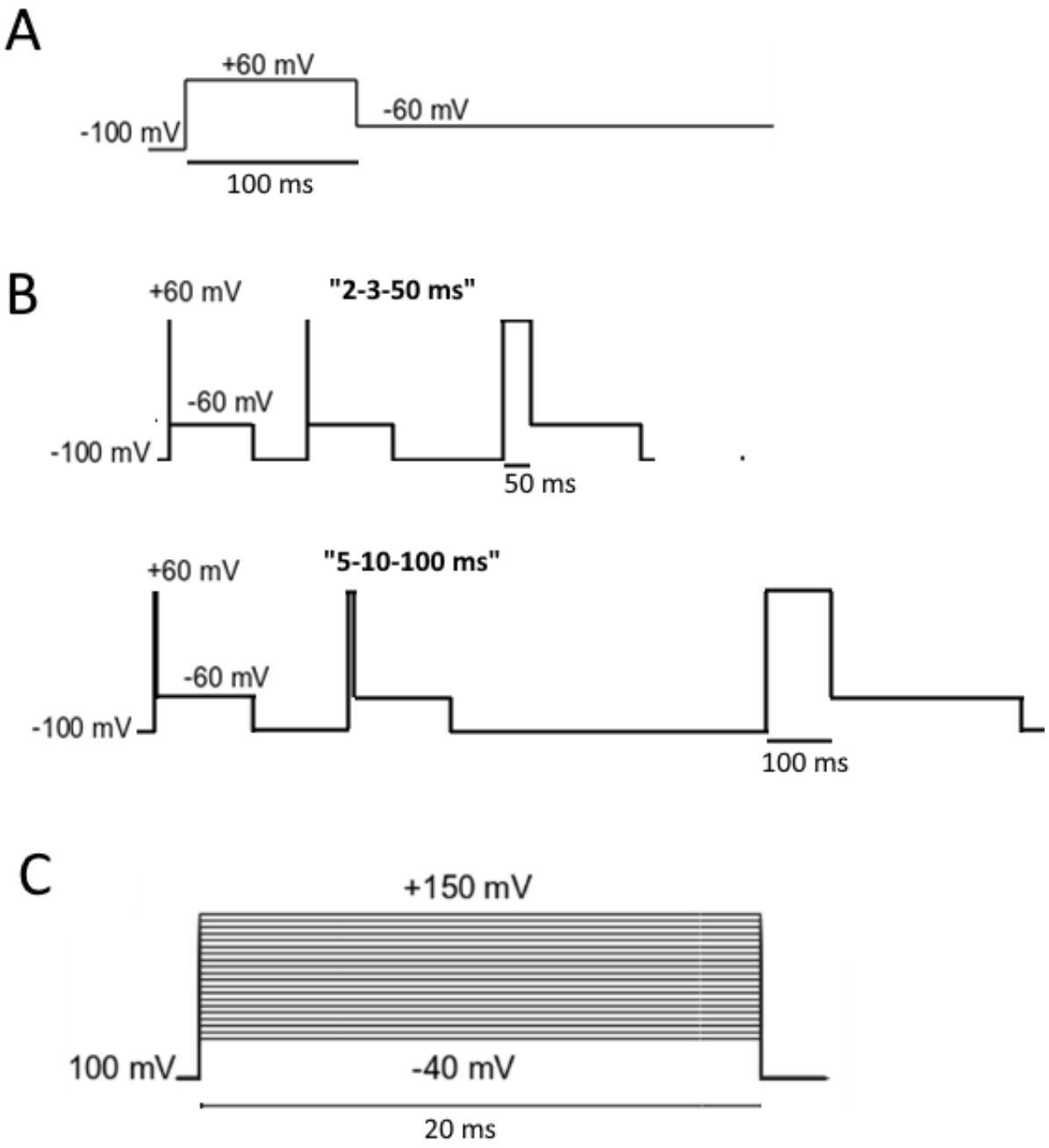

Figure 27: Stimulus protocols used to activate $Ca_V2.1$ channels.

A. The protocol used for the initial evaluation of mutation effects on KK-20's ability to modify gating. A single 100 ms step to +60mV from a -100 mV holding potential is applied, followed by repolarization to -60 mV. **B.** The "2-3-50 ms" (top) and "5-10-100 ms" (bottom) protocols used for the EC_{50} and K_D experiments, in which steps to +60 mV of three different lengths (2, 3, and 50 ms, or 5, 10, and 100ms) are applied during each sweep, with each step followed by repolarization to -60 mV to elicit tail currents and a return to the -100 mV holding potential prior to initiation of the following step. **C.** The protocol used to measure voltage-dependence of activation. Over the course of 20 sweeps, the 20 ms depolarizing step increases in 10 mV increments from -40 mV to +150 mV.

KK-20 was dissolved in DMSO at 50 mM to create a stock solution, aliquoted, and stored at -20°C before use. On the day of use, stock solutions were diluted into warmed extracellular saline at one of seven concentrations (0.1, 5, 25, 50, 100, or 200 μM) for application to cells. In the final saline, DMSO was kept below 0.1% (v/v), which has been shown to have no effects on calcium channel current in patch clamp recordings (Tarr et al., 2013b). Five or more control sweeps were recorded prior to drug application, then an additional five sweeps were recorded during continuous application of the drug. Drug solutions were delivered directly to a cell under study using a pressurized borosilicate glass pipette with a 50 μm diameter opening lowered over the cell during the recording.

4.2.4 Analysis of electrophysiological recordings

Electrophysiological recordings were analyzed using Clampfit 10.7 (pCLAMP). Data from each recording was used for analysis if the access resistance was less than 10 MΩ (after amphotericin access), and current leak was less than 100 pA (during a 10 mV test step depolarization). With 80-85% compensation of access resistance, and currents ranging from 200 pA to 20 nA, voltage error is estimated to be nonexistent during depolarizing steps to +60 mV (when the current is 0 pA) and to range from 0.15 mV to 40 mV at the peak of the tail current, decreasing as the tail current decays. In future experiments, we will eliminate data with access resistance greater than 8 MΩ, which will reduce the maximum voltage error to 24 mV.

Drug effect was measured by calculating the fold change in the normalized tail current integral following KK-20 application. To calculate the control normalized tail current integral (the "control integral"), the area under the curve of the last tail current prior to drug application was measured and normalized to the peak amplitude of the tail current. The same approach was used

to calculate the drug-modified normalized tail current integral (the "drug integral") of the first sweep after the drug began to be applied (skipping sweeps with partial drug effect, which were sometimes recorded at the very beginning of drug application). The drug integral was then divided by the control integral to calculate the fold change in normalized tail current integral ("fold change in integral"). In the exploratory mutagenesis experiments, the fold change in integral was compared between wild-type and mutant channels treated with 50 μM KK-20.

The fraction of open channels affected by the drug at the end of the depolarizing step was measured by calculating the fitting weight of the drug-modified tail current. The tail current decay was fit to a double exponential using Clampfit's weighted exponential formula quantifying the fast and slow components of the decay:

$$f(t) = K_0\left(\sum_{i=1}^{n} f_i e^{-K_i t}\right) + C \qquad \textbf{Equation 1}$$

where for each component *i, f* is the proportion of the tail current amplitude fit, K is the rate constant, K_0 is the 'weight', and C is the constant *y* offset. The time constant of the decay of each component, which we will refer to as tau_{deact}, is the inverse of the rate constant K. The proportion of the total decay accounted for by the slow component—the slow fitting weight, $f_1/(f_1+f_2)$—was interpreted as representing the slow closure of drug-modified channels (Buraei et al., 2005). In the exploratory mutagenesis experiments, the slow fitting weight was compared between wild-type and mutant channels treated with 5 μM KK-20. In unmodified currents, the same method was used to calculate the fast and slow components of control decay, with the slow component here representing an intrinsic long-opening mode of unmodified $Ca_V2.1$ channels,

KK-20 EC_{50}s for the wild-type and mutant channels were calculated by plotting the normalized tail current integral following the 100ms depolarizing step at each of seven

concentrations (0.1, 5, 10, 25, 50, 100, and 200 μM) and fitting the curve in Prism v.9 (Graphpad) using the "[Agonist] vs. response (three parameters)" method with the following formula:

$$Y = Bottom + X*(Top-Bottom)/(EC_{50} + X)) \quad \textbf{Equation 2}$$

where Y is fold change in normalized tail integral, X is KK-20 concentration, "Bottom" is the minimum response and "Top" is the maximum response. Data collected at the 5, 10, 25 and 50 μM concentrations were also used in calculating K_D (see below).

The KK-20 K_Ds for the wild-type and mutant channels were calculated as follows: At each of four different KK-20 concentrations (5, 10, 25, 50 μM), normalized tail current integrals were plotted as a function of depolarizing step length at 2, 3, 5, 10, 50, and 100 ms. Since drug binding and modification occurs only during the depolarizing step when channels are activated, these plots were considered to represent KK-20 binding at the given concentration as a function of time. (Fitting weight was not used as the measure of KK-20 binding because the double exponential could not be reliably fit when a very small or very large proportion of tail current decay was modified by the drug.) At each concentration, the normalized-integral-vs-time plot was fit to a single exponential using the "One-phase association" method in Prism v.9, with the following formula:

$$Y = Y0 + (Plateau-Y0)*(1-exp(-K*x)) \quad \textbf{Equation 3}$$

where Y is the fold change in normalized integral, Y0 is the Y value when time is 0, Plateau is the maximum response (the Y-value at infinite time), K is the rate constant (the inverse of the time constant, tau_{bind}), and X is time (the length of the depolarizing step in ms). The inverse of the time constant of the exponential fit ($1/tau_{bind}$, which is equal to the rate constant K) was plotted as a

function of KK-20 concentration. The plot of the four $1/tau_{bind}$ values as a function of KK-20 concentration were fit linearly to derive k_{off} (the y-intercept of the linear fit), k_{on} (the slope), and K_D (k_{off}/k_{on}). Buraei et al. (2005) previously used this approach of linearly fitting a plot of inverse tau_{on} vs drug concentration to calculate binding kinetics for *(R)*-roscovitine.

Data were statistically analyzed using Prism v.9. Outliers were detected and removed from analysis using Prism's ROUT method (Motulsky and Brown, 2006) with the maximum desired false discovery rate Q set to its default value of 1%. Statistical significance of differences between variables was analyzed in Prism v.9 by one-way Brown-Forsythe and Welch analysis of variance (ANOVA) with Dunnett's T3 multiple comparison post hoc analysis.

4.2.5 Molecular dynamics simulations

For the MD simulations to predict contacts between $Ca_V2.1$ residues and GV-58 side groups, we used the NAMD (NAnoscale Molecular Dynamics) software package (Phillips et al., 2005; Phillips et al., 2020) as described in Chapter 3. Simulations were performed in our open-state homology model of $Ca_V2.1$ (see Chapter 3) in solvated lipid bilayer. At the start of the simulation, the drug was placed inside the central cavity. Total simulation time was 90ns, and drug contacts were analyzed over the last 70ns. Water, lipid bilayer, and the protein backbone were fixed, and residue side chains and GV-58 were free to move.

4.2.6 Preparation of figures

Structural images were prepared using the PyMOL Molecular Graphics System (PyMOL, Version 2.0 Schrödinger, LLC). Data plots were prepared using Prism version 9.2.0 for Windows

(GraphPad Software, San Diego, California USA, www.graphpad.com). Images of stimulus protocols and current traces were prepared using Clampfit 10.7 (pCLAMP)

4.3 Results

4.3.1 Mutations within the $Ca_V2.1$ III/IV fenestration that inhibit slowing of deactivation by the *(R)*-roscovitine analog KK-20

To explore amino acid residues that might be involved in the binding of the (R)-roscovitine analog KK-20, we focused on mutating single residues in Cav2.1 (sensitive to KK-20) to their counterparts in Ca_V1 (insensitive to KK-20). We evaluated ten Ca_V2-to-Ca_V1 mutations of residues in the III/IV fenestration for their effects on KK-20-mediated slowing of deactivation in the initial exploratory mutagenesis experiments. These mutations were F1446I, F1453M, V1454M, A1459G, L1460F, I1461V and I1463V in IIIS6, and F1747M, S1750A, and M1753I in IVS6. Residues were chosen based in part on an alignment of $Ca_V1.1$-4 and Cav2.1-3 primary sequences (Figure 28B**)** showing that their identity was conserved across Ca_V2 subfamilies but different at the analogous position in Ca_V1, and that the identity of the analogous Cav1 residue was also shared across Ca_V1 subfamilies. (The sole exception was I1463, as this isoleucine is shared by $Ca_V1.4$.)

A

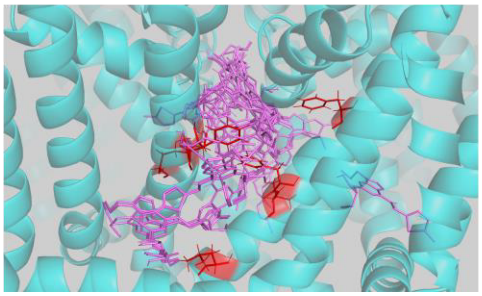

B

$Ca_V1.1$	(PDBID 5GJV)	1049	IILIAFFMMNIFVGFVIVT 1067
$Ca_V1.2$	(GenBank X15539)	1180	IIIIAFFMMNIFVGFVIVT 1198
$Ca_V1.3$	(GenBank AF370009)	1147	IIIVAFFMMNIFVGFVIVT 1165
$Ca_V1.4$	(NM_005183)	1121	IIIIAFFMMNIFVGFVIIT 1139
$Ca_V2.1$	(GenBank AY714490)	1446	**F**VVFPFF**FV**NIFV**ALI**I**I**T 1464
$Ca_V2.2$	(GenBank AF055477)	1397	FVVFPFFFVNIFVALIIIT 1415
$Ca_V2.3$	(GenBank L27745)	1407	FVVFPFFFVNIFVALIIIT 1425

Figure 28: Candidate GV-58/KK-20 binding residues selected for mutagenesis experiments.

A. Close-up of the inner pore through the III/IV fenestration, in our homology model of open $Ca_V2.1$. GV-58-binding poses from our Chapter 3 AutoDock4 simulations are shown in stick form (purple). Residues on IIIS6 and IVS6 within 6A of any of these binding poses that were chosen for mutagenesis are shown in stick form (red). **B.** Alignment of sequence in the lower third of IIIS6 segments between subtypes of the Ca_V1 and Ca_V2 families. Residues chosen for mutagenesis (bolded in the $Ca_V2.1$ sequence) are conserved across the Ca_V2 subtypes but different in the Ca_V1 subtypes (with the exception of I1463 in $Ca_V1.4$). A similar approach was used to select IVS6 residues for mutagenesis (not shown). Sequences were aligned in CLC Sequence Viewer 8.0 (QIAGEN CLC Genomics Workbench 20.0; https://digitalinsights.qiagen.com/).

In our homology model of an open $Ca_V2.1$ channel, most of the residues chosen for evaluation were located within 6 Å of one or more of the GV-58 binding poses predicted by our AutoDock simulations (see Chapter 3 and Figure 28A). Of these, F1446, V1454, F1747 and M1753 were of particular interest because the analogous residues in Ca_V1 are among the nine residues found to be necessary and sufficient for high-affinity DHP binding. We considered that KK-20 might exploit a similar mechanism to (S)-Bay K 8644 to stabilize the open pore, and that if so, it might interact with residues at these positions. Additionally, F1453M and F1747 were of interest because these residues participate in "pinching" the III/IV fenestration in the open state, which we believe prevents *(R)*-roscovitine analogs from moving through the fenestration to the binding site while the channel is open. In the context of the state-dependent fenestration access hypothesis (see Chapter 2), one possibility we considered was that the open-state positions of these residues form a binding pocket around a KK-20 molecule that has already entered the fenestration.

A1459, I1461, and I1463 were also evaluated despite being farther than 6 Å from the GV-58 binding poses. A1459 was of interest because the analogous glycine is part of the "GAGA ring" structural motif of small inner pore residues that were found to be energetically coupled to gating charges in Ca_V1 channels (see Figure 1), suggesting that these residues may participate in mediating pore opening and closure in response to VSD movement (Beyl et al., 2012; Depil et al., 2011). We considered that if A1459 has the same function in $Ca_V2.1$, it might be responsible for *(R)*-roscovitine analogs' effect of delaying both pore closure *and* gating charge deactivation on a similar time-course (Yarotskyy and Elmslie, 2009). A1459 was also of interest, along with I1461 and I1463, because these three residues are part of a motif in the domain III of Cav2 channels that is at the analogous position to motifs in domains II (Hohaus et al., 2005) and IV (Raybaud et al., 2007) which are implicated in VGCC deactivation kinetics. These conserved sequence and structural motifs, as well as structural evidence implicating A1459 and I1463 in stabilizing the closed intracellular gate, are discussed in more detail in Chapter 5.

Whole-cell barium currents through wild-type and mutant $Ca_V2.1$ channels were evoked with a 100ms depolarizing step to +60mV from the holding potential of -100mV, followed by repolarization to -60mV. Since deactivation kinetics are voltage-sensitive and tail currents decay extremely quickly upon repolarization to the -100mV holding potential, the -60mV repolarization potential was chosen to facilitate analysis of tail currents by slowing their deactivation. Currents were recorded in the same cell before and during application of 50μM KK-20. This concentration of KK-20 was chosen because it has been shown to be sufficient for maximal modification of wild-type $Ca_V2.1$ channels.

KK-20-mediated slowing of deactivation was quantified by calculating the fold increase in the normalized tail integral (the area of under the curve of the tail current, which we normalized

to the tail current peak amplitude to correct for effects of inactivation) upon application of the drug. The last unmodified test depolarization (experimental sweep) was used to calculate the control normalized tail current integral (the "control integral"), and the first subsequent sweep in which KK-20's effect on deactivation had reached equilibrium (omitting sweeps with partial drug effect, one or, rarely, two of which were sometimes recorded at the very beginning of drug application) was used to calculate the KK-20-modified normalized tail current integral (the "drug integral"). The drug integral was divided by the control tail current to calculate the fold increase.

Compared to the fold change in normalized tail integral measured in wild-type $Ca_V2.1$ (24.9 +/- 0.57), the fold changes measured in F1446I (12.9 +/- 0.74, $p < 0.0001$), F1453M (6.7 +/- 0.45, $p < 0.0001$), V1454M (18.07 +/- 0.85, $p < .001$), L1460F (11.53 +/- 0.81, $p < 0.0001$), and M1753 (11.16 +/-1.2, $p < .001$) were significantly smaller (Figure 29B). We found no significant effect of the mutations A1459G (19.30 +/- 1.7), I1461V (29.8 +/- 2.9), I1463V (26.9 +/- 2.2), F1747M (27.5 +/- 1.7), or S1750A (27.9 +/- 2.0) on this measure of drug action.

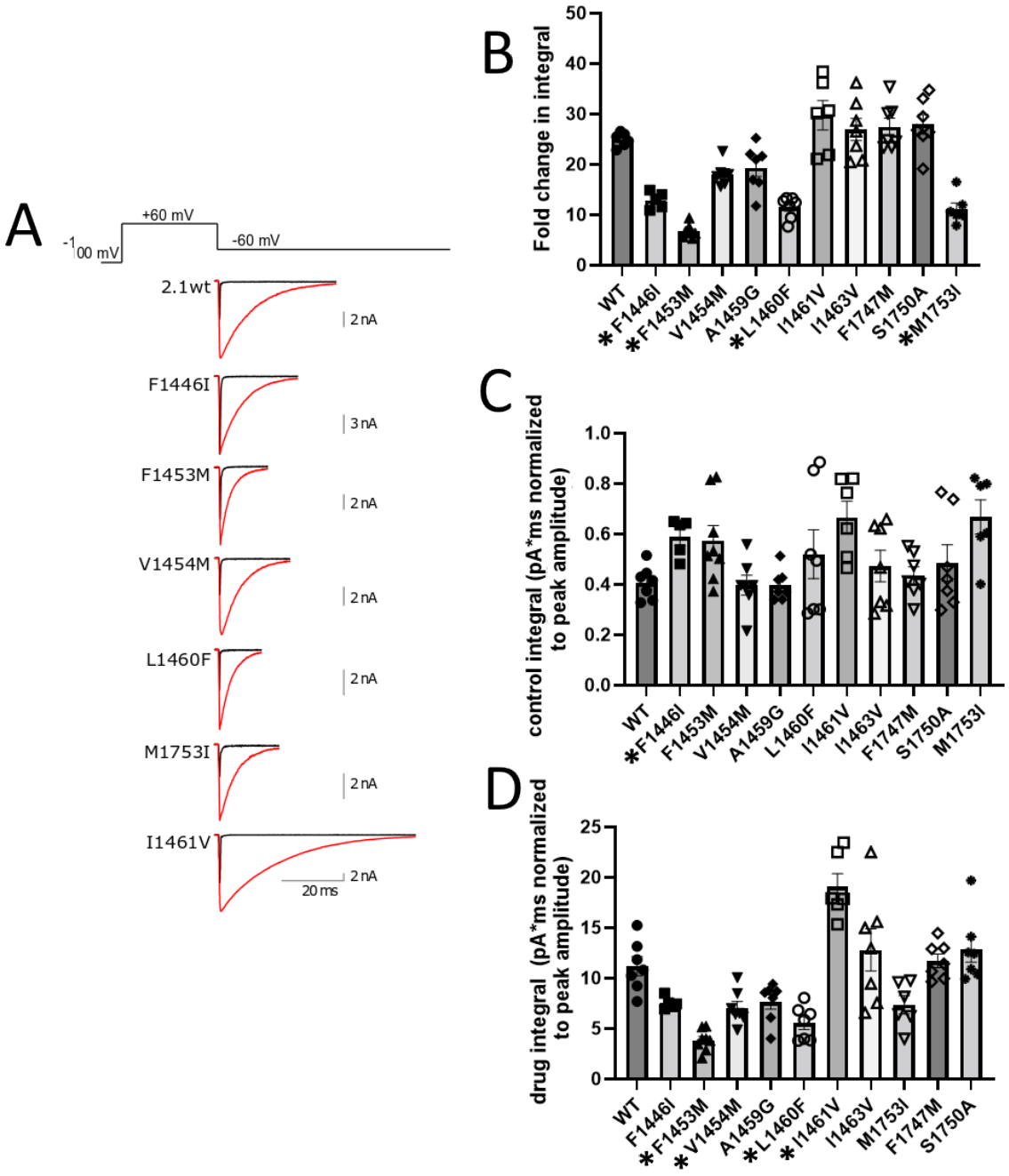

Figure 29: Effects of single-residue Ca_V2->Ca_V1 mutations on tail current integrals before and during application of 50 µM KK-20.

A. Representative tail currents before (black) and during (red) application of 50 µM KK-20 for the wild-type and a subset of mutant channels. The drug slows the decay of tail currents in all cases. **B.** Comparison between wild-type and mutant channels of the fold change in normalized tail current integral (area under the curve of the tail current normalized to the peak) upon application of 50 µM KK-20. **C.** Comparison between wild-type and mutant channels of the control (pre-drug) tail current integral. **D.** Comparison between wild-type and mutant channels of the tail current integral modified by 50 µM KK-20. In B, C, and D, mutations with significant effects (Brown-Forsythe and Welch one-way ANOVA with Dunnett's T3 multiple comparison post hoc analysis, $p < 0.05$) are marked with an asterisk. Bar height represents the mean value, and individual data points are shown. Error bars represent SEM.

The approach of using the fold change in normalized integral to quantify slowing of decay in whole-cell currents has previously been used to compare the effects of different *(R)*-roscovitine analogs on Ca_V2 channels (Liang et al., 2012; Tarr et al., 2013; Wu et al., 2018). In these previous experiments, the analogs were applied only to wild-type Ca_V2 channels; the control integral could therefore be expected to vary between individual cells, but not systematically between conditions. Conversely, our experiments compared the effects on a single *(R)*-roscovitine analog on several different Ca_V2 mutants, which meant our results could be influenced by both the mutations' effects on KK-20 action and their effects on the channel's control gating properties. Therefore, we considered the possibility that our results using the fold change in normalized integral measure could be explained by these mutations slowing control tail current decay, rather than impairing KK-20 action (since the formula for the fold change in normalized tail integral is the drug-modified integral divided by the control integral, either a smaller drug-modified integral or a larger control integral calculates to a smaller fold change). Therefore, we also compared the control (Figure 29C) and drug integrals (Figure 29D) between wild-type and mutant channels.

We found no significant differences between most mutant and wild-type control integrals, with the exception of F1446I (0.590 +/- 0.034, $p < 0.05$), whose control tail integral was larger than in wild-type $Ca_V2.1$ (0.407 +/- 0.025). It is also worth noting that the largest mean control tail integrals were observed in I1461V (0.667 +/- 0.064) and M1753I (0.668 +/- 0.068). Although these effects were not statistically significant, and we would not use them to draw conclusions about how these mutations affect channel gating, it is still possible that the larger mean control integrals confound our measure of fold change in integral.

Compared to the wild-type $Ca_V2.1$ drug integral (11.8 +/- 0.95), we found a significant decrease in drug integral in F1453M (3.8 +/- 0.38, $p < 0.001$), V1454M (7.1 +/- 0.64, $p < 0.05$),

and L1460F (5.5 +/- 0.63, $p < 0.01$), which is in agreement with the fold change in integral results for these mutations (Figure 28B). Surprisingly, we also found a significant *increase* in drug integral in I1461V (19.1 +/- 1.3, $p < 0.01$). We found no significant change in drug integral for F1446I (7.5 +/- 0.27) or M1753I (7.3 +/- 0.91), which raises the question of whether part or all of these mutations' effects on fold change in integral could be due to increased control integrals (even though the increase in control integral was non-significant in M1753I's case).

By definition, the fold change in normalized integral should be negatively correlated with the size of the control integral (the denominator in the fold-change-in-normalized-integral equation) and positively correlated with the size of the drug integral (the numerator in the equation). If differences in the fold change in normalized integral were primarily due to differences in the control integral, we would expect the control integral/fold change correlation to be stronger than the drug integral/fold change correlation. We found a significant negative correlation between control integral and fold change in integral across our Ca_V2->Ca_V1 mutants ($r = -0.325$, $p < 0.01$), but the positive correlation between drug integral and fold change in integral was stronger ($r = 0.753$, $p < 0.0001$) (Figure 30). Therefore, we attribute the differences in normalized tail integral primarily to effects of these mutations on KK-20 action, but acknowledge that this measure is also influenced by mutation effects on control integral. One challenge to interpreting the data is that it is uncertain whether KK-20's effect on open time is multiplicative (which is the assumption of the fold change in integral measure) or additive; it is possible that simply subtracting the control integral from the drug integral would yield a more accurate measure of the drug effect.

Given that F1446I and M1753I did not significantly decrease the drug integral compared to wild-type, we cannot rule out the possibility that their effects on the fold change measure of drug action can be at least partially explained by their (in M1753I's case, non-significant) effects

on control deactivation. It is also possible that I1461's (non-significantly) larger control integral could be masking an enhanced effect of the drug. We are most confident that the F1453M, V1454M, and L1460F mutations genuinely impair the drug's ability to prolong channel mean open time.

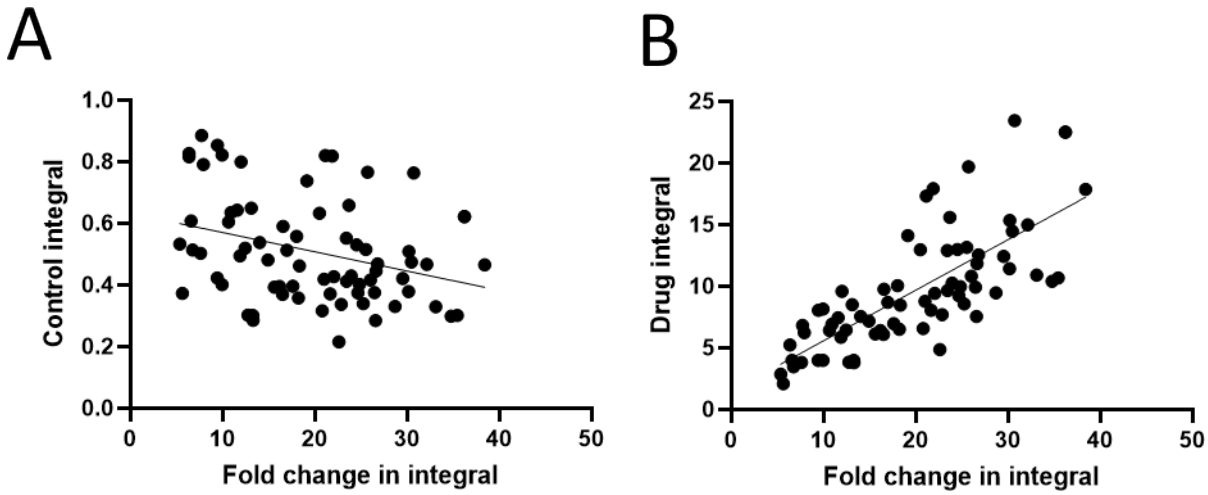

Figure 30: Correlation plots of control and KK-20-modified tail current integral vs the KK-20-mediated fold change in integral.

A. The fold change in integral for every individual recording in the section 4.3.1 experiments across the wild-type and all single-residue Ca_V2->Ca_V1 mutant channels, scatter plotted against the control integral recorded in the same cell and fit to a simple linear regression. r = -0.325, p (two-tailed) < 0.01. **B.** The fold change in integral for every individual recording across the wild-type and all mutant channels, plotted against the drug integral recorded in the same cell and fit to a simple linear regression. r = 0.753, p (two-tailed) < 0.0001.

4.3.2 Mutations that inhibit KK-20's prolongation of mean open time do not necessarily reduce its binding affinity

In our comparison of the effects of 50 μM KK-20 on tail current decay, we identified several inner pore mutations that reduce the fold increase in the normalized tail integral during drug application. Our comparison of drug integrals indicates that in at least three mutants—F1453M, V1454M, and L1460F—this is due to reduced prolongation of the mean open time in

KK-20-modified channels. However, these experiments do not provide information about the affinity of the binding site for KK-20. The proportion of channels modified by KK-20 at the end of the repolarizing step can be measured by fitting drug-modified tail current decay curves to a double exponential and calculating the fitting weight of the slow, drug-modified component of decay. However, in the presence of 50 μM KK-20, most or all of the tail current decay was slowed in the wild-type and single-mutant channels (see example recordings in Figure 29A), making this comparison difficult.

In order to distinguish between mutations that disrupt the KK-20 binding site (whether directly or allosterically) and mutations that only disrupt KK-20's mechanism of action, we needed to know which mutations might alter the channel's binding affinity for the drug. We began by applying 5 μM KK-20 to a subset of the mutant channels evaluated in 4.3.1 and 4.3.2. This concentration was chosen because it is close to the EC_{50} for KK-20 in wild-type Cav2.1 channels (Wu et al., 2018). In the presence of 5 μM KK-20, tail currents in the wild-type and all mutant channels had well-defined fast and slow components of decay, which we fit to a double exponential. We then compared the fitting weight of the drug-modified slow component between the wild-type and mutant channels to detect changes in the proportion of open channels modified by KK-20 at this concentration (Figure 30).

While these data alone were not sufficient to quantify KK-20's binding affinity for the wild-type and mutant channels, they provided an early indication of which mutations might or might not disrupt the binding site. We found that the proportion of current modified at this concentration was significantly reduced compared to the wild-type $Ca_V2.1$ channel (59.0 +/- 4.6%) in the mutants F1446I (32.4 +/- 1.5%, $p < 0.05$) and F1453M (26.5 +/- 1.7%, $p < 0.01$) both of which had been found to reduce KK-20's ability to slow tail current deactivation in our 50 μM

experiments (although we were less confident in that result for F1446I than F1453M). These findings would be consistent with either a role of F1446 and F1453 in binding KK-20, or an allosteric effect of the mutations on binding residues. Conversely, despite strong evidence that they impair KK-20-mediated slowing of deactivation, the V1454M and L1460F mutations did not significantly change the slow fitting weight at 5 μM. This suggests that wild-type residues at these positions might play a role in KK-20's mechanism of action without necessarily participating in binding.

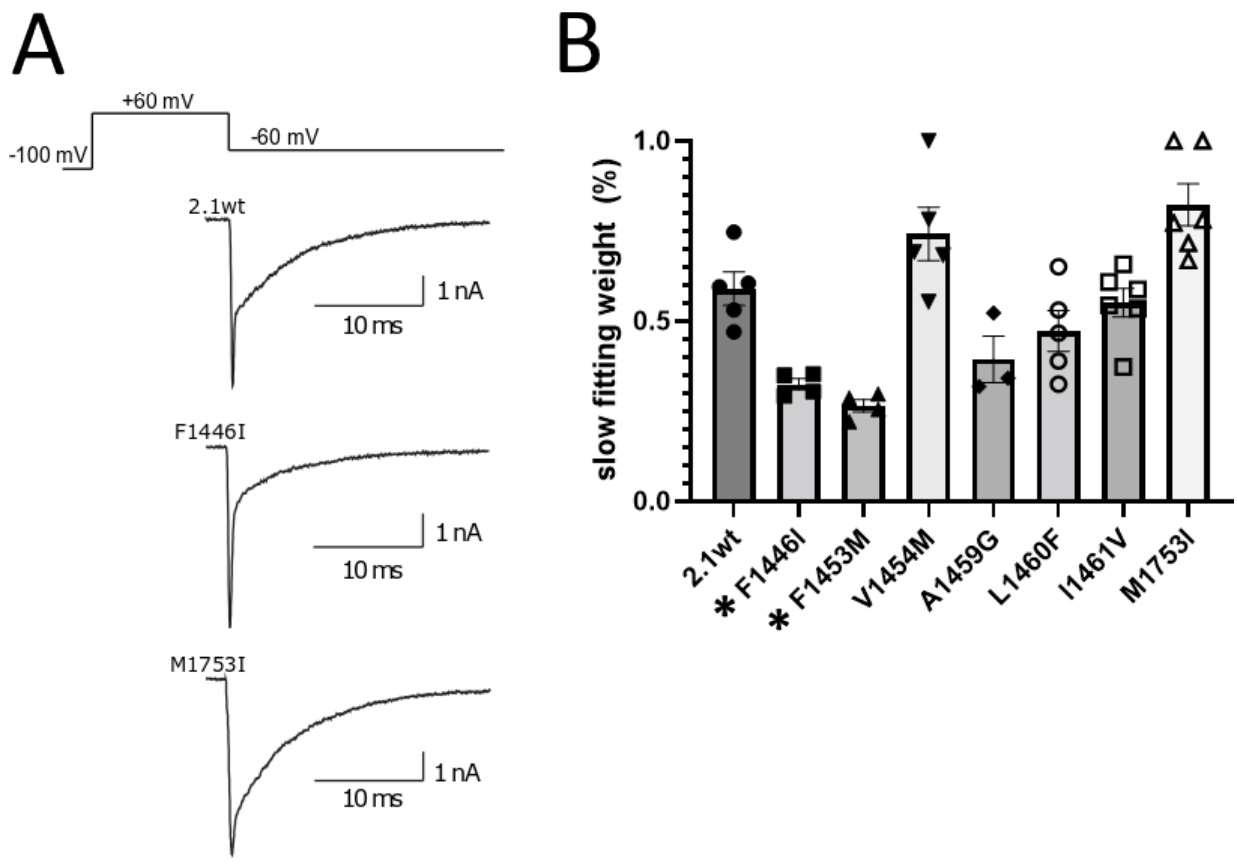

Figure 31: Effects of selected single-residue Ca_V2->Ca_V1 mutations on the proportion of current modified by 5uM KK-20.

A. Representative tail currents modified by 5 μM KK-20, showcasing a typical wild-type current (in which about half of the tail current decay is slowed by the drug) and recordings from mutant channels in which a smaller or larger proportion of the decay is slowed. **B.** Comparison between wild-type and mutant channels of the amplitude of tail current decay fit to the slow component of a double weighted exponential in the presence of 5 μM KK-20, representing the proportion of activated channels modified by KK-20 at the end of the depolarizing step. (See Equation 1 in section 4.2.4 for the formula used to fit the tail current decay.) Mutations with significant effects (Brown-Forsythe and Welch one-way ANOVA with Dunnett's T3 multiple comparison post hoc analysis, $p < 0.05$) are marked with an asterisk. Bar height represents the mean value, and individual data points are shown. Data points with a slow fitting weight of 1 indicate recordings in which 100% of the tail current decay was slowed by KK-20. Error bars represent SEM.

We did not identify any mutations that clearly interfered only with KK-20 binding and not the extent to which it prolongs channel opening. A1459G and I1461V reduced neither slowing of deactivation (as measured by fold change in tail current integral) in the 50 μM experiments, nor the slow fitting weight of tail currents in the 5 μM experiments. It could be the case that F1446I

primarily or solely disrupts binding, since it clearly reduced the slow fitting weight in the 5 μM experiments, yet it was ambiguous in the 50 μM KK-20 experiments whether it genuinely reduced KK-20's ability to slow deactivation. In the absence of a conclusive answer regarding F1446I, it is unclear whether it is possible to disrupt KK-20 binding without impairing the drug's ability to prolong channel opening.

4.3.3 Effects of single-site mutations on the efficacy and potency of KK-20

To follow up on our initial exploratory mutagenesis experiments, we collected concentration-response data for KK-20 in the wild-type channel and the F1446I, F1453M, L1460F, and M1753I mutants, using fold change in normalized tail integral as our measure of drug effect (Figure 32).

From our dose-response data, we calculated KK-20's EC_{50} in the wild-type Cav2.1 channel at 6.93 μM, which is very close to the 7.27 μM EC_{50} we previously reported in Wu et al., 2018. Consistent with our measurements of proportional binding at 5 μM, we found reduced KK-20 potency in the mutants F1446I (EC50 = 40.7 μM) and F1453M (EC_{50} = 52.0 μM). Comparatively, potency in L1460F was slightly reduced from wild-type (EC_{50} = 10.4 μM), and potency in M1753I was slightly increased (EC_{50} = 4.61 μM).

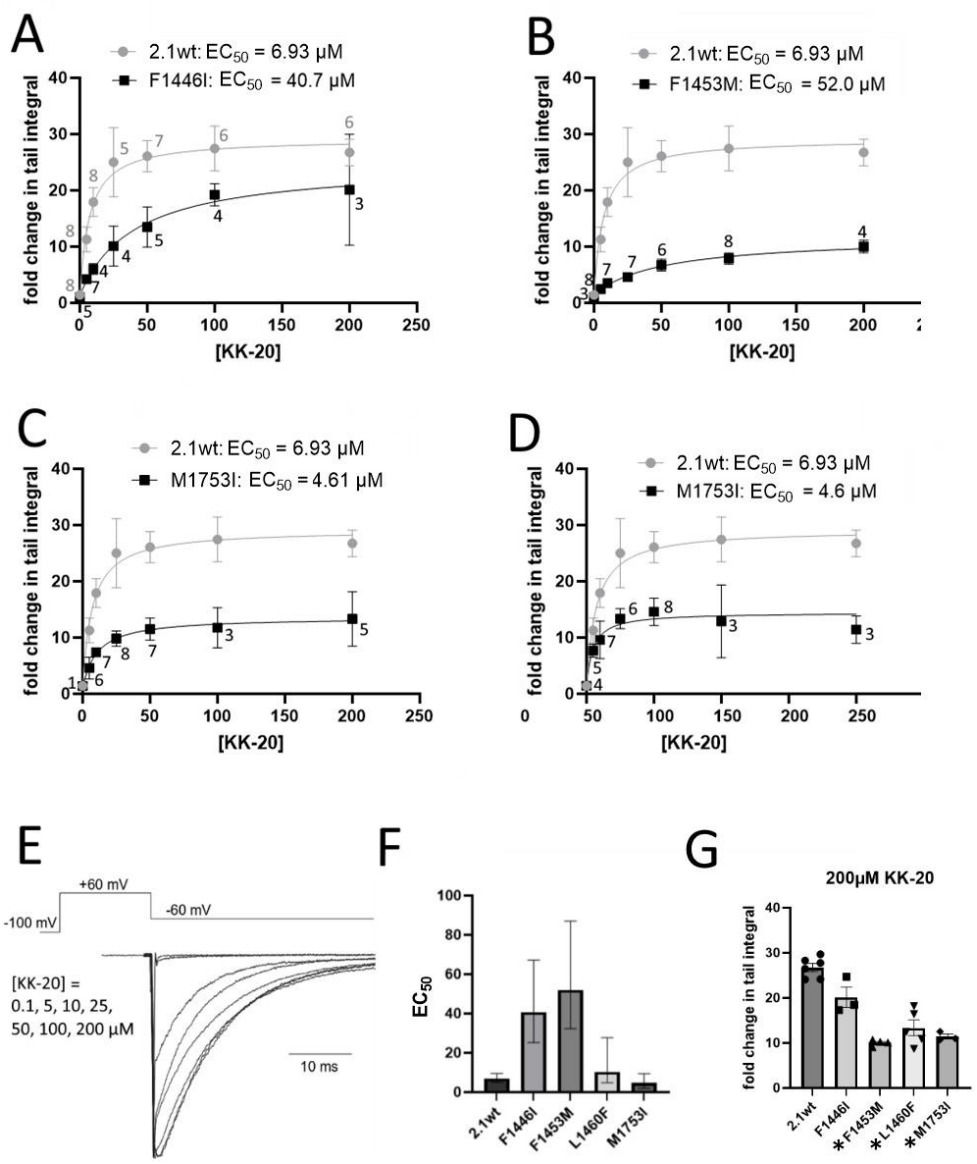

Figure 32: Concentration-response curves for KK-20 in wild-type and mutant channels.

A. Plot of mean fold change in normalized tail current integral vs concentration of KK-20 applied for F1446I (black), compared with the wild-type channel (grey). The mean fold change at each concentration is labeled with the N for that condition. Data were fit to a three-parameter agonist vs response curve to calculate EC_{50} (see Equation 2). Error bars represent SEM. **B.** As in A, comparing the concentration-response curve of F1453M vs wild-type $Ca_V2.1$. **C.** As in A, comparing the concentration-response curve of L1460F vs wild-type $Ca_V2.1$. **D.** As in A, comparing the concentration-response curve of M1753I vs wild-type $Ca_V2.1$. **E.** Representative tail currents in wild-type $Ca_V2.1$ prior to KK-20 application and in the presence of 0.1, 5, 10, 25, 50, 100, and 200 µM KK-20. The proportion of current modified increases with concentration. **F**. Bar graph comparison of the EC_{50} values calculated for each concentration-response curve. Error bars represent the 95% confidence interval. **G**. Bar graph comparison of the mean fold change in integral at 200 µM KK-20, the highest concentration evaluated. Bar height represents the mean value, and individual data points are shown. Error bars represent SEM. Mutations with significant effects (Brown-Forsythe and Welch one-way ANOVA with Dunnett's T3 multiple comparison post hoc analysis, $p < 0.05$) are marked with an asterisk.

In all evaluated mutants, the maximum observed response to KK-20 (at 200 μM) was smaller than in wild-type (fold change in tail current integral = 26.74 +/- 0.93), and this difference was statistically significant (per one-way Brown-Forsythe and Welch ANOVA with Dunnett's T3 multiple comparison post hoc analysis) in all mutants except F1446I (Figure 32G). F1453M had the smallest maximum response (10.01 +/- 0.35, $p < 0.0001$). Despite its negative effect on KK-20 potency, F1446I's maximum response (20.13 +/- 2.27, not significant) was higher than in L1460F (13.32 +/- 1.75, $p < 0.005$) or M1753I (11.41 +/- 0.56, $p < 0.0001$), whose responses plateaued at relatively low concentrations. This supports our speculation that F1446 is more important in coordinating KK-20 binding than in its mechanism of action.

4.3.4 Effects of single-site mutations on the binding kinetics of KK-20

Our EC_{50} measurements reflected the equilibrium of drug-bound channels at the end of a 100ms step, but did not clarify the factors underlying that equilibrium. Our next step was to determine how a subset of mutations affect the on- and off-rates of KK-20 binding. KK-20's on-rate for each mutant is of particular interest, since k_{on} determines the drug's speed of action, which in turn (as we discussed in Chapter 2) determines its ability to modify channels over the brief time-course of a physiological action potential. If there are specific residues that mediate k_{on}, then *(R)*-roscovitine analogs with improved speed of action could be designed by fine-tuning how the drug's side groups interact with these positions. The on- and off-rates could also be used to calculate KK-20's dissociation constant K_D ($K_D = k_{off}/k_{on}$), which represents the inverse of the binding affinity (thus, higher K_D indicates lower binding affinity).

Although we previously used the fitting weight of the slow component of drug-modified tail current to calculate the proportion of modified channels in 5 μM KK-20, here we used plots of

normalized tail integral versus step length to calculate K_D. The reason for this is that we found we could not reliably fit tail current decay to a double exponential at concentrations and step lengths where the fast component was very small, and at low concentrations and step lengths where very few channels were modified, the slow components we measured predominately represented the intrinsic long-opening mode of unmodified channels (Destefino et al., 2010). However, we predicted that the fold change in tail integral would serve as an acceptable measure of proportional binding when normalized to the maximum KK-20 effect at a given concentration. Buraei et al. (2005) previously calculated *(R)*-roscovitine's K_D in wild-type $Ca_V2.2$ channels as nearly equal to its EC_{50}, which implies a linear relationship of proportional binding to the size of the drug effect. Additionally, we observed little to no effect of step length or drug concentration on the time-course of drug-modified tail current decay, tau_{deact} (not shown), so we expected the increase in normalized tail integral at longer step lengths to be due solely to an increasing proportion of modified channels.

To calculate K_D, we plotted the normalized tail integral vs six depolarizing step lengths (2, 3, 5, 10, 50, and 100ms) at each of four KK-20 concentrations (5, 10, 25, and 50 μM). Since KK-20 only binds channels in the open state, these equated to plots of KK-20 binding as a function of time. We calculated the time-course of KK-20 binding, tau_{bind}, at each concentration (Figure 33), then applied a linear fit to a tau_{bind} vs concentration plot (Figure 34; see Table 1 for sample sizes). The slope of this linear fit equates to k_{on} and the y-intercept to ko_{ff}.

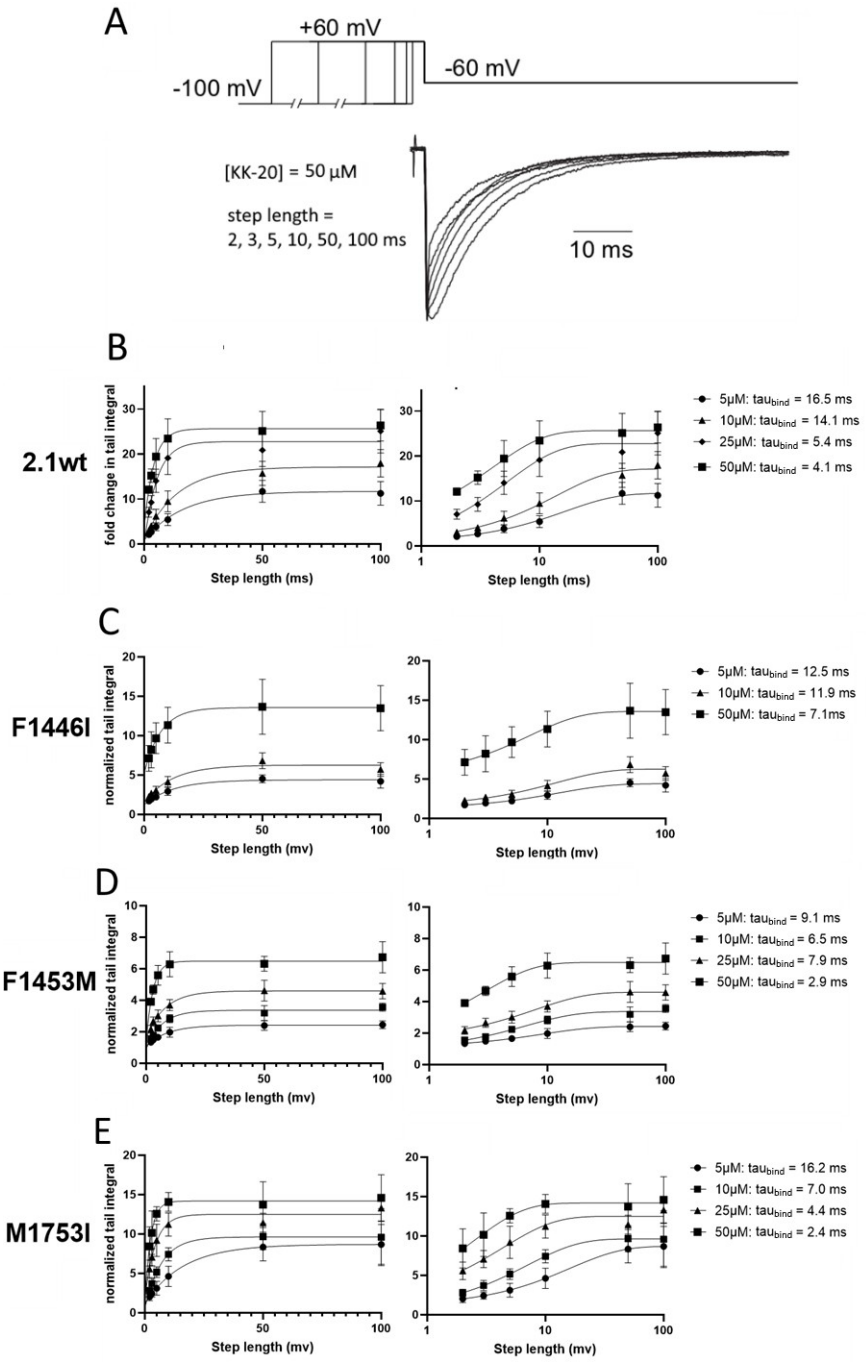

Figure 33: Time-dependence of modification plots for wild-type $Ca_V2.1$ and three single-residue Ca_V2->Ca_V1 mutant channels.

A. Representative tail currents in wild-type $Ca_V2.1$ in the presence of 50 µM KK-20 following depolarizing steps to +60 mV of 2, 3, 5, 10, 50, and 100 ms. The proportion of current modified increases with step length. **B.** For the wild-type $Ca_V2.1$ channel, time-dependence plots of mean fold change in normalized tail current integral vs linear (left) and logarithmic (right) duration of the +60mV depolarizing step to activate channels, at 5, 10, 25, and 50 µM KK-20. The time-dependence plot at each concentration is fit to a one-phase association equation (see Equation 3 in section 4.2.4) to calculate tau_{bind} (far right). Error bars represent SEM. **C.** As in A., for the F1446I mutant. Data were not collected at 25 µM KK-20 for this mutant. **D.** As in A., for the F1453M mutant. **E.** As in A., for the M1753I mutant.

Table 1: Sample sizes for the data shown in Figure 33

	5 µM KK-20	10 µM KK-20	25 µM KK-20	50 µM KK-20
2.1wt	N = 8 (2/3/50 ms) N = 8 (5/10/100 ms)	N = 8 (2/3/50 ms) N = 8 (5/10/100 ms)	N = 6 (2/3/50 ms) N = 5 (5/10/100 ms)	N = 8 (2/3/50 ms) N = 7 (5/10/100 ms)
F1446I	N = 8 (2/3/50 ms) N = 7 (5/10/100 ms)	N = 5 (2/3/50 ms) N = 5 (5/10/100 ms)	N/A	N = 5 (2/3/50 ms) N = 5 (5/10/100 ms)
F1453M	N = 8 (2/3/50 ms) N = 8 (5/10/100 ms)	N = 8 (2/3/50 ms) N = 7 (5/10/100 ms)	N = 7 (2/3/50 ms) N = 7 (5/10/100 ms)	N = 8 (2/3/50 ms) N = 6 (5/10/100 ms)
M1753I	N = 6 (2/3/50 ms) N = 6 (5/10/100 ms)	N = 7 (2/3/50 ms) N = 7 (5/10/100 ms)	N = 4 (2/3/50 ms) N = 6 (5/10/100 ms)	N = 9 (2/3/50 ms) N = 8 (5/10/100 ms)

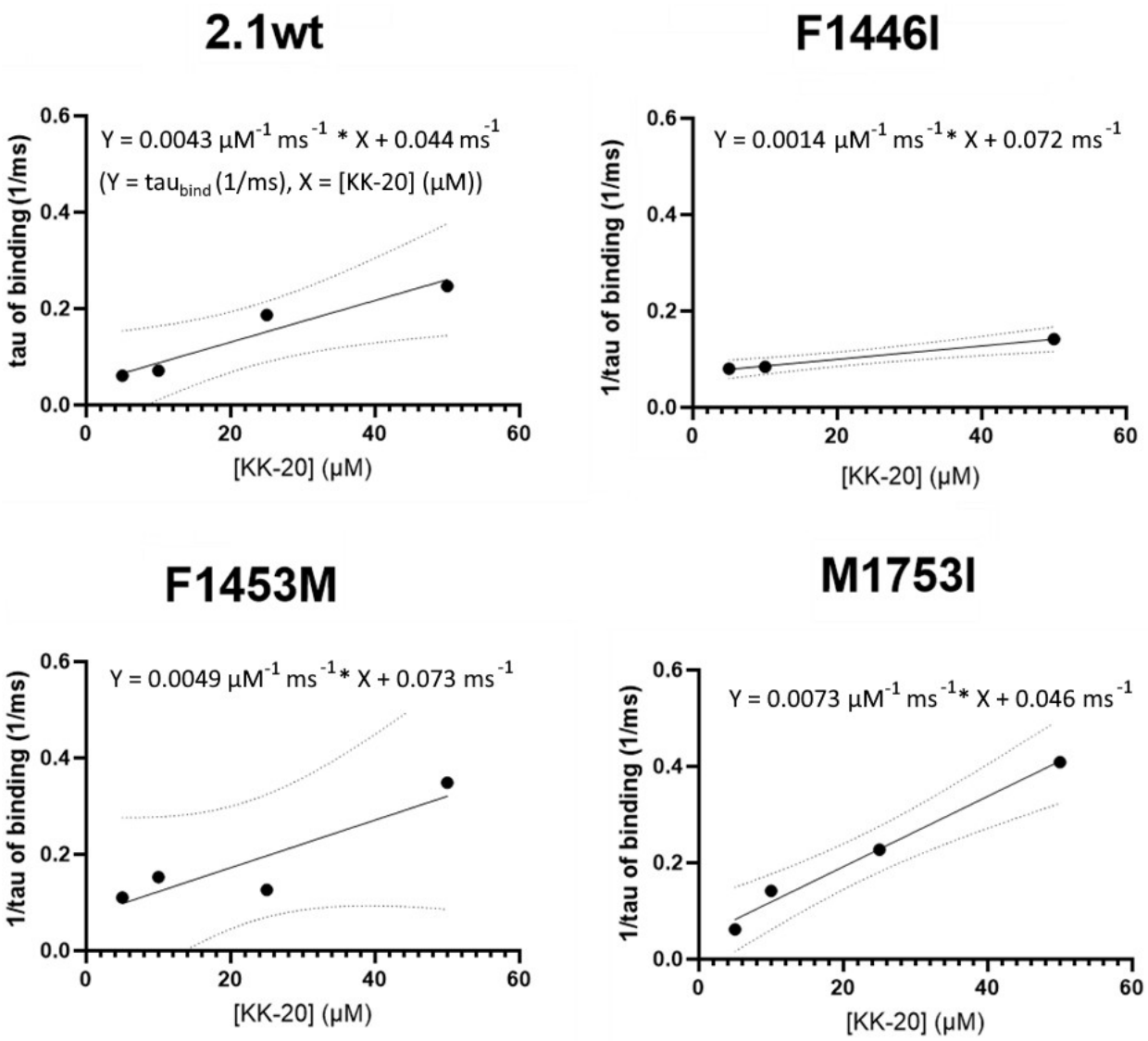

Figure 34: K_D plots for wild-type $Ca_V2.1$ and three single-residue Ca_V2->Ca_V1 mutant channels.

KK-20 concentration vs $1/tau_{bind}$ plots for wild-type $Ca_V2.1$ and the F1446I, F1453M, and M1753I mutant channels, using the tau_{bind} values shown in Figure 32. Plots were fit to a simple linear regression to derive the slope and y-intercept, to be used to calculate k_{off}, k_{on}, and K_D. Dotted lines represent 95% confidence bands for the linear regression.

Figure 35 shows comparisons of k_{on}, k_{off} and K_D values between wild-type and mutant channels, as well as direct comparisons of K_D vs EC_{50}. We calculated KK-20's k_{off} at 0.0440 ms^{-1}, its k_{on} at 0.0043 $\mu M^{-1}ms^{-1}$, and its K_D at 10.2 µM in wild-type $Ca_V2.1$. As expected, this K_D is similar to the wild-type EC_{50} (6.93 µM). The K_D of the F1446I mutant (51.9 µM) is ~5 times larger

than the wild-type K_D, and again is similar to the EC50 for this mutant (40.7 μM). The increased K_D is a function of both faster k_{off} (0.072 ms^{-1}) and slower kon (0.0014 $\mu M^{-1}ms^{-1}$) compared to wild-type.

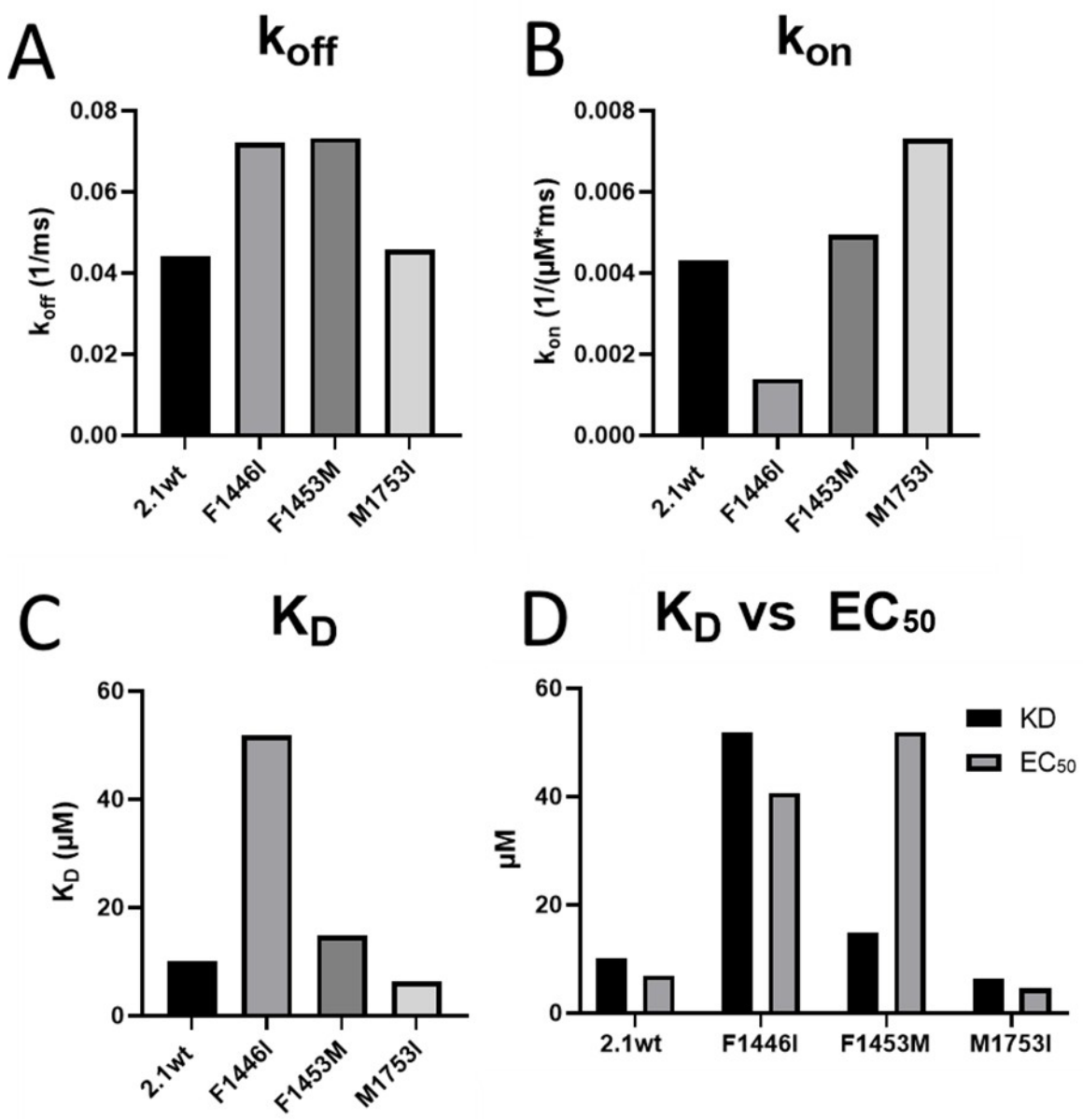

Figure 35: Comparison of k_{off}, k_{on}, K_D, and EC_{50} between wild-type $Ca_V2.1$ and three single-residue Ca_V2->Ca_V1 mutant channels.
A. Comparison of k_{off} values, calculated as the y-intercept of the linear regression equation for each mutant's concentration vs tau_{bind} plot, as shown in Figure 33. **B.** Comparison of k_{on} values, calculated as the slope of the linear regression equation for each mutant. **C.** Comparison of K_D values between the wild-type and mutant channels, calculated using the equation $K_D = k_{off}/k_{on}$. **D.** Comparison of the K_D for each wild-type or mutant channel with its EC_{50} (as shown in Figure 32.)

We found that compared to the wild-type channel, the M1753I mutation has slightly increased affinity for KK-20 (K_D = 6.3 μM), and this difference is attributable to large increase in the drug's on-rate (kon = 0.0073 $\mu M^{-1}ms^{-1}$) while the off-rate is essentially unchanged from wild-

type (koff = 0.046 ms^{-1}). This finding is in agreement with the results of our dose-response experiments in section 4.3.3. which showed that M1753I slightly increases KK-20 potency (EC_{50} = 4.6 μM). It is unclear whether these small differences in potency and binding affinity indicate that M1753 is involved in KK-20 binding, and interpretations of these findings are complicated by M1753I's effects on gating kinetics in unmodified channels (see discussion). However, we can conclude that the M1753I mutation does not *reduce* potency or binding affinity and, therefore, that this mutation's impairment of KK-20-mediated slowing of deactivation cannot be explained by disruption of the binding site.

Our most unusual result was that the F1453M mutation increased K_D to only 14.8 μM, in stark contrast to its EC_{50} of 52.0 μM. A large increase in F1453M's k_{off} compared to wild-type (0.073 ms^{-1}) is partially compensated by a smaller increase in k_{on} (0.0049 $\mu M^{-1}ms^{-1}$). This result challenged our assumption of a linear relationship between the proportion of modified channels and the normalized tail integral measure. However, reanalyzing the data using slow fitting weight as the measure of proportional KK-20 binding did not meaningfully change the calculated K_D (not shown). The poor linear fit of the F1453M concentration vs tau_{bind} data could also be a contributing factor, but it is unlikely that this alone could account for such a large discrepancy between K_D and EC_{50}.

We considered that our activity-dependence data might be confounded by an effect of the F1453M mutation on $Ca_V2.1$ activation kinetics. If the speed at which channels open (and thus become available for KK-20 binding) differs between mutants, this would have a disproportionate effect on the availability of channels to KK-20 during short depolarizations (2-5 ms), which would affect the activity-dependence curves and therefore the calculation of on- and -off-rates of binding. It was not possible to measure the time-course of activation (tau_{act}) at the +60mV voltage step used

in our KK-20 experiments, because this voltage is at or near the equilibrium potential for the channel and there is no measurable inward current during the step. Instead, we measured tau_{act} at voltages ranging from -10mV to +30mV by fitting the current during the depolarizing step with a single exponential (Figure 36). We found differences between mutants in speed of activation at more hyperpolarized potentials—in particular, the activation of F1446I was slowed compared to the wild-type channel, which points to potential involvement of the F1446 residue in channel gating mechanisms—but tau_{act} became increasingly similar between mutants the more depolarized the step potential. At +30mV, tau_{act} was approximately the same in all channels. We predict that there is unlikely to be a large difference in F1453M's speed of activation at +60mV that would explain the discrepancy between its EC_{50} and calculated binding affinity.

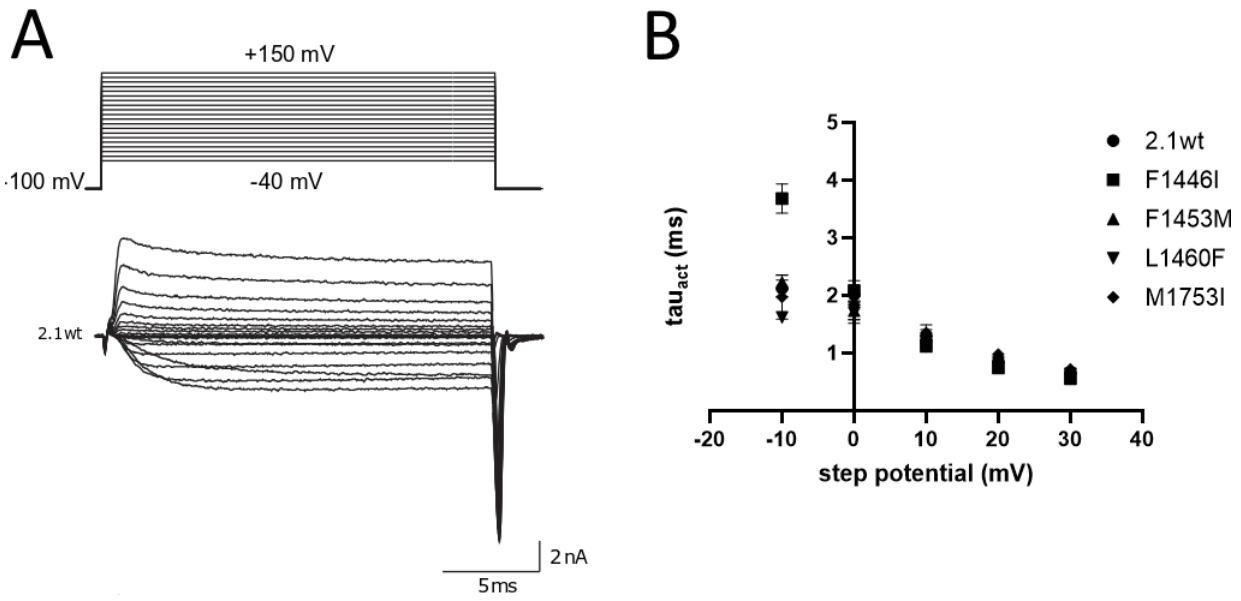

Figure 36: Effects of single-residue Ca_V2->Ca_V1 mutations on speed of activation.

A. Representative currents in a cell expressing wild-type $Ca_V2.1$ channels. 20ms depolarizing steps ranging from -40 mV to +150 mV, in 10 mV increments, were applied to activate currents. Currents during the steps ranging from -10mV to +30mV were fit to a single exponential to calculate the time constant of activation (tau_{act}). **B.** Comparison of tau_{act} vs voltage between wild-type and mutant channels. At step potentials more depolarized than 0 mV, tau_{act} is nearly indistinguishable between channels. Error bars represent SEM.

Another possible interpretation of our F1453M results is that rather than (or in addition to) disrupting KK-20's binding site, it alters the fenestration access pathway through which we believe it accesses that site. This possibility is covered in detail in the Discussion.

Our calculations of KK-20's off-rate in each mutant proved useful as a test of the consensus (discussed in Chapter 2) that although *(R)*-roscovitine analogues slow channel closure, drug unbinding is not required for the channel to close. In a model where unbinding is required for channel closure, the time constant of tail current decay, tau_{deact}, should be rate-limited by the time constant of unbinding, where $tau_{unbind} = 1/k_{off}$. We calculated the time constant of deactivation, tau_{deact}, for wild-type, F1446I, F1453M, and M1753I tail currents modified by KK-20 in our initial exploratory mutagenesis experiments (50µM KK-20, 100ms activation step), by fitting the tail current decay curve in each recording to a weighted exponential. We found that KK-20's tau_{unbind}

was slower than the mean tau_{deact} of KK-20-modified tail currents for the wild-type $Ca_V2.1$ and all mutants for which we calculated K_{off} (Figure 37). This indicates that channels close more quickly than KK-20 unbinds, which supports the interpretation that unbinding is not required for channel closure.

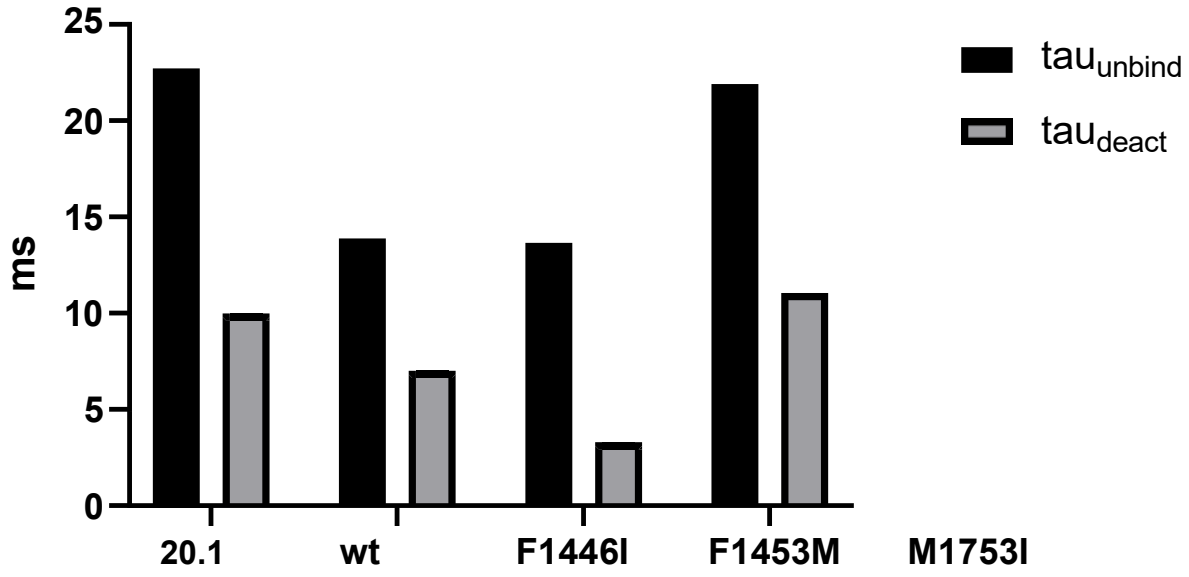

Figure 37: Time constants of KK-20 unbinding are not rate-limiting for tail current decay in wild-type and mutant channels.

While the F1446I, F1453M, and M1753 mutations have different effects on the time constant of KK-20 unbinding ($tau_{unbind} = 1/k_{off}$), the time constant of current decay (tau_{deact}) is faster than tau_{unbind} in all cases, indicating that KK-20-modified channels can close sooner than KK-20 unbinds.

4.3.5 Mutation effects on control voltage-dependence of activation may indirectly influence KK-20's effects on tail currents

Pore stability is an important determinant of the voltage-dependence of activation in calcium channels. Mutations to residues in the lower thirds of S6 segments that destabilize the closed state of the pore typically left-shift voltage-dependence of activation, with the size of the effect correlating to the decrease in hydrophobicity (Hering et al., 2008). Additionally, in the

Ca_V1/Ca_V2 chimera experiments discussed previously, Ca_V2 domains III and IV in particular were found to be required for the steeper voltage-dependence of activation observed in the wild-type Ca_V2 channels (compared to wild-type Cav1) (Yarotskyy et al., 2012). Therefore, we considered that our Ca_V2->Ca_V1 mutations in the lower thirds of S6 segments in domains III and IV might perturb voltage-dependence of activation,

To contextualize our characterization of KK-20 action in the F1446I, F1453M, L1460F and M1753I mutants, we collected current vs voltage data to calculate the half-maximal voltage (VD_{50}) in the unmodified wild-type and mutant channels (Figure 38). To generate fractional activation (I/I_{max}) vs voltage plots, we applied a series of voltage steps to increasingly depolarized potentials (-40mV to +150mV, in 10mV increments; see Figure 38A) and normalized the peak amplitude of the tail current at the end of each step to the maximum tail current amplitude recorded in the same cell. Since driving force at the -60mV repolarization potential is equal between all sweeps, the relative amplitude of the tail current should directly represent the fractional activation of channels at a given voltage. We found that compared to the wild-type channel (VD_{50} = 2.32 mV), the I/I_{max} vs voltage plots were left-shifted in the F1446I mutant (VD_{50} = -5.97) and slightly left-shifted in F1453M (VD_{50} = -2.34 mV), and right-shifted in L1460F (VD_{50} = 12.3 mV) and M1753I (VD_{50} = 13.7 mV) (Figure 38B). Mean fractional activation at +60mV, the voltage step we used to evaluate KK-20 action, is about 92.5% of maximum in the wild-type channel and F1453M, 94.7% in F1446I, 90.5% in F1453M, 85.2% in L1460F, and 84.2% M1753I. These effects suggest that the wild-type residues we mutated might be involved in pore gating mechanisms, or alternatively that the mutations allosterically modify pore gating mechanisms.

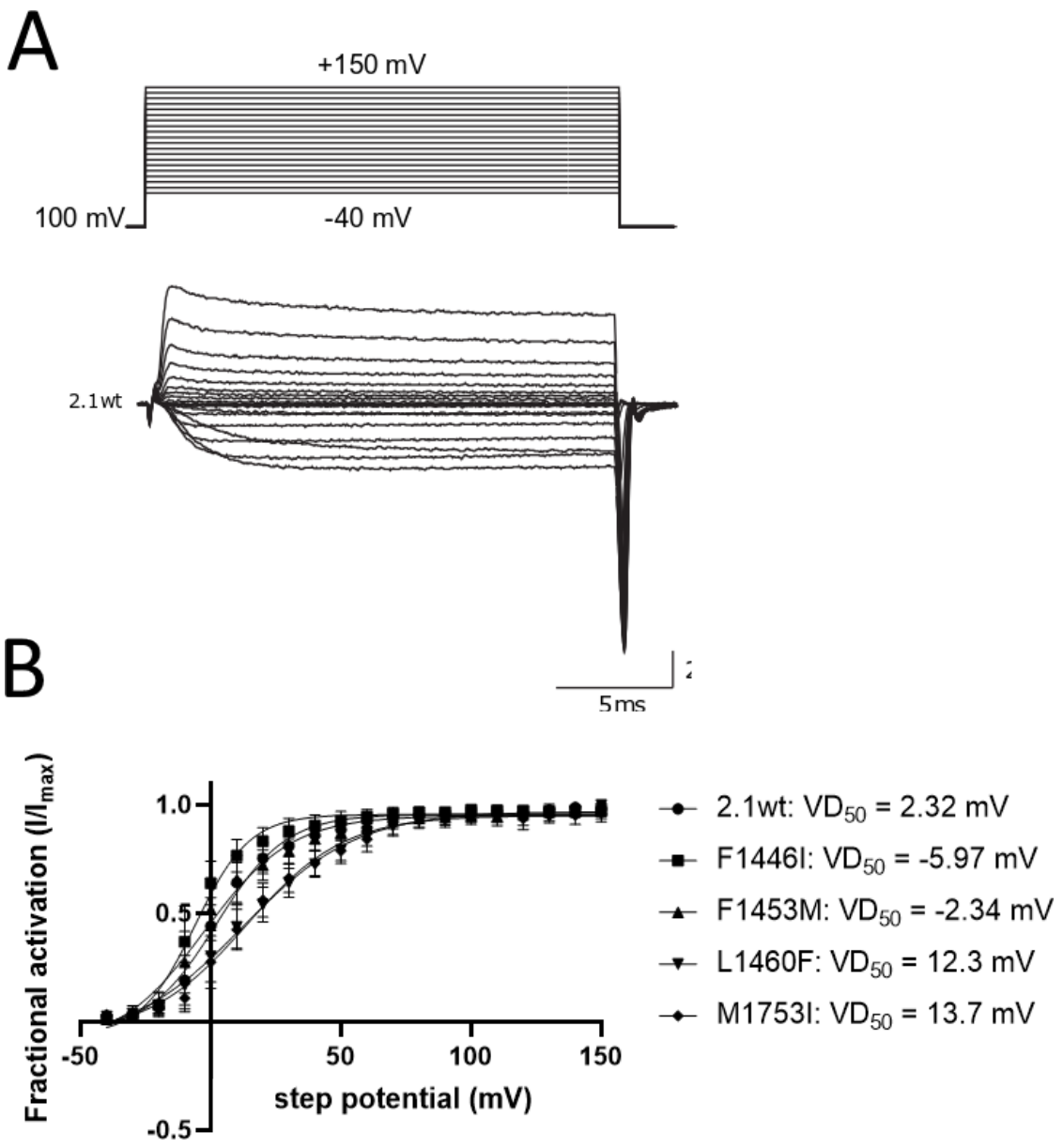

Figure 38: Effects of single-residue Ca_V2 -> Ca_V1 mutations on voltage-dependence of activation.

A. Representative currents in a cell expressing wild-type $Ca_V2.1$ channels, as also shown in Figure 35A. 20ms depolarizing steps ranging from -40 mV to +150 mV, in 10 mV increments, were applied to activate currents. Peak tail current amplitudes were measured at the end of each step and normalized to the largest amplitude in the same cell to calculate I/I_{max}. **B.** Fractional activation vs depolarizing step voltage plots for the wild-type $Ca_V2.1$ channel and the mutants F1446I, F1453M, L1460F, and M1753I. Each plot was fit to a Boltzmann sigmoidal equation to calculate VD_{50}. F1446I and F1453M left-shift voltage-dependence of activation, while L1460F and M1753I right-shift it. 2.1wt N = 8; F1446I N = 8; F1453M N = 7; L1460F N = 6; M1753I N = 8.

We considered how these differences in VD50 might relate to the mutation effects on KK-20 action that we have observed. KK-20's parent molecule *(R)*-roscovitine itself slightly left-shifts the voltage-dependence of activation at high concentrations (Buraei et al., 2005; Yarotskyy and Elmslie, 2009), and has been found to increase current amplitudes most strongly at voltages where P_O is neither very low (likely because of the lack of open channels available for the drug to bind), nor very high (Yarotskyy and Elmslie, 2009). Yarotskyy and Elmslie (2009 proposed that this is because *(R)*-roscovitine increases current amplitudes by shifting channels into a high-P_O state (if activated channels remain open for longer durations without a change in closed time, the probability of a channel being open at any given time increases), so if P_O is already near maximum, the drug has little further effect on amplitude.

An effect on tail current amplitudes alone should not affect our measurements of normalized tail integral, drug tau_{deact}, or slow fitting weight. However, since the fraction of channels available for KK-20 to bind is expected to vary with P_O, we considered whether there might be a relationship between P_O at +60mV and the slow fitting weight in 5 μM KK-20. In this case, we would expect to see reduced slow fitting weight compared to control in the mutants with right-shifted voltage-dependence of activation, L1460F and M1753I, and increased slow fitting weight in the mutant with left-shifted voltage-dependence of activation, F1446I. To the contrary, in our experiments described in 4.3.2 we observed increased slow fitting weight in M1753I (though this effect was not statistically significant) and significantly reduced slow fitting weight in F1446I. While slow fitting weight was reduced in L1460F, the effect was not significant.

Another consideration is that if KK-20 itself shifts voltage-dependence of activation by -10mV or more (as was observed in the parent molecule by Yarotskyy and Elmslie (2009)), it is possible that even the L1460F and M1753I mutants reach maximal P_O at +60mV in the presence

of the drug, in which case there would be no meaningful difference in P_O between mutants at the voltage used in our experiments. This possibility could be investigated by collecting voltage-dependence data for the wild-type and mutant channels in the presence of KK-20, but we currently do not see any consistent effect of differences in voltage-dependence of activation on our measures of drug action.

4.3.6 The F1446I and F1453M mutations have effects on KK-20 action and binding that are cumulative in the double mutant

Having demonstrated that certain mutations within the $Ca_V2.1$ III/IV fenestration inhibit KK-20-mediated slowed deactivation of the channel, we were curious whether multiple such mutations in the same channel would have a cumulative effect. Residues in the VGCC inner pore form extensive hydrophobic contacts with residues of neighboring segments, and these interactions (termed "adhesion points") have been proposed to cooperatively stabilize the closed conformation of the activation gate (Hering et al., 2008). Mutations to residues within these segments have also been predicted *in silico* to cause distortions of both their own and neighboring S6 helices, changing the orientations of residues and disrupting important hydrophobic contacts (Stary et al., 2008). These findings stemmed from deliberate mutagenic perturbation of the channel structure, e.g. by replacing hydrophobic inner pore residues with polar residues, whereas our Ca_V2->Ca_V1 substitutions are much more conservative. Nevertheless, we considered the possibility that the effects of our mutations on KK-20 action might be due not to their own independent interactions with KK-20 or its mechanistic pathway, but to their allosteric disruption of other residue orientations and/or interactions in the inner pore. For example, two different mutations might each indirectly inhibit KK-20 activity by allosterically displacing the same mutually adjacent KK-20

binding residue. In this case, we would not expect mutating both residues to have any further effect on KK-20 activity.

We tested this possibility for the F1446I and F1453M mutations, which our dose-response experiments suggest interfere with KK-20 binding. In our homology models of the closed and open $Ca_V2.1$ pore, F1446 and F1453 are only two helical turns apart in the IIIS6 segment and are both oriented into the III/IV fenestration (Figure 39), so we felt it was possible that mutating either residue would have similar disruptive allosteric effects on the inner pore structure. If both mutations inhibit KK-20 action by the same indirect mechanism, the effect of one mutation would be expected to occlude the effect of the other, such that including both mutations would not inhibit KK-20 action substantially more than either mutation does individually. In a similar vein, mutating one residue might have an independent effect on KK-20 action, while mutating the other affects KK-20 action indirectly by disrupting the orientation of the first residue; here again the presence of one mutation would occlude the effect of the other.

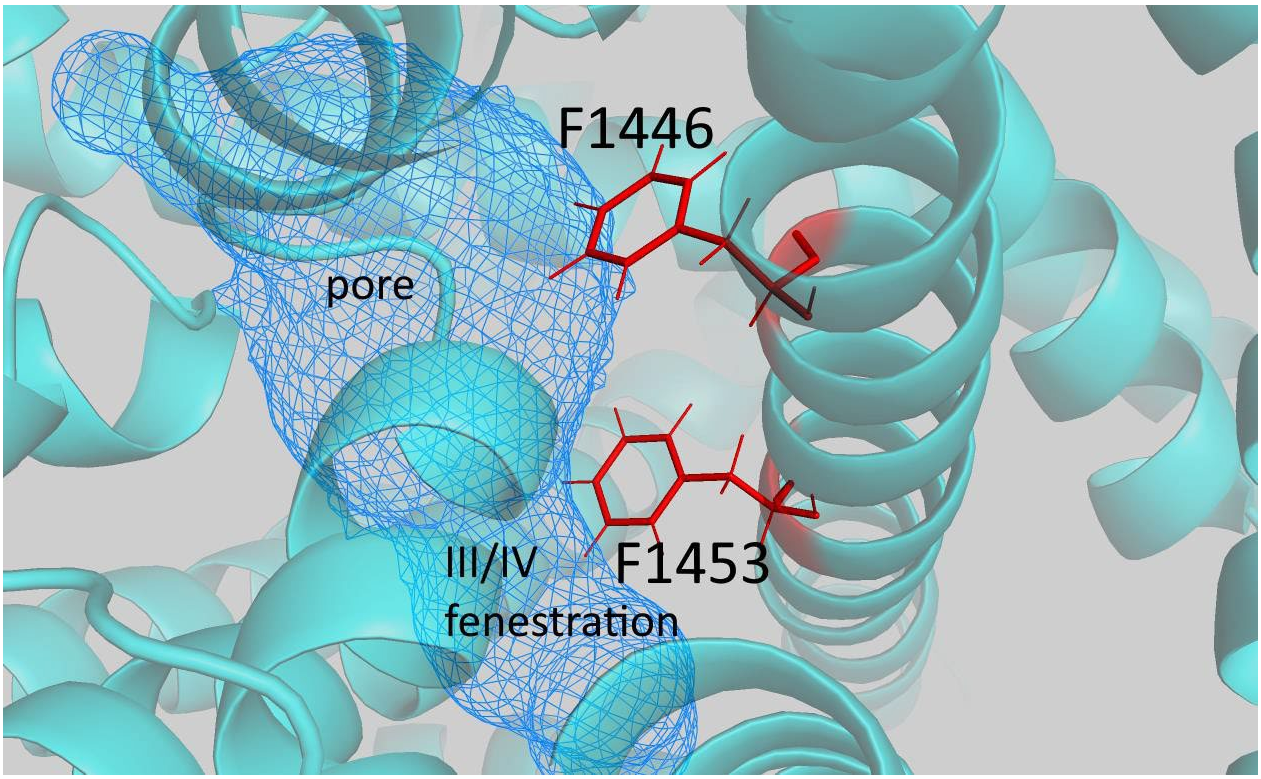

Figure 39: Relative positions of the F1446 and F1453 residues in our inactivated $Ca_V2.1$ homology model.

The F1446 and F1453 residues on IIIS6 are shown in stick form (red). Both are oriented toward the III/IV fenestration, F1453 near where the fenestration bottlenecks in the open state and F1446 where the fenestration opens into the central cavity.

In evaluating the effects of KK-20 on tail integrals in an F1446I/F1453M double mutant (Figure 40), we found that the normalized tail integral in F1446I/F1453M was significantly smaller (4.05 +/- 0.16) than the wild-type $Ca_V2.1$ channel (24.9 +/- 0.57, $p < 0.0001$), the F1446I single mutant (12.9 +/- 0.74, $p < 0.001$), and the F1453M single mutant (6.75 +/- 0.45, $p < 0.001$). We interpret this cumulative effect of the two mutations to mean that there is at least an independent component to each of their effects on KK-20 action.

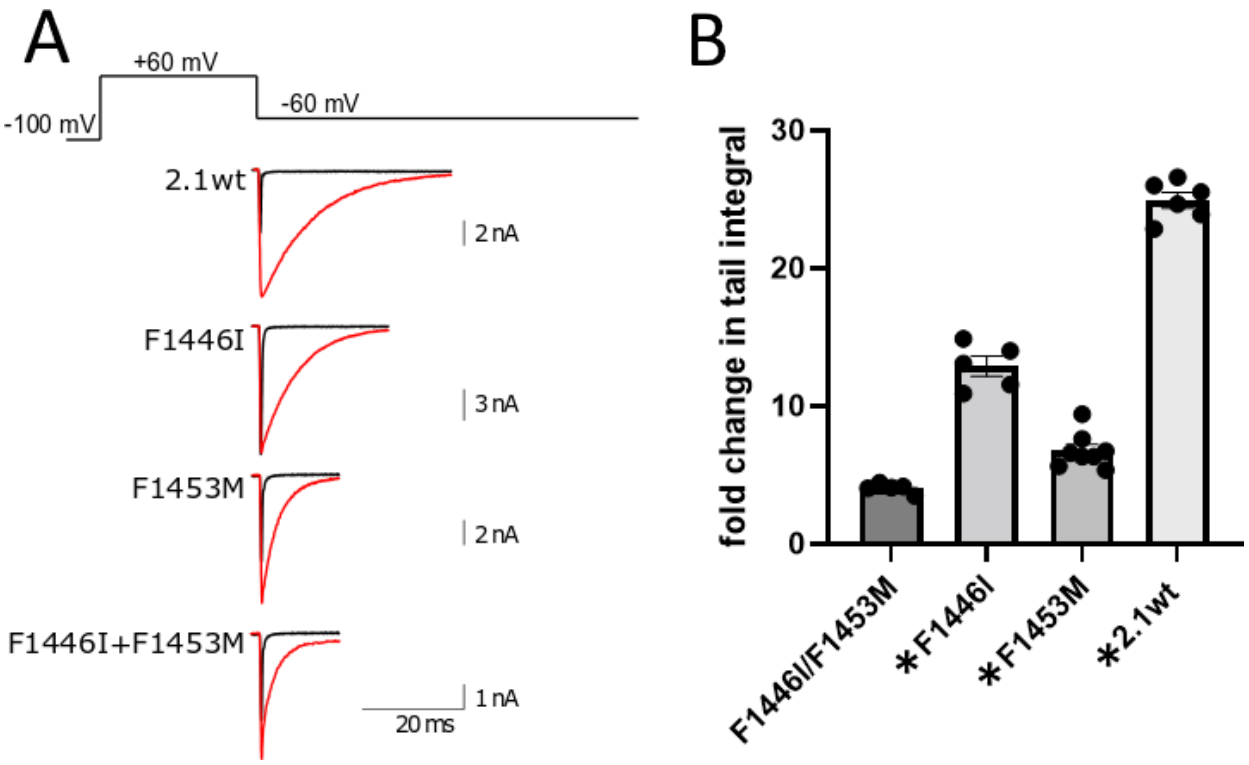

Figure 40: The F1446I mutation has a cumulative effect on KK-20 action and binding in combination with the F1453M mutation.

A. Representative tail currents of wild-type Cav2.1, F1446I, F1453M, and F1446I/F1453M double mutant channels before (black) and during (red) application of 50 µM KK-20. It can be observed that this concentration of KK-20 modifies most or all of the current decay in the wild-type and single mutant channels, but only partially modifies decay in the double mutant. **B.** Comparison of fold change in integral between the double mutant channel and the single mutant and wild-type channels. Fold change in either of the single mutants or the wild-type was larger than in the double mutant; these channels are labeled with an asterisk to represent significance. Error bars represent SEM.

Complicating this analysis is the fact that the F1446I/F1453M double mutant significantly increases the size of the control tail current integral (not shown). This is likely due to a cumulative effect of slowing of control deactivation by each of the single mutants (Figure 28). However, we also observed that when fitting the decay of F1446I/F1453M tail currents during application of 50 µM KK-20 to a double weighted exponential, the slow (drug-modified) component accounted for only 76.8 +/- 2.8% of the tail current amplitude (see example current in Figure 39A), whereas tail currents in both single mutants were primarily fit with the slow component. This effect on KK-20

binding cannot be explained only by slowing of control deactivation, and we believe that it represents a genuine cumulative effect of the two mutations on KK-20's interaction with the channel.

4.3.7 Molecular dynamics simulations predict drug side-group contacts with specific residues in the inner pore

Following the mutagenesis experiments, Dr. Rozita Laghaei performed molecular dynamics (MD) simulations of GV-58 molecules in the central cavity of our open-state $Ca_V2.1$ homology model. The frequency with which each of the three side groups of the drug—the -OH group of the Zone 3 (R)-2-amino-1-butanol side group, the Zone 2 thiophene side group, and the CH_3 group at the end of the Zone 4 n-propyl side group—contacts specific residues in the inner pore and the III/IV fenestration is charted in Figure 41. Of interest is the fact that the thiophene group is predicted to contact F1446 and M1753, and all three GV-58 side groups are predicted to contact F1453M (a small number of contacts also occurred between M1753 and the -CH3 group, although it is likely that the unsaturated n-propyl in KK-20 behaves differently). On the other hand, the -OH group extensively contacted the S1750 residue in the simulation, yet our mutagenesis experiments showed no effect of the S1750A mutation on KK-20-mediated slowing of deactivation. Anecdotally, we have also looked at a very small number of recordings of a T1409A mutant in the presence of 5 and 50 μM KK-20, as well as the S1750A mutant in the presence of 5 μM KK-20, and observed no apparent effect on KK-20 binding or slowing of deactivation for either mutation (not shown). Both the thiophene and -OH side groups are identical between GV-58 and KK-20, so we do not attribute this discrepancy to the different analogs used for simulations and experiments. Still, the MD simulations suggest a number of additional candidate *(R)-*

roscovitine analog binding residues in all four domains of the channel which could guide future mutagenesis experiments. As we identify more residues whose mutation effects on KK-20 potency and binding affinity suggest a role in coordinating its binding, we will be able to constrain the MD simulations by fixing different side groups in proximity to those residues.

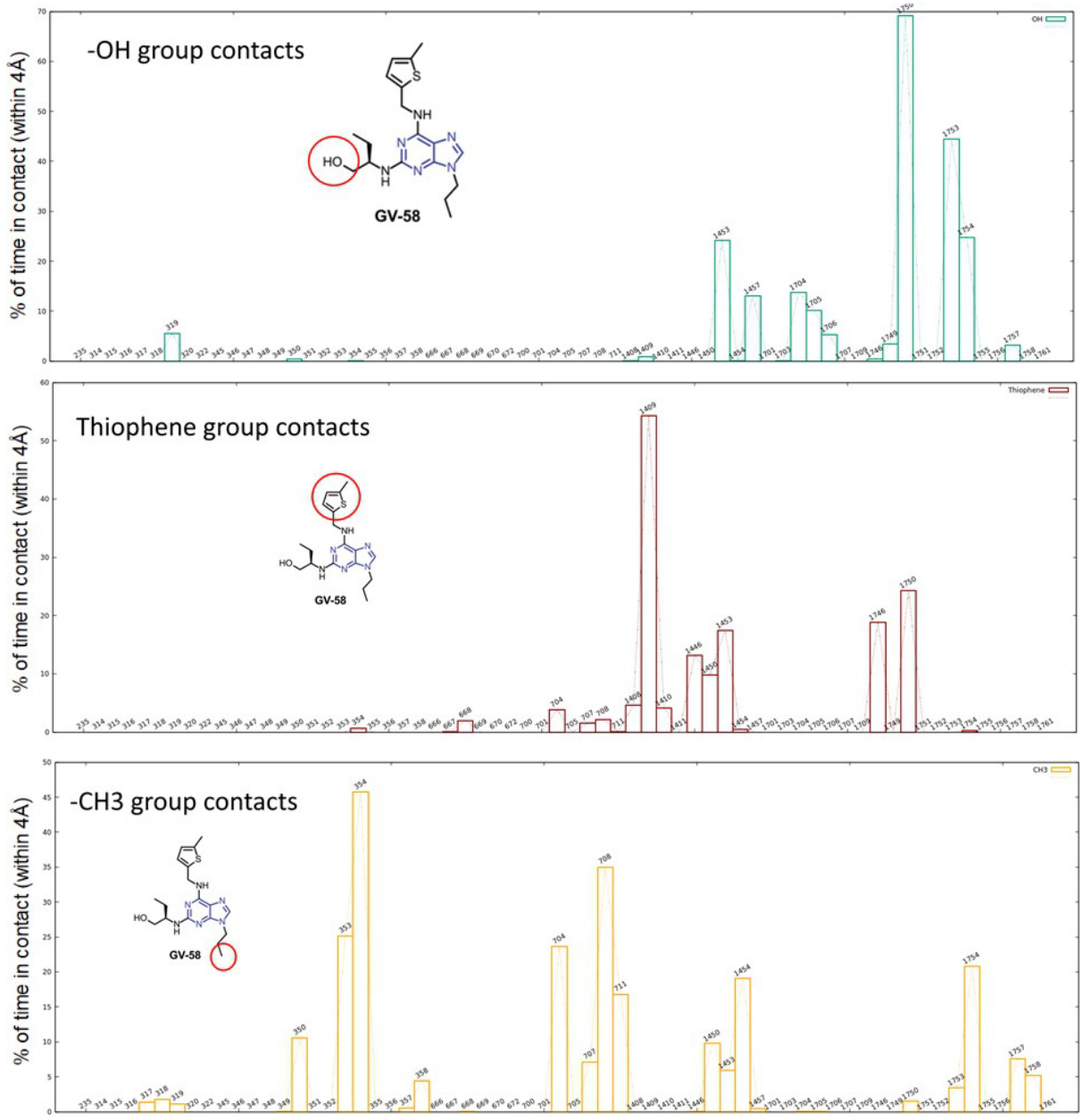

Figure 41: MD simulations predict GV-58 side-group interactions with inner pore residues.

MD simulations were run in which a simulated GV-58 molecule was free to move within the central cavity and attached fenestrations in our open-state homology model of $Ca_V2.1$ (see Chapter 3). The bar graphs display the frequency with which the -OH group (top; circled in the inset GV-58 structure), the thiophene group (center; circled in the inset GV-58 structure), and the -CH3 group (bottom; circled in the inset GV-58 structure) contacted specific residues during the last 70 ns of the MD simulations. The measure of frequency used is the percentage of the 70 ns during which KK-20 contacted a residue. A contact was defined as closer than 4 Å proximity between a drug side group and a residue side group. Each bar is labeled with the number of the residue it represents in the $Ca_V2.1$ sequence. GV-58 differs from KK-20 only in that its n-propyl group is saturated.

4.4 Discussion

4.4.1 Overlap between DHP-binding residues and analogous $Ca_V2.1$ residues involved in KK-20 action

In our initial search for Ca_V2 residues involved in KK-20-mediated slowing of channel closure, we evaluated four residues—F1446, V1454, F1747, and M1753—whose analogues in Ca_V1 channels are among those that are necessary and sufficient for high-affinity binding of the DHP agonist *(S)*-Bay K 8644. The Ca_V2->Ca_V1 mutations F1446I, V1454M, and M1753I impaired KK-20-mediated slowing of deactivation, and F1446I also decreased the drug's potency and binding affinity. It is tempting to speculate that KK-20 and *(S)*-Bay K 8644 interact with mechanisms that regulate open-vs-closed-state stability in the inner pore. The different hydrophobic residues at these positions in Ca_V1 vs Ca_V2 may have similar roles in regulating pore closure but are bound and modified by different drug side groups, hence the specificity of KK-20 for Ca_V2 and *(S)*-Bay K 8644 for Ca_V1 despite their similar effects on gating kinetics and potentially overlapping binding pockets.

4.4.2 The effect of KK-20 concentration on time-dependence of modification curves in our K_D experiments complicates the state-dependent fenestration access hypothesis

We were able to determine the KK-20 K_D in wild-type and mutant channels by calculating the time constant of KK-20 binding using depolarization steps of different lengths in the presence of different concentrations of KK-20. The inverse of the time constants of binding varied approximately linearly with KK-20 concentration, with faster binding occurring at higher

concentrations. However, according to our state-dependent fenestration access hypothesis, the binding site should be sealed off from the KK-20 in the PM and bath solution at the time that KK-20 is binding and modifying channels in the open state. Theoretically, the concentration of KK-20 applied to the cell should not factor into the rate at which the drug binds and modifies currents, and yet our K_D experiments showed that it clearly does. Possible explanations for this result in the context of the state-dependent fenestration access hypothesis are discussed in Chapter 6.

4.4.3 F1446 and F1453 are candidate KK-20 binding residues

Both the F1446I and F1453M mutations greatly reduce KK-20's efficacy (as measured by the fold change it induces in normalized tail integral) as well as its potency (as quantified by EC_{50}). Furthermore, the cumulative effect of mutating both residues supports the interpretation that each mutation has at least some independent effect on KK-20 action, rather than affecting it through a shared mechanism.

It was ambiguous whether F1446I truly inhibits slowing of deactivation in KK-20-modified channels, since this mutant's smaller fold change in tail current integral upon drug application, compared to wild-type $Ca_V2.1$, could be explained by its larger control tail current integral. However, our findings strongly support a disruptive effect of this mutation on KK-20 binding. In addition to reducing the effect of KK-20 on tail current deactivation at 50 μM (though not the maximal effect at 200 μM) and increasing its EC_{50}, the F1446I mutation reducing KK-20's binding affinity for the channel by simultaneously slowing its on-rate and hastening its off-rate. We consider it likely that F1446 participates in coordinating KK-20 binding, just as the analogous isoleucine binds DHP agonists and antagonists in Ca_V1 channels. The left-shift in voltage-dependence of activation and slowing of control deactivation that we observed in the F1446I

mutant are consistent with the mutation favoring the open state of the channel, which implies that the wild-type residue could play a role in pore stability, in which case it could be through this mechanism that KK-20 binding to F1446 stabilizes the open state.

Our results for F1453M were less consistent. F1453M had a larger effect than any other evaluated mutant on normalized tail integral, slow fitting weight at 5 μM, and EC_{50}. Nevertheless, compared to its effect on EC_{50}, its K_D was only moderately increased over wild-type; in fact, it was the only mutant we evaluated in which K_D was greatly dissimilar to EC_{50}.

As with F1446, one explanation for the reduced potency of KK-20 for the F1453M mutant could be that F1453 participates in KK-20 binding. However, the involvement of F1453 in "pinching" the III/IV fenestration (see Chapter 3) raises another possibility: that the F1453M mutation may instead reduce KK-20's potency by making it more difficult (but not impossible) for the drug to pass through the closed-state III/IV fenestration and access a binding site within the central cavity. (The candidate binding residue F1446, for example, would be accessible from within the cavity; see Figure 38.) If this is true, it could explain why we observed little change in K_D. In the context of the state-dependent fenestration access hypothesis, k_{on} and k_{off} represent the rates of binding and unbinding of KK-20 molecules that have already entered the channel via the fenestration. If the F1453M mutation impedes KK-20 movement through the III/IV fenestration, while the actual binding site lies beyond this fenestration in the central cavity, then this mutation would theoretically cause fewer KK-20 molecules to be available to binding sites at any given concentration (hence the large EC_{50} we observed compared to wild-type), while the rates of binding and unbinding for molecules that *are* in the vicinity of a binding site would be unchanged (hence our observation that there was little effect of the mutation on K_D). In this interpretation, the increased k_{off} we observed in the F1453M mutant could be due to an allosteric effect of the

F1453M mutation on a binding site in the central cavity. As an initial test of the plausibility of this hypothesis, the same *in silico* approach used in Chapter 3 to predict a high energy barrier to drug movement through the open-state III/IV fenestration could be used to predict whether or not the F1453M mutation could impede drug movement through this fenestration.

The recent publication of a cryo-EM structure of the inactivated $Ca_V2.2$ channel (activated VSDs, closed pore) provided new context for our speculation on F1453's role in KK-20 action. In our homology models of $Ca_V2.1$ based on a Ca_V1 structural template, F1453 is oriented into the III/IV fenestration in both the open and closed pore. In this orientation, F1453 is accessible to KK-20 entering the fenestration from within the PM. However, in the $Ca_V2.2$ cryo-EM structure—which revealed unique characteristics of the Ca_V2 inner pore structure that were not replicated in our homology model—F1453 is oriented away from the fenestration (Figure 42). Some possible interpretations include: 1., F1453 does not participate in binding, and the mutation's effects on our measures of KK-20 binding and action are allosteric; 2., F1453 reorients into the fenestration as part of the process of KK-20 docking in the binding pocket; 3., F1453 rotates into the fenestration when the pore opens and is only then available to interact with the drug and/or participate in narrowing the fenestration, hence the state-dependence of KK-20 binding and/or access to the binding site.

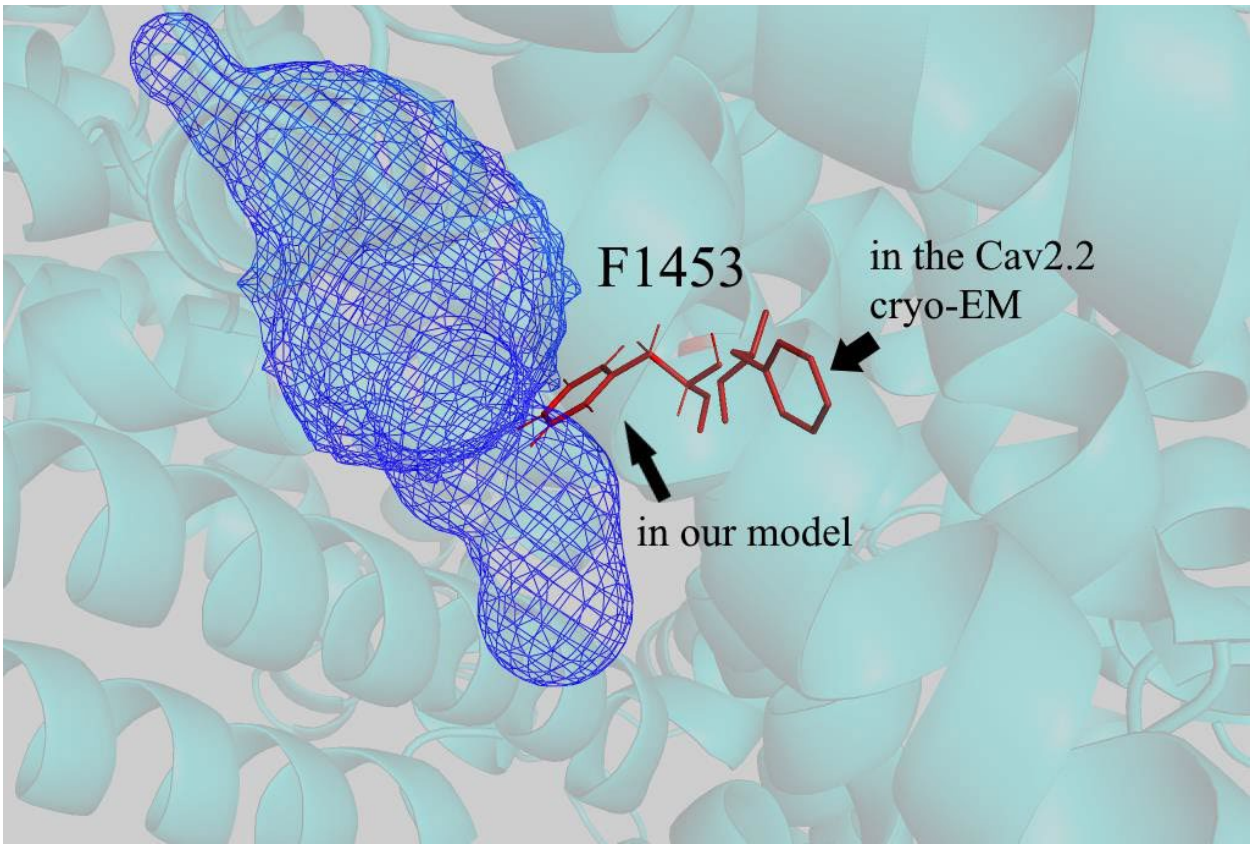

Figure 42: The orientation of F1453 differs between our homology model of inactivated $Ca_V2.1$ and a cryo-EM structure of inactivated $Ca_V2.2$.

View of the III/IV fenestration in our inactivated state $Ca_V2.1$ homology model (blue mesh), calculated using CAVER 3.0 as described in Chapter 3. The positions of the F1453 residue in $Ca_V2.1$ and the analogous residue in the $Ca_V2.2$ cryo-EM structure (Gao et al., 2021) are shown in stick form (red) against the inactivated $Ca_V2.1$ homology model backbone (cyan). F1453 orients into the fenestration in our homology model, but away from it in the cryo-EM structure.

Future experiments may clarify whether KK-20 interacts directly with F1446I and/or F1453M. One method that is commonly used to identify interactions between specific residues of peptide ligands and their protein targets is double mutant cycle analysis (Horovitz et al., 1996). In this approach, single residues are mutated in the ligand and target, and binding energies are calculated for the wild-type ligand/wild-type target, wild-type ligand/mutant target, mutant ligand/wild-type target, and mutant ligand/mutant target interactions. The results can be used to calculate coupling energies for the two residues, which can be used to derive the minimum distance

between them and potentially confirm a direct interaction (Naider et al., 2007). It should be possible to achieve a similar result by varying $Ca_V2.1$ residues and *(R)*-roscovitine analogue side groups, if two analogues can be identified whose action in $Ca_V2.1$ channels is differentially affected by the F1446I and/or F1453M mutations. We elaborate on this proposed approach in Chapter 6.

4.4.4 The effect of the L1460F mutation may be due to a role of L1460 in coupling VSD movement to pore closure and stabilizing the closed pore

We found that the L1460F mutation significantly reduced KK-20-mediated slowing of deactivation, but had little effect on KK-20's potency. Mutating a KK-20 binding residue would be expected to have a large negative effect on potency, like we observed in F1446I and F1453M; therefore, we consider it unlikely that L1460 participates in binding. In that case, the L1460F mutation must interfere with the mechanism by which KK-20 prolongs the open state in some other way.

One possibility is that L1460 is involved in KK-20's mechanism of action through a role in stabilizing the closed state of the channel pore. Hydrophobic interactions between residues on neighboring S6 segments, and between these hydrophobic residues and the "GAGA ring" residues (e.g., the A1459 residue sequentially adjacent to L1460), have been proposed to function as "adhesion points" that stabilize the close packing of S6 helices in the closed pore. Interestingly, L1460 (or more specifically, the leucine at the analogous position in $Ca_V2.3$) is hypothesized to participate in such an interaction (Hering et al., 2008).

KK-20's mechanism of action may involve an allosteric disruption of L1460's adhesion point interactions, which would make the transition into the closed state less energetically

favorable. In this case, one explanation for L1460F's effects on KK-20 action might be that this mutation itself disrupts the adhesion point interactions, precluding any further effect of KK-20. A counterpoint to this hypothesis is that mutation effects on measures of pore stability correlate to the change in hydrophobicity, and we substituted L1460 with a phenylalanine, which has very similar hydrophobicity to leucine at pH 7 (Monera et al., 1995); also, we observed no slowing of control deactivation in this mutant, and the L1460F mutation right-shifted voltage-dependence of activation, rather than left-shifting it as would be expected if this mutation impaired closed-state stability. This is not unexpected, given that the residue at the analogous position in wild-type Ca_V1 channels is also a phenylalanine (as a reminder, the single-residue mutations we evaluated in the above experiments, including L1460F, were mutations of $Ca_V2.1$ residues to their analogous Ca_V1 residues). It would be surprising if the residue at a critical position for regulating channel gating were dysfunctional in Ca_V1 channels; if 1460 *is* a key gating position, we would expect the Ca_V2 leucine and the Ca_V1 phenylalanine to fulfill similar roles. Therefore, a more compelling interpretation is that the phenylalanine mutation makes 1460's adhesion point interactions resilient to disruption by KK-20. In Chapter 5, below, we evaluate one possible closed-state stabilizing interaction involving L1460 that we hypothesized might be related to KK-20's mechanism of action.

L1460's possible involvement in the domain III adhesion point also suggests a way in which an allosteric interaction of KK-20 with this residue could mediated slowing of pore closure *and* voltage sensor deactivation. There is evidence in $Ca_V2.3$ channels that the domain II residue analogous to L1460 (an isoleucine, I714 in $Ca_V2.1$, that is highly conserved between VGCC subtypes) plays a role in electromechanical coupling between the VSD and pore. It was found that glycine substitution of either this isoleucine, or of a leucine in the IIS4-5 linker that is also

conserved, had effects consistent with stabilization of the open state or destabilization of the closed state (left-shifted voltage-dependence of activation and slowed deactivation compared to the wild-type channel). Furthermore, a double mutant cycle analysis showed that these two residues are energetically coupled, suggesting a role of an interaction between I714 and the IIS4-5 linker leucine in mediating pore opening/closure in response to S4 movement.

We speculate that in domain III, L1460 may play a similar role in VSD/pore coupling to I714's role in domain II. If this is correct, then the Ca_V1 phenylalanine analogous to L1460 likely fulfills the same VSD/pore coupling function, since a disruptive mutation to a critical gating residue would likely not have been tolerated by natural selection (although, hypothetically, the slight right-shifting of voltage-dependence of activation we observed in L1460F could reflect a role of the Ca_V1 phenylalanine vs the Ca_V2 leucine in regulating the distinct gating characteristics of these VGCC subtypes). It is possible that KK-20 binding has an allosteric effect on L1460 that slows voltage sensor deactivation and pore closure, and that the L1460F mutation preserves largely wild-type-like control gating characteristics but is less sensitive/insensitive to allosteric modification by KK-20. A series of planned experiments to investigate this hypothesis are described in Chapter 6, and an investigation into a possible role of the I714 residue itself in KK-20 action is described in Chapter 5.

4.4.5 The M1753I mutation is the sole domain IV residue that we identified as having a potential role in KK-20 action

We found that the M1753I mutation in IVS6 resulted in reduced slowing of deactivation by KK-20, yet slightly increased KK-20's potency and binding on-rate. Conversely, mutating the nearby residues F1747 and S1750, which are in close proximity to M1753 in our open-state $Ca_V2.1$

homology model, had no effect on KK-20 action. These effects on KK-20 binding and action therefore appear to be specific to the M1753I mutation, rather than just any perturbation in the lower third of IVS6.

Although the Ca_V2 domain III has been found to be both necessary and sufficient for *(R)*-roscovitine to slow deactivation (Yarotskyy et al., 2012)(see Chapter 2), suggesting that domain III contains the binding site, the apparent involvement of a domain IV residue is not surprising. Since the fenestration within or beyond which we believe KK-20 binds is located at the interface of domains III and IV, the bound drug would be in close proximity to domain IV inner pore residues (see Figure 27), which might participate in coordinating its binding. This would be consistent with a model in which KK-20 occupies a site analogous to the Ca_V1 DHP binding site, which contains residues from domains III and IV (Gao and Yan, 2021; Hockerman et al., 1997). Alternatively, since mutations in one S6 segment can cause helical unwinding and other distortions in neighboring segments, it is also possible that the M1753I mutation simply disrupts KK-20 binding by distorting the IIIS6 helix.

Given that cooperative interactions between inner pore residues from different segments and domains are important in stabilizing pore closure (Hering et al., 2018), another possibility is that M1753 plays a role in the drug's mechanism of action regardless of whether or not it directly participates in binding. For example, the wild-type methionine at this position might stabilize the drug-bound open pore conformation, or the drug might prolong the open state by disrupting a closed-state-stabilizing interaction between M1753 and a domain III binding residue. A mechanistic role of M1753 would be consistent with our finding that KK-20-modified tail current decay is not slowed as much in the M1753I mutant as in the wild-type channel. This could also explain why in chimeric channels made up of Ca_V1 and Ca_V2 domains, domain III alone is both

necessary and sufficient for *(R)*-roscovitine action, yet the drug does not slow deactivation as much in channels containing only the Ca_V2 domain III as it does in channels that also contain the Ca_V2 domain IV (Yarotskyy et al., 2012).

The findings that the M1753I mutation slightly *increased* KK-20's potency and binding affinity were unexpected. One possible explanation is that M1753 is a KK-20 binding residue, and an isoleucine at this position increases the binding site's affinity for the drug. Another is that the M1753I mutation has an allosteric effect on the conformation of the binding site, which results in increased affinity for KK-20. However, as the effects were small, it remains ambiguous whether the M1753I mutation affects the KK-20 binding site, directly or otherwise.

4.4.6 Conclusion

We found effects of several inner pore mutations within the $Ca_V2.1$ voltage-gated calcium channel domain III/IV fenestration on the action of the *(R)*-roscovitine analog KK-20, which slows deactivation in the Ca_V2 family of VGCCs. These findings support our hypothesis that *(R)*-roscovitine and its analogs access the channel by entering this fenestration from the plasma membrane. Residues at these positions are involved in endogenous pore gating mechanisms (Hering et al., 2018) and in binding other modifiers of VGCC gating kinetics (Gao and Yan, 2021); therefore, KK-20 binding in this part of the channel also makes sense from a mechanistic perspective. Of the mutations that reduced KK-20's efficacy at slowing channel deactivation, two substantially also affected the drug's potency, and one of these also increased KK-20's K_D, implying reduced binding affinity for the channel.

The relationship between mutation effects on control channel gating properties and drug action should be clarified in future experiments. Furthermore, mutant cycle analysis experiments

using single-mutant channels and different analogs of *(R)*-roscovitine may confirm direct interactions between this class of Ca_V2 modifiers and candidate binding residues. A similar approach has previously been used to characterize interactions between side chains of the drug mexiletine and residues in voltage-gated Na^+ channels (Desaphy et al., 2012).

5.0 The effects of mutations known to perturb Ca_V2 pore-gating mechanisms on control gating characteristics and KK-20 action

5.1 Introduction

In our mutagenesis experiments described in Chapter 4, we focused on residues that are different between the Ca_V1 and Ca_V2 families of VGCCs. This approach was optimal for our goal of identifying differences between these families that contribute to their differential sensitivity to *(R)*-roscovitine's effect of prolonging mean open time, while minimizing perturbation of control gating kinetics which might complicate our analysis of the drug effect.

However, the fact that Ca_V1 channels are insensitive to this effect of *(R)*-roscovitine and *(R)*-roscovitine-derived compounds does not mean that this class of drugs does not interact—directly or indirectly—with *any* residues that are shared between Ca_V1 and Ca_V2. Indeed, residues that are important to the intrinsic dynamics of the channel with which *(R)*-roscovitine interferes—the transition from the open to the closed pore, and the transition from the activated to the resting voltage sensors—are likely to be conserved across families, since mutations to functionally important residues are less likely to be tolerated by natural selection (Liu and Bahar, 2012). These conserved residues could be involved in *(R)*-roscovitine's mechanism of action, even if they are not sufficient on their own for Ca_V1 channel sensitivity to the drug.

If *(R)*-roscovitine analogs bind to S6 segments a short distance above the activation gate, as we strongly suspect based on our *in silico* predictions in Chapter 3 and our experimental findings in Chapter 4, it seems likely that they interact with existing gating mechanisms in this part of the channel. Experimental mutagenesis of conserved residues in the inner pore of VGCCs has shed

light on the machinery that contributes to pore closure and the coupling of VSD movement to pore conformation. Of particular interest are conserved sequence and structural motifs in the lower thirds of the S6 segments that may participate in hydrophobic helix-to-helix packing interactions that stabilize the closed state of the channel, in which the S6 helices converge into the pore to obstruct ion permeation (Hering et al., 2008; Hering et al., 2018). Mutations to these conserved residues—especially to less hydrophobic residues, like threonine or glycine—can have effects consistent with favoring of the open state over the closed state, including slowing of deactivation similar to what is caused by *(R)*-roscovitine and its analogs (Depil et al., 2011; Hohaus et al., 2005; Raybaud et al., 2007). These mutations are presumed to destabilize the closed state by disrupting the hydrophobic helix-packing interactions, increasing the energy barrier of the transition to the closed state and thereby delaying pore closure (Depil et al., 2011; Stary et al., 2008). Among the residues implicated in helix packing are the conserved glycines and alanines of the GAGA ring (Depil et al., 2011) that have also been found to be energetically coupled with the domain II VSD, suggesting that these residues may participate in the relationship between VSD deactivation and pore closure (Beyl et al., 2012).

Evidence points to a model of *(R)*-roscovitine action in which it does not physically "hold open" the pore, but instead stabilizes the channel in an open state from which exit is slow (Buraei et al., 2005; Yarotskyy and Elmslie, 2009). One possible interpretation is that *(R)*-roscovitine binding causes conformational changes that disrupt the closed-state-stabilizing helix-packing interactions, which would have the effect of favoring the open state. This would be consistent with the drug's apparent binding site at the interface of the lower thirds of IIIS6 and IVS6, in close proximity to closed-state-stabilizing residues.

To investigate this possibility, we mutated residues in these conserved S6 motifs to threonine and evaluated the effects of these mutations on the action of the *(R)*-roscovitine analog KK-20. In the same vein, we used our homology models of open and inactivated (closed-pore) $Ca_V2.1$ to predict a possible closed-state-stabilizing interaction involving L1460F (which our Chapter 4 results suggest is involved in KK-20's mechanism of action), and we used a double mutant cycle analysis to test the hypothesis that KK-20 slows deactivation in part by disrupting this interaction.

In addition, we followed up on our Chapter 3 finding that the I1461V mutation slightly but significantly increased the size of both control and KK-20-modified tail current integrals. We found that mutating I1461 to a phenylalanine dramatically enhanced KK-20-mediated slowing of deactivation.

5.2 Methods

5.2.1 Site-directed mutagenesis

Site-directed mutagenesis of the $Ca_V2.1$ α1 subunit was performed as described in 4.2.2. Briefly, mutations were introduced via whole-plasmid PCR using primers containing the desired mutations.

5.2.2 Whole-cell perforated patch clamp electrophysiology

Transfection and patch clamp of wild-type and mutant $Ca_V2.1$ α1 channels was performed as described in section 4.2.3, using the Ca_V subunit and GFP plasmids described in section 4.2.1.

To evaluate the effect of KK-20 on wild-type and mutant channels, a 100ms depolarizing step from a holding potential of -100mV to +60mV was used to activate channels, followed by repolarization to -60mV. KK-20 was applied at either 5 μM or 50 μM. In the 50 μM experiments, tail current integrals of the last sweep before KK-20 application and the first sweep at which the drug effect had reached equilibrium were normalized to their peaks, and drug effect was measured as the drug-mediated fold increase in the normalized integral. In the 5 μM experiments, tail current decay curves during KK-20 application (the first sweep at which the drug effect had reached equilibrium) were fit to a double exponential using Clampfit 10.7's weighted exponential function, and the proportion of current modified by the drug was calculated as the fitting weight of the slow component of deactivation.

To measure the effects of the mutations on the voltage of half-maximal activation (VD_{50}), current-voltage relationship, and speed of activation, currents were activated with a 100ms depolarizing step ranging from -40 mV to +150 mV, incrementing by +10mV per sweep (see Figure 27C). Tail current peak amplitudes were normalized to the largest amplitude recorded in the same cell to calculate fractional activation at each potential. Fractional activation vs voltage curves were fit to a Boltzmann sigmoidal function in Prism to calculate the VD_{50}. Currents during the depolarizing step were normalized to the largest amplitude recorded in the same cell and plotted against voltage.

To measure the effects of mutations on voltage-dependence of deactivation, currents were activated with a +60mV, 100ms step and the membrane was then repolarized to potentials ranging

from -80 mV to -30 mV, incrementing by +10mV per sweep. Tail current decay at each repolarization potential was fit to a single exponential to capture kinetics of decay that comprised the majority of the tail current repolarization.

5.2.3 Analysis of electrophysiological recordings

Electrophysiological recordings were analyzed using Clampfit 10.7 (pCLAMP) as described in section 4.2.4.

Drug effect was measured by calculating the fold change in the normalized tail current integral following application of 5 or 50 μM KK-20.

The fraction of open channels affected by the drug at the end of the depolarizing step was measured by calculating the fitting weight of the drug-modified tail current as described in 4.2.4. The proportion of the total decay accounted for by the slow component—the slow fitting weight—was interpreted as representing the slow closure of drug-modified channels (Buraei et al., 2005).

Data were statistically analyzed using Prism v.9. Outliers were detected and removed from analysis using Prism's ROUT method (Motulsky and Brown, 2006) with the maximum desired false discovery rate Q set to its default value of 1%. Statistical significance of differences between variables was analyzed in Prism v.9 by one-way Brown-Forsythe and Welch analysis of variance (ANOVA) with Dunnett's T3 multiple comparison post hoc analysis, or with an unpaired t test with Welch's correction for comparisons between only two groups.

5.2.4 Preparation of figures

Structural images were prepared using the PyMOL Molecular Graphics System (PyMOL, Version 2.0 Schrödinger, LLC). Data plots were prepared Prism version 9.2.0 for Windows (GraphPad Software, San Diego, California USA, www.graphpad.com).

5.3 Results

5.3.1 Selection of single threonine mutations in S6 segments to evaluate for effects on KK-20 action

To investigate possible mechanisms of KK-20-mediated slowing of deactivation, we measured the effects of the mutations I714T, A715T, A1459T, and V1758T on KK-20 action.

A1459 was among the residues we mutated to its Ca_V1 counterpart in our experiments in Chapter 4. The A1459G mutation did not significantly affect KK-20 action, so our experimental results appear to suggest it is not involved in the binding site or mechanistic pathway. However, as we have discussed, A1459 is part of a conserved structural motif of glycines and alanines, one in each domain's S6 segment and positioned near the activation gate, that have been implicated in closed-pore stabilization and VSD/pore coupling at "adhesion points" near the inner mouth of the pore (Beyl et al., 2012; Depil et al., 2011; Hering et al., 2008). When the glycine or alanine at each of these four positions was mutated to several different residues in $Ca_V1.2$ channels, most of the mutations had effects consistent with stabilization of the open state and/or destabilization of the closed state: a left-shift in the voltage-dependence of activation and slowed deactivation kinetics

(Depil et al., 2011). Homology modeling of a closed state of $Ca_V1.2$ showed that these residues were positioned at the interfaces of neighboring S6 helices and were surrounded by bulky hydrophobic residues, leading the authors to speculate that their small size allows them to participate in tight-fitting interactions with neighboring bulky hydrophobic residues that stabilize the close packing of S6 helices in the closed pore (Depil et al., 2011). Substituting these glycines or alanines with larger residues disrupts the helix packing, which destabilizes the closed state so that the channel more readily opens (hence the left-shift in voltage-dependence of activation) and remains open for longer due to the increased energy barrier of the closed-state transition (hence the slowed deactivation).

This glycine-and-alanine motif was termed the "GAGA ring" because in $Ca_V1.2$, where it was discovered (Depil et al., 2011), the residues are arranged in that order—glycines in domains I and III, and alanines in domains II and IV. The analogous domain III position in Ca_V2 channels is an alanine (making this motif the "GAAA ring" in Ca_V2s), but since a glycine-to-alanine mutation at this position in $Ca_V1.2$ did not appear to disrupt closed-state stability (the I-V curve midpoint was right-shifted slightly from -18.4 mV in wild-type to -12.1 mV in the alanine mutant, while mutating the same glycine to other residues left-shifted the midpoint to values ranging from -33.6 mV in the methionine mutant to -49.8 mV in the threonine mutant (Depil et al., 2011)), it is likely that either glycine or alanine is capable of participating in the helix-packing interactions.

It was later found that the GAGA ring residues are all energetically coupled to at least one voltage sensor, IIS4. Neutralizing all of the gating charges in this voltage sensor rescued any of the GAGA mutations' closed-state-destabilizing effects on voltage-dependence of activation and deactivation kinetics, but did not rescue the similar effects of mutations to nearby residues (Beyl et al., 2012). Beyl et al. (2012) did not evaluate potential coupling between the GAGA residues

and the other three voltage sensors because neutralizing any voltage sensor other than IIS6 resulted in a nonfunctional channel. The authors favored a "cooperative gating" interpretation of this finding, in which (for example) IIS4 interacts directly with IIS6, which is cooperatively linked with the rest of the pore domain and can therefore stabilize the closed-pore conformation for all four S6 segments in response to IIS4 deactivation (Figure 43). As we discussed in Chapter 2, *(R)*-roscovitine delays not only pore closure, but the return of the voltage sensors to their resting positions; in fact, pore closure and voltage sensor deactivation have a nearly identical time-course in *(R)*-roscovitine-modified channels, implying that both events are rate-limited by the channel's exit from the modified high P_o open state (Yarotskyy and Elmslie, 2009). Given that A1459 is in close proximity to candidate *(R)*-roscovitine analog binding residues and that it is both involved in closed-pore stabilization and energetically coupled to at least one voltage sensor, we hypothesized that *(R)*-roscovitine analogs might be able to disrupt both pore closure and voltage sensor deactivation through a mechanistic pathway involving this residue. If the cooperative gating model is correct, an effect of drug binding on A1459 could potentially affect all four voltage sensors via cooperative interactions with GAAA residues in other S6 segments.

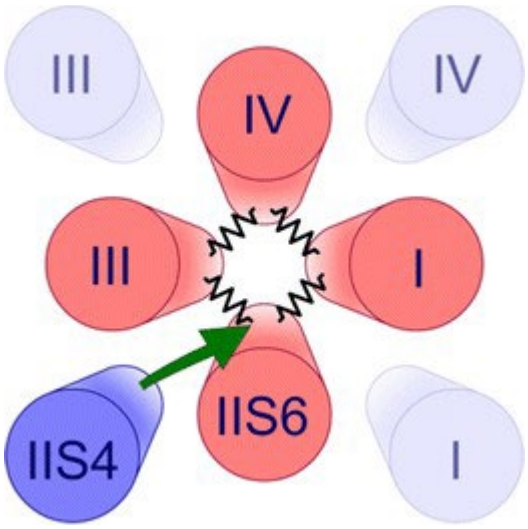

Figure 43: The cooperative pore gating model.

Diagram of a gating scheme in which a voltage sensor interacts with the S6 segment in the same domain, which facilitates closed-state formation by the entire pore domain via interactions between the S6 segments. From (Beyl et al., 2012), open access (https://creativecommons.org/licenses/by/2.0).

We considered that if KK-20 slows pore closure (in whole or, more likely, in part) by disrupting A1459's tight-fitting interactions with surrounding hydrophobic residues, it would probably affect our A1459G mutant in the same way, in which case this mutation would not substantially interfere with its effect on deactivation. This could mean that we overlooked a role of A1459 in KK-20 action in our Ca_V2->Ca_V1 mutagenesis experiments. However, if these closed-state-stabilizing interactions were *already* disrupted by an A1459T mutation (as was apparently the case for the $Ca_V1.2$ IIIS6 glycine-to-threonine mutant evaluated by Depil et al. (2011)), we would expect that to pre-empt their disruption by KK-20. In that case, we would expect to see both slowed control deactivation and a reduced effect of KK-20 in the A1459T mutant.

Among the hydrophobic residues implicated in closed-pore-stabilizing interactions at adhesion points are those found in the "LAIA" sequence motif in the lower third of IIS6 (Hohaus et al., 2005) and in the "VAVIM" sequence motif at the analogous position in IVS6 (Raybaud et

al., 2007). LAIA and VAVIM are conserved across all of the VGCC subtypes, and each contributes an alanine to the "GAAA ring" motif (the first alanine in LAIA, and the single alanine in VAVIM).

In $Ca_V1.2$, substituting any of the residues in LAIA with a proline—especially the isoleucine, which corresponds to I714 in our $Ca_V2.1$ sequence—was found to dramatically left-shift voltage-dependence of activation, and mutating the I714-analogous residue to either proline or threonine was shown to additionally slow tail current deactivation, indicating that these mutations favor the open state (Hohaus et al., 2005). The extent to which mutating the I714-analogous isoleucine favors the open state is not related to the substituted residue's mass or van der Waals volume, but does correlate with the negative change in hydrophobicity: the less hydrophobic the substituted residue in comparison to isoleucine, the more the mutation left-shifts voltage-dependence of activation (Hering et al., 2008). This finding is consistent with the interpretation that mutating this residue disrupts its closed-state-stabilizing hydrophobic interactions with nearby residues.

As we discussed in Chapter 4, the analogous residue to I714 in $Ca_V2.3$ channels has also been shown to be energetically coupled with a conserved leucine in the IIS4-5 linker, which itself has been shown to play a role in closed-state-stabilization (singly mutating it to glycine left-shifts voltage-dependence of deactivation and slows deactivation, like the I714T mutation does), suggesting a role of I714 in electromechanical coupling between the S4 voltage sensor and S6 via the S4-5 linker (Wall-Lacelle et al., 2011). This would be consistent with I714 being among the hydrophobic residues proposed to tightly pack with GAGA/GAAA ring residues to stabilize the closed pore in response to voltage sensor deactivation (Beyl et al., 2012; Depil et al., 2011).

In VAVIM, glycine mutations to different residues varied in their effects on gating; mutating the first valine (corresponding to V1758 in our $Ca_V2.1$ sequence) had little effect,

mutating either the alanine or second valine favored the open over the closed state, and mutating the isoleucine or methionine favored the closed over the open state (Raybaud et al., 2007).

As discussed in Chapter 4, residues in the LAIA and VAVIM motifs are at the analogous positions to several of the IIIS6 residues we evaluated for a possible role in KK-20 action, including A1459 (the domain III GAAA ring residue discussed above), L1460 (whose mutation to phenylalanine reduced KK-20's efficacy, but not its potency), and I1461 (whose mutation to valine significantly slowed deactivation kinetics in KK-20-modified currents, despite not significantly affecting our primary measure of drug effect, the fold change in the normalized tail current integral). Homology modeling of a $Ca_V2.3$ channel by Hering et al. (2008) predicted hydrophobic interactions between LAIA and VAVIM residues and analogous residues in IIIS6, which the authors hypothesize to participate in stabilizing the closed state. For example (converting the residue numbering in $Ca_V2.3$ to the numbering of the analogous residues in our $Ca_V2.1$ sequence), they predict closed-state-stabilizing interactions between I714 in the IIS6 LAIA motif and V1458 in IIIS6, and between L1460 in IIIS6 and V1758 in the IVS6 VAVIM motif. This suggests a mechanism by which KK-20 binding to residues in the lower third of IIIS6 could favor the open state through allosteric interactions with conserved residues in the LAIA and VAVIM motifs that regulate gating.

If *(R)*-roscovitine analogs do favor the open state by interacting with LAIA or VAVIM residues, that would be consistent with their effect of slowing channel deactivation. It would also be consistent with the slight but consistent left-shift in voltage-dependence of activation Buraei et al. (2005) observed in the presence of a high (100 μM) concentration of *(R)*-roscovitine (although Yan et al. (2002) found no shift in voltage-dependence of activation in the presence of a 50 μM *(R)*-roscovitine).

In order to investigate the hypothesis that KK-20's mechanism for prolonging channel opening relies on interactions between the drug and LAIA or VAVIM residues, we mutated the LAIA residues I714 and A715, and the VAVIM residue V1758, to threonine. As with the A1459T mutation, we expected that if KK-20 slows deactivation (in whole or in part) by disrupting one of these residues' participation in closed-state-stabilizing hydrophobic interactions, then we would see slowed control deactivation and a reduced KK-20 effect in the corresponding mutant.

5.3.2 Single threonine mutations of residues implicated in VGCC closed-state stabilization and VSD/pore coupling: effects on control gating characteristics

As we expected given the effects of mutating the analogous residues in $Ca_V1.2$ channels (Beyl et al., 2012; Depil et al., 2011; Hering et al., 2008; Hohaus et al., 2005), our I714T, A715T, and A1459T mutations left-shifted both the current-voltage relationship and the voltage-dependence of activation of $Ca_V2.1$ channels (Figure 44). This result is consistent with the interpretation that introducing polar residues at these positions disrupts closed-state-stabilizing mechanisms that rely on hydrophobic contacts. The voltage of half-maximal activation, VD_{50} (calculated from a fractional activation vs voltage plot derived from tail current amplitudes at each step, as in Chapter 4), was 2.32 mV in wild-type $Ca_V2.1$, -7.11 mV in A715T, and -20.1 mV in A1459T. VD_{50} could not be calculated for I714T because the fractional activation vs. voltage curve was shifted so far to the left that a Boltzmann sigmoidal could not be effectively fit over the range of voltages we examined. Plotting the peak amplitudes of current during the depolarizing steps showed that the current reversed between 50 and 60 mV in all wild-type and mutant channels, so the mutations do not appear to affect the channel's ion selectivity, as was previously reported by Hohaus et al. (2005) for the $Ca_V1.2$ mutation analogous to I714T.

Surprisingly, the V1758T mutation right-shifted the current-voltage relationship and voltage-dependence of activation (VD_{50} = 9.02 mV), suggesting that this mutation favors the closed state. Raybaud et al. (2007) found that a glycine mutation at the same position in $Ca_V2.3$ did not affect voltage-dependence of activation. However, they also found that mutating the isoleucine and methionine residues in the VAVIM motif to glycine had effects consistent with favoring the closed state, which supports the interpretation that conserved hydrophobic residues in the inner pore can contribute to open-state stability. One possibility is that, contrary to what Hering et al. (2008) predicted based on their $Ca_V2.3$ homology model, V1758 in fact participates in hydrophobic interactions with neighboring segments that stabilize the open-state positions of the S6 helices (in which case it would be unclear whether this function of V1758 is conserved across VGCC subtypes or is unique to $Ca_V2.1$). This finding is inconsistent with our hypothesis that KK-20 slows deactivation by disrupting V1758's ability to participate in closed-state-stabilizing hydrophobic interactions, although it does not, in and of itself, rule out involvement of this residue in KK-20's mechanistic pathway. For example, KK-20 binding could cause a conformational change that strengthens V1758's stabilizing hydrophobic contacts in the open state.

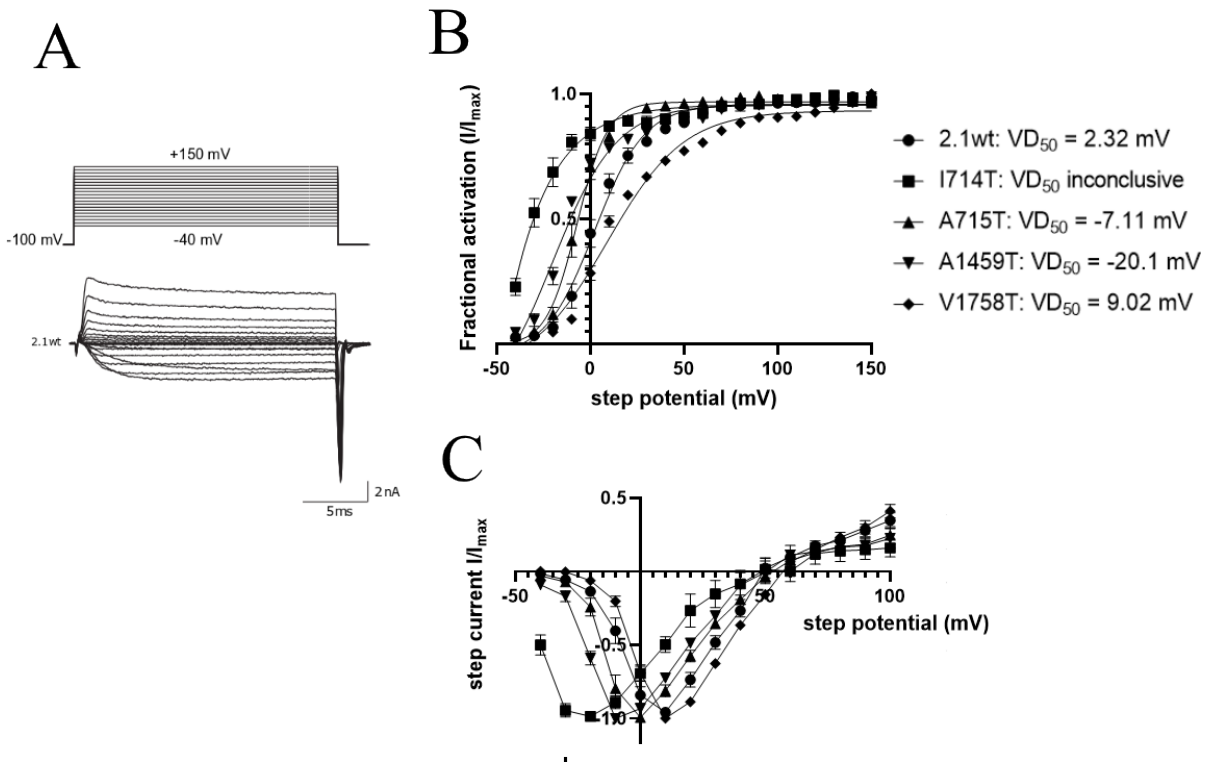

Figure 44: Effects of the threonine mutations on voltage-dependence of activation and the current-voltage relationship.

A. Representative currents in a cell expressing wild-type $Ca_V2.1$ channels, as also shown in Figure 35A. 20ms depolarizing steps ranging from -40 mV to +150 mV, in 10 mV increments, were applied to activate currents. Peak tail current amplitudes were measured at the end of each step and normalized to the largest amplitude in the same cell to calculate I/I_{max}. **B.** Fractional activation vs depolarizing step voltage plots for the wild-type $Ca_V2.1$ channel and the mutantsI714T, A715T, A1459T, and V1758T. Each plot was fit to a Boltzmann sigmoidal equation to calculate VD_{50}. I714T, A715T, and A1459T left-shift voltage-dependence of activation, while V1758T right-shifts it. **C.** The peak amplitude of current evoked during the depolarizing step normalized to the largest negative current within a cell and plotted against the depolarizing step voltage. For the wild-type and all mutant channels, current reverses from 50-60mV. Error bars represent SEM. 2.1wt N = 8; I714T N = 5; A715 N = 6; A1459T N = 4; V1758T N = 8.

Effects of the mutations on deactivation kinetics (Figure 45) were consistent with their effects on voltage-dependence of activation and their corresponding hypothesized roles in open- vs closed-state stability. I714T and A715T greatly increased tau_{deact} at all evaluated voltages, while V1758T's deactivation kinetics were nearly indistinguishable from those of wild-type $Ca_V2.1$. Voltage-dependent deactivation kinetics were not measured for A1459T.

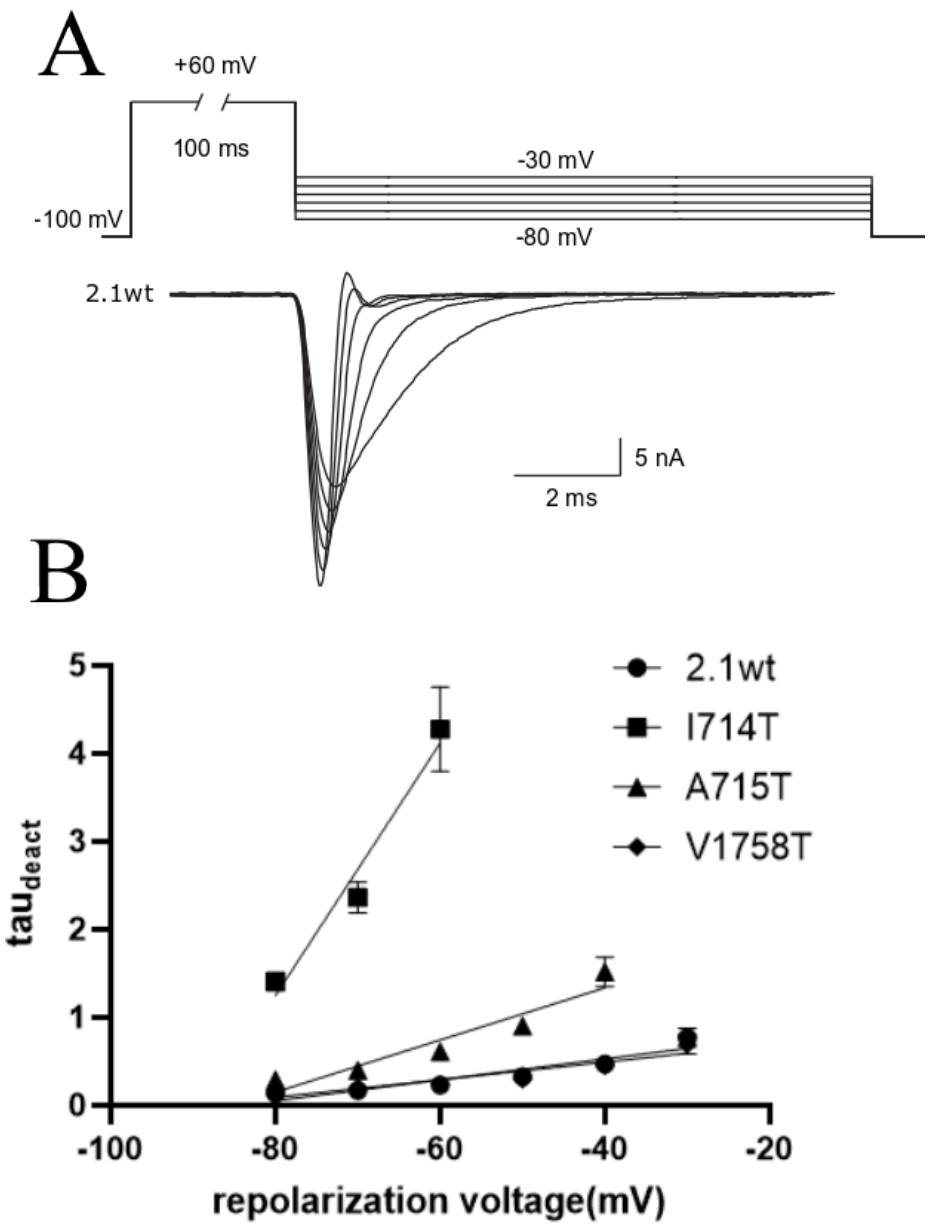

Figure 45: Effects of the threonine mutations on deactivation kinetics over a range of repolarization potentials.

A. Representative tail currents of wild-type $Ca_V2.1$, following a 100ms step to +60 mV and repolarization to voltages ranging from -80 mV to -30 mV, in +10 mV increments. The less hyperpolarized the repolarization voltage, the slower the current decays. **B.** The time course of tail current decay, tau_{deact}, at each repolarization voltage. Tail currents were fit to a single exponential to calculate tau_{deact}. Data are plotted for I714T and A715T only up to the -60 mV and -40 mV repolarization potentials, respectively, because current did not completely decay before the end of the repolarization step at less hyperpolarized potentials in these mutants. Data for each mutant are fit to a simple linear regression for visualization of the relative steepness of voltage-dependence of deactivation. Error bars represent SEM. 2.1wt N = 7; I714T N = 6; A715 N = 7; V1758T N = 7.

Interestingly, I714T and A715T also altered the deactivation kinetics to be more steeply voltage dependent than in wild-type $Ca_V2.1$. This effect was more pronounced in I714T, which had the most profound slowing effect on tau_{deact} of all three mutants, to the extent that its tail currents could not be fit at repolarization voltages above -60mV because they did not decay to baseline by the end of the repolarization step. This result was consistent with measurements of voltage-dependence of deactivation kinetics in the $Ca_V1.2$ mutant analogous to I714T (Hohaus et al., 2005). This could reflect an effect of the threonine mutations on the pore domain's sensitivity to voltage sensor deactivation. Alternatively, since I714 and A715 are structurally in close proximity to the loop connecting the S4-5 linker to S5, as shown in Figure 1 (Hering et al., 2018), it is possible that mutating them has both a closed-state-destabilizing effect on the pore domain and an allosteric effect on the local S4 segment that alters the voltage-dependence of its translocation from the activated to the resting position. Further investigation will be necessary to fully untangle how mutations in the LAIA and VAVIM motifs interact with the pore and voltage-sensing domains. For example, measuring gating currents directly would reveal whether or not these mutations affect the voltage-dependence of gating charge movement.

5.3.3 Single threonine mutations to residues implicated in VGCC closed-state stabilization and VSD/pore coupling: effects on KK-20-mediated slowing of deactivation

To evaluate the effects of the threonine mutations on KK-20's ability to slow deactivation, we measured the tail current integral before and during drug application, normalized each integral to the peak amplitude of the tail current, and calculated the KK-20-mediated fold change in the normalized integral (Figure 46).

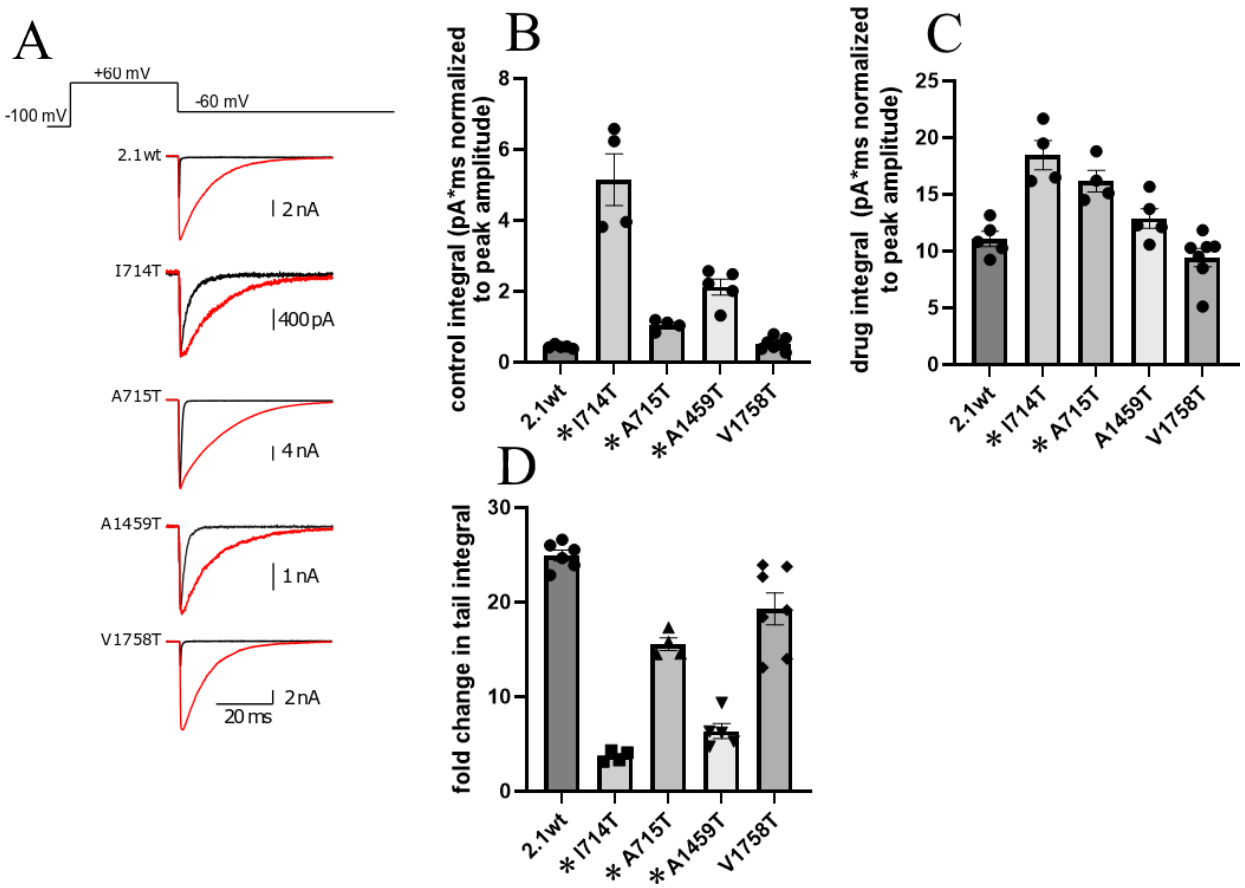

Figure 46: Effects of single threonine mutations on tail current integrals before and during application of 50 µM KK-20.

A. Representative tail currents before (black) and during (red) application of 50 µM KK-20 for the wild-type and a subset of mutant channels. The drug slows the decay of tail currents in all cases. The broader control currents in I714T, A715T, and A1459T compared to the wild-type channel are apparent. **B-D.** Comparison between wild-type and mutant channels of the control tail integral (B), the KK-20-modified tail integral (C), and the fold change in tail integral upon application of KK-20 (D). Mutations with significant effects (Brown-Forsythe and Welch one-way ANOVA with Dunnett's T3 multiple comparison post hoc analysis, $p < 0.05$) are marked with an asterisk. Bar height represents the mean value, and individual data points are shown. Error bars represent SEM.

The normalized tail integral prior to 50 µM KK-20 application (the control tail integral) was significantly increased compared to wild-type $Ca_V2.1$ (0.44 +/- 0.023) in the I714T (5.15 +/- 0.732, $p < 0.05$) and A715T (1.05 +/- 0.076, $p < 0.005$) mutants, consistent with their slowed deactivation kinetics, and it was also significantly increased in A1459T (2.12 +/- 0.224, $p < 0.01$). Normalized control tail integral was not significantly changed in V1758T (0.52 +/- 0.180).

The normalized tail integral during 50 μM KK-20 application (the drug tail integral) was significantly *larger* compared to wild-type (11.1 +/- 0.67, $p < 0.0001$) in the I714T (18.5 +/- 1.31, $p < 0.05$) and A715T (16.2 +/- 0.95, $p < 0.05$) mutants, and was not significantly changed in the A1459T (12.9 +/- 0.86) or V1758T (9.4 +/- 0.81) mutants.

The fold change in normalized tail integral following KK-20 application was significantly decreased compared to wild-type $Ca_V2.1$ (24.9 +/- 0.57) in the I714T (3.7 +/- 0.29, $p < 0.0001$), A715T (15.6 +/- 0.66, $p < 0.0001$), and A1459T (6.4 +/- 0.80, $p < 0.0001$) mutants, and was decreased, but not significantly, in V1758T (19.3 +/- 1.7).

We had hypothesized that mutating these conserved residues involved in gating would intrinsically disrupt hydrophobic interactions that would normally be disrupted by KK-20 binding in the wild-type channel, preventing KK-20 from further slowing deactivation by the same mechanism. In this case, we would expect to see larger control tail current integrals in the mutants and a reduced fold change in tail current integral upon KK-20 application, and this is in fact what we observed in the I714T, A715T, and A1459T mutants; but as with some of our mutations that slowed control deactivation in Chapter 4, it is ambiguous whether the reduced fold change reflects a real effect on drug action or is purely the result of the larger control integral.

To be clear, the fact that KK-20 was able to further slow deactivation in the mutant channels does not in itself mean that KK-20 binding and a given threonine mutation slow deactivation by wholly independent mechanisms. For example, KK-20 could favor the open state through the cumulative effects of disrupting multiple pairs of interacting hydrophobic residues, one or more of which are intrinsically disrupted by a given mutation, while the remainder remain available to be disrupted by KK-20 in the mutant channel. If we had observed a mutant with intrinsically slowed deactivation in which the KK-20-modified tail current integral was equal to

or smaller than the KK-20-modified tail current integral in wild-type, indicating the absence of any additive effect of the mutation and KK-20 on deactivation kinetics, that would strongly support the latter interpretation. However, although the fold change in the tail current integrals was smaller than in wild-type $Ca_V2.1$ for I714T, A715T, and A1459T, the absolute size of the KK-20-modified tail current integral was larger than in wild-type in all three cases (even if this effect was not significant in the case of A1459T). This means we cannot conclude with certainty that KK-20 "lost" a portion of its contribution to slowing deactivation to a mutation that intrinsically disrupts the same hydrophobic interaction(s) that it does. The mutation might slow deactivation without interfering with KK-20's mechanism of action at all, and KK-20 might simply further destabilize the closed state of the mutant channel to the same extent that it would in the wild-type channel in an additive manner, which could still result in a smaller fold change in tail current integral compared to wild-type due to the increased size of the mutant control integral.

Molecular dynamics simulations in homology models of wild-type and mutant $Ca_V1.2$ predict that the mutation analogous to I714T distorts not only the IIS6 segment on which it is located, but also the neighboring IIIS6 segment (Stary et al., 2008). This distortion resulted in the loss of at least one hydrophobic contact between a IIIS6 residue and a IIS6 residue other than the analogue to I714 (Stary et al., 2008). Therefore, it is likely that our highly structurally perturbing threonine mutations do not only disrupt the stabilizing hydrophobic interactions in which the mutated residues normally participate, but also allosterically disrupt stabilizing interactions between other pairs of hydrophobic residues. This could result in larger KK-20-modified tail current integrals in a mutant channel even if the drug and the mutation both target one or more of the same closed-state-stabilizing hydrophobic interactions, due to the mutation disrupting additional hydrophobic contacts that would be unaffected in KK-20-modified wild-type channel.

We may be seeing an additive effect of KK-20's disruption of one set of closed-state stabilizing mechanisms with the mutations' disruption of another set of closed-state-stabilizing mechanisms, and these two sets of mechanisms might or might not overlap. In either case, we would expect to observe what we did observe in $Ca_V2.1$ channels with the I714T or A715T mutation: slowing of both control and KK-20-modified deactivation in the mutant channels, compared to control and KK-20-modified deactivation in wild-type $Ca_V2.1$. Further investigation will be necessary to determine whether there is any shared component of the mechanistic effects of KK-20 and a given threonine mutation.

5.3.4 Single threonine mutations to residues implicated in VGCC closed-state stabilization: effects on KK-20 binding

Stary et al. (2008)'s prediction that threonine mutations in neighboring segments can distort the IIIS6 helix led us to consider that our mutations in IIS6 and IVS6 might allosterically alter the conformation of the KK-20 binding site, which we believe contains IIIS6 residues based on our findings described in Chapter 4. To check for any disruption of KK-20 binding by threonine mutations outside IIIS6, we evaluated the effects of the I714T, A715T, and V1758T mutations on the proportion of current modified by 5 μM KK-20 (Figure 47).

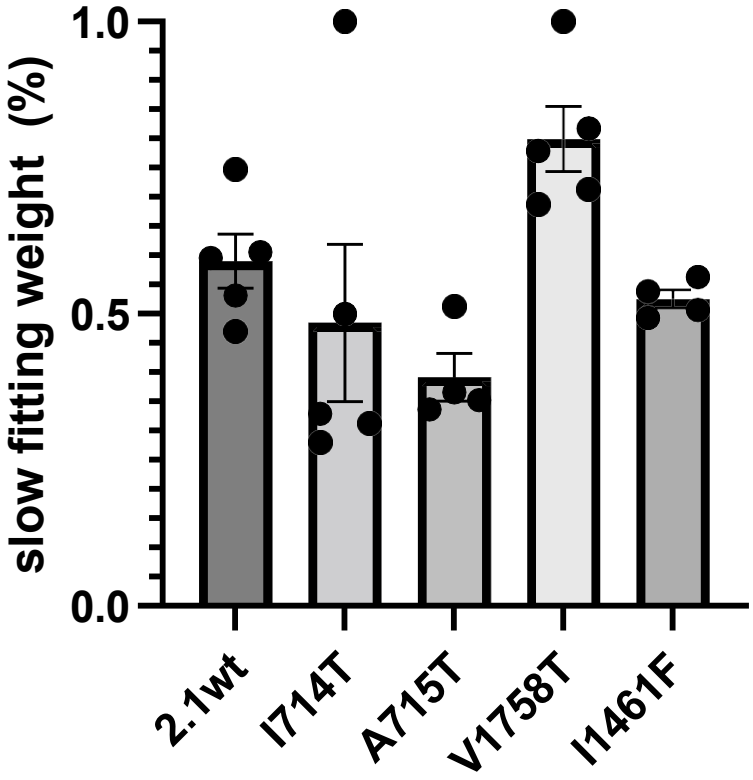

Figure 47: Effects of single-residue threonine mutations on the proportion of current modified by 5μM KK-20.

Comparison between wild-type and mutant channels of the amplitude of tail current decay fit to the slow component of a double weighted exponential in the presence of 5 μM KK-20, representing the proportion of activated channels modified by KK-20 at the end of the depolarizing step. None of the mutations had a significant effect on the slow fitting weight (Brown-Forsythe and Welch one-way ANOVA with Dunnett's T3 multiple comparison post hoc analysis, $p < 0.05$). Bar height represents the mean value, and individual data points are shown. Data points with a slow fitting weight of 1 indicate recordings in which 100% of the tail current decay was slowed by KK-20. Error bars represent SEM.

We found that the fitting weight of the slow (KK-20-modified) component of tail current decay was not significantly changed by any of the mutations, implying a lack of disruption of KK-20's binding site or fenestration access pathway. However, in the case of I714 this may be due to the effect of a single recording in which 100% of the tail current decay was slowed, as the slow fitting weights in other I714T recordings were consistently much smaller (~30-50% of tail current decay). Although GraphPad Prism v9's ROUT method (GraphPad Software) for outlier detection

did not identify this data point as an outlier, and we therefore did not remove it from the analysis, it may be prudent to calculate a full concentration-response curve in future experiments in order to determine whether there is an effect of I714T on KK-20's EC_{50}.

5.3.5 A double mutant cycle analysis of a hypothesized role of the hydrophobic residues L1460 and V1758 in KK-20 action

Hering et al. (2008) predicted a closed-state-stabilizing hydrophobic interaction between the $Ca_V2.3$ residues analogous to L1460 and V1758 in $Ca_V2.1$. This caught our attention because we had found (in our Chapter 4 experiments) that the mutation L1460F reduces KK-20-mediated slowing of deactivation in $Ca_V2.1$ channels without substantially changing its EC_{50}, implying a role of L1460 in KK-20's mechanism of action. Our homology models of $Ca_V2.1$ in open and inactivated states showed that these two residues are oriented away from each other in the open state, but rotate toward each other and come into close proximity as their respective S6 helices move into their closed-pore positions (Figure 48), which would be consistent with a hydrophobic interaction between these two residues stabilizing the closed pore. We hypothesized that KK-20 slows channel deactivation in part by causing a conformational change that disrupts this potential closed-state-stabilizing interaction between L1460 and V1758.

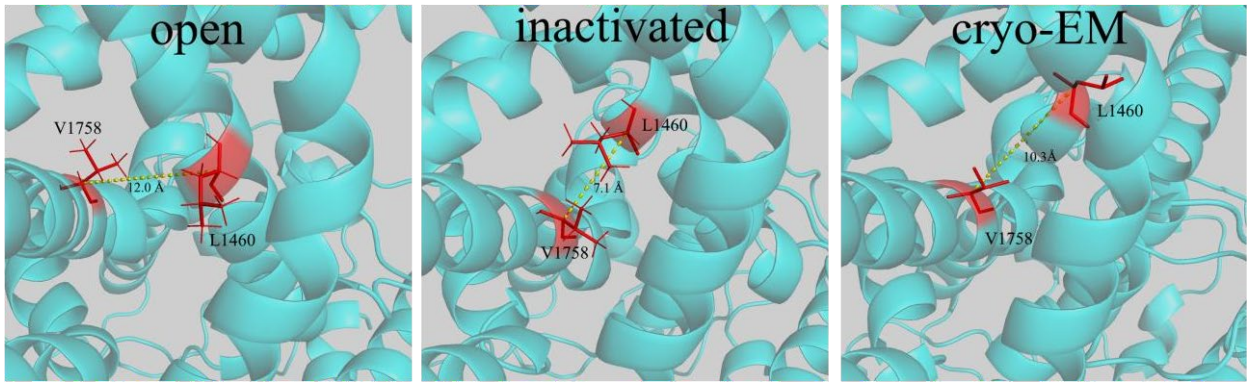

Figure 48: Our open and inactivated $Ca_V2.1$ homology models, but not a cryo-EM structure of inactivated $Ca_V2.2$, show a possible closed-state-stabilizing interaction of L1460 and V1758.

The residues V1758 and L1460 are shown in stick form (red) and labeled in our homology model of the open $Ca_V2.1$ channel (left), our homology model of the inactivated channel (center), and a cryo-EM structure of inactivated $Ca_V2.2$ (right) (Gao et al., 2021). Distances between the alpha carbons of each residue are shown with a dotted yellow line and labeled (12.0 Å in the open homology model, 7.1 Å in the inactivated homology model, 10.3 Å in the cryo-EM structure). The two residues are oriented facing each other only in the inactivated homology model.

There are several arguments against this hypothesis, some of which did not come to light until well into the project. First, the L1460F mutation exchanges the leucine for a residue of similar hydrophobicity. Hering et al. (2008) showed that the magnitude of the effect of mutating a hypothesized closed-state-stabilizing residue in $Ca_V1.2$ (the residue analogous to I714) was negatively correlated with the hydrophobicity of the substituted residue, but had no correlation with residue volume or mass. Therefore, we would not expect the L1460F substitution to disrupt stabilizing hydrophobic interactions. Indeed, the L1460F mutation did not significantly slow control (pre-drug) deactivation in our Chapter 4 experiments. In the same vein, we found that the V1758T mutation favors the closed state (see section 5.3.1 above), which seems to contradict the hypothesis that the wild-type residue participates in stabilizing the closed state. V1758 also did not significantly reduce KK-20's ability to slow deactivation. Finally, L1460F and V1758T do not face each other in a recently solved cryo-EM structure of the inactivated state of the $Ca_V2.2$ channel (Gao et al., 2021), which is more closely related to $Ca_V2.1$ than the $Ca_V1.1$ template (Wu et al.,

2016) used to make our inactivated homology model. This could mean that the two structures represent distinct inactivated states of the channel (since proteins are dynamic structures that can access multiple open, closed, and inactivated conformations); that these residues face each other in $Ca_V2.1$, but not $Ca_V2.2$; or that the apparent interaction between these two residues is an artifact of the $Ca_V1.1$ template used to build our model.

An alternative hypothesis is that, contrary to our and Hering et al. (2008)'s homology models, L1460 and V1758 interact to stabilize the positions of their respective S6 segments in the *open* pore. This would fit with our finding that V1758T right-shifts voltage-dependence of activation. In this interpretation, a possible explanation for the reduced effect of KK-20 in the L1460F mutant is that KK-20 binding in wild-type $Ca_V2.1$ causes a conformational change that strengthens this open-state-stabilizing interaction, and the L1460F mutation prevents the interaction from being strengthened.

If KK-20's effect on deactivation is mediated, in whole or in part, by the strengthening or disruption of an L1460/V1758 interaction, then mutating either residue would be sufficient to interfere with this mechanism. Thus, we would expect the effect of mutating one residue on KK-20 action to depend on whether or not the other residue is also mutated. We used a double mutant cycle analysis (Horovitz et al., 1996) to determine whether there is an interaction effect of L1460F and V1758T on either the fold change in tail current integral upon KK-20 application, or the time-course of KK-20-modified tail current deactivation, tau_{deact}. Briefly, we compared these measures of KK-20 effect the wild-type channel, the two single mutants, and the double mutant to calculate a coupling coefficient **Ω** (Figure 49). The formula for calculating **Ω**, using the tau of deactivation measure as an example, was as follows:

$$(tau_{L1460F/wt})(tau_{wt/V1758T}) \,/\, (tau_{wt/wt})(tau_{L1460F/V1758T}) \qquad \textbf{Equation 4}$$

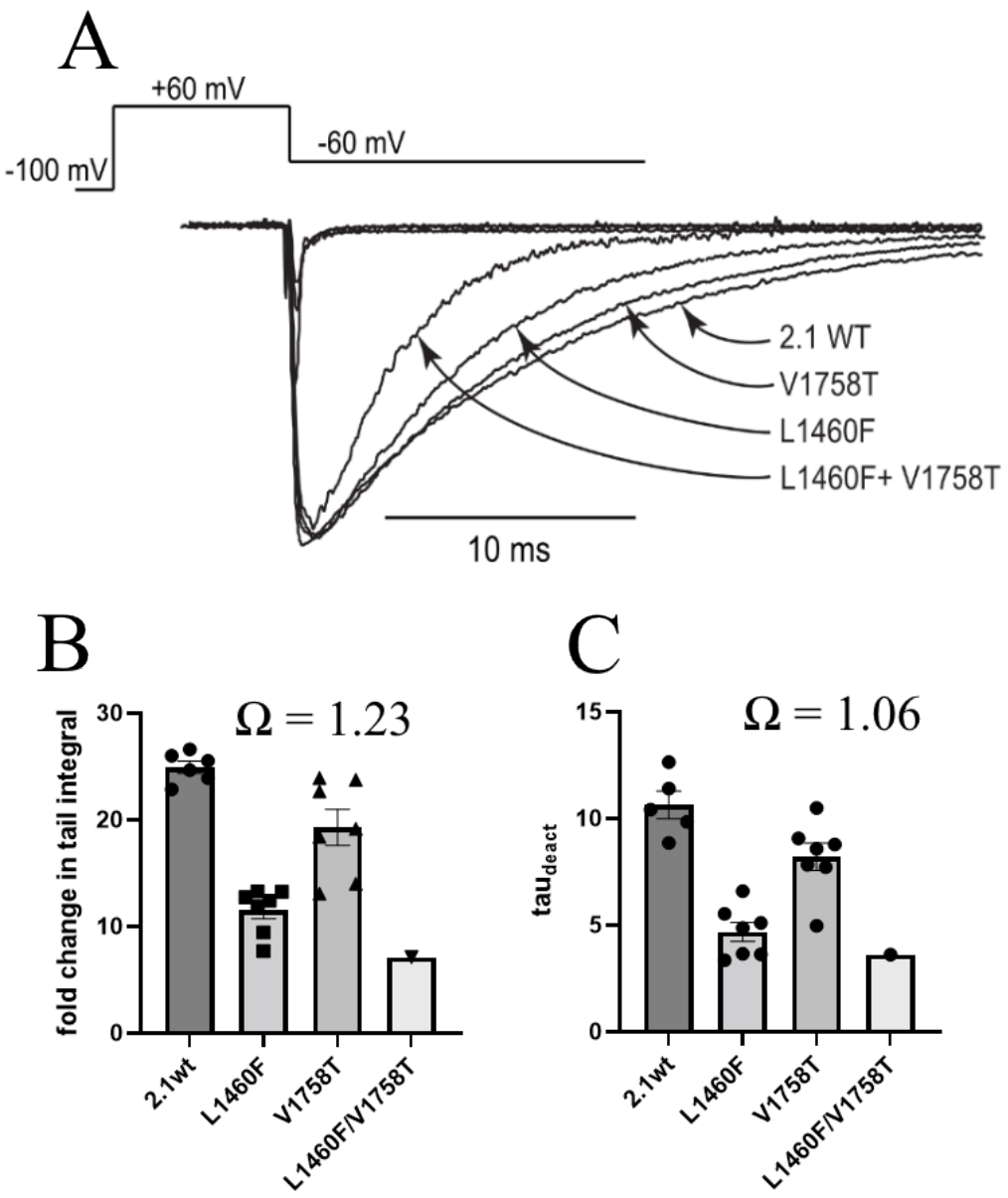

Figure 49: A double mutant cycle analysis shows no interaction effect of L1460F and V1758T on KK-20 action.

A. Representative tail currents before and during application of 50 μM KK-20 for the wild-type $Ca_V2.1$ channel, the single L1460F and V1758T mutants, and the double mutant. Both single mutations cause the current to decay faster than in wild-type, and the double mutation has a cumulative effect. **B.** Comparison of the fold change in tail current integral upon KK-20 application between the wild-type, single, and double mutant channels. The coupling coefficient Ω calculated for this measure is 1.23. **C.** Comparison of the time constant of deactivation, tau_{deact}, between the wild-type, single, and double mutant channels. Tail current decay was fit to a single standard exponential function to calculate tau_{deact}. The mutations' relative effects on this measure of KK-20 action are similar to their effects on fold change in integral. Ω = 1.06. Bar height represents the mean value, and individual data points are shown. Error bars represent SEM.

As described in our previous experiments, we calculated the mean KK-20-mediated fold change in tail current integral (following a 100ms depolarizing step to +60mV and repolarization to -60mV) in wild-type $Ca_V2.1$ at 24.9 +/- 0.57, in L1460F at 11.5 +/- 0.81, and in V1758T at 19.3 +/- 1.7. The mean fold change in tail current integral in the double mutant was 7.1. From these data, we calculated an Ω of 1.23, which we do not think is likely to represent an interaction between L1460F and V1758T in their effects on KK-20-mediated slowing of deactivation.

Our double mutant cycle results using the tau of tail current deactivation in the presence of KK-20, drug tau_{deact}, as the measure of KK-20's effect agree with the above result. Mean drug tau_{deact} (again following a 100ms depolarizing step to +60mV and repolarization to -60mV) is 10.6 +/- 0.65 ms in wild-type $Ca_V2.1$, 4.7 +/- 0.45 ms in L1460F, 8.2 +/- 0.64 ms in V1758, and 3.6 ms in the double mutant. From these data, we calculated an Ω of 1.06, which again does not support an interaction effect of these mutations on KK-20 action. (However, N = 1 for the double mutant in these calculations, so further data collection will be necessary to confirm or refute the result.) μ

Overall, our results do not support a mechanism of KK-20 action that involves strengthening or disrupting an interaction between L1460 and V1758. These residues may or may not interact, and L1460 likely does play some other role in KK-20 action given our Chapter 4 findings, but it does not appear that an L1460/V1758 interaction features in KK-20's mechanism of action.

5.3.6 KK-20 greatly slows tail current decay in the gain-of-function mutant I1461F

In our Chapter 4 experiments, we found that the mutation I1461V significantly increased the size of the KK-20-modified normalized tail current integral compared to wild-type $Ca_V2.1$. We were curious whether this effect was specific to the valine substitution or whether mutating I1461

to other residues might have the opposite effect. Since valine (Van der Waals volume = 105 $Å^3$) is less bulky than isoleucine (124 $Å^3$), we tried mutating to phenylalanine, which is bulkier (135 $Å^3$) than isoleucine (Dill et al., 2017).

We found that the I1461F mutation slightly left-shifts the voltage-dependence of activation and current-voltage relationships (Figure 50B), consisting with this mutation favoring the open state of the channel. We calculated its VD_{50} at -21.3 mV, compared to 2.32 mV in wild-type $Ca_V2.1$. This effect was somewhat surprising since although this residue, like the LAIA and VAVIM residues implicated in closed-state-stabilizing hydrophobic interactions, is located in close sequential proximity to a GAAA ring residue, there is very little difference in hydrophobicity between isoleucine and phenylalanine. We also observed slower tail current deactivation at all evaluated repolarization voltages and steeper voltage-dependence of deactivation compared to wild-type $Ca_V2.1$, although we hesitate to speculate on the implications of this observation because it is based on only one voltage-dependence of deactivation recording in I1461F. Further investigation will be necessary to understand how I1461F affects this gating characteristic.

The most interesting property of the I1461F mutation is its dramatic gain-of-function effect on KK-20-mediated slowing of deactivation. The control tail current integral in this mutant is increased from wild-type $Ca_V2.1$ (0.41 +/- 0.025) to 1.25 +/- 0.29 (Figure 50C), though the effect is not significant. In our other mutants with slowed control deactivation—e.g., I714T—the fold change in the tail current integral upon drug application was smaller than in wild-type, at least in part because larger control tail integrals increased the size of the denominator in the fold change equation. However, in I1461F, the drug integral is so large that the KK-20-mediated fold change in tail current integral is nearly twice as large as in the wild-type channel, despite being calculated from a larger control value. We calculated the drug integral at 60.0 +/- 19.8 (compared to 10.6 +/-

0.65 in wild-type) (Figure 50D), and the mean fold change at 46.7 +/- 5.4 ($p < 0.05$) (compared to 25.4 +/- 0.48 in wild-type) (Figure 50E). These values may underestimate the drug effect, since four recordings had to be excluded from the analysis because KK-20 slowed deactivation so much that their tail currents did not decay to baseline by the end of the repolarizing step, making it impossible to calculate the drug-modified tail current integral. It seems likely that whatever conformational changes KK-20 binding effects in the channel result in an extremely stable open state (or an extremely high energy barrier to the closed-state transition) when combined with the I1461F mutation, which may provide a clue to KK-20's mechanism of action.

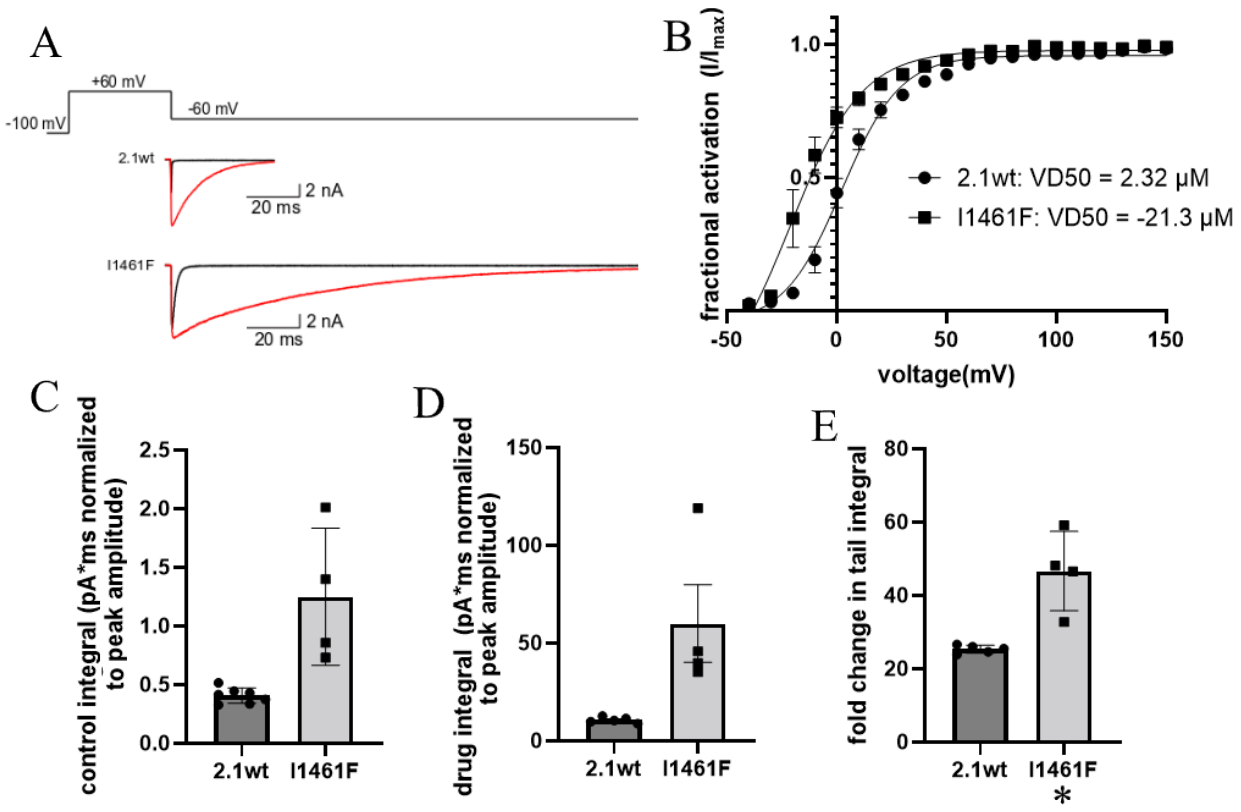

Figure 50: Mutating I1461F to a phenylalanine dramatically enhances KK-20-mediated slowing of deactivation.

A. Example tail currents before and during application of 50 µM KK-20 in wild-type $Ca_V2.1$ and the I1461F mutant channel, showcasing I1461's extremely slow tail current decay. The recording shown here is characteristic of those that were not analyzed because the current did not decay to baseline by the end of the step. **B.** Fractional activation vs depolarizing step voltage plot for the wild-type and mutant channels. I1461F left-shifts the voltage-dependence of activation. **C-E.** Comparison of control integrals (C), KK-20-modified integrals (D), and fold change in integral (E) for the wild-type and mutant channels. Significant differences are marked with an asterisk (unpaired t-test with Welch's correction, $p < 0.05$). Error bars represent SEM.

As in the threonine mutant experiments, we also evaluated I1461F for effects on the proportion of tail current decay modified by 5 µM KK-20 (Figure 51). We did not find a significant effect of this mutation on the fitting weight of KK-20-modified tail current decay (59.0 +/- 4.6%, vs 52.5 +/- 1.6% in wild-type). This suggests that I1461 does not directly participate in KK-20 binding, which is consistent with the predictions of our automated docking simulations (Chapter 3) that the structurally and functionally similar analog GV-58 binds somewhere above I1461 in

the pore, farther from the intracellular mouth. In our homology model of the $Ca_V2.1$ open state, tightly packed S6 hydrophobic residues appear to obstruct access to I1461 from the III/IV fenestration or central cavity (whose shapes and positions we calculated using CAVER 3.0; see Chapter 3), supporting that this residue is inaccessible for KK-20 binding. The effect of the mutation on KK-20-mediated slowing of deactivation is therefore likely to be mechanistic in nature.

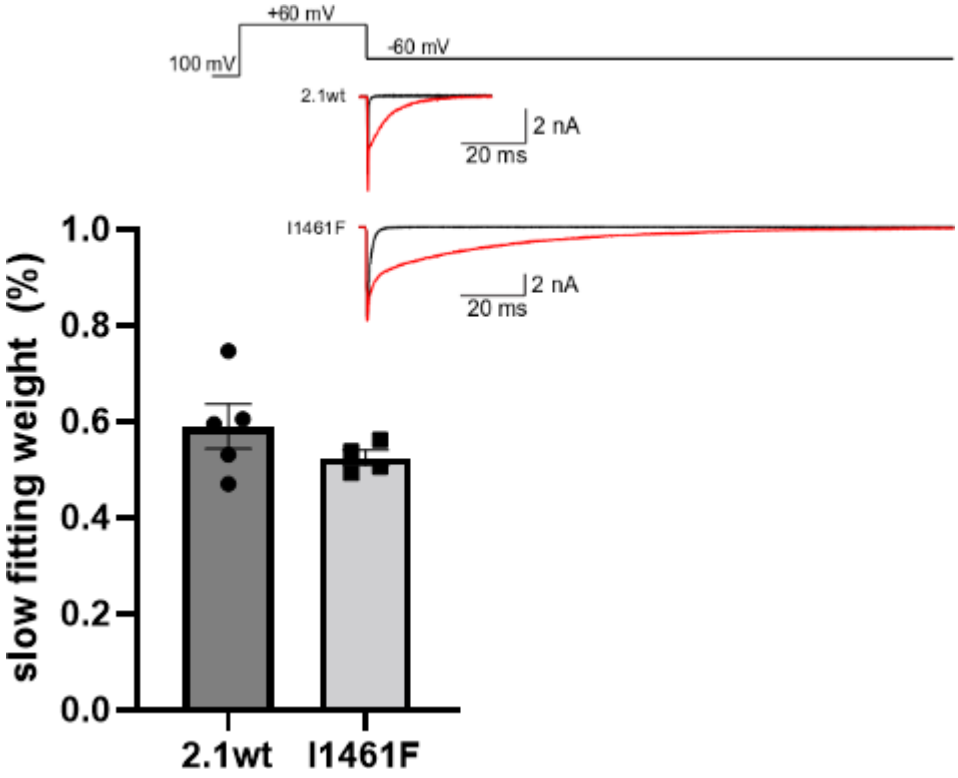

Figure 51: Mutating I1461F to a phenylalanine does not affect the proportion of tail current decay modified by 5 µM KK-20.

Comparison of the fitting weight of the slow (KK-20-modified) component of tail current decay between wild-type $Ca_V2.1$ and I1461F. There is no significant difference between wild-type and mutant. Representative control (black) and KK-20-modified (red) tail currents are inset.

5.3.7 Examining the effect of the I1461F mutation on the closed-pore activation gate structure *in silico*

In our homology model of the inactivated state of $Ca_V2.1$, the activation gate is formed by one residue from each domain that rotate into the pore as the channel closes. In this model, I1461 is located just below the domain III activation gate residue (F1457), separated from it by one helical turn and oriented into the pore on the intracellular side of the activation gate.

We were curious whether the I1461F mutation might slow deactivation in unbound and KK-20-modified channels by destabilizing the closed conformation of the activation gate. In our homology model of inactivated $Ca_V2.1$ (see Chapter 3), we mutated I1461 to phenylalanine and refined the resulting structure by energy minimization to predict how the mutation would affect the positions and orientations of nearby residues. We found that the I1461F mutation was not predicted to have any effect on the activation gate residues in our homology model (Figure 52). However (as we discussed in chapter 3), the recently published cryo-EM structure of a $Ca_V2.2$ channel revealed a unique Ca_V2 activation gate architecture, which might be disrupted by I1461F; see Discussion, below.

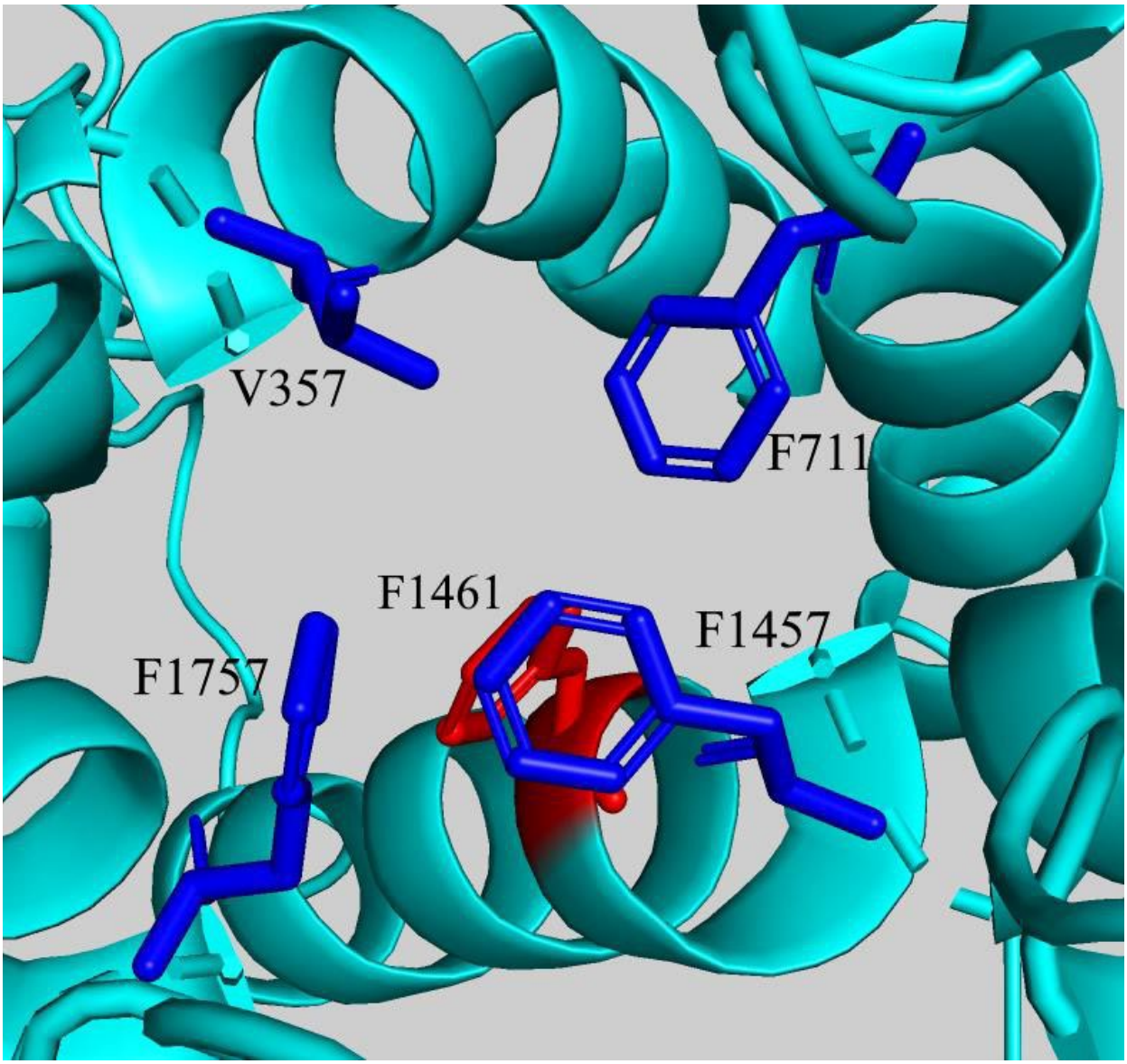

Figure 52: The I1461F mutation does not disrupt sealing of the pore by the activation gate residues in our $Ca_V2.1$ inactivated state homology model.

Top-down view of the inner pore activation gate of our inactivated state $Ca_V2.1$ homology model with the I1461F mutation. The channel backbone is colored cyan and shown in a semi-transparent ribbon cartoon representation. The residues that form the activation gate in this structure (V357, F711, F1457, F1757) are shown in stick representation and colored blue. The mutated residue, F1461, is shown in stick representation and colored red. In the open state homology model, all four residues are oriented away from the dilated pore. As in the wild-type inactivated state homology model (see Figure 16C), the S6 segments have converged to narrow the pore, and the activation gate residues have rotated into the pore to form a hydrophobic seal against ion permeation. The I1461F mutation does not disrupt the pore-sealing closed-state orientations of the activation gate residue residues.

5.4 Discussion

5.4.1 Threonine mutations in the LAIA, VAVIM, and GAAA motifs alter the control gating characteristics of $Ca_V2.1$ channels

We found that the I714T, A714T, and A1459T mutations had effects consistent with the existing literature (Depil et al., 2011; Hohaus et al., 2005) and with the interpretation that these mutations favor the open state of the channel: left-shifting of the voltage-dependence of activation and the current-voltage relationship, and slowing of deactivation. Slowing of deactivation was accompanied by a steeper dependence of deactivation kinetics on the repolarization voltage.

Interestingly, mutating V1758 to threonine right-shifted voltage dependence of activation, consistent with the mutation favoring the closed state. This seems at odds with Hering et al. (2008)'s prediction, based on homology models of the $Ca_V2.3$ channel, that this residue participates in a closed-state-stabilizing interaction with L1460. It could be the case that V1758 participates in both open- and closed-stabilizing interactions, or that the proposed interaction is unique to the $Ca_V2.3$ subtype. Additional mutagenesis experiments in this region of the channel could help to clarify how individual S6 residues contribute to pore gating, which in turn would be useful in forming hypotheses about how *(R)*-roscovitine analogs might interact with these mechanisms.

5.4.2 Threonine mutations in the LAIA and GAAA motifs may or may not affect KK-20's ability to modify the channel

We found that the I714T, A715T, and A1459T mutations significantly slowed both control and drug-modified tail current decay. The result was a reduced fold change in tail current integral upon KK-20 application. This could represent pre-emptive disruption by these mutations of closed-state-stabilizing mechanisms that KK-20 would normally disrupt, thus simultaneously slowing control deactivation and denying KK-20 a means of slowing it further. In this interpretation, KK-20 must slow deactivation by multiple mechanisms, since if its *only* mechanism for slowing deactivation were pre-empted by the mutation, we would expect the control integral to resemble the wild-type drug integral and for KK-20 to fail to modify currents further. However, another possible interpretation is that the mutations slow control deactivation, KK-20 additively slows deactivation further by mechanisms unrelated to the mutations, and the resulting fold change in normalized integral is still reduced due to the larger denominator. A double-mutant cycle analysis approach could be used to identify residue interactions that affect KK-20 action, in order to detect shared mechanisms of mutation-mediated and KK-20-mediated slowing of deactivation. We used this method to evaluate a hypothesized closed-state-stabilizing interaction between the residues L1460 and V1758, but found no evidence that an interaction between these residues plays any role in KK-20's effect on deactivation.

As we have discussed, Stary et al. (2008) found that a threonine mutation in IIS6 is likely to distort both IIS6 itself and the neighboring IIIS6 helix. Thus, the effects of these mutations are not necessarily localized to their interaction partners and other residues in their immediate vicinity, but can be propagated allosterically to sequentially distant inner pore residues. The slowed deactivation kinetics observed in most of our threonine mutants could be the cumulative effect of

these single mutations' wide-ranging effects on the inner pore architecture, potentially masking individual closed-state-destabilizing mechanisms shared by the mutations and KK-20.

Stary et al. (2008) also found that the inclusion of a helix-stabilizing alanine mutation in IIS6 alongside the threonine mutation prevented the helical distortion. It may be possible to use this stabilizing alanine mutation approach to rescue the wider allosteric effects of our threonine mutations, which would allow us to better isolate the effects of disrupting hydrophobic interactions that directly participate on KK-20's ability to slow channel deactivation. This, combined with the use of double mutant cycles to evaluate specific interacting pairs that might play a role in KK-20's mechanism of action, might help to clarify how KK-20 binding affects the conformation of the inner pore and how this affects gating.

The cryo-EM structure of inactivated $Ca_V2.2$ (Gao et al., 2021) will be useful for guiding the aforementioned double mutant cycle experiments by predicting closed-state-stabilizing hydrophobic interactions that may be specific to Ca_V2 channels. However, one challenge posed by the dynamic nature of proteins is that KK-20 might plausibly interfere with hydrophobic interactions that stabilize a transitional state between the open and closed pore, and which therefore might not be apparent in a single static closed-pore structure. As a comparison, the translocation of S4 sensors across the plasma membrane depends upon transient ion-pair interactions between the gating charges and nearby residues to stabilize the intermediate positions of S4 in which the gating charges move through the hydrophobic membrane environment. If KK-20 disrupts interactions that similarly stabilize the transition from the open to the closed pore conformation, it may be possible to identify candidate transitional interactions using software tools like ANMPathway, which uses a coarse-grained modeling approach to predict global conformational transitions between two endpoints (Das et al., 2014).

5.4.3 KK-20 dramatically slows deactivation of the I1461F mutant

The extreme enhancement of KK-20-mediated slowing of deactivation by the I1461F mutation is interesting in light of the recent cryo-EM structure of $Ca_V2.2$ (Gao et al., 2021). In our Ca_V1-based homology model of the closed pore in the inactivated state of $Ca_V2.1$, the I1461 is located below the activation gate, and mutating 1461 to phenylalanine *in silico* did not change the positions of the pore-sealing residues. However, as we discussed in Chapter 3, the cryo-EM structure of $Ca_V2.2$ reveals an apparently Ca_V2-specific activation gate structure located below (intracellular to) the gate seen in Ca_V1 and our homology models. This gate consists of a thick core of hydrophobic residues, with a ring of four residues at its base secured by a tryptophan contributed by the Ca_V2-specific $CH2_{II}$ helix (Gao et al., 2021). The domain III residue at the base of the activation gate is I1463, and I1461 is located just above it, facing away from the pore-sealing hydrophobic core (see Figure 21). One possibility is that the I146IF mutation distorts the base of the IIIS6 helix and destabilizes the hydrophobic core. In this case, the conformational changes due to KK-20 binding that disfavor the closed state may synergize with this effect of the mutation, resulting in an extremely high energy barrier for the channel to transition to the closed state. It would be interesting to mutate I1461F *in silico* in the new cryo-EM structure and observe how this affects the positions of residues in the activation gate. Double mutant cycle analysis might also be useful to experimentally confirm or rule out interactions between I1461 and activation gate residues.

An understanding of the mechanism by which I1461F enhances KK-20's ability to modify the channel might aid the design of *(R)*-roscovitine analogs with improved efficacy. I1461's position in the $Ca_V2.1$ structure must allow the perturbation of this residue—by mutation, and perhaps also by allosteric effects of drug binding—to prolong the open state of the channel. It may

be possible to design an *(R)*-roscovitine structure that exploits I1461's key positioning via allosteric perturbation of the wild-type I1461 residue, or of a key gating residue found to be perturbed by the I1461F mutation. Alternatively, perturbation of I1461 may already be part of KK-20's mechanism of action, in which case knowing that would bring us one step closer to understanding its effects on channel conformation.

6.0 General Discussion

6.1 *In silico* predictions of *(R)*-roscovitine analog binding and experimental mutagenesis findings point to a binding site in the inner pore at the interface of domains III and IV.

The results of our Ca_V2->Ca_V2 single-residue mutagenesis experiments are summarized in Table 2.

Table 2: Summary of Ca_V2->Ca_V1 single-residue mutagenesis findings.

Summary of data compiled from the experiments described in Chapter 4. Where applicable, asterisks represent a statistically significant difference from wild-type. Cells were marked "N/A" for measures of KK-20 action/binding that were not evaluated in a given mutant.

	Fold change in tail current integral (50 µM KK-20)	Slow fitting weight (5 µM KK-20)	EC_{50}	K_D
$Ca_V2.1$ wt	24.9x	59.0%	6.9 µM	10.2 µM
F1446I	12.9x*	32.5%*	40.7 µM	51.9 µM
F1453M	6.8x*	26.5%*	52.0 µM	14.8 µM
V1454M	18.1x*	74.2%	N/A	N/A
A1459G	19.3x	39.4%	N/A	N/A
L1460F	11.5x*	47.3%	10.4 µM	N/A
I1461V	29.8x	55.1%	N/A	N/A
I1463V	26.9x	N/A	N/A	N/A
F1747M	27.5x	N/A	N/A	N/A
S1750A	27.9x	N/A	N/A	N/A
M1753I	11.2x*	82.3%	4.6 µM	6.3 µM

Overall, the results of these experiments support the predictions of our automated docking simulations in $Ca_V2.1$ homology models that *(R)*-roscovitine analogs bind to S6 residues at the interface of domains III and IV in the inner pore, either within the fenestration itself near where it opens into the central cavity, or to residues lining the central cavity itself. This suggests that *(R)*-roscovitine analogs may exploit similar mechanisms to the DHP agonist *(S)*-Bay K 8644, which has similar effects on Ca_V1 deactivation as *(R)*-roscovitine does in Ca_V2 channels and also binds in the domain III/IV fenestration, although *(S)*-Bay K 8644 binds closer to the PM mouth of the fenestration (Gao and Yan, 2021; Hockerman et al., 1997b.) Our strongest experimental evidence for a binding site in this part of the channel was that the F1446I mutation had a large negative effect on KK-20's potency (quantified as a large increase in EC_{50}) as well as its binding affinity (quantified as a large increase in K_D, which resulted from a reduced on-rate and increased off-rate of the drug). This is likely to reflect either direct or allosteric disruption of the binding site; one possibility is that F1446 itself participates in binding KK-20. Our MD simulations support a possible contact of the drug's thiophene side group with F1446. On the other hand, S6 residues of different domains are in close proximity in the pore, and it is possible that different side groups of *(R)*-roscovitine bind to residues from different domains (which would also be consistent with our MD simulations). Further mutagenesis experiments will be necessary to characterize the binding site; ideally, we will identify a set of Ca_V2 residues that are necessary and sufficient for KK-20 binding, as was accomplished for DHP ligands in Ca_V1 (Hockerman et al., 1997b).

We were surprised by our finding that the F1453M mutation reduced KK-20 potency, but had little effect on K_D. As we discussed in Chapter 4, one possible explanation—given that F1453 is one of the residues our Chapter 3 homology models implicate in "pinching" the bottleneck in the open-state III/IV fenestration—is that rather than disrupting the binding site, this mutation

narrows the fenestration access pathway in the closed pore, impeding the diffusion of KK-20 from the PM to the binding site. Alternatively, the wild-type residue might participate in coordinating KK-20's movement through the fenestration to the central cavity, and the methionine mutation might not do so as effectively. In either case, this would mean that at a given concentration of KK-20, fewer molecules of drug would be in position to bind and modify channels than in wild-type $Ca_V2.1$, hence the large increase in EC_{50} we observed in F1453M; however, the rate of binding for KK-20 molecules already in position would be largely unaffected, hence little change in K_D. As a next step in interpreting these findings, we can mutate F1453 to methionine *in silico* in an inactivated-state homology model of $Ca_V2.1$ (ideally one based on the cryo-EM structure of $Ca_V2.2$ as a template (Gao et al., 2021), in order to more accurately represent the $Ca_V2.1$ fenestrations compared to our previous Ca_V1-based homology model), and then use CAVER 3.0 and CaverDock to determine how the mutation affects the diameter of the domain III/IV fenestration and the binding free energy for GV-58 or KK-20 moving through it. If this interpretation of our findings is correct, we would expect an increase in the drug's binding free energy at positions in the fenestration near F1453M, which might or might not be accompanied by a narrowing of the fenestration.

Other nearby residues in IIIS6 and IVS6 were found to have effects consistent with disruption of KK-20's mechanism of action for slowing deactivation, without interfering with its binding. A hypothesized role of one of these residues, L1460, in KK-20's mechanistic pathway is described in section 6.3 below.

As for our threonine mutations in II, III, and IVS6, we were ultimately unable to draw meaningful conclusions about these residues' involvement in KK-20 action due to the mutations' dramatic and potentially confounding effects on control gating characteristics. We were able to

confirm in $Ca_V2.1$ the open-state-favoring effects of mutating the residues I714, A715, and A1459 that were previously reported for the analogous residues in other VGCC subtypes (Depil et al., 2011; Hering et al., 2008; Hohaus et al., 2005; Kudrnac et al., 2009; Stary et al., 2008), and we also found a closed-state-favoring effect of the V1758T mutation that has not been reported. A double mutant cycle analysis of a potential interaction effect of the L1460F and V1758T mutations on KK-20 action yielded a negative result. Additional experiments, including double mutant cycles of other possible interacting pairs, will be needed to determine if and how KK-20 disrupts closed-state-stabilizing hydrophobic interactions in the inner pore; see section 6.4 below.

More informative was the I1461F gain-of-function mutation that dramatically enhanced KK-20-mediated slowing of deactivation without disrupting its binding. We speculate that this mutation favors the open state by disrupting the structure of the activation gate, rather than an adhesion point, and that KK-20 binding enhances or stabilizes this activation gate disruption. An experiment to begin investigating this hypothesis is discussed in section 6.4.

One potential confounding factor we hope to account for in future mutagenesis experiments is the fact that deactivation kinetics are voltage dependent. Comparing control and KK-20-modified deactivation kinetics between wild-type and mutant channels is potentially problematic when mutations might alter the relationship between voltage and the time-course of tail current decay, as we observed for our threonine mutants in Chapter 5. Yarotskyy et al. (2012) addressed this by measuring deactivation kinetics over a range of voltages, which may be the more robust approach, although the challenge is that *(R)*-roscovitine analogs' enhancement of inactivation complicate comparisons between tail currents at successively more depolarized repolarization voltages during drug application in a single cell.

6.2 The state-dependent fenestration access hypothesis

Our modeling predictions and mutagenesis experiments have yielded both results in support of the state-dependent fenestration access hypothesis for *(R)*-roscovitine analogs, and results that appear to contradict it. To recap, the state-dependent access hypothesis proposes that *(R)*-roscovitine analogs access the part of the channel containing the binding site that mediates slowed deactivation from the plasma membrane while the channel is in the closed state, then bind and modify the channel when it is in the open state. The binding site (which we believe is only available to bind the drug when the channel is open) is proposed to lie inside the channel, either within the fenestration itself, or in the central cavity to which the fenestration connects. This would explain the finding that GV-58 modifies $Ca_V2.1$ currents effectively when extracellularly applied and washed off prior to a depolarizing step, but not when it is applied only during the depolarizing step (Wu et al., 2018).

In support of the state-dependent fenestration access hypothesis, our homology models of the open and inactivated $Ca_V2.1$ channel have a fenestration at the interface of domains III and IV that connects to the central cavity and is bottlenecked in the open state; our CaverDock simulations support that GV-58 can freely diffuse through this fenestration in the inactivated state, but not when it is bottlenecked in the open state; and a III/IV fenestration is also present in the recently solved cryo-EM structure of inactivated $Ca_V2.2$. (Although this would be difficult to test experimentally, we believe the drug can access the channel when it is inactivated as well as when it is closed; the III/IV fenestration is located in the pore, so its diameter should be dependent on the open vs the closed conformation of the pore, not on the voltage sensor positions.) In addition (as we covered in the previous section), our experimental mutation of the F1453 residue, which our models predict participates in pinching the fenestration at the open-state bottleneck, resulted

in greatly reduced KK-20 potency (as quantified by EC_{50}) but little change in its binding affinity (as quantified by K_D), which could be the result of this mutation changing the diameter of the inactivated-state fenestration and therefore hampering KK-20's access to the binding site. In this interpretation, fewer molecules of KK-20 diffuse through fenestrations and become available for binding at any given concentration, but their rate of binding from within the fenestration or central cavity is unchanged.

On the other hand, the very fact that we were able to calculate K_D from the time-course of drug binding (the tau of the activity-dependence curves) at 3-4 different concentrations stands in apparent contradiction of the fenestration access hypothesis. If binding occurs in the open state, but the binding site is sealed off from the PM and extracellular environment by the fenestration bottleneck in the open state, then the concentration of KK-20 applied to the cell should not factor into the rate at which the drug binds and modifies currents. The rate of current modification should depend only KK-20 molecules' intrinsic rate of transition from "unbound inside the channel" to "docked in the binding site."

At the same time, it remains true that *(R)*-roscovitine analogs require membrane depolarization to bind and modify channels, yet KK-20 does not effectively modify channels when applied while they are in the open state (Wu et al., 2018). The difficulty lies in reconciling our experimental results in this study with the results of the previous fast-perfusion experiments. Any interpretation that relies on drug being able to access the binding site from outside the channel during the open state—for example, "the drug freely diffuses through the III/IV fenestration in the open state," or "the drug enters through the pore, a different fenestration, or some other pathway that is available in the open state"—contradicts the finding that there is little modification of current by drug applied during depolarizing steps.

Another possibility is that multiple KK-20 molecules can simultaneously occupy the central cavity and bind the channel from within it during the open state. In this interpretation, the average number of molecules inside the channel during the open state is a function of the concentration of KK-20 in the plasma membrane. The binding rate in turn depends on the number of molecules inside the channel; therefore, the binding rate can vary with the external concentration of KK-20. This model requires the $Ca_V2.1$ central cavity and attached fenestrations to be able to accommodate enough molecules of KK-20 to explain the differences we observe in the activity-dependence taus at different concentrations. The largest difference we observed was a 6.6-fold faster modification of M1753I current by 50 μM compared to 5 μM KK-20; the next largest was a 4-fold faster modification of wild-type $Ca_V2.1$ current by 50 μM compared to 5 μM KK-20 (see Figure 32). One would assume that if the central cavity were spacious enough to contain 6-7 molecules of KK-20, that would be enough to explain the concentration-dependent differences in the open-state binding rate. However, anecdotally, we have attempted to manually place multiple molecules of the structurally near-identical analog GV-58 in the central cavity of our $Ca_V2.1$ open-state homology model, and it could not energetically accommodate more than 5 (not shown); and we cannot predict whether even this many molecules of the drug could plausibly diffuse into the cavity from the PM, since the timescales over which this could occur are too long for MD simulations to be practical. If binding rate can vary nonlinearly with the quantity of a very small number of ligand molecules, a range of 0-5 molecules in the central cavity could potentially be enough to explain our experimental results, but we have not been able to find a source that sheds light on whether or not this is possible.

Overall, we do not yet have a theoretical model that satisfactorily reconciles the results of our K_D experiments with the results of Wu et al. (2018)'s fast-perfusion experiments. What might

help would be to further experimentally interrogate the assumptions underlying the state-dependent fenestration access hypothesis. New information could lead to refinement of the model, or even to an alternative model that reconciles our previous experimental findings.

For example, one major assumption of the fenestration access hypothesis is that *(R)*-roscovitine analogues cannot reach the binding site by entering the channel through the extracellular mouth of the pore. We can test this experimentally by examining the ability of cadmium (Cd^{2+}), a rapidly reversible ionic pore blocker that binds to Ca^{2+} sites above (extracellular to) our hypothesized *(R)*-roscovitine analog binding site in the inner pore, to influence GV-58 modulation. Using the fast-perfusion approach described in Wu et al. (2018), we could perfuse Cd^{2+} onto the cell for 300-500 ms or as long as it takes to fully block the pore. We could then perfuse on Cd^{2+} plus KK-20 for 100 ms, followed by a 100 ms wash with Cd^{2+} to remove KK-20 from the extracellular solution while maintaining Cd^{2+} block. Next, we could remove the Cd^{2+} block with a 100 ms saline wash and apply a voltage step to activate current and measure its modulation by KK-20. Wu et al. (2018) showed that KK-20, applied for 100 ms and washed off 200 ms before a depolarizing voltage step, strongly modulates $Ca_V2.1$ tail currents (**figure 14**). If Cd^{2+} block during KK-20 application does not affect the proportion of current modified by the drug, this would support the interpretation that GV-58 does not access its binding site through the pore.

It should also be possible to test our predictions, based on our modeling experiments in Chapter 3, that *(R)*-roscovitine analogues can move through the III/IV fenestration in the closed but not the open pore. As we showed in Figures 19 and 25, we can use CAVER 3.0 to predict the effects of residue mutations on fenestration diameter. This could allow us to identify open-state residue mutations that widen the bottleneck so that KK-20 can access the binding site as easily in

the open state as in the closed state (using CaverDock, as in Figure 23, to predict how easily the drug can move through the mutated fenestration). If the state-dependence KK-20 action is, in fact, caused by the open-state fenestration bottleneck, then KK-20 should be able to strongly modulate $Ca_V2.1$ channels with fenestration-widening mutations even when applied only during the depolarizing step. By the same token, if we can predict mutations that bottleneck the fenestration in the closed state, we should be able to severely reduce KK-20 binding or eliminate it entirely. If these assumptions were not borne out by the experiments, it would be necessary to rethink the fenestration access hypothesis, at least with respect to the III/IV fenestration being the access pathway. Ideally, the *in silico* predictions of fenestration-modifying mutations in the closed pore should use a $Ca_V2.1$ homology model based on the $Ca_V2.2$ cryo-EM structure (Gao et al., 2021).

One potential complication to these fenestration-altering experiments is that our only experimental evidence of changes in fenestration diameter would be the effects we observed on KK-20 action. An *in silico* prediction that specific mutations will narrow the fenestration does not guarantee that they will do so in practice. If the prediction were wrong, and the mutations failed to bottleneck the fenestration in the closed state, we would observe no inhibition of KK-20 binding. If the mutations successfully introduced a bottleneck, but the state-dependent fenestration access hypothesis was incorrect and the bottleneck thus failed to prevent KK-20 from accessing the binding site by some other means, we would again observe no inhibition of KK-20 binding.

Another concern is that we predict KK-20 binds either within the III/IV fenestration or to IIIS6/IVS6 residues in the central cavity just beyond it, so mutations in the fenestration could have effects on the binding site that would be difficult to disambiguate from effects on the fenestration access pathway. For example, we have speculated that the F1453M mutation might have disrupted KK-20 binding by altering the fenestration, the actual binding site, or both.

Despite the obstacles involved, we believe these experiments will provide valuable information about how *(R)*-roscovitine analogs interact with Ca_V2 channels. The state-dependent fenestration access hypothesis is based on extensive but circumstantial evidence, and it will be important to challenge it directly.

6.3 A mechanistic hypothesis in which the IIIS6 residue L1460 mediates *(R)*-roscovitine-analog-induced slowing of both pore closure and voltage sensor relaxation

We have alluded several times in previous chapters to the "adhesion point" hypothesis of closed-state-stabilization and VSD/pore coupling. To recap and expand on this concept, there are four conserved glycine or alanine residues in the lower thirds of S6 segments, one per domain (the GAGA ring in Ca_V1., or the GAAA ring in Ca_V2), which are believed to participate in tight-fitting interactions with nearby hydrophobic residues that contribute to closed-pore stability—the "adhesion point" in each domain. A homology model of $Ca_V1.2$ predicted that each GAGA residue contacts not only hydrophobic residues that are nearby in sequence on its own S6 segment, but also a subset of the GAGA residues of neighboring S6 segments and the hydrophobic residues surrounding them (Depil et al., 2011); additionally, both $Ca_V1.2$ and $Ca_V2.3$ homology models predicted interactions between the hydrophobic adhesion point residues of neighboring S6 segments (Hering et al., 2008). These helix-helix interactions between the adhesion point residues are believed not to directly seal the pore against ion permeation, but to stabilize the close packing of the S6 helices as they converge in the closed state and position the activation gate residues to seal the pore.

Experimental evidence supports the involvement of several hydrophobic residues in particular in closed-state-stabilizing adhesion point interactions. These include bulky hydrophobic residues flanking the domain II and IV GAGA/GAAA residues in the highly conserved LAIA (IIS6) and VAVIM (IVS6) sequence motifs. Mutations of any of the GAGA/GAAA residues, any of the LAIA residues, or the second valine in VAVIM have effects consistent with stabilization of the open state or destabilization of the closed state, including left-shifting the channel's voltage-dependence of activation and slowing its deactivation. In the case of the GAGA/GAAA residues, it is believed that mutating these small glycines and alanines to larger residues sterically disrupts closed-state stabilizing adhesion point interactions that depend on the small size of the wild-type residues (Depil et al., 2011). In the case of the bulky hydrophobic residues, the most dramatic open-state-favoring effects are observed for mutations of the LAIA isoleucine analogous to I714 in $Ca_V2.1$ (Hering et al., 2008; Hohaus et al., 2005; Stary et al., 2008). The magnitude of the effect of mutating this residue is correlated with how much less hydrophobic the substituting residue is compared to the wild-type isoleucine (Hering et al., 2008). This is consistent with the interpretation that mutating I714 favors the open state by disrupting this residue's hydrophobic adhesion point interactions (Hering et al., 2008). The residue analogous to I714 in $Ca_V1.2$ channels has also been shown to be energetically coupled with a conserved serine near the IS6 adhesion point, which may also contribute to closed-state-stability (Kudrnac et al., 2009).

There is evidence that the adhesion point residues participate in mediating the relationship between voltage sensor movement and closed-state stability. For example, the GAGA/GAAA residues of all four domains have been shown to be energetically coupled with IIS4; the open-state-stabilizing effects of mutating any of these residues (but not nearby hydrophobic adhesion point residues) are reversed by neutralization of the IIS4 gating charges (Beyl et al., 2012). Beyl

et al. (2012) proposed that the coupling of IIS4 to GAGA/GAAA residues in other domains is mediated by a high degree of cooperativity in the pore (see Figure 42), as exemplified (and possibly mediated) by the adhesion point interactions between S6 segments; in this interpretation, deactivation of a voltage sensor causes the S6 segment in the same domain to translocate into its closed-state position, and this S6 segment adopting its closed position in turn increases the probability that the other S6 segments will do so.

The electromechanical coupling between the movement of a voltage sensor and the movement of its corresponding S6 is understood to be mediated by the S4-5 linker. Interestingly, despite not being energetically coupled to IIS4, the residue analogous to I714 in $Ca_V2.3$ channels *has* been found to be energetically coupled to a conserved leucine in the IIS4-5 linker, corresponding to L609 in $Ca_V2.1$ (Wall-Lacelle et al., 2011). (In fact, Wall-Lacelle et al. (2011) found that of the first three residues of the LAIA motif—including the domain II GAGA/GAAA residue, corresponding to A713 in $Ca_V2.1$—are energetically coupled to this IIS4-5 leucine, though the calculated coupling energy was largest for I714). Mutating L609 to glycine slows channel deactivation (Wall-Lacelle et al., 2011), as does mutating I714 to glycine (Hering et al., 2008); and mutating either I714 or L609 individually, or both residues together, left-shifts the voltage-dependence of activation *and* the voltage-dependence of gating charge movement, to a similar extent for each single mutation or the double mutation (Wall-Lacelle et al., 2011). The lack of an additive effect of the two individual mutations in the double mutant is consistent with the interpretation that these residues contribute to VSD movement and closed-pore stability in a concerted manner, with either mutation disrupting this concerted mechanism. Additionally, Beyl et al. (2014) attribute the left-shifted voltage-dependence of activation in the Ca_V1 mutant analogous to I714T both to destabilization of the closed pore (35% contribution), and to a shift in

the equilibrium between the activated and deactivation positions of the voltage sensors (65% contribution). These findings suggest a role of I714 in the electromechanical coupling of VSD deactivation to the closed-state-stabilizing adhesion point mechanisms. They also demonstrate that not only can VSD movement affect the conformation of the pore, but modification of an S6 residue can affect voltage sensor movement via VSD/pore coupling mechanisms.

To connect this model of VSD/pore coupling and closed-pore stability to our investigation of KK-20's mechanism of action, there is compelling evidence to support that the adhesion points are at analogous positions in each of the four domains, and more specifically that residue L1460 in $Ca_V2.1$—which our Chapter 4 experiments suggest contributes mechanistically to KK-20-mediated slowing of deactivation— participates in the domain III adhesion point. L1460 is adjacent to the domain III GAAA residue, A1459, and is at the analogous position in IIIS6 to I714 in IIS6. Although most functional characterization of potential adhesion point residues has been carried out within the LAIA and VAVIM motifs, the mutation L1460G in $Ca_V2.3$ channels was also found to left-shift the voltage-dependence of activation and (slightly) slow deactivation kinetics, consistent with this mutation favoring the open state (Hering et al., 2008). As with mutations to the I714 analogues in $Ca_V1.2$ and $Ca_V2.3$, substituting L1460 with different residues revealed a correlation between the negative change in hydrophobicity of the substituting residue and the magnitude of the left-shift in voltage-dependence of activation, implying that these mutations disrupt closed-state-stabilizing hydrophobic interactions (Hering et al., 2008).

The analogous positions and similar open-state-favoring mutation effects of I714 and L1460 raise the possibility that they may play the same functional role in their respective domains, in which case L1460 might also mediate VSD/pore coupling via an interaction with a conserved S4-5 linker residue. Recall that a mutation of the $Ca_V2.3$ residue analogous to I714 was found to

affect voltage sensor movement (Wall-Lacelle et al., 2011), which suggests the same may be possible for a mutation or other modification of L1460. We hypothesize that the binding of *(R)*-roscovitine analogs to IIIS6 residues has an allosteric effect on L1460 that interferes with pore closure, via L1460's participation in hydrophobic S6 helix packing interactions that stabilize the closed pore. We further hypothesize that this allosteric effect on L1460 also interferes with voltage sensor deactivation, via L1460's hypothesized energetic coupling with a conserved residue in the S4-5 linker and/or the adjacent A1459 residue's energetic coupling with the linker residue and S4 segment(s).

In future experiments, we intend to test these hypotheses. The first step will be to determine whether the L1460G mutation has open-state-favoring effects on $Ca_V2.1$ gating similar to what was observed for the analogous mutation in $Ca_V2.3$ (Hering et al., 2008). The next step will be to search for a residue in the IIIS4-5 linker that contributes to closed-state-stabilization and is energetically coupled with L1460. The most likely candidate is the conserved V1321 residue, which is at the domain III position corresponding to L609 in domain II. We would first need to determine whether the V1321G mutation has open-state-favoring effects—again, left-shifted voltage-dependence of activation and slowed deactivation—similar to mutating the L609 analogue to glycine in $Ca_V2.3$. It would also be valuable to glycine scan residues that are close to V1321 in the $Ca_V2.1$ amino acid sequence, either to find an alternative candidate for mediating VSD/pore coupling if the V1321G mutation does not favor the open state, or, if it does, to determine whether the open-state-favoring effects of glycine mutation are specific to V1321.

If a candidate IIIS4-5 linker residue can be identified (whether V1321 or a nearby residue) the next step will be to use a double mutant cycle analysis to determine whether L1460 and this linker residue are energetically coupled. We will use the same approach that Wall-Lacelle et al.

(2011) used to calculate coupling energies for the residues analogous to I714 and L609 in $Ca_V2.3$. Briefly, we will fit a plot of tail current voltage to a Boltzmann equation to calculate the voltage of half-maximal activation (VD50) and slope factor in the wild-type, single-mutant, and double-mutant channels, then use these values to calculate the free energy of activation for each wild-type and mutant channel using the formula

$$\Delta G_{act} = z \cdot F \cdot VD_{50} \qquad \textbf{Equation 5}$$

where ΔG_{act} is the free energy of activation and F is the Faraday constant. We will then calculate the coupling energy, or energy of interaction, using the formula

$$\Delta\Delta G_{interact} = (\Delta G_{act,WT} + \Delta G_{act,double}) - (\Delta G_{act,V1321G} + \Delta G_{act,L1460G}) \qquad \textbf{Equation 6}$$

where $\Delta\Delta G_{interact}$ is the coupling energy, calculating by subtracting the sum of the activation energies of the single mutant channels from the sum of the activation energies of the wild-type and double mutant channels. If there is no interaction between the residues, the effect of each mutation in the double mutant should be additive, thus $(\Delta G_{act,WT} + \Delta G_{act,double}) = (\Delta G_{act,V1321G} + \Delta G_{act,L1460G})$ and $\Delta\Delta G_{interact} = 0$. If the residues are coupled, the effects of the individual mutations will not be additive in the double mutant and $\Delta\Delta G_{interact}$ will be different from 0. Wall-Lacelle et al. (2011) used a threshold of $|\Delta\Delta G_{interact}| > 2$ kcal mol^{-1} to determine whether coupling energy between two residues was significant. A sufficiently high coupling energy would support a direct interaction between the residues, although it is also possible that they are allosterically coupled. Wall-Lacelle et al. (2011) predicted a distance of 10.6 Å between the C-α atoms of the residues analogous to I714 and L609 (which suggests a direct interaction is unlikely), using a $Ca_V2.3$ homology model based on an open-state potassium channel structure. Our open state $Ca_V2.1$ homology model

predicts a distance of 7.1 Å between the C-α atoms of L1460 and V1321 with the residues facing each other, which could represent a direct interaction; our inactivated state homology model predicts a similar distance of 7.6 Å with the residues facing each other; and the cryo-EM structure of $Ca_V2.2$ predicts a distance of 13.6 Å with the residues oriented away from each other, which would not be consistent with a direct interaction.

If we identify a IIIS4-5 linker residue that is energetically coupled to L1460 and is important for closed-state-stabilization, the final step of these experiments will be to perform a double mutant cycle similar to the one we performed for the L1460F and V1758T mutations in Chapter 5. Briefly, we will measure the drug tau_{deact} in the wild-type, L1460G, the S4-5 linker residue glycine mutation (e.g., V1321G), and the double mutant, and use these values to calculate a coupling coefficient **Ω** which will be different from 1 if the effect of one mutation on KK-20 depends on whether the other mutation is also present. If we calculate an **Ω** significantly different from 1, that would support our hypothesis that KK-20's effect of prolonging pore opening depends on L1460/V1321 coupling in some manner (e.g., KK-20 prolongs opening by disrupting the coupling of these residues). This would suggest that KK-20 interacts with the mechanisms that couple voltage sensor deactivation to closed-state stability. Explicitly showing an interaction effect (or lack thereof) on KK-20-mediated slowing of voltage sensor deactivation may also be possible, but would require recording gating currents.

To more fully characterize the gating mechanisms in domain III and their possible relationship to *(R)*-roscovitine action, it would also be useful to evaluate whether A1459 is coupled to the IIIS4-5 linker residue and, if so, whether there is an interaction effect of mutating both residues on KK-20-mediated slowing of deactivation. In the same vein, we could neutralize the gating charges in IIS4 and see if there is an interaction effect of the A1459/IIS4 coupling on KK-

20 action. Given what is known about the functional roles of GAAA/GAGA residues and our experimental results in Chapter 4, there is a possibility that KK-20 slows pore closure and VSD deactivation by allosterically modifying A1459, that the A1459G mutation does not interfere with its ability to do so, and that the adjacent L1460F mutation *does*. While this is a more convoluted interpretation than the one in which we implicate L1460 in KK-20 action directly, it may nevertheless be worth exploring.

In addition, it would be interesting to investigate whether the coupling of A713 to IIS4 is mediated by the S4-5 linker residue with which it is also energetically coupled. This is a relatively straightforward hypothesis that could lead to a better understanding of the "pathway" that connects voltage sensor movement to pore opening and closure, though it also seems at odds with the findings that I714 is coupled to the linker residue (Wall-Lacelle et al., 2011), but not IIS4 (Beyl et al., 2012).

Finally, since our double-mutant cycle of L1460F and V1758T did not show an interaction effect of these residues on KK-20 action, it would be valuable to further investigate possible closed-state-stabilizing interactions between L1460 and other hydrophobic S6 residues. The experiments proposed above will provide insight into L1460's relationship to the S4-5 linker, but a complete characterization of its hypothesized role in coupling VSD movement to pore conformation would also describe how it contributes to closed-state stability.

As a start, we could repeat the L1460/V1758 double mutant cycle using an L1460G mutation, since it is possible these residues *do* interact despite the negative result of our previous double mutant cycle. This could be the case if the conservative L1460F mutation does not disrupt the L1460/V1758 interaction, or if the interaction is unrelated to KK-20's mechanism of action. For these double mutant cycle experiments, we would first use the method described for

L1460G/V1321G above (calculating the free energy of activation of the wild-type, single mutant, and double mutant channels from VD_{50}) to directly look for an interaction effect of these residues on the free energy of activation. If we find they are energetically coupled, we would then evaluate whether their interaction plays a role in KK-20 action. In addition, we could compare homology models of open and inactivated $Ca_V2.1$ (again, using an inactivated model based on the cryo-EM $Ca_V2.2$ template) to identify other hydrophobic adhesion point residues in segments IS6, IIIS6, or IVS6 that might form closed-state-dependent interactions with L1460.

Overall, we consider the L1460/S4-5 linker hypothesis to be our most promising mechanistic explanation for *(R)*-roscovitine-analog-mediated slowing of deactivation, given the following factors:

1. The fact that *(R)*-roscovitine is delays voltage sensor deactivation (Yarotskyy and Elmslie, 2009);
2. the results of our exploratory mutagenesis experiments, which support the involvement of L1460 in KK-20's mechanism of action; and
3. the prior characterization of the involvement of adhesion point residues in closed-state stability and VSD/pore coupling in the literature described above.

6.4 Miscellaneous plans for additional mutagenesis experiments based on our MD predictions of GV-58 binding and a solved cryo-EM structure of the inactivated $Ca_V2.2$ channel

Aside from the L1460/V1321 and A1459 experiments described above, there are a several additional avenues we could pursue in future single-site mutagenesis experiments to explore residues involved in KK-20 binding and action.

First, it should be possible to use a double mutant cycle approach like the one described above for L1460G/V1321G to determine whether the I1461 residue is coupled with residues implicated in securing the base of the Ca_V2-specific activation gate structure revealed by the cryo-EM structure of $Ca_V2.2$ (Gao et al., 2021). We hypothesize that the I1461F mutant slows deactivation by directly disrupting the conformation of the activation gate, potentially by either sterically interfering with the movement of activation gate residues into their pore-sealing positions, or simply increasing the energy barrier of this transition. We would likely first want to look for coupling between I1461 and I1463, the domain III residue that contributes to the base of the activation gate. To detect coupling between these two residues, we would use a double mutant cycle approach with free energy of activation (calculated from VD_{50}) as the measure of mutation effects on gating, as described in section 6.3. It should be possible to use the I1463V mutant in the double mutant cycle, since this mutation right-shifts the voltage-dependence of activation (not shown).

Second, we have not yet evaluated all of the residues that our MD simulations predicted are likely to contact GV-58. For example, we have not yet evaluated the effects of any domain I mutations on *(R)*-roscovitine analog binding and action. The inner pore residues contributed by the S6 segments of each domain are in such close structural proximity that it is possible that any

of the domain I S6 residues predicted to contact the zone 4 n-propyl group—S350, M353, L354, and L358—might play a role in coordinating *(R)*-roscovitine analog binding, even if other side groups of *(R)*-roscovitine analogs simultaneously interact with IIIS6 residues. These specific residues are conserved between Ca_V1 and Ca_V2 channels, so their involvement in binding would not contradict the chimera experiments showing that the Ca_V2 domain I was not necessary for chimeric channels to be sensitive to *(R)*-roscovitine.

The fact that these residues are conserved poses the challenge of choosing substitutions that would disrupt binding by the n-propyl side group without substantially altering the channel's gating properties. This could be accomplished by evaluating candidate substitutions *in silico* for effects on conformations of the open and closed pore, followed by MD simulations to determine whether the mutated residue is less likely to contact GV-58 than in the simulations performed in wild-type $Ca_V2.1$. In this vein, it would also be valuable to repeat our MD simulations with KK-20, in case there is any difference in the predicted residue contacts for its unsaturated n-propyl group compared to GV-58's saturated n-propyl. The conserved IIS6 residues also predicted by the MD simulations to contact the n-propyl group—particularly L708 and F711—are also of interest due to their close sequential proximity to the LAIA motif.

Third, as we discussed in section 5.4.2., there is evidence that the helix-distorting effects of mutating a hydrophobic adhesion point residue can be rescued with the additional inclusion of a helix-stabilizing alanine mutation (Stary et al., 2008). It would be interesting to see how introducing stabilizing alanine mutations to the I714T, A715T, and A1459T mutant channels affects their control deactivation kinetics and their response to KK-20 application. It would be most straightforward to begin with I714T, since Stary et al. (2008) has already identified a stabilizing alanine position for the analogous $Ca_V1.2$ mutant. The first step would be to introduce

this alanine mutation to an *in silico* structure of $Ca_V2.1$ containing the I714T mutation, refine the resulting double-mutant structure by energy minimization, and see whether MD simulations in this structure agree with Stary et al. (2008)'s prediction that the alanine mutation rescues IIS6 and IIIS6 helical distortion in $Ca_V1.2$. It might be useful to use the inactivated cryo-EM structure of $Ca_V2.2$ (Gao et al., 2021) for these modeling experiments, since this solved structure likely represents the architecture of the Ca_V2-family inner pore more accurately than our $Ca_V2.1$ homology models do.

If MD simulations and experimental characterization of a double threonine-alanine mutant channel confirm the rescue effect of the alanine mutation, we could use this approach to investigate potential roles of conserved residues that regulate pore gating in the *(R)*-roscovitine analog mechanism of action in a more targeted manner than we have thus far. Potentially, we could use this approach in double-mutant cycle analyses of possible closed-state-stabilizing hydrophobic interactions between I714/A715/A1459 and nearby residues that might be disrupted by KK-20 as part of its mechanism of slowing deactivation. On the other hand, while the alanine mutation could eliminate the confounding effects of widespread allosteric distortion of the inner pore structure, it might itself confound the double-mutant cycle results if it cannot be included in all of the channels whose effects on KK-20 action are being compared. For example, in an investigation of an interaction of I714 and some other residue, the I714T-stabilizing alanine mutation could only be included in the I714T single mutant and the double mutant, as it might cause helical distortion itself if it is not compensating for an existing mutation (Stary et al. (2008) found that the single alanine mutation in $Ca_V1.2$ resulted in a nonfunctional channel). Whether or not we pair double mutant cycle analyses with stabilizing alanine mutations, comparing the inactivated cryo-EM structure of $Ca_V2.2$ with our open-state $Ca_V2.1$ homology model may reveal potential closed-state-

stabilizing interactions to analyze that were not apparent from our inactivated $Ca_V2.1$ homology model due to its Ca_V1-like activation gate structure.

Another way to apply the double mutant cycle approach to our investigation of *(R)*-roscovitine analogs' interactions with the channel could be to use it to confirm direct interactions between drug side groups and candidate binding residues. Double mutant cycle analyses are commonly used to calculate coupling energies between residues of peptide ligands and their protein targets. In this method, a single residue is mutated in either the target protein, the ligand, or both, and the binding free energy of the ligand-protein interaction is compared between the "both wild-type," "target mutant," "ligand mutant," and "both mutant" conditions. The differences in side groups and effects on $Ca_V2.1$ channels between the many analogs of *(R)*-roscovitine we have characterized presents an opportunity to apply a similar approach in our investigation. If we use MD simulations to predict how the differences in side groups between *(R)*-roscovitine analogs affect which residues they are likely to interact with, we should be able to identify pairs of analogs that will respond differently to a given mutation. We believe it would then be viable to use the double mutant cycle approach to detect a drug-residue interaction by comparing the "analog 1, target wild-type," "analog 1, target mutant," "analog 2, target wild-type" and "analog 2, target mutant" conditions—effectively substituting the different side groups between the two analogs for the wild-type and mutant residues of a peptide ligand. Ideally, there would be only one side-group difference between the two analogs. It would be especially interesting to use this approach to determine whether F1446 directly interacts with KK-20, as our single-site mutagenesis results suggest it might.

In our double mutant cycle in Chapter 5, in order to simply determine whether the effect of one mutation on KK-20 action depended on whether the other mutation was also present, it was

sufficient to compare the fold change in tail current integral and drug tau_d between the wild-type and single and double-mutant channels. For these proposed experiments, however, we would want to convert the coupling coefficient to a coupling energy, in order to use the magnitude of the coupling energy to determine whether the residues are likely to interact directly. This would be appropriate only if we used a measure related to free energy to calculate the coupling coefficient. It would therefore likely be necessary to calculate the K_D for each analog-$Ca_V2.1$ interaction, which we could then use to calculate the binding free energy. Using activation energy derived from voltage-dependence of activation data to calculate coupling energies would not be ideal, since *(R)*-roscovitine analogs enhance inactivation and this would confound measurements of tail current amplitude following depolarizing steps to different voltages in a single cell.

Finally, if we can obtain an open-state model of $Ca_V2.1$ that represents the unique Ca_V2 activation gate structure (Gao et al., 2021), it would be interesting to rerun our automated docking simulations in this model to see if GV-58 is predicted to dock in proximity to different residues than in our Na_VMs-based model. The intrinsic functional dynamics of proteins, such as the transitions between open and closed conformations of the VGCC pore, are encoded in their structures (Bahar et al., 2015). Therefore, it may be possible to predict the desired structure by using a computational method such as anisotropic network modeling (Eyal et al., 2015) to search the inactivated cryo-EM $Ca_V2.2$ structure's conformational space for energetically favorable open conformations.

6.5 An approach for resolving the structure of GV-58 covalently bound to Cav2.1, using a combination of photoaffinity labeling and cryogenic electron microscopy techniques

Thus far, our approach to probing how *(R)*-roscovitine analogs interact with the channel has been to use *in silico* methods to predict residues that might be involved in drug access, binding, or mechanism of action, then perform functional assays of channels with those residues mutated. The experimental mutagenesis approach has been successful in locating binding residues for DHP compounds that act as agonists and antagonists of Ca_V1 channels (Hockerman et al. 1997b), and our experiments in this vein have already yielded valuable insight into *(R)*-roscovitine analog binding.

However, a more direct approach would be to solve the structure of the binding site experimentally. For example, the results of the mutagenesis experiment that characterized DHP-binding residues were later confirmed through cryo-electron microscopy of DHP-bound $Ca_V1.1$ channels, which allowed direct examination of the binding site and residue/drug side group interactions at atomic resolution (Gao and Yan, 2021; Zhao et al., 2019).

Briefly, cryo-EM is a burgeoning technique in electron microscopy in which proteins are rapidly frozen in a layer of vitreous ice and imaged at extremely low temperatures, which allows the use of a higher-intensity electron beam (necessary for high-resolution imaging) without damaging the protein structure; 2D electron microscope images of the protein in many different orientations are then reconstructed into a 3D structure (Milne et al., 2013). A major advantage of cryo-EM over traditional X-ray crystallography for resolving the structures of large membrane proteins like $Ca_V2.1$ is that it circumvents the need to crystallize the channel. Crystallizing large membrane proteins, while not impossible, is extremely difficult and requires a time-intensive process of trial and error, and the resulting crystals are fragile and difficult to resolve at high

resolution (Kermani, 2020). Cryo-EM can also be carried out using purified protein embedded in lipid nanodiscs that emulate the plasma membrane, in order to better capture the native structure of transmembrane proteins (Efremov et al., 2017).

The major obstacle to using this technique to solve the $Ca_V2.1$/GV-58 complex is that GV-58, as we have discussed, likely binds Ca_V2 channels only in the open state (Buraei et al., 2005; Buraei et al., 2007; DeStefino et al., 2010). Since the purified proteins used in cryo-EM are not subject to a membrane potential while they are incubated with ligand and subsequently frozen (or put another way, they are subject to a potential of 0 mV), they are typically imaged in an inactivated conformation. For example, cryo-EM structures of $Ca_V1.1$ and $Ca_V2.2$ were both resolved in inactivated states (Gao et al., 2021; Wu et al., 2016), and this was also true for $Ca_V1.1$ bound by *(S)*-Bay K 8644 (Gao and Yan, 2021; Zhao et al., 2019), which (like *(R)*-roscovitine) is believed to prolong channel opening (Nowycky et al., 1985). While it is possible that GV-58 incubated with $Ca_V2.1$ at 0 mV could enter the central cavity via the III/IV fenestration, it is unlikely that it could bind the channel in its inactivated state, which would preclude capturing EM images of the GV-58-bound channel.

This obstacle could potentially be overcome with the use of photoaffinity labeling to covalently bind GV-58 to a population of $Ca_V2.1$ channels. In this technique, a photoreactive ligand is incubated with its target protein and triggered to covalently bind to (or "crosslink") its target site by irradiation with UV light (Robinette et al., 2006; Smith and Collins, 2015). We are presently collaborating with Dr. Peter Wipf (University of Pittsburgh, Department of Chemistry) to synthesize an analog of GV-58 with a photoreactive azide (Smith and Collins, 2015) attached to its thiophene side group. Our extensive structure-activity relationship information about GV-58, gleaned from the characterization of over 200 analogs through our collaboration with the Wipf

lab, suggests that this photoreactive analog of GV-58 will retain its ability to bind and modify $Ca_V2.1$ channels, although alternative approaches (e.g., attaching a photoreactive diazirine instead (Dubinsky et al., 2012)) could be attempted if the azide analog proved to be nonfunctional.

Although cryo-EM requires a much smaller quantity of protein for successful imaging than X-ray crystallography does, successful cryo-EM of the $Ca_V2.1$/GV-58 complex would still require enough protein that it would need be purified from many cells (Bhella, 2019). To crosslink GV-58 with a large number of $Ca_V2.1$ channels, we would transiently transfect a plate of HEK293 cells with the $Ca_V2.1$ α1 complex and auxiliary subunits, incubate them with GV-58, and briefly depolarize the entire population of cells via bath stimulation. By flashing the cells with UV light during the depolarization, we would activate crosslinking of the photoaffinity-labeled GV-58 during its binding to the open-state-dependent binding site. The covalently bound $Ca_V2.1$/GV-58 complex could then be purified and imaged via cryo-EM without risk of GV-58 dissociating from inactivated channels.

A potential, but surmountable, complication to this approach is that HEK293 cells have an unusually depolarized resting membrane potential that causes $Ca_V2.1$ channels to inactivate when not subject to voltage clamp. As discussed in Chapter 3, we have used *in silico* methods to predict that GV-58 can easily move through the III/IV fenestration in inactivated state $Ca_V2.1$. However, if in reality GV-58 can only access its binding site via this fenestration in the true closed, resting state of the channel, it would be necessary to incubate GV-58 with $Ca_V2.1$ under hyperpolarized conditions prior to depolarization and photoactivation in order to obtain the covalently bound $Ca_V2.1$/GV-58 complex. This could be accomplished by overexpressing two-pore domain potassium channels in the HEK293 cells, which has been shown to hyperpolarize the membrane resting potential in these cells via K^+ leak current (MacKenzie et al., 2014).

In the event that we are unable to find a collaborator with cryo-EM expertise, or attempts at cryo-EM of the $Ca_V2.1$/GV-58 complex are unsuccessful, an alternative approach would be to use tandem mass spectrometry to identify the residues with which the covalently bound GV-58 interacts (Jahn et al., 2003). However, the cryo-EM approach would have benefits beyond simply identifying the binding residues, as it would provide the opportunity to examine how the bound drug affects the conformation of the channel. For example, our and Buraei et al. (2005)'s experimental findings support that drug unbinding is not required for channel closure, which could be confirmed if the solved $Ca_V2.1$/GV-58 complex is found to be in an inactivated state, or refuted if the drug-bound pore is found to be trapped in an open conformation. While we do not think it is likely, if covalently bound GV-58 *did* prevent the channel from inactivating at 0 mV, this could be a way to obtain a solved open-state structure of $Ca_V2.1$. Alternatively, in the event that covalently GV-58-bound $Ca_V2.1$ channels inactivate as expected, we speculate—based on our hypothesis that GV-58 prolongs the open state by increasing the energy barrier of the transition from the open to the closed pore—that solving the $Ca_V2.1$ structure both with and without GV-58 may reveal a less stable, higher-energy conformation of the closed pore in the bound channel. If so, comparing the bound and unbound pore structures—and then experimentally interrogating hypotheses based on this comparison—could provide new insight not only into GV-58's mechanism of action, but into the intrinsic mechanisms that regulate pore gating in $Ca_V2.1$.

Bibliography

Alvares, D. S., dos Santos Cabrera, M. P., & Neto, J. R. (2016). Strategies for exploring electrostatic and nonelectrostatic contributions to the interaction of helical antimicrobial peptides with model membranes. In *Advances in Biomembranes and Lipid Self-Assembly* (Vol. 24, pp. 43-73). Academic Press. doi:10.1016/bs.abl.2016.05.001

Akaike, N., Tsuda, Y., & Oyama, Y. (1988). Separation of current-and voltage-dependent inactivation of calcium current in frog sensory neuron. *Neuroscience letters, 84*(1), 46-50. doi:10.1016/0304-3940(88)90335-7 PMID: 2450318

Arikkath, J., & Campbell, K. P. (2003). Auxiliary subunits: essential components of the voltage-gated calcium channel complex. *Current opinion in neurobiology, 13*(3), 298-307. doi:10.1016/s0959-4388(03)00066-7 PMID: 12850214

Altschul, S. F., Madden, T. L., Schäffer, A. A., Zhang, J., Zhang, Z., Miller, W., & Lipman, D. J. (1997). Gapped BLAST and PSI-BLAST: a new generation of protein database search programs. *Nucleic acids research*, *25*(17), 3389-3402. doi: 10.1093/nar/25.17.3389 PMID: 9254694 PMCID: PMC146917

Bahar, I., Cheng, M. H., Lee, J. Y., Kaya, C., & Zhang, S. (2015). Structure-encoded global motions and their role in mediating protein-substrate interactions. *Biophysical journal*, *109*(6), 1101-1109. doi:10.1016/j.bpj.2015.06.004 PMID: 26143655 PMCID: PMC4576147

Beske, P. H., Hoffman, K. M., Machamer, J. B., Eisen, M. R., & McNutt, P. M. (2017). Use-dependent potentiation of voltage-gated calcium channels rescues neurotransmission in nerve terminals intoxicated by botulinum neurotoxin serotype A. *Scientific reports, 7*(1), 1-11. doi:10.1038/s41598-017-16064-3 PMID: 29158500 PMCID: PMC5696531

Bettayeb, K., Baunbæk, D., Delehouze, C., Loaëc, N., Hole, A. J., Baumli, S., Endicott, J., Douc-Rasy, S., Bénard, J., Oumata, N., Galons, H., & Meijer, L. (2010). CDK inhibitors roscovitine and CR8 trigger Mcl-1 down-regulation and apoptotic cell death in neuroblastoma cells. *Genes & cancer, 1*(4), 369-380. doi:10.1177/1947601910369817 PMID: 21779453 PMCID: PMC3092200

Beyl, S., Kügler, P., Kudrnac, M., Hohaus, A., Hering, S., & Timin, E. (2009). Different pathways for activation and deactivation in CaV1. 2: a minimal gating model. *Journal of General Physiology, 134*(3), 231-241. doi:10.1085/jgp.200910272 PMID: 19687230 PMCID: PMC2737230

Beyl, S., Depil, K., Hohaus, A., Stary-Weinzinger, A., Linder, T., Timin, E., & Hering, S.

(2012). Neutralisation of a single voltage sensor affects gating determinants in all four pore-forming S6 segments of CaV 1.2: a cooperative gating model. *Pflügers Archiv-European Journal of Physiology, 464*(4), 391-401. doi: 10.1007/s00424-012-1144-5 PMID: 22941337 PMCID: PMC3790253

Beyl, S., Kügler, P., Hohaus, A., Depil, K., Hering, S., & Timin, E. (2014). Methods for quantification of pore–voltage sensor interaction in CaV 1.2. *Pflügers Archiv-European Journal of Physiology, 466*(2), 265-274. doi: 10.1007/s00424-013-1319-8 PMID: 23873350 PMCID: PMC3902079

Beyl, S., Hohaus, A., Andranovits, S., Timin, E., & Hering, S. (2016). Upward movement of IS4 and IIIS4 is a rate-limiting stage in Ca v 1.2 activation. *Pflügers Archiv-European Journal of Physiology, 468*(11), 1895-1907. doi:10.1007/s00424-016-1895-5 PMID: 27796578 PMCID: PMC5138263

Bezanilla, F. (2000). The voltage sensor in voltage-dependent ion channels. *Physiological reviews, 80*(2), 555-592. doi:10.1152/physrev.2000.80.2.555 PMID: 10747201

Bezanilla, F. (2018). Gating currents. *Journal of General Physiology, 150*(7), 911-932. doi:10.1085/jgp.201812090 PMID: 29941430 PMCID: PMC6028497

Bhella, D. (2019). Cryo-electron microscopy: an introduction to the technique, and considerations when working to establish a national facility. *Biophysical reviews, 11*(4), 515-519. doi:10.1007/s12551-019-00571-w PMID: 31359340 PMCID: PMC6682334

Boiteux, C., Vorobyov, I., French, R. J., French, C., Yarov-Yarovoy, V., & Allen, T. W. (2014). Local anesthetic and antiepileptic drug access and binding to a bacterial voltage-gated sodium channel. *Proceedings of the National Academy of Sciences, 111*(36), 13057-13062. doi: 10.1073/pnas.1408710111 PMID: 25136136 PMCID: PMC4246943

Branchaw, J. L., Banks, M. I., & Jackson, M. B. (1997). Ca2+-and voltage-dependent inactivation of Ca2+ channels in nerve terminals of the neurohypophysis. Journal of *Neuroscience, 17*(15), 5772-5781. doi:10.1523/JNEUROSCI.17-15-05772.1997 PMID: 9221775 PMCID: PMC6573212

Bruhova, I., & Zhorov, B. S. (2010). A homology model of the pore domain of a voltage-gated calcium channel is consistent with available SCAM data. *Journal of General Physiology*, *135*(3), 261-274. doi:10.1085/jgp.200910288 PMID: 20176854 PMCID: PMC2828909

Buraei, Z., Anghelescu, M., & Elmslie, K. S. (2005). Slowed N-type calcium channel (CaV2. 2) deactivation by the cyclin-dependent kinase inhibitor roscovitine. *Biophysical journal, 89*(3), 1681-1691. PMID: 15951378 PMCID: PMC1366672 doi:10.1529/biophysj.104.052837

Buraei, Z., Schofield, G., & Elmslie, K. S. (2007). Roscovitine differentially affects CaV2 and

Kv channels by binding to the open state. *Neuropharmacology, 52*(3), 883-894. doi:10.1016/j.neuropharm.2006.10.006 PMID: 17125805

Buraei, Z., & Elmslie, K. S. (2008). The separation of antagonist from agonist effects of trisubstituted purines on CaV2. 2 (N-type) channels. *Journal of neurochemistry, 105*(4), 1450-1461. doi:10.1111/j.1471-4159.2008.05248.x PMID: 18221369

Buraei, Z., & Yang, J. (2010). The β subunit of voltage-gated Ca2+ channels. *Physiological reviews*, *90*(4), 1461-1506. doi:10.1152/physrev.00057.2009 PMID: 20959621 PMCID: PMC4353500

Cao, Y. Q., & Tsien, R. W. (2005). Effects of familial hemiplegic migraine type 1 mutations on neuronal P/Q-type Ca2+ channel activity and inhibitory synaptic transmission. *Proceedings of the National Academy of Sciences, 102*(7), 2590-2595. doi:10.1073/pnas.0409896102 PMID: 15699344 PMCID: PMC548328

Catterall, W. A. (1995). Structure and function of voltage-gated ion channels. *Annual review of biochemistry, 64*(1), 493-531. doi:10.1146/annurev.bi.64.070195.002425 PMID: 7574491

Catterall, W. A. (2000). Structure and regulation of voltage-gated Ca2+ channels. *Annu Rev Cell Dev Biol., 16*(1), 521-55. doi:10.1146/annurev.cellbio.16.1.521 PMID: 11031246

Catterall, W. A., Perez-Reyes, E., Snutch, T. P., & Striessnig, J. (2005). International Union of Pharmacology. XLVIII. Nomenclature and structure-function relationships of voltage-gated calcium channels. *Pharmacological reviews, 57*(4), 411-425. doi:10.1124/pr.57.4.5 PMID: 16382099

Catterall, W. A. (2010). Ion channel voltage sensors: structure, function, and pathophysiology. *Neuron, 67*(6), 915-928. doi:10.1016/j.neuron.2010.08.021 PMID: 20869590 PMCID: PMC2950829

Catterall, W. A. (2011). Voltage-gated calcium channels. *Cold Spring Harbor perspectives in biology, 3*(8), a003947. doi:10.1101/cshperspect.a003947 PMID: 21746798 PMCID: PMC3140680

Chae, T., Kwon, Y. T., Bronson, R., Dikkes, P., Li, E., & Tsai, L. H. (1997). Mice lacking p35, a neuronal specific activator of Cdk5, display cortical lamination defects, seizures, and adult lethality. *Neuron, 18*(1), 29-42. doi:10.1016/s0896-6273(01)80044-1 PMID: 9010203

Chen, J., Billings, S. E., & Nishimune, H. (2011). Calcium channels link the muscle-derived synapse organizer laminin β2 to Bassoon and CAST/Erc2 to organize presynaptic active zones. *Journal of Neuroscience, 31*(2), 512-525. doi:10.1523/JNEUROSCI.3771-10.2011 PMID: 21228161 PMCID: PMC3723116

Cho, S., & Meriney, S. D. (2006). The effects of presynaptic calcium channel modulation by roscovitine on transmitter release at the adult frog neuromuscular junction. *European Journal of Neuroscience, 23*(12), 3200-3208. doi:10.1111/j.1460-9568.2006.04849.x PMID: 16820010

Chovancova, E., Pavelka, A., Benes, P., Strnad, O., Brezovsky, J., Kozlikova, B., ... & Damborsky, J. (2012). CAVER 3.0: a tool for the analysis of transport pathways in dynamic protein structures. *PLoS Computational Biology 8: 8*(10), e1002708. doi:10.1371/journal.pcbi.1002708 PMID: 23093919 PMCID: PMC3475669

Cicenas, J., Kalyan, K., Sorokinas, A., Stankunas, E., Levy, J., Meskinyte, I., Stankevicius, V., Kaupinis, A., & Valius, M. (2015). Roscovitine in cancer and other diseases. *Annals of translational medicine, 3*(10). doi:10.3978/j.issn.2305-5839.2015.03.61 PMID: 26207228 PMCID: PMC4486920

Clapham, D. E. (2007). Calcium signaling. *Cell, 131*(6), 1047-1058. doi:10.1016/j.cell.2007.11.028 PMID: 18083096

Collins, I., & Garrett, M. D. (2005). Targeting the cell division cycle in cancer: CDK and cell cycle checkpoint kinase inhibitors. *Current opinion in pharmacology*, *5*(4), 366-373. doi:10.1016/j.coph.2005.04.009 PMID: 15964238

Das, A., Gur, M., Cheng, M. H., Jo, S., Bahar, I., & Roux, B. (2014). Exploring the conformational transitions of biomolecular systems using a simple two-state anisotropic network model. *PLoS computational biology, 10*(4), e1003521. doi:10.1371/journal.pcbi.1003521 PMID: 24699246 PMCID: PMC3974643

De Azevedo, W. F., Leclerc, S., Meijer, L., Havlicek, L., Strnad, M., & Kim, S. H. (1997). Inhibition of cyclin-dependent kinases by purine analogues: crystal structure of human cdk2 complexed with roscovitine. *European journal of biochemistry*, *243*(1-2), 518-526. doi:10.1111/j.1432-1033.1997.0518a.x PMID: 9030780

Demers-Giroux, P. O., Bourdin, B., Sauvé, R., & Parent, L. (2013). Cooperative activation of the T-type CaV3.2 channel: interaction between domains II and III. *Journal of Biological Chemistry, 288*(41), 29281-29293. doi:10.1074/jbc.M113.500975 PMID: 23970551 PMCID: PMC3795230

Depil, K., Beyl, S., Stary-Weinzinger, A., Hohaus, A., Timin, E., & Hering, S. (2011). Timothy mutation disrupts the link between activation and inactivation in Cav1. 2 protein. *Journal of Biological Chemistry, 286*(36), 31557-31564. doi:10.1074/jbc.M111.255273 PMID: 21685391 PMCID: PMC3173108

Desaphy, J. F., Dipalma, A., Costanza, T., Carbonara, R., Dinardo, M. M., Catalano, A., Carocci, A., Lentini, G., Franchini, C., & Conte Camerino, D. (2012). Molecular insights into the local anesthetic receptor within voltage-gated sodium channels using hydroxylated analogs of mexiletine. *Frontiers in pharmacology, 3*, 17. doi: 10.3389/fphar.2012.00017

PMID: 22403541 PMCID: PMC3279704

DeStefino, N. R., Pilato, A. A., Dittrich, M., Cherry, S. V., Cho, S., Stiles, J. R., & Meriney, S. D. (2010). (R)-roscovitine prolongs the mean open time of unitary N-type calcium channel currents. *Neuroscience, 167*(3), 838-849. doi:10.1016/j.neuroscience.2010.02.041 PMID: 20188151 PMCID: PMC2854255

Dietrich, D., Kirschstein, T., Kukley, M., Pereverzev, A., von der Brelie, C., Schneider, T., & Beck, H. (2003). Functional specialization of presynaptic Cav2. 3 Ca2+ channels. *Neuron*, *39*(3), 483-496. doi:10.1016/s0896-6273(03)00430-6 PMID: 12895422

Dill, K., Jernigan, R. L., & Bahar, I. (2017). *Protein actions: Principles and modeling*. Garland Science.

Dolphin, A. C. (2006). A short history of voltage-gated calcium channels. *British journal of pharmacology*, *147*(S1), S56-S62. doi:10.1038/sj.bjp.0706442 PMID: 16402121 PMCID: PMC1760727

Dolphin, A. C. (2009). Calcium channel diversity: multiple roles of calcium channel subunits. *Current opinion in neurobiology*, *19*(3), 237-244. doi:10.1016/j.conb.2009.06.006 PMID: 19559597

Dolphin, A. C. (2012). Calcium channel auxiliary α 2 δ and β subunits: trafficking and one step beyond. *Nature Reviews Neuroscience*, *13*(8), 542-555. doi:10.1038/nrn3311 PMID: 22805911

Dolphin, A. C. (2018). Voltage-gated calcium channels: their discovery, function and importance as drug targets. *Brain and neuroscience advances*, *2*, 2398212818794805. doi:10.1177/2398212818794805 PMID: 30320224 PMCID: PMC6179141

Dubinsky, L., Krom, B. P., & Meijler, M. M. (2012). Diazirine based photoaffinity labeling. *Bioorganic & medicinal chemistry, 20*(2), 554-570. doi:10.1016/j.bmc.2011.06.066 PMID: 21778062

Durell, S. R., & Guy, H. R. (1992). Atomic scale structure and functional models of voltage-gated potassium channels. *Biophysical Journal, 62*(1), 238-250. doi:10.1016/S0006-3495(92)81809-X PMID: 1600096 PMCID: PMC1260525

Eaton, L. M., & Lambert, E. H. (1957). Electromyography and electric stimulation of nerves in diseases of motor unit: observations on myasthenic syndrome associated with malignant tumors. *Journal of the American Medical Association, 163*(13), 1117-1124. doi:10.1001/jama.1957.02970480021005 PMID: 13405774

Efremov, R. G., Gatsogiannis, C., & Raunser, S. (2017). Lipid nanodiscs as a tool for high-

resolution structure determination of membrane proteins by single-particle cryo-EM. *Methods in enzymology, 594,* 1-30. doi:10.1016/bs.mie.2017.05.007 PMID: 28779836

Ertel, E. A., Campbell, K. P., Harpold, M. M., Hofmann, F., Mori, Y., Perez-Reyes, E., Schwartz, A., Snutch, T. P., Tanabe, T., Birnbaumer, L., Tsien, R.W., & Catterall, W. A. (2000). Nomenclature of voltage-gated calcium channels. *Neuron, 25*(3), 533-535. doi:10.1016/s0896-6273(00)81057-0 PMID: 10774722

Eyal, E., Lum, G., & Bahar, I. (2015). The anisotropic network model web server at 2015 (ANM 2.0). *Bioinformatics*, *31*(9), 1487-1489. doi:10.1093/bioinformatics/btu847 PMID: 25568280 PMCID: PMC4410662

Fellin, T., Luvisetto, S., Spagnolo, M., & Pietrobon, D. (2004). Modal gating of human CaV2. 1 (P/Q-type) calcium channels: II. The b mode and reversible uncoupling of inactivation. The *Journal of general physiology, 124*(5), 463-474. doi: 10.1085/jgp.200409035 PMID: 15504897 PMCID: PMC2234006

Ferreira-Camargo, L. S., Tran, M., Beld, J., Burkart, M. D., & Mayfield, S. P. (2015). Selenocystamine improves protein accumulation in chloroplasts of eukaryotic green algae. *AMB Express*, *5*(1), 1-11. doi:10.1186/s13568-015-0126-3 PMID: 26137911 PMCID: PMC4489976

Fernández-Quintero, M. L., El Ghaleb, Y., Tuluc, P., Campiglio, M., Liedl, K. R., & Flucher, B. E. (2021). *Structural determinants of voltage-gating properties in calcium channels. Elife, 10*, e64087. doi:10.7554/eLife.64087 PMID: 33783354 PMCID: PMC8099428

Filipovic, J., Vavra, O., Plhak, J., Bednar, D., Marques, S.M., Brezovsky, J., Matyska,L., & Damborsky, J. (2019). CaverDock: a novel method for the fast analysis of ligand transport. *IEEE/ACM transactions on computational biology and bioinformatics, 17*(5), 1625-1638. doi:10.1109/TCBB.2019.2907492

Fletcher, C. F., Tottene, A., Lennon, V. A., Wilson, S. M., Dubel, S. J., Paylor, R., Hosford, D. A., Tessarollo, L., McEnergy, M. W., Pietrobon, D., Copeland, N. G., & Jenkins, N. A. (2001). Dystonia and cerebellar atrophy in Cacna1a null mice lacking P/Q calcium channel activity. *The FASEB Journal, 15*(7), 1288-1290. doi:10.1096/fj.00-0562fje PMID: 11344116

Flink, M. T., & Atchison, W. D. (2002). Passive transfer of Lambert-Eaton syndrome to mice induces dihydropyridine sensitivity of neuromuscular transmission. *The Journal of physiology, 543*(2), 567-576. doi:10.1113/jphysiol.2002.021048 PMID: 12205190 PMCID: PMC2290502

Franckowiak, G., Bechem, M., Schramm, M., & Thomas, G. (1985). The optical isomers of the 1, 4-dihydropyridine BAY K 8644 show opposite effects on Ca channels. *European journal of pharmacology, 114*(2), 223-226. doi:10.1016/0014-2999(85)90631-4 PMID: 2412855

Fukuda, T., Motomura, M., Nakao, Y., Shiraishi, H., Yoshimura, T., Iwanaga, K., Tsujihata, M., Dosaka-Akita, H., & Eguchi, K. (2003). Reduction of P/Q-type calcium channels in the postmortem cerebellum of paraneoplastic cerebellar degeneration with Lambert-Eaton myasthenic syndrome. *Annals of Neurology: Official Journal of the American Neurological Association and the Child Neurology Society, 53*(1), 21-28. doi:10.1002/ana.10392 PMID: 12509844

Fukuoka, T., Engel, A. G., Lang, B., Newsom-Davis, J., Prior, C., & W.-Wray, D. (1987). Lambert-Eaton myasthenic syndrome: I. Early morphological effects of IgG on the presynaptic membrane active zones. *Annals of Neurology: Official Journal of the American Neurological Association and the Child Neurology Society, 22*(2), 193-199. doi: 10.1002/ana.410220203 PMID: 3662451

Fukunaga, H., Engel, A. G., Lang, B., Newsom-Davis, J., & Vincent, A. (1983). Passive transfer of Lambert-Eaton myasthenic syndrome with IgG from man to mouse depletes the presynaptic membrane active zones. *Proceedings of the National Academy of Sciences, 80*(24), 7636-7640. doi:10.1073/pnas.80.24.7636 PMID: 6584877 PMCID: PMC534395

Gao, S., & Yan, N. (2021). Structural Basis of the Modulation of the Voltage-Gated Calcium Ion Channel Cav1.1 by Dihydropyridine Compounds. *Angewandte Chemie, 133*(6), 3168-3174. doi10.1002/anie.202011793 PMID: 33125829 PMCID: PMC7898392

Gao, S., Yao, X., Yan, N (2021). Structure of human Cav2.2 channel blocked by the painkiller ziconotide. *Nature, 596*(7870), 143-147. doi:10.1038/s41586-021-03699-6 PMID: 34234349

Gibson, D. G., Young, L., Chuang, R. Y., Venter, J. C., Hutchison, C. A., & Smith, H. O. (2009). Enzymatic assembly of DNA molecules up to several hundred kilobases. *Nature methods*, *6*(5), 343-345. doi:10.1038/nmeth.1318 PMID: 19363495

Glasgow, N. G., Povysheva, N. V., Azofeifa, A. M., & Johnson, J. W. (2017). Memantine and ketamine differentially alter NMDA receptor desensitization. *Journal of Neuroscience, 37*(40), 9686-9704. doi:10.1523/JNEUROSCI.1173-17.2017 PMID: 28877967 PMCID: PMC5628409

Guidelli, R. (2020). The common features of tetrameric ion channels and the role of electrostatic interactions. *Electrochemistry Communications*, *121*, 106866. doi:10.1016/j.elecom.2020.106866

Gurnett, C. A., Felix, R., & Campbell, K. P. (1997). Extracellular interaction of the voltage-dependent Ca2+ channel α2δ and α1 subunits. *Journal of Biological Chemistry, 272*(29), 18508-18512. doi:10.1074/jbc.272.29.18508 PMID: 9218497

Haliloglu, T., & Bahar, I. (2015). Adaptability of protein structures to enable functional

interactions and evolutionary implications. *Current opinion in structural biology*, *35*, 17-23. doi:10.1016/j.sbi.2015.07.007 PMID: 26254902 PMCID: PMC4688206

Helton, T. D., Xu, W., & Lipscombe, D. (2005). Neuronal L-type calcium channels open quickly and are inhibited slowly. *Journal of Neuroscience, 25*(44), 10247-10251. doi:10.1523/JNEUROSCI.1089-05.2005 PMID: 16267232 PMCID: PMC6725800

Hering, S., Beyl, S., Stary, A., Kudrnac, M., Hohaus, A., Guy, R. H., & Timin, E. (2008). Pore stability and gating in voltage-activated calcium channels. *Channels, 2*(2), 61-69. doi:10.4161/chan.2.2.5999 PMID: 18849656 PMCID: PMC3196840

Hering, S., Zangerl-Plessl, E. M., Beyl, S., Hohaus, A., Andranovits, S., & Timin, E. N. (2018). Calcium channel gating. *Pflugers Arch - Eur J Physiol 470*, 1291–1309. doi:10.1007/s00424-018-2163-7 PMID: 29951751

Hille, B. (1977a). Local anesthetics: hydrophilic and hydrophobic pathways for the drug-receptor reaction. *Journal of General Physiology, 69*(4), 497-515. doi:10.1085/jgp.69.4.497 PMID: 300786 PMCID: PMC2215053s

Hille, B. (1977b). The pH-dependent rate of action of local anesthetics on the node of Ranvier. *The Journal of general physiology, 69*(4), 475-496. doi: 10.1085/jgp.69.4.475 PMID: 16078 PMCID: PMC2215051

Hockerman, G. H., Peterson, B. Z., Johnson, and, B. D., & Catterall, W. A. (1997). Molecular determinants of drug binding and action on L-type calcium channels. *Annual review of pharmacology and toxicology*, *37*(1), 361-396. doi:10.1146/annurev.pharmtox.37.1.361 PMID: 9131258

Hockerman, G. H., Peterson, B. Z., Sharp, E., Tanada, T. N., Scheuer, T., & Catterall, W. A. (1997b). Construction of a high-affinity receptor site for dihydropyridine agonists and antagonists by single amino acid substitutions in a non-L-type Ca2+ channel. Proceedings of the National Academy of Sciences, 94(26), 14906-14911. doi:10.1073/pnas.94.26.14906 PMID: 9405712 PMCID: PMC25136

Hohaus, A., Beyl, S., Kudrnac, M., Berjukow, S., Timin, E. N., Marksteiner, R., Maw, M., & Hering, S. (2005). Structural determinants of L-type channel activation in segment IIS6 revealed by a retinal disorder. *Journal of Biological Chemistry, 280*(46), 38471-38477. doi:10.1074/jbc.M507013200 PMID: 16157588 PMCID: PMC3189691

Horn, R., Ding, S., & Gruber, H. J. (2000). Immobilizing the moving parts of voltage-gated ion channels. *The Journal of general physiology, 116*(3), 461-476. doi:10.1085/jgp.116.3.461 PMID: 10962021 PMCID: PMC2233689

Horovitz, A. (1996). Double-mutant cycles: a powerful tool for analyzing protein structure and function. *Folding and Design, 1*(6), R121-R126. doi:10.1016/S1359-0278(96)00056-9 PMID: 9080186

Humphrey, W., Dalke, A., & Schulten, K. (1996). VMD: visual molecular dynamics. *Journal of molecular graphics*, *14*(1), 33-38. doi:10.1016/0263-7855(96)00018-5 PMID: 8744570

Jahn, O., Tezval, H., Spiess, J., & Eckart, K. (2003). Tandem mass spectrometric characterization of branched peptides derived from photoaffinity labeling. *International Journal of Mass Spectrometry, 228*(2-3), 527-540. doi:10.1016/S1387-3806(03)00159-3

Jo, S., & Bean, B. P. (2014). Sidedness of carbamazepine accessibility to voltage-gated sodium channels. *Molecular pharmacology, 85*(2), 381-387. doi:10.1124/mol.113.090472 PMID: 24319110 PMCID: PMC3913360

Kelley, L. A., Mezulis, S., Yates, C. M., Wass, M. N., & Sternberg, M. J. (2015). The Phyre2 web portal for protein modeling, prediction and analysis. *Nature protocols*, *10*(6), 845-858. doi:10.1038/nprot.2015.053 doi: 10.1038/nprot.2015.053

Kermani, A. A. (2020). A guide to membrane protein X-ray crystallography. *The FEBS journal, 288*(20), 5788–5804. doi:10.1111/febs.15676 PMID: 33340246

Kesner, V. G., Oh, S. J., Dimachkie, M. M., & Barohn, R. J. (2018). Lambert-Eaton myasthenic syndrome. *Neurologic clinics, 36*(2), 379-394. doi:10.1016/j.ncl.2018.01.008 PMID: 29655456 PMCID: PMC6690495

Kumar, S., & Nussinov, R. (2002). Close-range electrostatic interactions in proteins. *ChemBioChem*, *3*(7), 604-617. doi:10.1002/1439-7633(20020703)3:7<604::AID-CBIC604>3.0.CO;2-X PMID: 12324994

Laghaei, R., Ma, J., Tarr, T. B., Homan, A. E., Kelly, L., Tilvawala, M. S., ... & Dittrich, M. (2018). Transmitter release site organization can predict synaptic function at the neuromuscular junction. *Journal of neurophysiology*, *119*(4), 1340-1355. doi:10.1152/jn.00168.2017 PMID: 29357458 PMCID: PMC5966726

Lambert, E. H., & Elmqvist, D. (1971). Quantal components of end-plate potentials in the myasthenic syndrome. *Annals of the New York Academy of Sciences, 183*(1), 183-199. doi:10.1111/j.1749-6632.1971.tb30750.x PMID: 4330759

Lang, B., Newsom-Davis, J., Prior, C., & Wray, D. W. (1983). Antibodies to motor nerve terminals: an electrophysiological study of a human myasthenic syndrome transferred to mouse. *The Journal of physiology, 344*(1), 335-345. doi:10.1113/jphysiol.1983.sp014943 PMID: 6655585 PMCID: PMC1193844

Lee, J., Kim, D., & Shin, H. S. (2004). Lack of delta waves and sleep disturbances during non-rapid eye movement sleep in mice lacking α1G-subunit of T-type calcium channels. *Proceedings of the National Academy of Sciences, 101*(52), 18195-18199. doi:10.1073/pnas.0408089101 PMID: 15601764 PMCID: PMC539778

Lenaeus, M. J., Burdette, D., Wagner, T., Focia, P. J., & Gross, A. (2014). Structures of KcsA in complex with symmetrical quaternary ammonium compounds reveal a hydrophobic binding site. Biochemistry, 53(32), 5365-5373. doi: 10.1021/bi500525s PMID: 25093676 PMCID: PMC4139162

Leuranguer, V., Dirksen, R. T., & Beam, K. G. (2003). Potentiated L-type Ca2+ channels rectify. *The Journal of general physiology*, *121*(6), 541-550. doi:10.1085/jgp.200308833 PMID: 12743165 PMCID: PMC2217356

Liang, M., Tarr, T. B., Bravo-Altamirano, K., Valdomir, G., Rensch, G., Swanson, L., DeStefino N.R., Mazzarisi C. M., Olszewski, R. A., Wilson, G. M., Meriney, S. D., & Wipf, P. (2012). Synthesis and biological evaluation of a selective N-and P/Q-type calcium channel agonist. *ACS medicinal chemistry letters, 3*(12), 985-990. doi:10.1021/ml3002083 PMID: 24936234 PMCID: PMC4056936

Lin, Y., McDonough, S. I., & Lipscombe, D. (2004). Alternative splicing in the voltage-sensing region of N-Type CaV2. 2 channels modulates channel kinetics. *Journal of neurophysiology, 92*(5), 2820-2830. doi:10.1152/jn.00048.2004 PMID: 15201306

Lindquist, S., & Stangel, M. (2011). Update on treatment options for Lambert–Eaton myasthenic syndrome: focus on use of amifampridine. *Neuropsychiatric disease and treatment, 7*, 341. doi:10.2147/NDT.S10464 PMID: 21822385 PMCID: PMC3148925

Liu, Y., & Bahar, I. (2012). Sequence evolution correlates with structural dynamics. *Molecular biology and evolution*, *29*(9), 2253-2263. doi:10.1093/molbev/mss097 PMID: 22427707 PMCID: PMC3424413

Long, S. B., Campbell, E. B., & MacKinnon, R. (2005). Voltage sensor of Kv1. 2: structural basis of electromechanical coupling. *Science, 309*(5736), 903-908. doi:10.1126/science.1116270 PMID: 16002579

Luo, F., Dittrich, M., Stiles, J. R., & Meriney, S. D. (2011). Single-pixel optical fluctuation analysis of calcium channel function in active zones of motor nerve terminals. *Journal of Neuroscience, 31*(31), 11268-11281. doi:10.1523/JNEUROSCI.1394-11.2011 PMID: 21813687 PMCID: PMC3412372

Luo, F., Dittrich, M., Cho, S., Stiles, J. R., & Meriney, S. D. (2015). Transmitter release is evoked with low probability predominately by calcium flux through single channel openings at the frog neuromuscular junction. *Journal of neurophysiology, 113*(7), 2480-2489. doi:10.1152/jn.00879.2014 PMID: 25652927 PMCID: PMC4416571

MacKenzie, G., Franks, N. P., & Brickley, S. G. (2015). Two-pore domain potassium channels enable action potential generation in the absence of voltage-gated potassium channels. *Pflügers Archiv-European Journal of Physiology, 467*(5), 989-999. doi:10.1007/s00424-014-1660-6 PMID: 25482670 PMCID: PMC4428809

Mangoni, M. E., Traboulsie, A., Leoni, A. L., Couette, B., Marger, L., Le Quang, K., Kupfer, E., Cohen-Solal, A., Vilar, J., Shin, H., Escande, D., Charpentier, F., Nargeot, J., & Lory, P. (2006). Bradycardia and slowing of the atrioventricular conduction in mice lacking CaV3. 1/α1G T-type calcium channels. *Circulation research, 98*(11), 1422-1430. doi:10.1161/01.RES.0000225862.14314.49 PMID: 16690884

Mareska, M., & Gutmann, L. (2004, June). Lambert-Eaton myasthenic syndrome. *In Seminars in neurology* (Vol. 24, No. 02, pp. 149-153). Copyright© 2004 by Thieme Medical Publishers, Inc., 333 Seventh Avenue, New York, NY 10001, USA. doi:10.1055/s-2004-830900 PMID: 15257511

Matthews, B. W. (1993). Structural and genetic analysis of protein stability. *Annual review of biochemistry*, *62*(1), 139-160. doi:10.1146/annurev.bi.62.070193.001035. PMID: 8352587

Meriney, S. D., & Dittrich, M. (2013). Organization and function of transmitter release sites at the neuromuscular junction. *The Journal of physiology, 591*(13), 3159-3165.

Meriney, S. D., Umbach, J. A., & Gundersen, C. B. (2014). Fast, Ca2+-dependent exocytosis at nerve terminals: Shortcomings of SNARE-based models. *Progress in neurobiology*, *121*, 55-90. doi:10.1016/j.pneurobio.2014.07.001. Epub 2014 Jul 17. PMID: 25042638

Meriney, S. D., Tarr, T. B., Ojala, K. S., Wu, M., Li, Y., Lacomis, D., Garcia-Ocano, A., Liang, M., Valdomir, G., & Wipf, P. (2018). Lambert-Eaton myasthenic syndrome: mouse passive-transfer model illuminates disease pathology and facilitates testing therapeutic leads. *Annals of the New York Academy of Sciences, 1412*(1), 73. doi:10.1111/nyas.13512 PMID: 29125190 PMCID: PMC5790601

Meriney, S., & Fanselow, E. (2019). *Synaptic transmission*. Academic Press.

Milne, J. L., Borgnia, M. J., Bartesaghi, A., Tran, E. E., Earl, L. A., Schauder, D. M., Lengyel, J., Pierson, J., Patwardhan, A., & Subramaniam, S. (2013). Cryo-electron microscopy–a primer for the non-microscopist. *The FEBS journal, 280*(1), 28-45. doi:10.1111/febs.12078 PMID: 23181775 PMCID: PMC3537914

Mitterdorfer, J., Wang, Z., Sinnegger, M. J., Hering, S., Jörg, S., Grabner, M., & Glossmann, H. (1996). Two amino acid residues in the IIIS5 segment of L-type calcium channels differentially contribute to 1, 4-dihydropyridine sensitivity. *Journal of Biological Chemistry, 271*(48), 30330-30335. doi:10.1074/jbc.271.48.30330 PMID: 8939992

Monera, O. D., Sereda, T. J., Zhou, N. E., Kay, C. M., & Hodges, R. S. (1995). Relationship of sidechain hydrophobicity and α-helical propensity on the stability of the single-stranded amphipathic α-helix. *Journal of peptide science: an official publication of the European Peptide Society*, *1*(5), 319-329. doi:10.1002/psc.310010507 PMID: 9223011

Motomura, M., Lang, B., Johnston, I., Palace, J., Vincent, A., & Newsom-Davis, J. (1997).

Incidence of serum anti-P/Q-type and anti-N-type calcium channel autoantibodies in the Lambert-Eaton myasthenic syndrome. *Journal of the neurological sciences, 147(*1), 35-42. doi:10.1016/s0022-510x(96)05303-8 PMID: 9094058

Motulsky, H. J., & Brown, R. E. (2006). Detecting outliers when fitting data with nonlinear regression–a new method based on robust nonlinear regression and the false discovery rate. *BMC bioinformatics, 7*(1), 1-20. doi:10.1186/1471-2105-7-123 PMID: 16526949 PMCID: PMC1472692

Nagel, A., Engel, A. G., Lang, B., Newsom-Davis, J., & Fukuoka, T. (1988). Lambert-Eaton myasthenic syndrome IgG depletes presynaptic membrane active zone particles by antigenic modulation. *Annals of Neurology: Official Journal of the American Neurological Association and the Child Neurology Society, 24*(4), 552-558. doi:10.1002/ana.410240412 PMID: 2853605

Nagwaney, S., Harlow, M. L., Jung, J. H., Szule, J. A., Ress, D., Xu, J., ... & McMahan, U. J. (2009). Macromolecular connections of active zone material to docked synaptic vesicles and presynaptic membrane at neuromuscular junctions of mouse. *Journal of Comparative Neurology*, *513*(5), 457-468. doi:10.1002/cne.21975 PMID: 19226520 PMCID: PMC4288958

Naider, F., Becker, J. M., Lee, Y. H., & Horovitz, A. (2007). Double-mutant cycle scanning of the interaction of a peptide ligand and its G protein-coupled receptor. *Biochemistry*, *46*(11), 3476-3481. doi:10.1021/bi602415u PMID: 17298081 PMCID: PMC2590777

Nakao, Y. K., Motomura, M., Fukudome, T., Fukuda, T., Shiraishi, H., Yoshimura, T., Tsujihata, M., & Eguchi, K. (2002). Seronegative Lambert-Eaton myasthenic syndrome: study of 110 Japanese patients. *Neurology, 59*(11), 1773-1775. doi:10.1212/01.wnl.0000037485.56217.5f PMID: 12473768

Nishimune, H. (2012). Molecular mechanism of active zone organization at vertebrate neuromuscular junctions. *Molecular neurobiology, 45*(1), 1-16. doi:10.1007/s12035-011-8216-y PMID: 22135013 PMCID: PMC3890249

Nishimune, H., Sanes, J. R., & Carlson, S. S. (2004). A synaptic laminin–calcium channel interaction organizes active zones in motor nerve terminals. *Nature, 432*(7017), 580-587. doi:10.1038/nature03112 PMID: 15577901

Noda, Masaharu, Shin Shimizu, Tsutomu Tanabe, Toshiyuki Takai, Toshiaki Kayano, Takayuki Ikeda, Hideo Takahashi et al. "Primary structure of Electrophorus electricus sodium channel deduced from cDNA sequence." *Nature* 312, no. 5990 (1984): 121-127. doi:10.1038/312121a0 PMID: 6209577

Nowycky, M. C., Fox, A. P., & Tsien, R. W. (1985). Long-opening mode of gating of neuronal

calcium channels and its promotion by the dihydropyridine calcium agonist Bay K 8644. *Proceedings of the National Academy of Sciences, 82*(7), 2178-2182. doi:10.1073/pnas.82.7.2178 PMID: 2580308 PMCID: PMC397516

Fox, A. P., Nowycky, M. C., & Tsien, R. W. (1987). Kinetic and pharmacological properties distinguishing three types of calcium currents in chick sensory neurones. *The Journal of physiology*, *394*(1), 149-172. doi:10.1113/jphysiol.1987.sp016864 PMID: 2451016 PMCID: PMC1191955

Oh, S. J. (2017). Distinguishing features of the repetitive nerve stimulation test between Lambert–Eaton myasthenic syndrome and myasthenia gravis, 50-year reappraisal. *Journal of clinical neuromuscular disease, 19*(2), 66-75. doi:10.1097/CND.0000000000000190 PMID: 29189551

Oh, S. J., Claussen, G. G., Hatanaka, Y., & Morgan, M. B. (2009). 3, 4-Diaminopyridine is more effective than placebo in a randomized, double-blind, cross-over drug study in LEMS. *Muscle & Nerve: Official Journal of the American Association of Electrodiagnostic Medicine, 40*(5), 795-800. doi:10.1002/mus.21422 PMID: 19722254

Oh, S. J., Hatanaka, Y., Claussen, G. C., & Sher, E. (2007). Electrophysiological differences in seropositive and seronegative Lambert–Eaton myasthenic syndrome. *Muscle & nerve, 35*(2), 178-183. doi: 10.1002/mus.20672 PMID: 17058271

Oh, S. J., Kurokawa, K., Claussen, G. C., & Ryan Jr, H. F. (2005). Electrophysiological diagnostic criteria of Lambert–Eaton myasthenic syndrome. *Muscle & Nerve: Official Journal of the American Association of Electrodiagnostic Medicine, 32*(4), 515-520. doi:10.1002/mus.20389 PMID: 16003742

Ojala, K.S.; Kaufhold, C.J.; Davey, M.R.; Liang, M.; Wipf, P.; Meriney, S.D. (2020, June 11-14) GV-58, a selective calcium channel gating modifier, can increase muscle strength and neurotransmission in untreated and ASO-treated SMA model mice. In Proceedings of the Cure SMA Conference, Orlando, FL, USA.

Ojala, K. S., Ginebaugh, S. P., Wu, M., Miller, E. W., Ortiz, G., Covarrubias, M., & Meriney, S. D. (2021). A high-affinity, partial antagonist effect of 3, 4-diaminopyridine mediates action potential broadening and enhancement of transmitter release at NMJs. *Journal of Biological Chemistry, 296*. doi:10.1016/j.jbc.2021.100302 PMID: 33465376 PMCID: PMC7949096

O'Neill, J. H., Murray, N. M. F., & Newsom-Davis, J. _. (1988). The Lambert-Eaton myasthenic syndrome: a review of 50 cases. *Brain, 111*(3), 577-596. doi:10.1093/brain/111.3.577 PMID: 2838124

Ophoff, R.A., Terwindt., G.M., Vergouwe, M. N., van Eijk, R., Oefner, P. J., Hoffman, S.M., Lamerdin, J.E., Mohrenweiser, H. W., Bulman, D.E., Ferrari, M., Haan, J., Lindhout, D., Ommen, G. J. B., Hofker, M. H., Ferrari, M. D., Frants, R. R. (1996). Familial

hemiplegic migraine and episodic ataxia type-2 are caused by mutations in the Ca2+ channel gene CACNL1A4. *Cell, 87*(3), 543-552. doi:10.1016/s0092-8674(00)81373-2 PMID: 8898206

Pace, C. N. (1995). [24] Evaluating contribution of hydrogen bonding and hydrophobic bonding to protein folding. *Methods in enzymology*, *259*, 538-554. doi:10.1016/0076-6879(95)59060-9 PMID: 8538471

Pascuzzi, R. M. (2002). Myasthenia Gravis and Lambert-Eaton Syndrome. *Therapeutic apheresis, 6*(1), 57-68. doi:10.1046/j.1526-0968.2002.00403.x PMID: 11886578

Pantazis, A., Savalli, N., Sigg, D., Neely, A., & Olcese, R. (2014). Functional heterogeneity of the four voltage sensors of a human L-type calcium channel. *Proceedings of the National Academy of Sciences, 111*(51), 18381-18386. doi:10.1073/pnas.1411127112 PMID: 25489110 PMCID: PMC4280600

Peterson, B. Z., Tanada, T. N., & Catterall, W. A. (1996). Molecular Determinants of High Affinity Dihydropyridine Binding in L-type Calcium Channels (∗). *Journal of Biological Chemistry, 271*(10), 5293-5296. doi:10.1074/jbc.271.10.5293

Peterson, B. Z., Johnson, B. D., Hockerman, G. H., Acheson, M., Scheuer, T., & Catterall, W. A. (1997). Analysis of the Dihydropyridine Receptor Site of L-type Calcium Channels by Alanine-scanning Mutagenesis. *Journal of Biological Chemistry, 272*(30), 18752-18758. doi:10.1074/jbc.272.30.18752 PMID: 9228048

Pettersen, E. F., Goddard, T. D., Huang, C. C., Couch, G. S., Greenblatt, D. M., Meng, E. C., & Ferrin, T. E. (2004). UCSF Chimera—a visualization system for exploratory research and analysis. *Journal of computational chemistry, 25*(13), 1605-1612. doi:10.1002/jcc.20084 PMID: 15264254

Phillips, J. C., Hardy, D. J., Maia, J. D., Stone, J. E., Ribeiro, J. V., Bernardi, R. C., Buch, R., Fiorin, G., Hénin, J., Jiang, W., McGreevy, R., Marcelo C. R. M., Radak, B. K., Skeel, R. D., Singharoy, A., Wang, Y., Roux, B., Aksimentiev, A., Luthey-Schulten, Z., Kalé, L. V., Schulten, K., Chipot, C., & Tajkhorshid, E. (2020). Scalable molecular dynamics on CPU and GPU architectures with NAMD. *The Journal of chemical physics, 153*(4), 044130. doi:10.1063/5.0014475 PMID: 32752662 PMCID: PMC7395834

Phillips, J. C., Braun, R., Wang, W., Gumbart, J., Tajkhorshid, E., Villa, E., Chipot, C., Skeel, R.D., Kalé, M., & Schulten, K. (2005). Scalable molecular dynamics with NAMD. *Journal of computational chemistry, 26*(16), 1781-1802. PMID: 16222654 PMCID: PMC2486339

Pragnell, M., De Waard, M., Mori, Y., Tanabe, T., Snutch, T. P., & Campbell, K. P. (1994). Calcium channel β-subunit binds to a conserved motif in the I–II cytoplasmic linker of the α1-subunit. *Nature, 368*(6466), 67-70. doi:10.1038/368067a0 PMID: 7509046

Raybaud, A., Baspinar, E. E., Dionne, F., Dodier, Y., Sauvé, R., & Parent, L. (2007). The role of distal S6 hydrophobic residues in the voltage-dependent gating of CaV2. 3 channels. *Journal of Biological Chemistry, 282*(38), 27944-27952. doi: 10.1074/jbc.M703895200 PMID: 17660294

Richards, K. S., Swensen, A. M., Lipscombe, D., & Bommert, K. (2007). Novel CaV2. 1 clone replicates many properties of Purkinje cell CaV2.1 current. European Journal of Neuroscience, 26(10), 2950-2961. doi:10.1111/j.1460-9568.2007.05912.x PMID: 18001290

Richards, M. W., Butcher, A. J., & Dolphin, A. C. (2004). Ca2+ channel β-subunits: structural insights AID our understanding. *Trends in pharmacological sciences*, *25*(12), 626-632. doi: 10.1016/j.tips.2004.10.008 PMID: 15530640

Robinette, D. N. (2006). Photoaffinity labeling combined with mass spectrometric approaches as a tool for structural proteomics. *Expert review of proteomics, 3*(4), 399-408. doi:10.1586/14789450.3.4.399 PMID: 16901199 PMCID: PMC2266983

Ruiz, R., Cano, R., Casañas, J. J., Gaffield, M. A., Betz, W. J., & Tabares, L. (2011). Active zones and the readily releasable pool of synaptic vesicles at the neuromuscular junction of the mouse. *Journal of Neuroscience*, *31*(6), 2000-2008. doi:10.1523/JNEUROSCI.4663-10.2011 PMID: 21307238 PMCID: PMC6633039

Satake, S. I., & Konishi, S. (2020). Roscovitine differentially facilitates cerebellar glutamatergic and GABAergic neurotransmission by enhancing Cav2. 1 channel-mediated multivesicular release. *European Journal of Neuroscience, 52*(3), 3002-3021. doi:10.1111/ejn.14771 PMID: 32383214

Schneggenburger, R., & Neher, E. (2000). Intracellular calcium dependence of transmitter release rates at a fast central synapse. *Nature, 406*(6798), 889-893. doi:10.1038/35022702 PMID: 10972290

Schneggenburger, R., & Neher, E. (2005). Presynaptic calcium and control of vesicle fusion. *Current opinion in neurobiology, 15*(3), 266-274. doi:10.1016/j.conb.2005.05.006 PMID: 15919191

Schneider, T., Dibué, M., & Hescheler, J. (2013). How "Pharmacoresistant" is Cav2. 3, the major component of voltage-gated R-type Ca2+ channels?. *Pharmaceuticals*, *6*(6), 759-776. doi:10.3390/ph6060759 PMID: 24276260

Schneider, M. F., & Chandler, W. K. (1973). Voltage dependent charge movement in skeletal muscle: a possible step in excitation–contraction coupling. *Nature, 242*(5395), 244-246. doi:10.1038/242244a0 PMID: 4540479

Schuster, A., Lacinova, L., Klugbauer, N., Ito, H., Birnbaumer, L., & Hofmann, F. (1996). The

IVS6 segment of the L-type calcium channel is critical for the action of dihydropyridines and phenylalkylamines. The EMBO Journal, 15(10), 2365-2370. doi:10.1002/j.1460-2075.1996.tb00592.x PMID: 8665843 PMCID: PMC450166

Sedehizadeh, S., Keogh, M., & Maddison, P. (2012). The use of aminopyridines in neurological disorders. *Clinical neuropharmacology, 35*(4), 191-200. doi:10.1097/WNF.0b013e31825a68c5 PMID: 22805230

Slater, C. R. (2015). The functional organization of motor nerve terminals. *Progress in neurobiology, 134*, 55-103. doi:10.1016/j.pneurobio.2015.09.004 PMID: 26439950

Smart, O. S., Neduvelil, J. G., Wang, X., Wallace, B. A., & Sansom, M. S. (1996). HOLE: a program for the analysis of the pore dimensions of ion channel structural models. *Journal of molecular graphics*, *14*(6), 354-360. doi:10.1016/s0263-7855(97)00009-x PMID: 9195488

Smith, D. O., Conklin, M. W., Jensen, P. J., & Atchison, W. D. (1995). Decreased calcium currents in motor nerve terminals of mice with Lambert-Eaton myasthenic syndrome. *The Journal of physiology, 487*(1), 115-123. doi:10.1113/jphysiol.1995.sp020865 PMID: 7473242 PMCID: PMC1156603

Smith, E., & Collins, I. (2015). Photoaffinity labeling in target-and binding-site identification. *Future medicinal chemistry, 7*(2), 159-183. doi:10.4155/fmc.14.152 PMID: 25686004 PMCID: PMC4413435

Stary, A., Kudrnac, M., Beyl, S., Hohaus, A., Timin, E., Wolschann, P., Guy, H.R., & Hering, S. (2008). Molecular dynamics and mutational analysis of a channelopathy mutation in the IIS6 helix of Cav1. 2. *Channels, 2*(3), 216-223. doi:10.4161/chan.2.3.6160 PMID: 18836301 PMCID: PMC3196984

Stotz, S. C., Jarvis, S. E., & Zamponi, G. W. (2004). Functional roles of cytoplasmic loops and pore lining transmembrane helices in the voltage-dependent inactivation of HVA calcium channels. *The Journal of physiology, 554*(2), 263-273. doi:10.1113/jphysiol.2003.047068 PMID: 12815185 PMCID: PMC1664770

Sula, A., Booker, J., Ng, L. C., Naylor, C. E., DeCaen, P. G., & Wallace, B. A. (2017). The complete structure of an activated open sodium channel. *Nature communications*, *8*(1), 1-9. doi:10.1038/ncomms14205 PMID: 28205548 PMCID: PMC5316852

Tao, X., Lee, A., Limapichat, W., Dougherty, D. A., & MacKinnon, R. (2010). A gating charge transfer center in voltage sensors. *Science, 328*(5974), 67-73. doi:10.1126/science.1185954 PMID: 20360102 PMCID: PMC2869078

Tarr, T. B., Dittrich, M., & Meriney, S. D. (2013). Are unreliable release mechanisms conserved from NMJ to CNS?. *Trends in neurosciences, 36*(1), 14-22. doi:10.1016/j.tins.2012.09.009 PMID: 23102681 PMCID: PMC4076818

Tarr, T. B., Malick, W., Liang, M., Valdomir, G., Frasso, M., Lacomis, D., Reddel, S. W., Garcia-Ocano, A., Wipf, P., & Meriney, S. D. (2013b). Evaluation of a novel calcium channel agonist for therapeutic potential in Lambert–Eaton myasthenic syndrome. *Journal of Neuroscience, 33*(25), 10559-10567.

Tarr, T. B., Lacomis, D., Reddel, S. W., Liang, M., Valdomir, G., Frasso, M., Wipf, P., & Meriney, S. D. (2014). Complete reversal of Lambert–Eaton myasthenic syndrome synaptic impairment by the combined use of a K+ channel blocker and a Ca2+ channel agonist. *The Journal of physiology, 592*(16), 3687-3696. doi:10.1113/jphysiol.2014.276493 PMID: 25015919 PMCID: PMC4229355

Tarr, T. B., Wipf, P., & Meriney, S. D. (2015). Synaptic pathophysiology and treatment of Lambert-Eaton myasthenic syndrome. *Molecular neurobiology, 52*(1), 456-463. doi:10.1007/s12035-014-8887-2 PMID: 25195700 PMCID: PMC4362862

Takamori, M., Takahashi, M., Yasukawa, Y., Iwasa, K., Nemoto, Y., Suenaga, A., Nagataki, S., & Nakamura, T. (1995). Antibodies to recombinant synaptotagmin and calcium channel subtypes in Lambert-Eaton myasthenic syndrome. Journal of the neurological sciences, 133(1-2), 95-101. doi:10.1016/0022-510x(95)00162-u PMID: 8583238

Takamori, M., Motomura, M., Fukudome, T., & Yoshikawa, H. (2007). Autoantibodies against M1 muscarinic acetylcholine receptor in myasthenic disorders. European journal of neurology, 14(11), 1230-1235. doi:10.1111/j.1468-1331.2007.01931.x PMID: 17764462

Takamori, M. (2008). Lambert–Eaton myasthenic syndrome: search for alternative autoimmune targets and possible compensatory mechanisms based on presynaptic calcium homeostasis. *Journal of neuroimmunology, 201*, 145-152. doi:10.1016/j.jneuroim.2008.04.040 PMID: 18653248

Titulaer, M. J., Lang, B., & Verschuuren, J. J. (2011). Lambert–Eaton myasthenic syndrome: from clinical characteristics to therapeutic strategies. *The Lancet Neurology, 10*(12), 1098-1107. doi:10.1016/S1474-4422(11)70245-9 PMID: 22094130

Tottene, A., Pivotto, F., Fellin, T., Cesetti, T., van den Maagdenberg, A. M., & Pietrobon, D. (2005). Specific kinetic alterations of human CaV2. 1 calcium channels produced by mutation S218L causing familial hemiplegic migraine and delayed cerebral edema and coma after minor head trauma. *Journal of Biological Chemistry, 280*(18), 17678-17686. doi:10.1074/jbc.M501110200 PMID: 15743764

Tyson, J. R., & Snutch, T. P. (2013). Molecular nature of voltage-gated calcium channels: structure and species comparison. *Wiley Interdisciplinary Reviews: Membrane Transport and Signaling, 2*(5), 181-206. doi:10.1002/wmts.91

Urbano, F. J., Piedras-Rentería, E. S., Jun, K., Shin, H. S., Uchitel, O. D., & Tsien, R. W. (2003).

Altered properties of quantal neurotransmitter release at endplates of mice lacking P/Q-type Ca2+ channels. *Proceedings of the National Academy of Sciences, 100*(6), 3491-3496. doi:10.1073/pnas.0437991100 PMID: 12624181 PMCID: PMC152320

US Food and Drug Administration. (2018). FDA approves first treatment for Lambert-Eaton myasthenic syndrome, a rare autoimmune disorder. https://www.fda.gov/news-events/press-announcements/fda-approves-first-treatment-lambert-eaton-myasthenic-syndrome-rare-autoimmune-disorder

Vargas, E., Yarov-Yarovoy, V., Khalili-Araghi, F., Catterall, W. A., Klein, M. L., Tarek, M., Lindahl, E., Schulten, K., Perozo, E., Bezanilla, F. & Roux, B. (2012). An emerging consensus on voltage-dependent gating from computational modeling and molecular dynamics simulations. *Journal of General Physiology, 140*(6), 587-594. doi:10.1085/jgp.201210873 PMID: 23183694 PMCID: PMC3514734

Vavra, O., Filipovic, J., Plhak, J., Bednar, D., Marques, S., Brezovsky, J., Pavelka, A., Matyska, L., Damborsky, J. CAVERDOCK: A New Tool for Analysis of Ligand Binding and Unbinding Based on Molecular Docking, In preparation, 2018.

Vavra, O., Filipovic, J., Plhak, J., Bednar, D., Marques, S. M., Brezovsky, J., Stourac, J., Matyska, L., & Damborsky, J. (2019). CaverDock: a molecular docking-based tool to analyse ligand transport through protein tunnels and channels. Bioinformatics, 35(23), 4986-4993. doi:10.1093/bioinformatics/btz386 PMID: 31077297

Verschuuren, J. J., Wirtz, P. W., Titulaer, M. J., Willems, L. N., & van Gerven, J. (2006). Available treatment options for the management of Lambert-Eaton myasthenic syndrome. *Expert opinion on pharmacotherapy, 7*(10), 1323-1336. doi:10.1517/14656566.7.10.1323 PMID: 16805718

Vincent, A., Lang, B., & Newsom-Davis, J. (1989). Autoimmunity to the voltage-gated calcium channel underlies the Lambert-Eaton myasthenic syndrome, a paraneoplastic disorder. *Trends in neurosciences, 12*(12), 496-502. doi:10.1016/0166-2236(89)90109-4 PMID: 2480664

Wall-Lacelle, S., Hossain, M. I., Sauvé, R., Blunck, R., & Parent, L. (2011). Double mutant cycle analysis identified a critical leucine residue in the IIS4S5 linker for the activation of the CaV2. 3 calcium channel. *Journal of Biological Chemistry, 286*(31), 27197-27205. doi:10.1074/jbc.M111.237412 PMID: 21652722 PMCID: PMC3149313

Webb, B., & Sali, A. (2016). Comparative protein structure modeling using MODELLER. *Current protocols in bioinformatics*, *54*(1), 5-6. doi: 10.1002/cpbi.3 PMID: 27322406 PMCID: PMC5031415

Williams, T., & Kelley, C. (2011). Gnuplot 4.4. 3: an interactive plotting program.

Wu, L. G., Borst, J. G. G., & Sakmann, B. (1998). R-type Ca2+ currents evoke transmitter

release at a rat central synapse. *Proceedings of the National Academy of Sciences*, *95*(8), 4720-4725. doi:10.1073/pnas.95.8.4720 PMID: 9539805 PMCID: PMC22557

Wu, J., Yan, Z., Li, Z., Qian, X., Lu, S., Dong, M., ... & Yan, N. (2016). Structure of the voltage-gated calcium channel Ca v 1.1 at 3.6 Å resolution. *Nature, 537*(7619), 191-196. doi:10.1038/nature19321 PMID: 27580036

Wu, L. G., Westenbroek, R. E., Borst, J. G. G., Catterall, W. A., & Sakmann, B. (1999). Calcium channel types with distinct presynaptic localization couple differentially to transmitter release in single calyx-type synapses. *Journal of Neuroscience*, *19*(2), 726-736. doi:10.1523/JNEUROSCI.19-02-00726.1999 PMID: 9880593 PMCID: PMC6782194

Wu, M., White, H. V., Boehm, B. A., Meriney, C. J., Kerrigan, K., Frasso, M., Liang, M., Gotway, E. M., Wilcox, M. R., Johnson, J. W., Wipf, P., & Meriney, S. D. (2018). New Cav2 calcium channel gating modifiers with agonist activity and therapeutic potential to treat neuromuscular disease. *Neuropharmacology, 131*, 176-189. doi:10.1016/j.neuropharm.2017.12.022 PMID: 29246857 PMCID: PMC5820137

Xie, C., Zhen, X. G., & Yang, J. (2005). Localization of the activation gate of a voltage-gated Ca2+ channel. *Journal of General Physiology, 126*(3), 205-212. doi:10.1085/jgp.200509293 PMID: 16129771 PMCID: PMC2266579

Yan, Z., Chi, P., A. Bibb, J., A. Ryan, T., & Greengard, P. (2002). Roscovitine: a novel regulator of P/Q-type calcium channels and transmitter release in central neurons. *The Journal of physiology, 540*(3), 761-770. doi:10.1113/jphysiol.2001.013376 PMID: 11986366 PMCID: PMC2290289

Yang, J., Elllnor, P. T., Sather, W. A., Zhang, J. F., & Tsien, R. W. (1993). Molecular determinants of Ca 2+ selectivity and ion permeation in L-type Ca 2+ channels. *Nature, 366*(6451), 158-161. doi:10.1038/366158a0 PMID: 8232554

Yang, N., George Jr, A. L., & Horn, R. (1996). Molecular basis of charge movement in voltage-gated sodium channels. *Neuron, 16*(1), 113-122. doi:10.1016/s0896-6273(00)80028-8 PMID: 8562074

Yarotskyy, V., & Elmslie, K. S. (2007). Roscovitine, a cyclin-dependent kinase inhibitor, affects several gating mechanisms to inhibit cardiac L-type (Ca (V) 1.2) calcium channels. *British journal of pharmacology, 152*(3), 386-395. doi:10.1038/sj.bjp.0707414 PMID: 17700718 PMCID: PMC2042960

Yarotskyy, V., & Elmslie, K. S. (2009). Open-state occupancy prevents gating charge relaxation of N-type (CaV2. 2) calcium channels. *Biophysical journal, 97*(9), 2446-2455. doi:10.1016/j.bpj.2009.08.014 PMID: 19883587 PMCID: PMC2770605

Yarotskyy, V., Gao, G., Du, L., Ganapathi, S. B., Peterson, B. Z., & Elmslie, K. S. (2010).

Roscovitine binds to novel L-channel (CaV1. 2) sites that separately affect activation and inactivation. *Journal of Biological Chemistry, 285*(1), 43-53. doi:10.1074/jbc.M109.076448 PMID: 19887376 PMCID: PMC2804190

Yarotskyy, V., Gao, G., Peterson, B. Z., & Elmslie, K. S. (2012). Domain III regulates N-type (CaV2. 2) calcium channel closing kinetics. *Journal of neurophysiology, 107*(7), 1942-1951. doi:10.1152/jn.00993.2011 PMID: 22205645 PMCID: PMC3331666

Yarov-Yarovoy, V., DeCaen, P. G., Westenbroek, R. E., Pan, C. Y., Scheuer, T., Baker, D., & Catterall, W. A. (2012). Structural basis for gating charge movement in the voltage sensor of a sodium channel. *Proceedings of the National Academy of Sciences, 109*(2), E93-E102. doi:10.1073/pnas.1118434109 PMID: 22160714 PMCID: PMC3258622

Yokoyama, C. T., Westenbroek, R. E., Hell, J. W., Soong, T. W., Snutch, T. P., & Catterall, W. A. (1995). Biochemical properties and subcellular distribution of the neuronal class E calcium channel alpha 1 subunit. *Journal of Neuroscience, 15*(10), 6419-6432. doi:10.1523/JNEUROSCI.15-10-06419.1995 PMID: 7472405 PMCID: PMC6577977

Yu., F.H., & Catterall, W. A. (2004). The VGL-chanome: a protein superfamily specialized for electrical signaling and ionic homeostasis. *Science Signaling, 2004*(253), re15. doi:10.1126/stke.2532004re15 PMID: 15467096

Zamponi, G. W., Striessnig, J., Koschak, A., & Dolphin, A. C. (2015). The physiology, pathology, and pharmacology of voltage-gated calcium channels and their future therapeutic potential. *Pharmacological reviews*, *67*(4), 821-870. doi:10.1124/pr.114.009654 PMID: 26362469 PMCID: PMC4630564

Zhao, Y., Huang, G., Wu, J., Wu, Q., Gao, S., Yan, Z., ... & Yan, N. (2019). Molecular basis for ligand modulation of a mammalian voltage-gated Ca2+ channel. *Cell*, *177*(6), 1495-1506. doi:10.1016/j.cell.2019.04.043 PMID: 31150622

Zhen, X. G., Xie, C., Fitzmaurice, A., Schoonover, C. E., Orenstein, E. T., & Yang, J. (2005). Functional architecture of the inner pore of a voltage-gated Ca2+ channel. *The Journal of general physiology, 126*(3), 193-204. doi:10.1085/jgp.200509292 PMID: 16129770 PMCID: PMC2266581

Zhuchenko, O., Bailey, J., Bonnen, P., Ashizawa, T., Stockton, D. W., Amos, C., ... & Lee, C. C. (1997). Autosomal dominant cerebellar ataxia (SCA6) associated with small polyglutamine expansions in the α 1A-voltage-dependent calcium channel. *Nature genetics, 15*(1), 62-69. doi:10.1038/ng0197-62 PMID: 8988170